THE UNIVERSITY OF
SYDNEY

Phase-referenced Interferometry and Narrow-angle Astrometry with SUSI

Yitping Kok

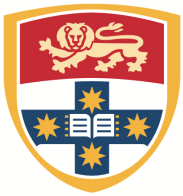

THE UNIVERSITY OF SYDNEY

A thesis submitted for the degree of Doctor of Philosophy

Faculty of Science
The University of Sydney

2014

To my parents

Abstract

This thesis describes the development of an astrometric facility at the Sydney University Stellar Interferometer (SUSI) with an aim to measure at high precision the relative astrometry of bright close binary stars and ultimately to detect the presence of exoplanets within those binary star systems through observations of the systems' perturbed motion. At the core of the facility is a new beam combiner that is phase-referenced to an existing primary beam combiner in the visible wavelength regime. The latter provides post-processed fringe-tracking information to the former for fringe stabilization and coherent integration of pre-recorded stellar fringes using newly developed data reduction software. Interference fringe packets of a binary star are recorded alternately; first the fringe packet of the primary, then the secondary, finally back to the primary again. The measurement of the fringe packet separation is facilitated by an air-filled differential delay line and a network of interferometer-based metrology systems. Characterizations and initial astronomical observations carried out with the dual beam combiner setup demonstrated for the first time the success of the dual-star phase-referencing technique in visible ($<1\mu$m) wavelengths. The current astrometric precision is larger than 100μas while the long term astrometric accuracy is yet to be characterized. In a parallel development, a complementary observing method using only the primary beam combiner is also demonstrated in this thesis. Relative astrometry of binary stars up to $\sim 0.8''$ separation with this technique has been demonstrated to have precision of better than 100μas. A simple detection limit analysis based on a list of target binary stars estimates up to two exoplanet detections can be achieved with SUSI if the new astrometric facility attains precision of 10μas while the primary beam combiner operates at its designed peak performance. Finally, one new stellar companion was resolved and a preliminary astrometry for another suspected companion was estimated from the astronomical observation data collected throughout the course of this thesis.

Acknowledgement

I would like to express my sincere thanks to all the people who have helped me with my thesis. They are namely my supervisors, Mike Ireland, Gordon Robertson and Peter Tuthill; my colleagues in the SUSI group, Benjamin Warrington, Bill Tango and Mike Hill; and my fellow interferometrists, Vicente Maestro, Xavier Haubois and Aaron Rizzuto. I would also like to thank my mentors and friends in other parts of the world whom I met at conferences and have learned so much about optical stellar interferometry from through both formal and informal conversations, namely, Francoise Delplancke, Christian Schmid, Roberto Abuter and Andreas Glindemann.

This thesis would not have been successful without the mentorship of my three admirable supervisors. Besides helping me with the overall project planning, my primary supervisor, Peter Tuthill, also provided me with a lot of opportunities to meet various people in the field. Other than that, I also owe a special thanks to Peter for helping me to submit this thesis from Sydney. A special thanks also goes to Gordon Robertson who is always the first to proofread my manuscripts and to give words of encouragement after every iteration. Last but not least, I must emphasize my gratitude to Mike Ireland whom I have spent many hours with discussing about every detail of the project and learning the art of optical interferometry.

Financial support from the University of Sydney International Scholarship (UsydIS), which funded my thesis and from other grants, namely the Postgraduate Research Scholarship Scheme (PRSS), the Fizeau Program and the grants that funded MUSCA and SUSI, which partially funded my travels to SUSI, VLTI, ESO and various conferences are gratefully acknowledged.

Finally, I would like to express my utmost gratitude to my wife Shiaohuey for the unconditional moral support provided throughout the course of this thesis even though she was at the same time undergoing the same if not even more challenging circumstances as a PhD student herself, and to my daughter Jiayu for cheerfully neutralizing the stress level at home.

Declaration of Originality

This thesis describes the work carried out at the Sydney University Stellar Interferometer (SUSI) and the Sydney Institute of Astronomy (SIfA) of the School of Physics of The University of Sydney. The work described is of my own except where acknowledged otherwise. The initial conceptual design of the astrometric facility described in this work was part of a proposal for an Australian Research Council Discovery Project research grant awarded to Ireland (2010a) and which funded the project. Significant contributions to many other subsystems of SUSI from other people in the SUSI group (past and present) are highlighted in Section 2.3.

Yitping Kok

Date

Publications

The following papers which have been published in or submitted to refereed journals are results from the work done in this thesis and other related research collaboration. The content of the papers have been reproduced in Chapter 3, 4, 5 and 6.

- Kok, Y., Ireland, M.J., Tuthill, P.G., Robertson, J.G., Warrington, B.A. & Tango, "Phase-referenced interferometry and towards narrow-angle astrometry with SUSI", JAI, 2013, accepted.

- Kok, Y., Ireland, M.J., Tuthill, P.G., Robertson, J.G., Warrington, B.A. & Tango, "Low-cost scheme for high-precision dual-wavelength laser metrology", Appl. Opt., **52** (12), 2808–2814, 2013.

- Kok, Y., Maestro, V., Ireland, M.J., Tuthill, P.G. & Robertson, J.G., "Simulating a dual beam combiner at SUSI for narrow-angle astrometry", Exp. Astron., **36**, 195–221, 2013.

- Maestro, V., Che, X., Huber, D., Ireland1, M.J., Monnier, J.D., White, T.R., Kok, Y., Schaefer, G.H., ten Brummelaar, T.A. & Tuthill, P.G., "Optical interferometry of early-type stars with PAVO@CHARA I. Fundamental stellar properties", MNRAS, **434**, 1321–1331, 2013.

- Antoci, V., Handler, G., Grundahl, F., Carrier, F., Brugamyer, E.J., Robertson, P., Kjeldsen, H., Kok, Y., Ireland, M. & Matthews, J.M., "Searching solar-like oscillations in δ Scuti star ρ Puppis", MNRAS, **435**, 1563–1575, 2013.

- Rizzuto, A.C., Ireland, M.J., Robertson, J.G., Kok, Y., Tuthill, P.G., Warrington, B.A., Haubois, X., Tango, W.J., Norris, B., ten Brummelaar, T.A., Kraus, A.L., Jacob, A.P. & Laliberte-Houdeville, C., "Long-baseline interferometric multiplicity survey of the Sco-Cen OB association", MNRAS, **436**, 1694–1707, 2013.

In addition, the following are publications in conference proceedings resulted from the work done in this thesis and other related research collaboration.

- Kok, Y., Ireland, M.J., Tuthill, P.G., Robertson, J.G., Warrington, B.A. & Tango, W.J., "Self-phase-referencing interferometry with SUSI", Proc. SPIE, **8445**, 844521, July 2012.
- Maestro, V., Kok, Y., Huber, D., Ireland, M.J., Tuthill, P.G., White, T., Shaefer, G., ten Brummelaar, T.A., McAlister, H.A., Turner, N., Farrington, C. & Goldfinger, P.J., "Imaging rapid rotators with the PAVO beam combiner at CHARA", Proc. SPIE, **8445**, 84450G, July 2012.
- Allouche, F., Hadjara, M., Kok, Y., Vakili, F., Abe, L., & Gori, P.-M., "DIFFRACT: DIFFerential Remapped Aperture Coronagraphic Telescope", Proc. SPIE, **8446**, 84467E, July 2012.
- Robertson, J.G., Ireland, M.J., Tango, W.J., Tuthill, P.G., Warrington, B.A., Kok, Y., Rizzuto, A.C., Cheetham, A. & Jacob, A.P., "Science and technology progress at the Sydney University Stellar Interferometer", Proc. SPIE, **8445**, 84450N, July 2012.
- Feiden, G., Guinan, E., Boyajian, T., Kok, Y., Basturk, O., Roberson, A. & Ribas, I., "Mining the Kepler Mission Database: Rotations, Starspots, Ages and Possible Tidal Interactions of Stars with Close-in Planets", AAS Meeting #217, 140.18, 2011.
- Robertson, J.G., Ireland, M.J., Tango, W.J., Davis, J., Tuthill, P.G., Jacob, A.P., Kok, Y. & ten Brummelaar, T.A., "Instrumental developments for the Sydney University Stellar Interferometer", Proc. SPIE, **7734**, 773405, July 2010.

List of Abbreviations

AO	adaptive optics
APD	avalanche photodiode
CCD	charged-coupled device
DDL	differential delay line
DL	dual laser
FFT	Fast Fourier Transform
FOV	field of view
FP	fringe packet
GPS	Global Positioning System
GUI	graphical user interface
IM	intermediate mass
IR	infra-red
LED	light emitting diode
LHS	left hand side
NTP	Network Time Protocol
OLBI	Optical Long Baseline Interferometry
OPD	optical path difference
PR	phase-referenced
PZT	piezoelectric transducer
RHS	right hand side
rms	root mean square
RV	radial velocity
SL	single laser
SNR	signal to noise ratio
WL	white light

Contents

Chapter 1

Introduction

The aim of this research is to design and build an instrument to perform high-precision astrometry as a means to search for extra-solar planets (or exoplanets) around bright close binary stars, which have angular separations between ∼0.02 to 2 arcseconds (″) in the sky. These binary stars are also known as visual binaries although many are not easily split in the image plane of even a powerful telescope.

1.1 Motivations

The context for the research in this thesis is illustrated in this section by noting five key aspects which motivated its timeliness and relevance to the present state of the art.

Astrometry is a proven technique

Astrometry is the science of measuring the position of a celestial body on the celestial sphere. Astrometry is not a new technique. Ancient civilizations had used astrometry to measure the position of stars (Kanas, 2007) which eventually led to the discovery of Earth's precession (de Santillana & von Dechend, 1977, p. 66), to measure the motion of the Sun and the Moon which led to accurate predictions of solar eclipses, etc (Caussin de Perceval, 1804; Hartner, 1980; King, 1973). In the field of planet detection, Neptune in our solar system was first detected by astrometry. It was discovered when the observed positions of the planet Uranus differed from the predicted positions by about 1–2″ (Airy, 1846).

But if an unknown planet in the vicinity, which was later discovered to be Neptune, was included in the model calculation the discrepancy was removed.

Astronomers have been trying to use the same technique to detect planets orbiting other stars (Muterspaugh et al., 2010b; Pravdo & Shaklan, 2009). In order to do so, like observing the perturbation of Uranus' orbit, astronomers observe and detect the reflex motion of an exoplanet host star. A star with an orbiting planet exhibits a reflex motion as a result of the gravitational pull of the planet as it orbits the star. The amplitude of the periodic reflex motion of the star, which is proportional to the mass of the planet and the orbital distance of the planet from the star but inversely proportional to the mass of the star and the distance of the exoplanetary system from Earth, is extremely small. For example, a Sun-like star with a Jupiter-mass planet in a 5AU orbit exhibits a reflex motion in the order of 50 microarcseconds if the star is 100pc away from Earth. This is the typical size of motion to search for in potential exoplanet host stars. The angle subtended by an arcsecond is $\frac{1}{3600}$ of a degree. A milliarcsecond (abbreviated as mas) is one thousandth of an arcsecond and a microarcseond (abbreviated as μas) is one millionth of an arcsecond.

Measuring the position of a star to an accuracy of 10–50μas is not an easy task even now. The wide-angle (absolute) astrometric precision that a single telescope can achieve is about 0.7–0.9mas (Perryman et al., 1997) while the narrrow-angle (relative) astrometric precision is about 0.1–0.3mas (Fritz et al., 2010; Kervella et al., 2013) for star separations of less than $3''$. The former achievement was carried out in space, in the absence of atmospheric turbulence. A purpose built astrometric optical long baseline interferometer can only routinely measure absolute stellar positions to an accuracy of 1–2mas (Armstrong et al., 1998). A preliminary proof-of-concept of high-precision interferometric narrow-angle astrometry was demonstrated at the Palomar Testbed Interferometer (PTI) with the PHASES experiment (Lane & Muterspaugh, 2004). PHASES selected 15 binaries out of a total of 51 targets surveyed for extended observations and found one candidate planet (Muterspaugh et al., 2010a) with its astrometric precision of $\sim$10μas. The candidate planet, which is in great need of follow-up observations, is slightly more massive than Jupiter.

In a nutshell, detection of any exoplanets with astrometry is possible but difficult. At the time writing, no confirmed exoplanet has been discovered using astrometry (Anglada-Escudé et al., 2010; Bean et al., 2010; Pravdo & Shaklan, 2009).

Astrometry complements existing detection methods

The first exoplanet orbiting a normal star was found in 1995 by observing the Doppler effect of light from the host star (Mayor & Queloz, 1995). The spectrum of the starlight is red- and blue-shifted as the host star orbits around a common center of gravity with the nearby planet. The amount of shift in the spectrum depends on the radial velocity (RV) of the host star in its orbit around the center of gravity. The higher the velocity, due the presence of a more massive and closer in planet, the larger the shift in the spectrum. For instance, the host star with a 1-2 Jupiter mass (M_J) planet found in the first detection (Mayor & Queloz, 1995) has an RV signature of about 60ms^{-1} (zero-to-peak amplitude). Ever since the first detection the RV technique has become the work horse of exoplanetary detection with significant improvements in sensitivity along the way. Just recently, an Earth size planet was detected orbiting the nearest star from Earth, α Cen B, which exhibits a minute RV signature of not more than 51cms^{-1} (Dumusque et al., 2012). Fig. 1.1 shows the distribution of exoplanets found until October 2012[1] and the 0.5-1ms^{-1} RV sensitivity cutoff lines which distinctly group the planets onto one side of the plot. The horizontal axis, a_P, in the plot is the semi-major axis of an elliptical orbit of the planet around its host star.

Despite such exquisite precision, the RV technique is not sensitive in detecting planets in B- and A-type (AB) stars, which are relatively bright in the night sky and usually more massive and have shorter lifetime than main sequence G-type stars like the Sun. This is evident in Fig. 1.1 as the exoplanets are color-coded with the stellar type of their host stars. AB stars are difficult targets for the RV technique (Galland et al., 2005) because their spectrum has fewer lines from which Doppler shift are detected and in addition the lines are broadened by high rotational velocity of the star itself. Although an optimized data analysis technique, which used a Fourier transform instead of the usual cross-correlation approach (Chelli, 2000), was proposed and experimented on to overcome this problem, the large uncertainties in the measurements restricted the kinds of planets ($a_P < 0.5$AU) such a method could detect (Galland et al., 2006, 2005). Although the technique managed to detect several planets around evolved A stars due to their smaller rotation speed (Johnson et al., 2010), none has been detected around AB main sequence stars using the RV technique. Consequently, other methods such as direct imaging with adaptive optics (AO) (Marois et al., 2008), sparse aperture masking (Kraus & Ireland, 2012) or astrometry, must be used.

Although direct imaging techniques are best at imaging hot young planets at distances far out from their host stars, they cannot observe planets which are closer

[1] `http://www.exoplanet.eu`

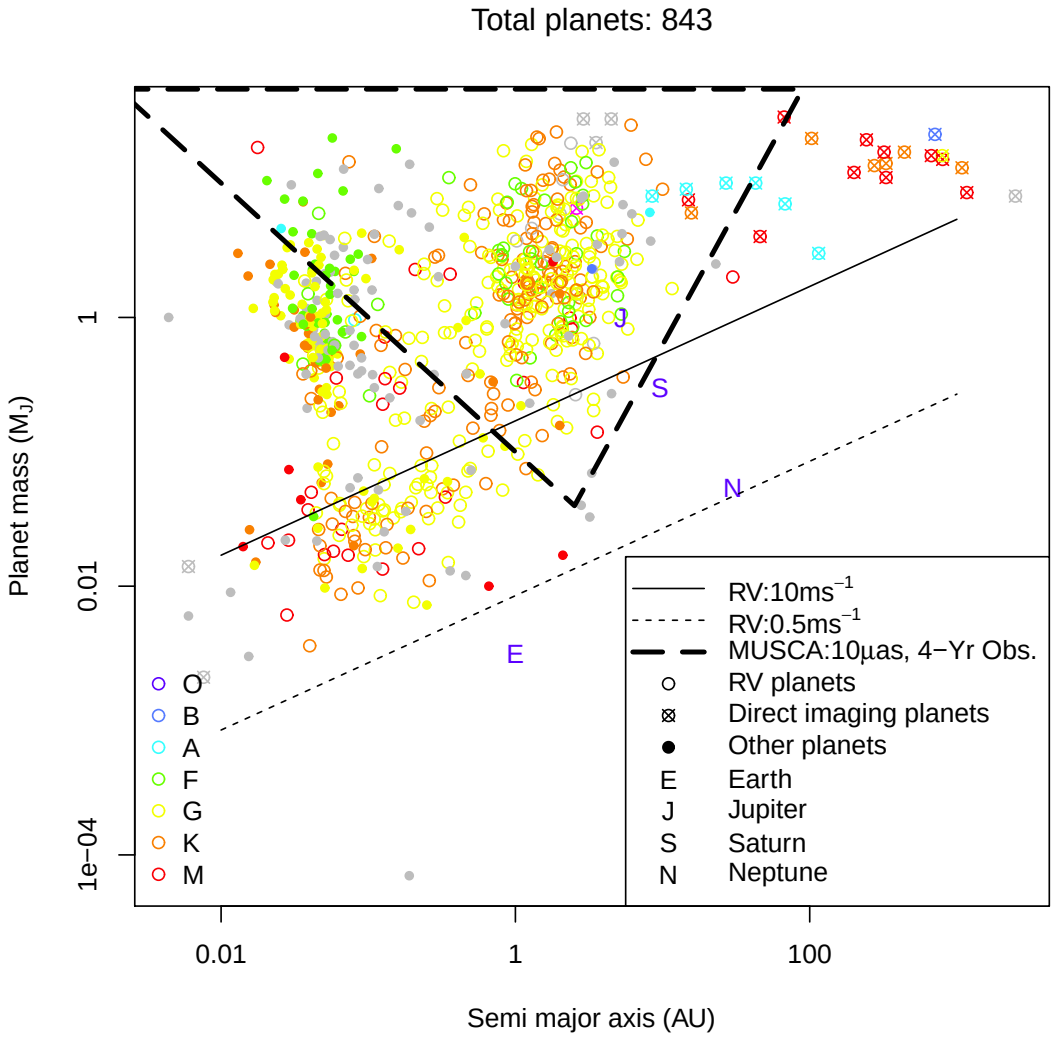

Figure 1.1: Distribution of exoplanets (circle symbols are color coded to the spectral type of the planets' host stars) discovered until October 2012 and the limits of exoplanet detection between radial velocity (RV) and astrometry technique such as MUSCA.

in because they are fundamentally limited by the diffraction-limited image size of the star which is defined by the diameter of the telescope used. Therefore the best method to search for planets, especially giant ones, around AB stars in this region of observational blind spot ($a_P < 20$AU) is astrometry.

Unlike the RV technique, astrometry is more sensitive to planets with a large orbital radius, a_P. With a detection limit of 10μas, the types of planets detectable with astrometry are indicated by the area bounded by the long dashed lines in Fig. 1.1. Further details on the principle of astrometric exoplanet detection are given in Chapter 8.

Intermediate-mass stars have high probability of hosting giant planets

Stars that are 1.5–10× more massive than the Sun (1.5–10$M_\odot$), a category which most AB stars belong to, are also referred to as intermediate mass (IM) stars. Statistics extracted from planets detected around IM stars (1.5–2$M_\odot$), mostly evolved A-type stars, show that (1) planets formed around these stars have minimum masses and semi-major axes different from those found around Sun-like stars (Bowler et al., 2010) and (2) the Jupiter-mass exoplanets occurrence rate around IM stars is higher, ∼9% (Lovis & Mayor, 2007), ∼11% (Johnson et al., 2010) or even as high as ∼27% (Bowler et al., 2010), compared to Sun-like stars (∼6%) (Bonavita & Desidera, 2007), which supports the theory that planetary formation is more efficient for higher mass stars (Kennedy & Kenyon, 2008). Similar statistics, 5.9–18.8%, were reported from an AO direct imaging survey (Vigan et al., 2012), which did not have the same limitation as the RV surveys and probed distances further than 5AU from the host star (illustratively planets in the top right corner of Fig. 1.1).

Only optical long baseline interferometry (OLBI) offers the required precision for ground-based observation

There are two methods to perform high-precision astrometry, each exploiting a different aspect of optics technology.

The first is by means of imaging. This classical and conventional method measures the position of stellar images created and projected onto an array of photodetectors by an imaging system. Before the CCD cameras were invented, images were recorded with photographic plates and measurements were done on the plates. Ground-based astrometry using this technique is limited by the atmospheric turbulence for faint stars and the quality of the optics for bright stars. The limiting

precision of each factor was estimated to be $\sim$300μas and $\sim$130μas respectively over a field of view of $\lesssim 3''$ (Fritz et al., 2010). Recently, a 100μas precision narrow-angle astrometry of a $0.6''$ separation binary star system was demonstrated using this technique (Kervella et al., 2013).

In order to overcome the limitation imposed by the atmosphere and optics, future high precision astrometric observations based on the imaging technique is planned to be carried out in space with a very long focal length telescope over a long exposure time. Using a sophisticated algorithm to measure the position of an image of a star to an accuracy of one-millionth of a pixel, this technique could achieve astrometric precision of 10μas or better (Casertano et al., 2008; Malbet et al., 2012; Sozzetti, 2011). GAIA is an instrument designed to do just this. It is the successor of the Hipparcos instrument. It is built by the European Space Agency (ESA) and will be launched into a Lissajous orbit around the Lagrange point L2 of the Sun-Earth system in 2013. It is capable of measuring positions of stars to an accuracy of 10μas. However, it is designed to achieve such accuracy with stars not brighter than 12th magnitude. Its accuracy is expected to degrade when observing brighter stars.

The second method is by means of optical long baseline interferometry (OLBI). An optical long baseline interferometer uses two or more telescopes like slits in the famous Young's double slit experiment to form interference fringes with starlight. Each star is a light source and the interferometer is able to measure the separation of the stars by accurately measuring the difference in optical delay between their fringes (see Section 2.4 for details). Although it is still very difficult to achieve 10–50μas accuracy over a wide field of view even with a purpose built astrometric optical long baseline interferometer, the technical difficulties are relaxed if measurement of a star's relative position in the sky is sufficient.

The potential of an optical long baseline interferometer and its advantage over a single mirror telescope in achieving high-precision narrow-angle astrometry was first realized by Shao & Colavita (1992). This method has since been demonstrated with PHASES (Muterspaugh et al., 2010b) at PTI (Colavita et al., 1999) in the infra-red wavelengths and achieved a narrow-angle astrometric precision of about 35μas (with binary stars of less than $1''$ separation) within 70 minutes of observation. Despite their narrow-angle astrometric capability, optical long baseline interferometers are very sensitive to atmospheric turbulence, have very low light throughput and therefore are limited to observing bright stars (not fainter than 8th magnitude in the visible wavelengths).

The SUSI advantage

The Sydney University Stellar Interferometer (SUSI) is a university owned optical long baseline interferometer located near Narrabri, Australia (Davis et al., 1999). The furthest distance between two siderostats (mirrors used to collect starlight) in the SUSI array, also known as the baseline, is 160m, although it can be extended to 640m which will then make it the world's longest. SUSI is designed to operate in the visible wavelengths and in combination of its long baselines, it has the longest baseline per unit wavelength ($\sim 2 \times 10^8$) in the southern hemisphere. This is an important metric because it determines the fundamental angular resolution limit of an interferometer. It is also a factor that determines the narrow-angle astrometric precision an optical long baseline interferometer can achieve (Shao & Colavita, 1992). Precision increases with longer baseline. The next longest baseline ($\sim 1 \times 10^8$) in the southern hemisphere is at the Very Large Telescope Interferometer (VLTI) on top of Cerro Paranal, Chile (Glindemann et al., 2000) and the current longest of all ($\sim 5 \times 10^8$) is at the Center for High Angular Resolution Astronomy (CHARA) array on top of Mount Wilson, California (McAlister et al., 2005).

SUSI, being a university owned instrument, has the advantage of running dedicated science programs for its local research group. SUSI can carry out frequent observations of a list of target stars and such advantage is very useful for exoplanet search programs which require long uninterrupted observation.

For added convenience, SUSI has recently been upgraded to be fully remotely controllable (Robertson et al., 2010). This feature is significant because it provides a quicker and worldwide access to the instrument considering that SUSI is situated about 560km from Sydney, where its home institute is based, and has no full-time staff on-site.

1.2 Methodology

The technique that is used in this thesis to facilitate the measurement of the optical delay of stellar fringes is phase-referencing interferometry. Phase-referencing in interferometry is a technique which uses the phase information in the interferometric signal of a reference object to correct the phase of the signal from a target object for path length fluctuations in the atmosphere. The target object can either be the same or a nearby object. This technique has been widely used in radio interferometry but was first used in optical long baseline interferometry in the early 1990s (Colavita, 1992; Shao & Colavita, 1992).

Unlike radio interferometry where phase-referencing can be achieved by rapidly slewing the antennas back and forth between the target object and the reference, both objects must be observed simultaneously in optical interferometry because the time interval during which the fringes appear static (i.e. the atmospheric coherence time) is measured in milliseconds. Therefore, phase-referencing optical interferometers usually have two beam combiners to record interferometric signals from two objects at the same time.

The approach to building the dual beam combiner needed for an astrometric exoplanet search is based on two key ideas, reusability and simplicity. By reusability, it means the instrument is to be built by maximizing the usage of existing hardware. This kept the cost of the development to its minimum and reduced development time. And by simplicity, it means the design of the instrument is to be kept as simple as possible so that systematic errors in the measurements could be easily identified and corrected.

A beam combiner is where beams of light are combined and form interference fringes. It is also the instrument where science measurements are performed. The existing beam combiner in SUSI is the Precision Astronomical Visible Observation (PAVO) instrument. PAVO is designed to measure the visibility of stellar fringes. It has a closed feedback loop controller that allows it to track stellar fringes during observation. This is important because stellar fringes are constantly moving due to atmospheric turbulence. In order to complement PAVO's capability for astrometry, a new beam combiner is built and additional supporting subsystems installed. The new beam combiner is named the Microarcsecond University of Sydney Companion Astrometry (MUSCA) instrument. MUSCA and the new supporting subsystems are designed to measure the separation between stellar fringe packets[2] from two closely separated stars in optical delay while PAVO is tracking on fringes of a reference star.

Unlike the approach taken by other instruments designed for similar application (Delplancke, 2008; Muterspaugh et al., 2010b), both PAVO and MUSCA operate in the visible wavelengths and are unusual in that they perform dual-star phase-referencing and measurement in post-processing. This means that the main observable, i.e. the separation of the fringe packets, is not measured in real time but computed from recorded measurements of related physical quantities after an observation has ended. Operating in the visible wavelengths offers the beam combiners at SUSI a potential of measuring the relative position of a target star about three times more accurately at a cost of tighter tolerances and a post-processing

[2]A fringe packet is an interference pattern produced by a light source of finite bandwidth (e.g. starlight) whereby the fringe visibility diminishes quickly to zero as the optical path difference (OPD) producing the fringes deviates away from zero.

approach to phase-referencing allows PAVO to perform real time stellar fringe tracking at a much lower computing bandwidth. At the same time, it allows MUSCA to operate without a closed feedback loop controller thereby keeping its design at its most basic.

PAVO and MUSCA operate in a master-slave configuration, where PAVO is the master and MUSCA is the slave. During observation, PAVO acquires and tracks stellar fringes while MUSCA records the fringes for later processing. At the same time, a network of interferometry based metrology systems (one of several new supporting subsystems) also measures the length of the optical paths between and within the two beam combiners so that the separation of the stellar fringe packets can be computed at high precision using the data reduction pipeline.

The new astrometric capability of SUSI was then tested with several on-sky observations to evaluate the performance of the instruments before a full scale search program is to be conducted. Only observations of bright close binary stars could be performed because of optical limitations of SUSI. Close binary stars are double stars which orbit each other around a common center of mass and are separated by not more than a few arcseconds on the sky. Despite the limitation, the list of observable targets still represents the general population of IM stars well because more than 70% of IM stars form in binary or multiple systems (Kobulnicky & Fryer, 2007; Kouwenhoven et al., 2007) and exoplanets are equally likely to form around single as well as binary/multiple star systems (Bonavita & Desidera, 2007; Raghavan et al., 2010).

Finally, an estimated number of exoplanet detections that could be made with PAVO and MUSCA at SUSI is presented if a full survey is carried out.

1.3 Outline of thesis

This thesis consists of nine chapters.

Chapter 2 provides an overview of the basic principles of optical long baseline interferometry (OLBI). It introduces the Sydney University Stellar Interferometer (SUSI) and discusses important subsystems that make up the interferometer. It also gives a theoretical introduction to the application of OLBI in narrow-angle astrometry, which includes challenges in achieving precision of tens of microarcseconds.

Chapter 3 describes the dual beam combiner setup at SUSI in detail. It also

explains the solution adopted at SUSI to address one of the challenges mentioned in the previous chapter.

Chapter 4 discusses a computer simulation framework which was written to assist the development and verify the result of the dual beam combiner data reduction pipeline. It also presents the simulated phase-referencing performance of the dual beam combiner operation.

Chapter 5 describes a network of metrology systems put in place to measure and monitor the optical path length variation in paths which are non-common to the two beam combiners and affect their phase-referencing performance. It also discusses a novel and inexpensive displacement metrology system that can deliver measurements at a precision of several nanometers, a level which is required for narrow-angle astrometric application.

Chapter 6 provides a detailed discussion of the dual beam combiner data reduction pipeline. The discussion also includes how the metrology information embedded in the raw scientific data are extracted and used for phase-referencing. It also covers the data analysis to compute the relative astrometry of stars.

Chapter 7 showcases a collection of reduced data and results from astronomical observations made with the astrometric facility developed for this thesis.

Chapter 8 gives an estimate of the probability of exoplanet detection with the astrometric facility based on the number of target stars observable and its projected astrometric precision.

Chapter 9 concludes all findings of this thesis. The chapter also outlines recommendations for future development and sensitivity improvement.

Six appendices are included at the end of this thesis.

Chapter 2

Optical long baseline interferometry

An optical long baseline interferometer is an interferometer that has an interconnected array of light collecting elements separated at large but known distances to measure physical properties of astronomical sources. It has many subsystems within to (1) transport the light collected at each element to a central location and (2) ensure the difference of optical paths from the source to the central location along each arm of the interferometer is near zero.

The first optical long baseline interferometer was a 20-foot ($\sim$6m) interferometer mounted on the frame of the Hooker Telescope at the Mount Wilson Observatory. It was used to measure the angular diameter of Betelgeuse, the brightest star in the constellation of Orion, and found it to be $0.047''$ within 10% of uncertainty (Michelson & Pease, 1921). Optical long baseline interferometers are also used to create images of astronomical sources and measure positions of stars.

2.1 Inteferometric observables

In optical interferometry, light is regarded as a form of electromagnetic waves and obeys the principle of superposition. Although light waves vary in space and time, it is adequate to only discuss its properties in terms of spatial component and ignore the time component throughout this thesis because optical stellar interferometry seldom exploit the latter component for measurements[1]. The wavenumber

[1]The number of photons per second per wavelength bandwidth (μm) per frequency (Hz) is very small ($\ll 1$)

of a light wave is represented by the symbol σ in this thesis while its reciprocal or the wavelength is represented by the symbol λ unless stated otherwise.

Optical path difference and phases

In a simple two-element optical long baseline interferometer, illustrated by the schematic diagram in Fig. 2.1, light from an astronomical source is collected from two apertures using either plane mirrors or telescopes. The orientation and the separation of the apertures are known as the baseline of the interferometer. It is a vector quantity and is represented as $\vec{B}$ or simply B for its magnitude. The position of the astronomical source in the sky with respect to the baseline, defined by a unit vector $\hat{s}$, causes light waves collected at one aperture to be at a different phase compared to the other. The difference in phase between two locations is determined by the optical path difference (OPD) and its wavelength,

$$\Delta\phi = 2\pi\frac{\text{OPD}}{\lambda}. \tag{2.1}$$

Beams of light collected from the apertures are then transported by reflection from plane mirrors to a central location where they are combined. If the optical path length of each arm of the example interferometer in Fig. 2.1 is $x^{(i)}$, then the recombination of light at the central location is in phase if the OPD between the arms is zero or an integer multiple of the wavelength of light, λ, where,

$$\text{OPD} = \hat{s}\cdot\vec{B} + x^{(1)} - x^{(2)}. \tag{2.2}$$

The difference in optical path length should be scaled by the refractive indices of media along the optical path, but for simplicity sake the two arms of the interferometer are assumed to be in vacuum. The central location where the OPD is defined typically lies in the center of the field of view of the beam combiner. The OPD computed at this fiducial location is not unique and has different values for different stars because of the term $\hat{s}$. For example, constructive interference of light from two stars separated by an angular distance of λ/B radians in the direction parallel to the baseline can occur at the central location simultaneously because their OPDs differ by λ. Fig. 2.2 illustrates a similar scenario but the interference pattern from the second star is out of phase with respect to the first star's because their OPDs differ by $\lambda/2$.

Fringes and visibility

According to the principle of superposition, the amplitude of light waves doubles when the recombination is in phase (constructive interference) and nulls when it

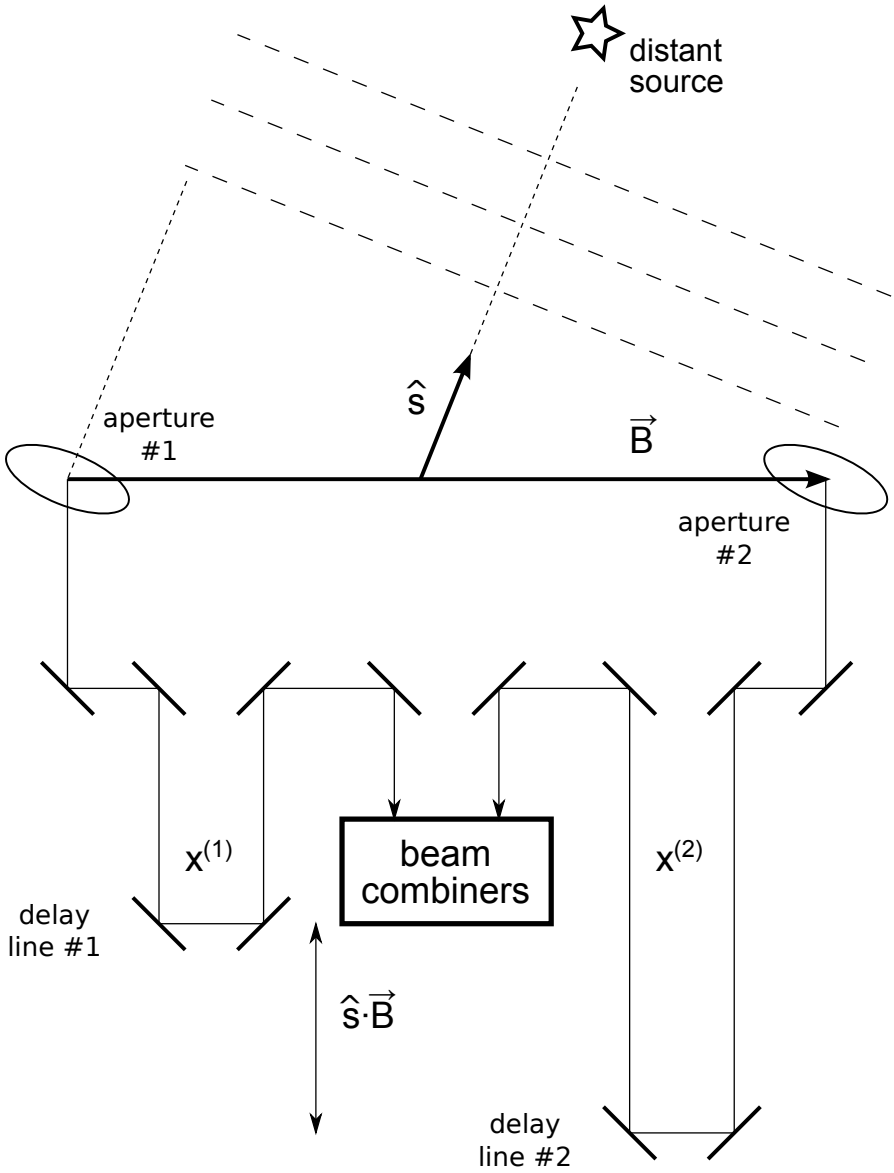

Figure 2.1: A minimalist 2-element optical long baseline interferometer

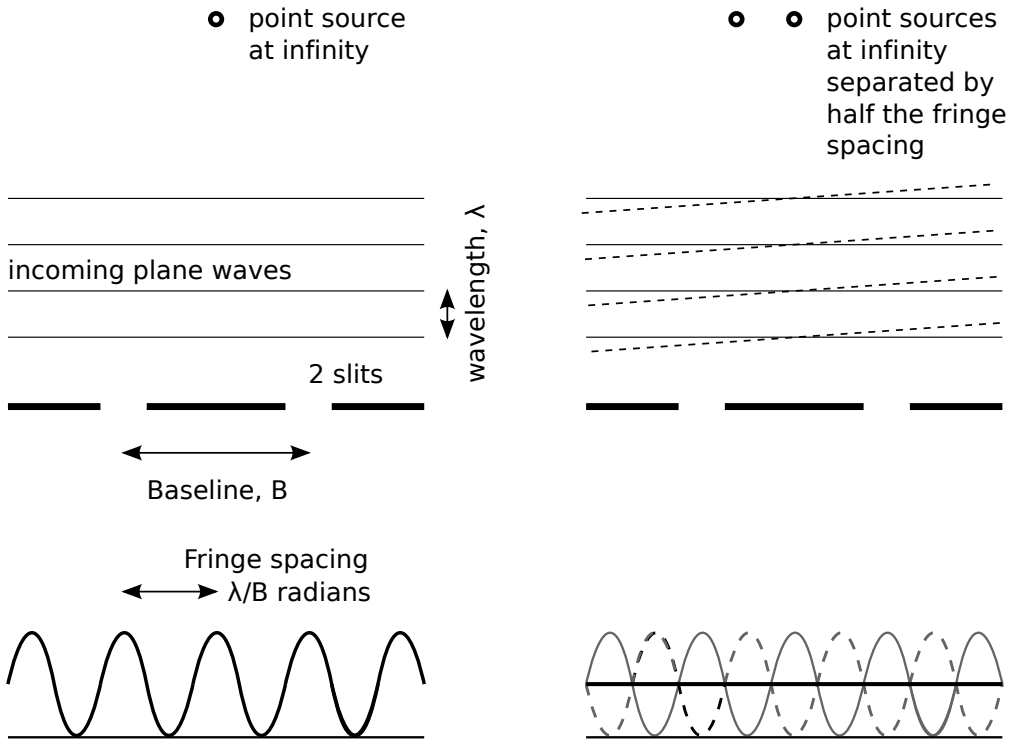

Figure 2.2: A form of Young's double slit experiment illustrating the principles of stellar interferometry and the relation between angular separation versus fringe phases (The above schematic is inspired by Monnier (2003)). The interference pattern on the left side of this figure has high visibility while the interference pattern on the right has zero visibility (constant intensity) because of the addition of an out of phase interference pattern from the second star. Both stars are assumed to have equal irradiance.

is out of phase (destructive interference). Since the intensity of light is the mean of the square of the amplitude, there will be a periodic variation in the intensity of light if the OPD is modulated. Such pattern is known as interference fringes. The visibility of the fringes is defined as,

$$V = \frac{I_{\max} - I_{\min}}{I_{\max} + I_{\min}}, \tag{2.3}$$

where $I_{\max}$ and $I_{\min}$ are the maximum and minimum intensity of light as a result of the OPD modulation. The visibility of the fringes depends on the state of the optics of the interferometer and morphology of the source. The square of the visibility of the fringes can be decomposed as,

$$V^2 = \frac{4I_1 I_2}{(I_1 + I_2)^2} V_{\text{inst}}^2 V_{\text{source}}^2, \tag{2.4}$$

where I_1 and I_2 are the intensities of light in the two arms of the interferometer. V_{inst} is the visibility due to the instrument and V_{source} is the modulus of the complex degree of coherence of the source, which according to the Van Cittert-Zernike theorem is related to the Fourier transform of its brightness distribution (Zernike, 1938). The visibility of the instrument is a measure of the alignment and perfection of the optics within the interferometer and can be obtained from observation of a point source (e.g. an unresolved single star) or a resolved single star with a well-known angular diameter.

Coherence length and fringe packet

Unless the light source is monochromatic, the interference fringes do not exist at all values of OPD. For a polychromatic light source (e.g. a star), the visibility of the fringes suffers the bandwidth-smearing effect where it decreases gradually to zero when the OPD deviates from zero. Ignoring the effect of dispersion, fringe visibility is maximum at zero OPD. The OPD value at which the fringes disappear is known as the coherence length (symbol L_{coh}) and it is inversely proportional to the spectral bandwidth of light undergoing interference, which is usually defined by wavelength filters within an interferometer. The coherence length is given as,

$$L_{\text{coh}} = \frac{1}{\Delta\sigma} \approx \frac{\bar{\lambda}^2}{\Delta\lambda}, \tag{2.5}$$

where $\bar{\lambda} \approx 1/\bar{\sigma}$ is the mean wavelength of the polychromatic light. The value of $\bar{\lambda}$ is also equal to the difference in OPD between successive fringes (interval between two intensity maxima or minima in the interference pattern). Due to

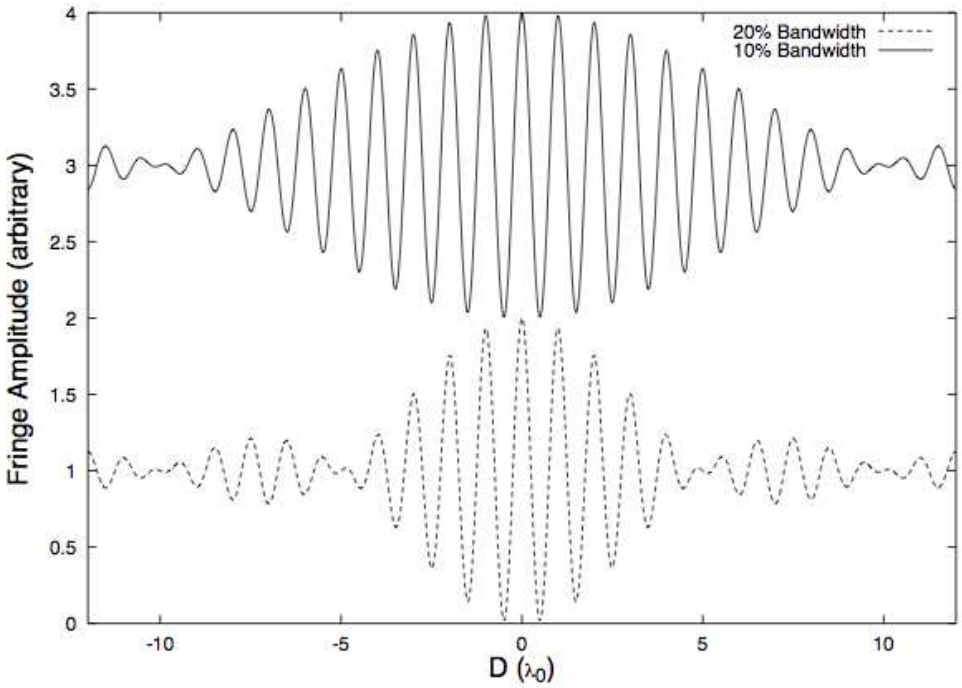

Figure 2.3: Interference fringe packet and coherence length of polychromatic sources at different bandwidth ratio, $\Delta\lambda/\bar{\lambda}$ (Boden, 1999).

the localization of the fringes, the interference pattern produced is usually known as a fringe packet. It is a common practice in optical interferometry to increase the width of the fringe packet by limiting the spectral bandwidth of the source. Typical values of L_{coh} in stellar interferometry range from several to hundreds of micrometers. Fig. 2.3 shows fringe packets of different width produced by light sources of different bandwidth ratio ($\Delta\lambda/\bar{\lambda}$).

As a consequence of the bandwidth-smearing effect, the internal optical path length of the interferometer must be set so that the OPD is zero or at least within the coherence length of the star light at the central location in order to produce interference fringes. As a star under observation moves across the sky, the position of some mirrors along the light propagation path, which form the optical delay lines of an optical long baseline interferometer, are adjusted to always keep the OPD at or near zero.

Phase and group delay

In signal processing, the phase delay of a time-varying sinusoidal signal is defined as the time difference (delay) between a given phase of the sinusoid and a reference (time). In the context of optical interferometry, the sinusoidal signal is the interference fringes and the phase delay of fringes is defined as the OPD between two arms of an interferometer computed at a fiducial location. Phase delay describes fringes at one particular wavelength.

For a polychromatic light source, fringes at different wavelengths have different phase delays. The gradient of the phase delay function over wavenumber at a certain wavelength is defined to be the group delay of the fringes at that wavelength. If ϕ is the wavelength-dependent phase delay[2], then the group delay is given as,

$$\xi = \frac{1}{2\pi} \frac{d\phi}{d\sigma}, \tag{2.6}$$

The group delay at the mean wavenumber, $\bar{\sigma}$, turns out to be the position of the peak of the envelope of a fringe packet. In the absence of optical dispersion, the group delay is constant across spatial frequency and its value is the same as the phase delay at the mean spatial frequency.

Effect of dispersion

However, dispersion of light is characteristic of common optical media (e.g. air, glass, etc). Dispersion occurs when the refractive index of an optical medium is a function of wavenumber. In the presence of dispersive media, the group delay is no longer constant across wavenumber and the peak of the fringe packet envelope does not coincide with the zero OPD position at the mean wavenumber. The shape of a fringe packet may even be distorted (e.g. Fig. 2.4) depending on the magnitude of the higher order dispersion coefficients of the optical media (Tango, 1990).

2.2 Effect of atmospheric turbulence

The discussion about stellar fringes and fringe packets so far has neglected the effect of atmospheric turbulence. Atmospheric turbulence arises from differences in the temperature of air in the atmosphere, which in turns produces a variation in

[2]Similar to the definition in Eq. (2.1) but in this context, phase is zero when OPD is zero at the fiducial location so the notation Δ is dropped

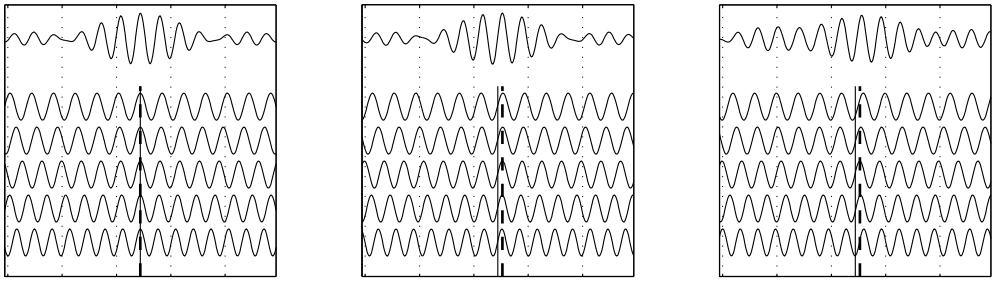

Figure 2.4: The left panel shows a fringe packet (top plot), which is a sum of fringes from a range of wavelengths (decomposed below the fringe packet), in the absence of longitudinal dispersion. The group delay (indicated by the solid vertical line in middle of the panel) and phase delay (indicated by the vertical dashed line) coincide with each other. The middle panel shows a fringe packet in the presence of longitudinal dispersion of the first order. The peak of fringe packet envelope and the phase delay no longer coincide. The right panel shows the effect of serious longitudinal dispersion which produces a fringe packet with a poorly defined peak.

the refractive index of air. As a result, the optical path lengths of two parallel paths of identical length but separated by a distance in space are no longer the same. Since a difference in optical path length relates to a difference in the phase for a light wave (Eq. (2.1)), a uniform phase over a plane wavefront will be perturbed after propagating through the atmosphere.

It has been shown that the variation in refractive index of air follows Kolmogorov statistics (Obukhov, 1949) and the phase variation between two points in a two-dimensional space has a power spectrum in the form (Noll, 1976),

$$\Phi(\vec{\kappa}) = 0.0229\, r_0^{-5/6}\, \kappa^{-11/3} \quad [\mathrm{rad}^2/\mathrm{m}^{-2}], \tag{2.7}$$

where $\kappa = |\vec{\kappa}|$ is the reciprocal of the distance between the two points or spatial frequency in a two-dimensional space and r_0 is the Fried parameter, which defines a circular region of interest with a diameter of r_0 that has a mean square phase fluctuation of 1 rad^2 (Fried, 1965). The dependence on only the magnitude of $\vec{\kappa}$ in the equation suggests that the phase variation is statistically isotropic. Although variation in the refractive index of air exists in a three-dimensional space, a two-dimensional space is adequate to describe the phase variation across a wavefront (a cross section of a light beam).

If the phase variation is small (weak turbulence), the effect of a turbulent atmosphere onto a downward propagating wavefront (towards a ground based observer) can be approximated by phase perturbation originating effectively from a thin turbulent layer and the atmosphere everywhere else is still and homogeneous. This

is called the near-field approximation. In the case of astronomical observations, this is a good approximation for stars near zenith (directly overhead) but becomes invalid for stars with distances from zenith exceeding 60° (Roddier, 1981).

Fringe motion

The phase variation on the two-dimensional thin turbulent surface in the sky, which has a power spectrum defined by $\Phi(\vec{\kappa})$, causes the phase delay of stellar fringes produced in an interferometer to vary. The OPD in Eq. 2.1 now has an additional term, $\frac{\lambda}{2\pi}\Delta\varphi$, where $\Delta\varphi$ is the difference of phase between light waves collected at two different locations below the atmosphere. The mean value of $\Delta\varphi$ is zero but the variance is non-zero and can be obtained from the phase structure function, $D_\varphi(\vec{r})$, which is given as (Fried, 1965),

$$D_\varphi(\vec{r}) = \left\langle |\varphi(\vec{r}' + \vec{r}) - \varphi(\vec{r}')|^2 \right\rangle = 6.88 \left(\frac{r}{r_0}\right)^{5/3} \quad [\mathrm{rad}^2], \tag{2.8}$$

where $\vec{r}'$ is the position vector of a reference location. Following this, the variance of the phase delay of stellar fringes observed with a ground-based optical long baseline interferometer is given as,

$$\sigma^2_{\mathrm{OPD}} = \frac{\lambda^2}{4\pi^2} D_\varphi(\vec{B}) = 0.17\lambda^2 \left(\frac{B}{r_0}\right)^{5/3}, \tag{2.9}$$

where B is the baseline of the interferometer. The variance does not depend on wavelength because $r_0 \propto \lambda^{6/5}$ and therefore the term $\lambda^2\, r_0^{-5/3}$ is constant. Given that the Fried parameter at SUSI is typically ∼7cm at $\lambda = 0.5\mu$m (ten Brummelaar, 1994), if a 100m baseline is used, the standard deviation of the phase delay of the fringes from its nominal position is $\sim 90\mu$m. This length is several times longer than the width of a typical stellar fringe packet. Depending on the OPD modulation, the fringes may disappear from the field of view of the beam combiner instrument if the delay line is set to compensate the nominal optical path length defined by the position of the star with respect to the baseline, $\hat{s} \cdot \vec{B}$, without allowance for atmospheric effects.

Since the air in the atmosphere is not static but always in motion under the combined influence of wind and temperature fluctuations, the phase variation at a point on the two-dimensional surface in the sky is therefore constantly changing with time. Using the hypothesis of a frozen atmosphere drifting in the direction of the wind (Taylor, 1938), the temporal variance of $\Delta\varphi$ can be obtained from Eq. (2.8) by substituting r with $\bar{v}t$, where $\bar{v}$ is the effective wind speed and t is the

time it takes for a region with a cross-sectional length of r to drift over a point in the sky. If t_0 is defined as the time interval over which the mean square of the phase difference at that point is 1 rad^2, then the temporal phase structure function is,

$$D_\varphi(t) = \left\langle |\varphi(t'+t) - \varphi(t')|^2 \right\rangle = \left(\frac{t}{t_0}\right)^{5/3} \quad [\text{rad}^2]. \tag{2.10}$$

The parameter t_0 is known as the atmospheric coherence time. By its definition above, which is similar to the one by Buscher (1994), it is related to the Fried parameter as $t_0 = 0.314 r_0/\bar{v}$. However if the phase difference is measured at two different points which are spatially uncorrelated, then $t_0 = 0.207 r_0/\bar{v}$ because the phase structure function coefficient is twice the coefficient in Eq. 2.8. The second definition is applicable for optical long baseline interferometry because $B \gg \bar{v} t_0$ (Colavita et al., 1999). Hereafter, the latter definition is used throughout this thesis unless otherwise stated.

As a consequence of atmospheric turbulence, a beam combiner must be able to record fringes of a star under observation within the timeframe of t_0 or less otherwise the fringe visibility decreases or is lost totally due to fringe motion. The typical value of t_0 at SUSI was measured to be around ∼0.7–5ms at a wavelength of 0.443μm (Davis & Tango, 1996). This means, in a worst case scenario, fringes of a star will begin to significantly lose visibility if the integration time of a beam combiner operating at that wavelength is 5ms or more.

Differential fringe motion

In scenarios where the motion of one stellar fringe packet with respect to another from a different nearby star is of concern, e.g. in phase-referencing interferometry and narrow-angle astrometry using OLBI, the differential fringe motion can be computed from the differential phase structure function,

$$D_{\Delta\varphi} = 2 \times 6.88 \left(\frac{\Delta s\, \bar{h}}{r_0}\right)^{5/3}, \tag{2.11}$$

where $\Delta s = |\hat{s}_1 - \hat{s}_2|$ is the separation of the two stars in the sky and $\bar{h}$ is the effective altitude of the turbulent layer in the atmosphere. For small angles, the angle subtended by the unit vectors that point to the two stars, $\hat{s}_1$ and $\hat{s}_2$, can be approximated by Δs. Substituting $D_\varphi(\vec{B})$ with $D_{\Delta\varphi}(\Delta s\, \bar{h})$, the variance of differential phase delay, σ^2_{dOPD}, can be computed. If $\bar{h} = 4$km, $\Delta s = 2''$ and $r_0 = 7$cm at $\lambda = 0.5\mu$m, then $\sigma_{\text{dOPD}} \approx \lambda/3$. The size of differential OPD fluctuation is more than two orders of magnitude smaller than the OPD fluctuation of a single

fringe packet. Having a greatly reduced fringe motion is the one of the advantages of phase-referencing fringes from a target star to a reference star.

The temporal differential fringe motion can be obtained from its power spectrum, which is given in Appendix A. It was first derived by Shao & Colavita (1992) and again in a more intuitive way by Glindemann (2011). Glindemann (2011, pg. 189) has shown that the temporal differential fringe motion of two nearby stars ($\Delta s\,\bar{h}$ much smaller than the diameter of light collecting aperture) is proportional to $\Delta s\,\bar{h}\,(t/t_0)^{4/3}$. So, even with an integration time, t, of 20ms and using the same values as above for the rest of the parameters, the differential fringe motion is $\sim\lambda/8$. This means targets which are 1.5 magnitude fainter can now have their fringes recorded without too much loss in visibility. This is another advantage of phase-referencing interferometry.

Due to their random fringe motion, a single measurement of the fringe packet separation will not yield the true separation. The standard deviation of the fringe packet separation is given as,

$$\begin{aligned}\sigma_{\mathrm{dOPD},T} &\approx 0.79\lambda\, r_0^{-5/6}\,\bar{v}^{-1/2}\,\bar{h}\,\Delta s\,B^{1/3}\,T^{-1/2}\\ &\approx \mathcal{A}\,\Delta s\,B^{1/3}\,T^{-1/2}\end{aligned}\quad, \tag{2.12}$$

where $\mathcal{A}$ is an atmospheric scaling factor for a given observation site and T is the amount of time in seconds spent in measuring the separation which is not equivalent to integration time. Integration time, t, is the time taken by a photodetector (or a camera) to record the stellar fringes, which is usually less than the atmospheric coherence time t_0, while the total measurement time, $T \simeq N \times t$, where N is the number of records taken. The derivation (Glindemann, 2012, private communication) is shown in Appendix A. In order to obtain a more precise measurement of the separation, a longer observation time, which means more measurements, is necessary.

The terms $\bar{v}$ and $\bar{h}$ are used in the equation because the derivation assumed the source of the phase variation originated effectively from a single turbulent layer in the atmosphere. However in a more rigorous derivation where contributions from many turbulent layers at different altitudes are integrated together, the averaging is over the term h^2v^{-1}. The scaling factor $\mathcal{A}$ in Eq. (2.12) has been shown to be proportional only to $\overline{h^2v^{-1}}$ which in turn depends only on the turbulence profile and the wind profile of the atmosphere at an observation site (Shao & Colavita, 1992). Nevertheless, the form presented in Eq. (2.12) is very useful for estimating and comparing atmospheric conditions at different sites because turbulence and wind profiles are not as commonly available as individual parameters like r_0 and t_0.

It is also important to note that the atmospheric scaling factor, $\mathcal{A}$, is inversely proportional to $\cos\zeta$, where ζ is the zenith distance or the angle of observation from zenith. In Eq. (2.12), this dependency is contained within the Fried parameter, r_0, because $r_0 \propto (\cos\zeta)^{3/5}$.

The term $\bar{v}^{-1/2}$ in the equation suggests a counterintuitive relation between the standard deviation of the fringe packet separation and the atmospheric coherence time, t_0. A smaller t_0 (due to its dependency on $\bar{v}^{-1}$), which means more vigorous fringe motion, causes a smaller $\sigma_{\mathrm{dOPD},T}$. This is the case because there are more samples of the fringe packets' positions for a given amount of time spent measuring the fringe packet separation. This scenario assumes the integration time, t, of the photodetector to record the fringes is short enough to freeze the fringe motion. However, in practice, a smaller t_0 is not desirable because the fringes are much harder to track and their visibilities are reduced in such atmospheric conditions.

2.3 SUSI

SUSI is a 2-element optical long baseline interferometer (Davis et al., 1999). It has a North-South (N-S) oriented baseline which is made up of a combination of 2 (one from each arm) out of 7 usable siderostats[3]. By selecting different pairs of siderostats, the length of SUSI's baseline is configurable from 5m to 160m.

The following is a list of subsystems in SUSI which are essential for its operation. The function of each subsystem and its relative location within the interferometer is elaborated and schematically shown in Fig. 2.5.

Siderostats (S)

The siderostats are plane mirrors of 20cm diameter. They are used to collect and reflect starlight into the evacuated pipes. Apart from replacing tarnished mirrors with freshly silvered ones, installing alignment LEDs at the back of the mirrors for the narrow-angle astrometry application and replacing the electronics and computer control (Tango & Ireland, 2010), no significant mechanical upgrade has been carried out for the siderostats. The usage of the alignment LEDs is discussed further in Section 2.4 and 3.3.

[3]SUSI has a total of 11 siderostat mount points.

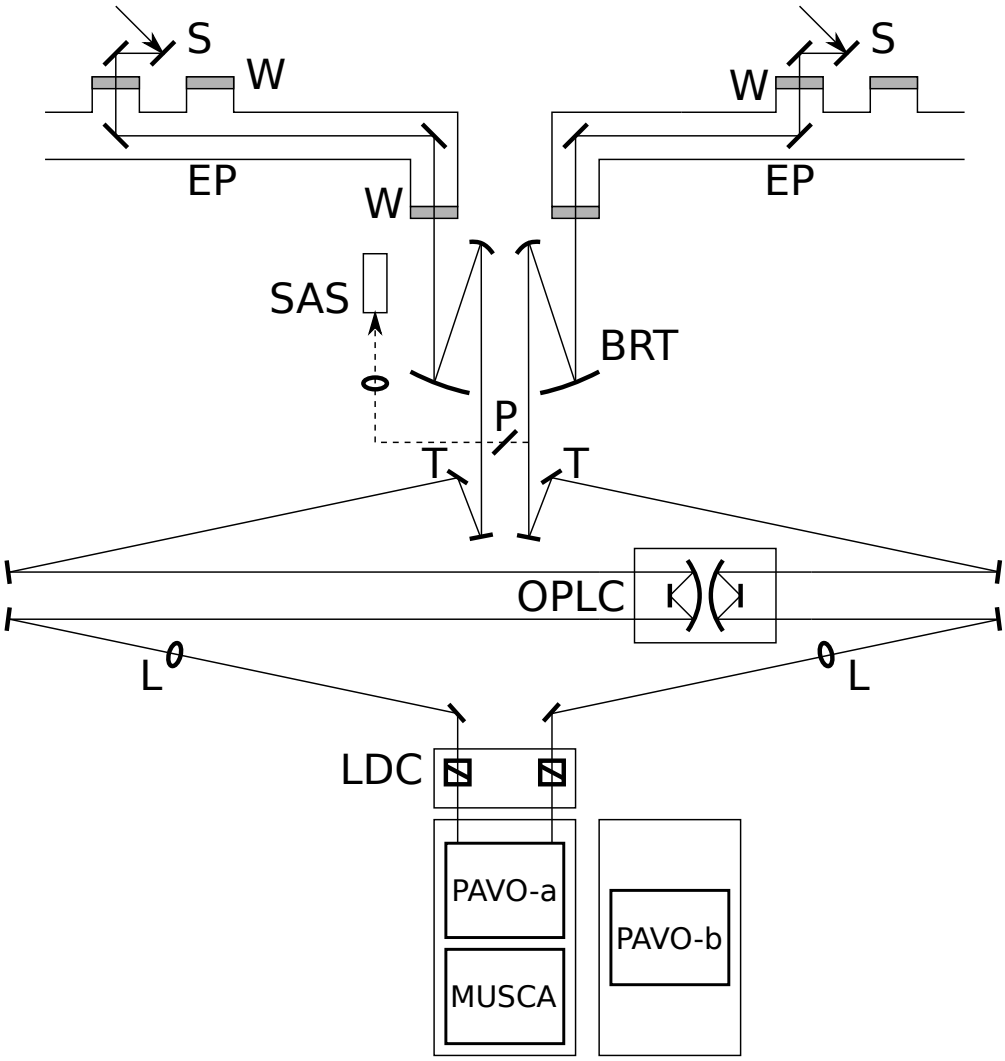

Figure 2.5: Overall optical setup of SUSI. Light from the star enters the interferometer via the siderostats (S). The main components; namely the siderostats (S), the beam reducing telescope (BRT), the optical path length compensator (OPLC), the longitudinal dispersion compensator (LDC), and other components are discussed in Section 2.3.

Evacuated pipes and windows (EP and W)

Mirrors in the vacuum sealed pipes transport beams of starlight from the siderostats into the optical lab. The pressure in the pipes had been maintained at <1 Torr during operations, and significantly sub-atmospheric at other times and was only returned to atmospheric pressure briefly once in April 2013 for servicing a badly aberrated mirror.

Beam reducing telescope (BRT)

This 2-element afocal telescope compresses the diameter of the beams by a factor of 3 so that optics of smaller diameter could be used. The primary and the secondary mirrors were recently replaced because the previous pair had poor optical quality (Ireland, 2006) and to allow the possibility of enlarging the field of view of the optical system by inserting a field lens in between the mirrors. The new primary mirror has a diameter of ∼200mm, a focal length of 3m and is spherical. The new secondary mirror has a diameter of ∼80mm and a focal length of 1m. It has a conic constant of -3.9917 and has a highly hyperbolic surface (Robertson et al., 2012). The mirrors for the new BRT are no longer single mirrors. Instead there is one BRT system for each arm of the interferometer. As a consequence, the positions of the North and the South beams are no longer swapped. It means, beyond the BRTs, the North beam propagates into the North tunnel and the South beam into the South tunnel.

The optical quality of each new BRT was characterized in-situ by setting up a Twyman-Green interferometer that had one of its arm passing through the BRT under test and using a green laser as the light source. The characterization was carried out in January 2011 by the author but the the details of the technique are described in (Ireland, 2006). The interference fringes produced were recorded with a handheld digital camera by projection onto a viewing card. Several images were recorded in quick succession because internal lab seeing was seen to perturb the fringes. The interferogram with the best fringe visibility was used for optical aberration analysis. The analysis fits a wavefront surface described by a sum of Zernike polynomials to the interferogram. Polynomials of up to the 3rd radial order were used. The coefficients of the polynomials (except the zeroth and first radial order) are used to estimate the total optical aberration in terms of the peak-to-valley (P-V) deviation from an ideal surface. The coefficient that corresponds to the defocus term is also ignored because this aberration can be minimized by adjusting the distance between the primary and secondary mirror. The P-V surface error of the North and South BRTs (over the full aperture of the primary

and secondary) are found to be 0.33λ and 0.34λ respectively. The aberration of the new North BRT is smaller than the previous system (0.36λ) but the new South BRT is worse (0.28λ). Although the latter is unexpected, it is acceptable and should not affect the astrometric performance of MUSCA because the reference and the target stars are fed into the instrument using the same part of both BRTs. Fig. 2.6 shows the interferograms recorded from the test setup and the corresponding fitted models. The coefficients of the Zernike polynomials obtained from the fit are given in Appendix B.

Star acquisition system and pellicle (SAS and P)

This system uses a CCD camera with a larger field of view to acquire a star into the field of view of the beam combiner. It was first commissioned by Seneta (1992) and later upgraded by North in 2002 (as cited in Ireland (2006)). The latest upgrade for the acquisition system, which involved converting the operating system of its software controller from Microsoft Windows based to Linux based, was completed by ten Brummelaar & Ireland (2008, private communication).

Tip-tilt system (T)

This system maintains the image of a star in the field of view of the beam combiner via a closed loop control system in order to track the star. The tip-tilt system in SUSI has been upgraded together with each introduction of new generation beam combiner. The system before the current one was installed by Ireland (2006) for the *red table* beam combiner and was a standalone system. However the current system was an upgrade from the previous and at the same time was integrated into the PAVO beam combiner (Ireland et al., 2013, in prep.). The tip-tilt system and the science measurements now use the same electron multiplying CCD camera.

Optical path length compensator (OPLC)

This system measures and provides the mechanism to equalize the OPD between two arms of the interferometer. It was first described in its original working form by Gilliand (1992). Detailed descriptions are also given by Davis et al. (1999). Its main components consist of (1) a carriage on rails that carries a pair of parabolic mirrors and a flat mirror at the focus of each pair forming a 2-in-1 delay line and (2) a pair of IR (1.152591μm) laser metrology systems, one for each arm of the interferometer. The metrology has a precision of 9nm (one 128th of a wave)

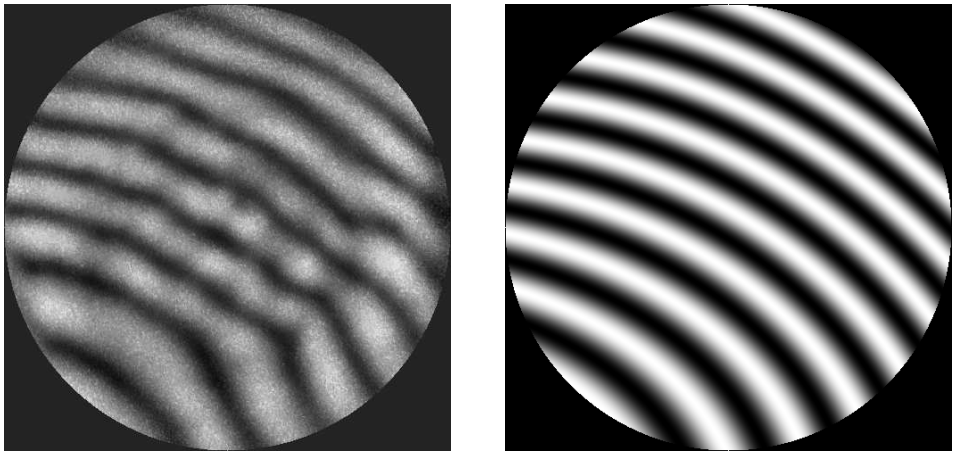

(a)

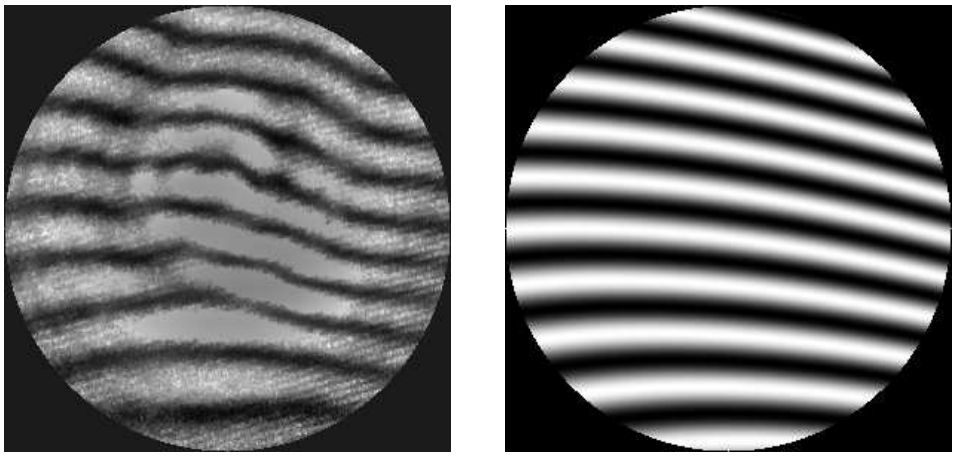

(b)

Figure 2.6: Interferograms of the new (a) North and (b) South BRTs. The wavefront from one arm of the Twyman-Green interferometer setup is deliberately tilted to produced the spatially modulated fringes seen in the figure. Any departure from regular spacing between the fringes indicates aberration. The images on the left column are actual photographs of the interference patterns while images on the right are the fitted models using the first 10 Zernike polynomial terms. Note there are some higher order aberrations at the center of the South BRT and near the edge of the North BRT apertures not fitted by the model which correspond to approximately additional $\lambda/4$ to $\lambda/2$ peak-to-valley aberration in double pass.

(Ireland et al., 2013, in prep.), which is smaller than the variation in optical path length introduced by atmospheric turbulence in a period of good seeing. The system is SUSI's main delay line and can compensate a difference in optical path of up to 100m. The computer software that controls of the system was upgraded once by North (2007) and later by Warrington in 2012. The latest upgrade also saw the electronics for the laser fringe phase counting and the microprocessor for the system's close-loop controller replaced with a faster and more integrated single chip solution (Robertson et al., 2012).

Focusing lenses (L)

These 2-element very long focal length lenses focus collimated beams of starlight into the beam combiners. In order to achromatize the pair, one of the elements is made of BK7 glass and the other of silica. Each set is made up of 50mm in diameter plano-convex and plano-concave lenses. The distance between the lenses is tweaked in order to adjust the focal length to ∼35m. The lenses were originally installed for the PAVO beam combiner (Ireland et al., 2013, in prep.).

Longitudinal dispersion corrector (LDC)

This system compensates the dispersive effect on fringes due to excess air path in one arm of the interferometer as a result of the carriage position in the OPLC. It inserts flat and wedged glass blocks into the optical path on both arms of the interferometer. The amount of glass to be inserted is calculated based on a model defined by the optical media used (Tango, 1990). It was originally designed for broad-band fringe tracking at blue wavelengths using two types of glass but it is now used with just one type (BK7) after its open-loop computer control software was upgraded.

2.4 Application to narrow-angle astrometry

Optical long baseline interferometry is applicable to astrometry because the position of a star (or any celestial object) in the sky is related to the net optical path length of the delay lines of an interferometer (see Eq. (2.2)). However, the discussion about the application cannot continue without a discussion on how the position of an object in the sky is defined. The position of a celestial body in the sky can be defined by many different coordinate systems. However, the most widely used coordinate system is the equatorial coordinate system although in the case of

narrow-angle astrometry, especially in binary star astronomy, a two-dimensional polar coordinate system is common.

Equatorial coordinate system

The equatorial coordinate system is a spherical coordinate system and it is similar to the longitude-latitude coordinate system used to describe a position on Earth. The two orthogonal axes for the equatorial system are right ascension (symbol α, abbreviated as RA) and declination (symbol δ, abbreviated as *dec*). The RA axis is quoted in the unit of sidereal hour[4] and like the longitude axis points Eastward but from the vernal equinox, which is the position where the Sun crosses the celestial equator from the South to the North celestial hemisphere. The declination axis is quoted in angular degrees and like the latitude axis points Northward from the celestial equator towards the North celestial pole (NCP). The NCP is aligned with the spin axis of the Earth and the celestial equator is aligned with the equator on Earth. This means the position directly overhead, or zenith, of an observer at a given latitude, ϕ_{LAT}, has a declination of $\delta = \phi_{\mathrm{LAT}}$.

Polar coordinate system

In the narrow-angle regime, the polar coordinate system is also commonly used to express the position of a star with respect to a reference star (see Fig. 2.7). This coordinate system is 2 dimensional and its two axes, namely separation (symbol ρ) and position angle (symbol θ), lie in a plane that is tangential to the celestial sphere at the reference star. ρ points to the target from the reference star and represents the angular separation of the stars in the sky. θ is the bearing of ρ which, by convention established by binary star astronomers, goes positive in the direction from to the NCP to the East. Conventionally ρ is quoted in arcseconds and θ is quoted in degrees between 0 and 360°.

Narrow-angle astrometry with OLBI

Developing from the relation between position in the sky and optical path length in Eq. (2.2), an optical long baseline interferometer determines the projected separation of two stars in the sky by measuring the difference in optical delay of the their fringe packets. In other words, the difference in optical delay between fringe

[4] 1 sidereal hour = 15°

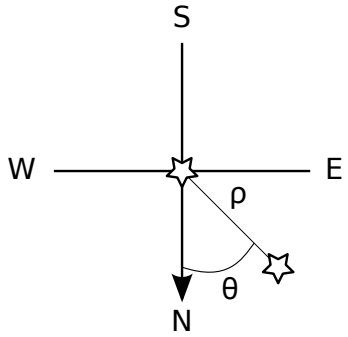

Figure 2.7: The definition of ρ and θ in a polar coordinate system. The orientation of North (towards the celestial pole (NCP)) pointing downward and East pointing right is a standard binary star convention.

packets of two nearby stars is,

$$S = \hat{s}_2 \cdot \vec{B} - \hat{s}_1 \cdot \vec{B} = \Delta\vec{s} \cdot \vec{B} = \Delta s_p \, B, \tag{2.13}$$

where $\hat{s}_i \cdot \vec{B}$ is the optical path length in one arm of an optical long baseline interferometer that must compensated in order to obtain zero OPD for one star (as defined and explained in Section 2.1) and $\Delta\vec{s}$ is the angular separation vector of two stars. The subscripts 1 and 2 are used to denote the two different stars, i.e. a reference and a target star respectively. The projected separation of the two stars, Δs_p, in the equation is defined as $\Delta\vec{s}$ projected onto $\vec{B}$.

Suppose a local rectangular coordinate system whose x-axis points to the East, y-axis points to the North and z-axis points to zenith is used to describe the pointing vector of each star, $\hat{s}_i$, then,

$$\hat{s}_i = \begin{bmatrix} -\cos\delta_i \sin \mathrm{HA}_i \\ \cos\phi_{\mathrm{LAT}} \sin\delta_i - \sin\phi_{\mathrm{LAT}} \cos\delta_i \cos \mathrm{HA}_i \\ \sin\phi_{\mathrm{LAT}} \sin\delta_i + \cos\phi_{\mathrm{LAT}} \cos\delta_i \cos \mathrm{HA}_i \end{bmatrix}. \tag{2.14}$$

The hour angle, HA_i, is defined as $\mathrm{LST} - \alpha_i$ where LST is the local sidereal time. By expressing the coordinates of a target star, (α_2,δ_2), in terms of the coordinates of the reference star, (α_1,δ_1),

$$\alpha_2 = \alpha_1 + \Delta\alpha, \quad \delta_2 = \delta_1 + \Delta\delta. \tag{2.15}$$

and substituting Eq. (2.15) and Eq. (2.14) into Eq. (2.13), it can be shown that Δs_p is a time-dependent non-linear multivariate function of $\Delta\alpha$ and $\Delta\delta$, and at least 2 observations at different times are required to determine the true separation

of the two stars. In a narrow field of view, the offsets in RA and *dec* can also be expressed in terms of ρ and θ as,

$$\Delta\alpha \simeq \rho \sin\theta, \quad \Delta\delta \simeq \rho \cos\theta. \tag{2.16}$$

Although any ground based observation cannot avoid the detrimental effect of atmospheric turbulence, the astrometric uncertainty of the projected star separation measurement, $\sigma_{\Delta s_p}$, is found to decrease with increasing baseline to the 2/3 power in a narrow-angle regime (>10m for a FOV of $\ll 10'$), because,

$$\sigma_{\Delta s_p} = \frac{\sigma_{\mathrm{dOPD},T}}{B} \propto \Delta s_p \, B^{-2/3} \, T^{-1/2}. \tag{2.17}$$

The definition of $\sigma_{\mathrm{dOPD},T}$ is given in Eq. (2.12). This means that high-precision astrometric measurement can be performed with a very long baseline interferometer and this potential was first realized by Shao & Colavita (1992).

2.4.1 Methods

There are more than two methods to perform narrow-angle astrometry with OLBI but the one which involved closure phases (Monnier, 2007) is not applicable to SUSI because it requires the use of more than 2 telescopes or siderostats at the same time. Therefore the discussion in this subsection focuses on the only two methods that are applicable. Both methods measure the same physical quantity, S, i.e. the difference in optical delay between two stellar fringe packets. One method approaches the measurement indirectly while the other measures the quantity directly. Both methods require the baseline of the interferometer to be known.

Method 1: Measure V^2 of stellar fringes (indirect)

This method measures the variation of the visibility of the stellar fringes due to coherent and incoherent summation of the fringes from two nearby stars whose separation is to be measured. This method requires fringe packets from the stars to be overlapping each other. The visibility is higher when the fringes are in phase and lower when the fringes are out of phase. The fringe visibility varies with time and the wavelength of light because it is an effect of a constant change in OPD between fringe packets of the stars due to the rotation of the Earth.

The squared visibility of the combined stellar fringes, V^2, is given as (Tango, 2006),

$$V_{1,2}^2 = \frac{V_1^2 + V_2^2\beta^2 \,\mathrm{sinc}^2\left(\phi\,\Delta\lambda/2\lambda\right) + 2\sqrt{V_1^2 V_2^2}\,\beta\,\mathrm{sinc}\left(\phi\,\Delta\lambda/2\lambda\right)\cos\phi}{\left(1+\beta\right)^2}, \tag{2.18}$$

where V_1^2 and V_2^2 are the visibility squared of the fringes of the individual stars, β is the brightness ratio of the second star to the first, $\Delta\lambda/\lambda$ is the bandwidth ratio of the spectral channel as discussed in Section 2.1 and,

$$\phi = 2\pi S(t)/\lambda. \tag{2.19}$$

The *sinc* function in the equation is defined as $\mathrm{sinc}(x) = \sin \pi x/\pi x$. In this method, S and several other parameters (β, V_1^2 and V_2^2) are extracted by fitting the above model to a set of measured $V_{1,2}^2$. However given the straightforward relation between S and Δs_p, it is common to extract the latter directly from the model fitting instead.

This method has the advantage of not needing any additional optical setup beside the main science beam combiner. The uncertainty of the projected separation obtained is in the sub-milliarcseconds regime (Armstrong et al., 2004; Davis et al., 2005; Tango et al., 2009).

However, due to the need to overlap fringe packets, this method is only applicable to a scenario where the OPD between the fringe packets is smaller than the coherence length of the individual fringe packet. The coherence length of a fringe packet is inversely proportional to the bandwidth ratio of the stellar spectrum used for interference. Using SUSI's main beam combiner as an example, the typical coherence length of spectrally dispersed fringe packets is $\sim 30\mu$m. This corresponds to an angular size of $\sim$62mas with a 100m baseline or $\sim$620mas with a 10m baseline. This means this indirect method is not suitable for narrow-angle astrometry for stars that have a wider projected separation. This is the main reason why most of the past experiments (Armstrong et al., 2004; Davis et al., 2005; Tango et al., 2009) using this method is limited to speckle binaries and relatively short baselines.

Method 2: Measure separation of fringe packets (direct)

Another method of determining the relative astrometry of two stars is by directly measuring the difference in optical path length between the fringe packets of the stars. This method is straightforward and complements the previous one because it requires the fringe packet pair to be non-overlapping in order to measure their OPD. Contrary to the previous method, this direct method has a minimum requirement on the star separation it can measure. The maximum star separation measurable is not limited by the method itself but depends on the field of view of the interferometer which can be as wide as $120''$ (Delplancke, 2008), or even wider from the high Antarctic plateau.

The uncertainty of the projected separation measurement depends on the uncertainty of the optical path length measurement and the uncertainty of the baseline of the interferometer. This relation is derived from the Eq. (2.13) and is given below:

$$\frac{\delta\,\Delta s_p}{\Delta s_p} = \sqrt{\left(\frac{\delta S}{S}\right)^2 + \left(\frac{\delta B}{B}\right)^2}. \tag{2.20}$$

The term $\delta(\cdot)$ in this context denotes the uncertainty of a measurement. In order to achieve a precision of 10μas in projected separation measurement, the uncertainty of the optical path length measurement, δS, has to be less than 5nm per 100m baseline and the uncertainty of the baseline, δB, has to be less than 1mm per 100m baseline for a given projected separation of $>1''$.

The drawback of this method is the need for additional beam combiners, metrology systems and infrastructure to measure the optical path length and baseline of an interferometer to the required precision. This means additional cost and complexity.

Despite its drawback, this method is the preferred method for high precision narrow-angle astrometry because of the straightforwardness of the approach and the absence of a limitation on the maximum star separation the method can measure. Therefore this method was also chosen to be implemented for this thesis.

2.4.2 Challenges and solutions

The challenges in measuring the relative astrometry of a target star with high precision using the direct method (Method 2) are spelled out in Eq. (2.20) and elaborated in the previous section.

Uncertainty in the optical path length measurement

In order to address the first challenge regarding the accuracy of the optical path delay measurement, the measurement is usually carried out by measuring the phase delay of the fringes instead of the group delay (which is the location of the peak of the envelope) of the fringes. Measuring the former is 20× more accurate than measuring the latter (Lawson et al., 2000) for typical bandpasses. In order to do so in the presence of atmospheric turbulence which not only corrupts the phases and reduces the visibility of the fringes, but also makes the position of the fringes fluctuate randomly in delay space, a technique called phase-referencing is

employed to stabilize the position of the fringes (Colavita, 1992). The technique reduces the fringe motion of a target fringe packet by compensating its motion with phase delays measured with a reference fringe packet. This is a result of reduced differential fringe motion which has been discussed in Section 2.2.

The phase-referencing technique only solves half of the challenges. The remaining half, which is to measure the optical delay between fringes, is solved by a network of optical metrology systems. More than one metrology system is required because the phase-referencing technique, which is discussed in detail in Chapter 5 and 6, uses two beam combiners and measuring the non-common paths between the beam combiners demands additional metrology systems. The network of metrology systems put in place for this thesis is discussed in Section 5. The optics of the beam combiners are discussed in Section 3.

Since a single measurement of the fringe packet separation does not yield its true value due to the effect of atmospheric turbulence, there is a minimum number of measurements to be made in order to achieve the required 5nm precision. Suppose the uncertainty of the fringe packet separation measurement is affected only by atmospheric turbulence, then according to Eq. (2.12), the cumulative measurements made under a typical seeing condition at SUSI (r_0 = 7cm at λ = 0.5μm and t_0 = 1ms) must last for at least 5 minutes. This estimation assumes a 100m baseline is used and the effective turbulent layer altitude is 4km. Since there is no published information on the latter at or near SUSI, the value is obtained from an average turbulence profile (Lindegren, 1980). The estimation of the minimum measurement time is not unrealistic because the scaling factor $\mathcal{A}$ (in Eq. (2.12)) for SUSI, which is $\sim$780 $\mathrm{m}^{2/3}\,\mathrm{s}^{1/2}\,\mathrm{arcsec}^{-1}$, is about 1.5–2.5$\times$ those estimated for very good sites like the Mauna Kea Observatory (Shao & Colavita, 1992) or the best conditions at the VLTI (as cited in Delplancke (2008)).

Uncertainty in the baseline solution

In order to address the second challenge regarding the accuracy of the baseline of the interferometer, the wide-angle and narrow-angle baseline must be aligned to better than $\sim$1mm.

The wide-angle baseline of an interferometer is defined as a vector between pivot points of two siderostats. The pivot point of a siderostat is a virtual point where the two rotational (elevation and azimuth) axes of the siderostat intersect and typically coincides with the center of the siderostat mirror. In the case of an imperfectly constructed siderostat where the axes do not intersect, the pivot point of the siderostat is the mean of the position of the center of the entrance pupil of

one arm of the interferometer projected onto the siderostat itself. The wide-angle baseline vector is obtained by observing stars separated by large angles and located in various part of the celestial sphere, noting the differences between the expected and the actual optical delays (offsets) required to produce stellar fringes based on a set of estimated dimensions and finally solving the simultaneous equations of offsets to obtain a correction to the estimated baseline vector initially used. This is a common method for optical long baseline interferometers (Woillez & Lacour, 2013, Section 3.3) and a detailed description of this method for interferometers with siderostats (instead of telescopes) is presented in Appendix C. The uncertainty of the wide-angle baseline obtained with this method is in the regime of several micrometers in principle, and $\sim$100μm for SUSI once all errors are taken into account.

On the other hand, the narrow-angle baseline of the same interferometer is defined as a vector between the center of two entrance pupils of a beam combiner projected onto the siderostats. The following is an example to easily understand the relation between the wide- and narrow-angle baselines. Suppose a two-hole aperture-mask is put over each siderostat mirror, fringes from each pair of apertures (one from each siderostat) can be used to make astrometric measurements of a binary star on a slightly different narrow-angle baseline simultaneously, despite the aperture pairs between the two masks share the same pivot points, which defines the wide-angle baseline of the two interferometers.

Due to optical misalignment, the wide- and narrow-angle baselines can differ by more than 1mm. The optical system is misaligned when the center of a back-projected entrance pupil does not coincide with the pivot point of the siderostat the pupil is being back-projected to. In the case of this scenario, using the wide-angle baseline solution for narrow-angle astrometry of a pair of nearby stars is erroneous and limits the precision of the astrometric measurement. If the misalignment between the center of the back-projected pupil and the pivot point of the siderostat is represented by a vector $\vec{e}$, then the relation between the wide- and narrow-angle baseline is given as,

$$\vec{B}_{\rm NA} = \vec{B}_{\rm WA} + (\vec{e}_2 - \vec{e}_1), \tag{2.21}$$

where the subscript 1 and 2 denotes two siderostats forming the baseline and the wide-angle baseline vector, $\vec{B}_{\rm WA}$, points from siderostat 1 to siderostat 2. $\vec{B}_{\rm NA}$ is the narrow-angle baseline.

The optical setup and alignment procedure put in place for this thesis to address this challenge is discussed in Section 3.3.

Chapter 3

Dual beam combiner at SUSI

A dual beam combiner setup for an optical long baseline interferometer is usually used in a way analogous to an adaptive optics (AO) instrument for a single-mirror imaging telescope. One beam combiner is used to track the group or phase delay of stellar fringes as they vary under the influence of atmospheric turbulence while the other, usually located downstream in the optical path, is first fed with the estimated phase delay from the former beam combiner to stabilize the fringes of the same or another star and then used to collect science measurements from the stabilized fringes.

The first dual beam combiner setup was introduced at the Palomar Testbed Interferometer (PTI) (Colavita et al., 1999) to carry out phase-referencing interferometry. One of the most successful experiments using such a technique is the Palomar High-precision Astrometric Search for Exoplanet Systems (PHASES) program at PTI (Muterspaugh et al., 2010b). The program concerned narrow-angle astrometry of close binary stars. A similar dual beam combiner setup was also employed at the Keck Interferometer (KI) to carry out phase-referencing measurement. In the Southern hemisphere, the Very Large Telescope Interferometer (VLTI) has two identical beam combiners as part of its Phase-referenced Imaging and Microarcsecond Astrometry (PRIMA) facility aimed at conducting narrow-angle astrometric observations. The VLTI is also expecting another dual beam combiner instrument (GRAVITY) to be installed at the interferometer (Gillessen et al., 2010).

Joining this list is SUSI with its PAVO and MUSCA beam combiners. PAVO is the main instrument in the dual beam combiner setup and takes the role of a fringe tracker while MUSCA is a companion instrument that makes astrometric measurements during astronomical observations. PAVO can be used standalone for

other scientific measurements but MUSCA must always be used with the former for astrometric measurements. The two beam combiners are fed with a pair of starlight beams from the two arms of the interferometer but they each use a different part of the visible light spectrum. They share the same main delay line for the tracking of stellar fringes. In addition, MUSCA has a differential delay line (DDL) for switching between fringe packets of two nearby stars. The DDL is the key feature that allows MUSCA to make astrometric measurements. It is needed because the optical path modulation used to sweep through a fringe packet in MUSCA is smaller than the typical path length between peaks of the envelope of the fringe packet pair. With such a setup, a measurement of the displacement of the DDL and the difference in phase delay of the pair of stellar packets constitutes the main observable of this dual beam combiner configuration.

The content of this chapter is partially reproduced from the following paper: "Phase-referenced interferometry and towards narrow-angle astrometry with SUSI", which has been accepted for publication in the Journal of Astronomical Instrumentation.

3.1 PAVO

The Precision Astronomical Visible Observations (PAVO) beam combiner was assembled and obtained its first stellar fringes in November 2008. A similar setup (Ireland et al., 2008) is also operational at the Center for High Angular Resolution Astronomy (CHARA) array. PAVO is a multi-axially aligned Fizeau-type interferometer. But unlike a typical Fizeau interferometer, PAVO forms spatially modulated interference fringes in the pupil plane of the interferometer and then spectrally disperses the fringes. It also employs spatial filtering in its image plane and an array of cylindrical lenslets to utilize the full multi-r_0 aperture of the siderostats at SUSI. Fig. 3.1 shows the schematic diagram of the PAVO beam combiner.

The actual optical setup is divided into 2 parts: a front-end and a back-end arrangement. The front-end optics splits the incoming beams into various components while the back-end optics (Fig. 3.1) recombines the beams. Fig. 3.2 shows the overall arrangement of the PAVO optics. Fig. 3.1(a) also shows the location of the metrology sources which are discussed in Chapter 5. The setup was rearranged to accommodate MUSCA. The original setup before re-arrangement can be found in a separate paper (Tuthill et al., 2008). The naming convention for optical elements in SUSI is given in Appendix B.

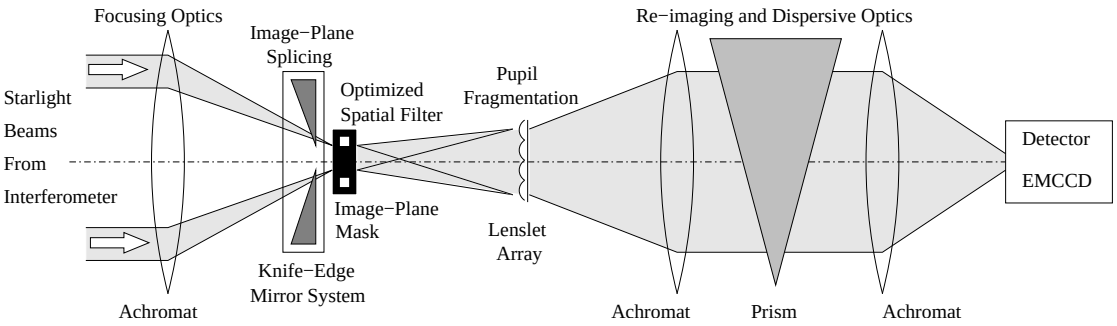

Figure 3.1: Schematic diagram of the PAVO beam combiner at SUSI.

The North (N) and the South (S) beams from the siderostats propagate from the left to right in Fig. 3.2(b). A pair of dichroic filters, ND1 and SD1, separate the tip-tilt from the science beams. The filters reflect light of wavelength shorter than 0.54μm and transmit light of longer wavelengths. The reflected blue end of the spectrum is fed into a tip-tilt system which acts as a first order AO system that removes the tip and tilt (or phase ramp) from the wavefront of a pupil. The science beams are then separated by wavelength into 2 parts, one for PAVO and another for MUSCA, by another pair of dichroic filters, M16, where M16 includes both N16 and S16 (see Appendix B). These filters reflect light of wavelength shorter than 0.79μm and transmit light of longer wavelengths. As a consequence, the middle part of the spectrum ($0.540.79\mu$m) is reflected into PAVO while the red end of the spectrum is transmitted to MUSCA. The profile of both types of dichroic filters, ND1/SD1 and M16, are given in Appendix B for reference.

The beams are actually converging ($\sim f/700$) because there is a focusing lens (labeled L in Fig. 2.5) in each arm of the interferometer which focuses to an image plane located at the PAVO two-hole mask. Each of the $\sim$1.2mm apertures on the mask corresponds to a field of view of $\sim 2''$ in the sky. The holes are separated by twice their width and are used as low-pass spatial filters to clean aberrated images of stars. A knife-edge mirror is used to align the beams through the apertures of the mask.

After passing through the apertures, the beams are multi-axially aligned at the pupil plane to form spatially modulated fringes. Fringes are formed in the pupil plane so that they are less sensitive to seeing and misalignment. At the pupil plane, different parts of the combined pupil are sampled by an array of cylindrical lenslets that act as virtual slits across the image plane of a spectrograph. The spectrograph, which consists of an anti-reflection coated 36° BK7 prism from Melles-Griot and a pair of six-element 50mm lenses by Schneider, spectrally disperses the fringes before they are re-imaged onto a back-illuminated DU-897 electron-multiplied CCD

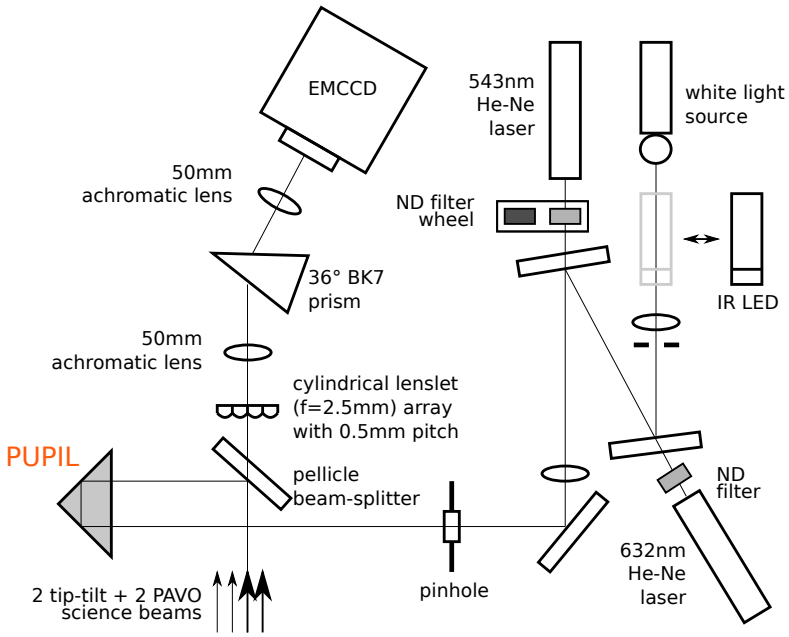

(a)

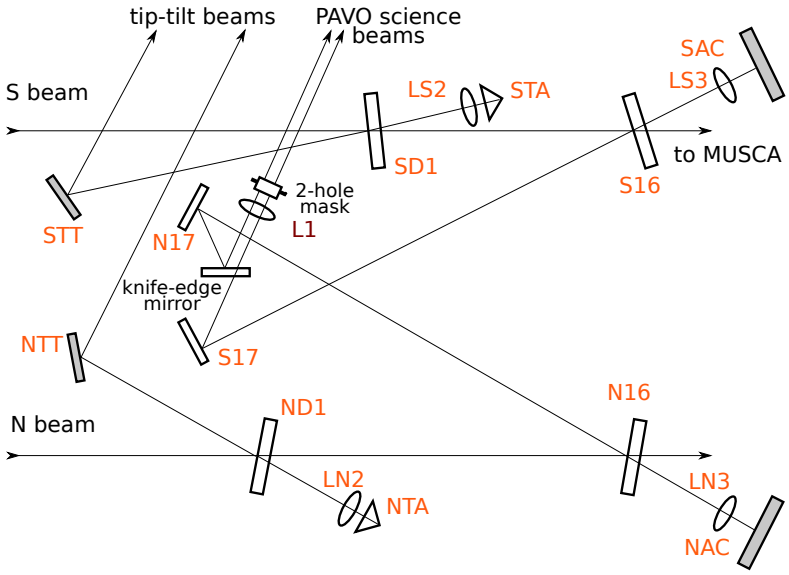

(b)

Figure 3.2: Optical setup of PAVO (a) backend and (b) front-end. The diagrams are arranged in such a way that the science and tip-tilt beams in the front-end and backend are aligned.

(EMCCD) camera from Andor[1]. There are 512×512 pixels on the camera but only a small portion of the detector, 512×32 pixels, is used.

A more in-depth description of PAVO at SUSI can be found in several other papers (Ireland et al., 2008; Robertson et al., 2010, 2012).

Although the current optical arrangement of PAVO is different from its pre-MUSCA version, there are several features that have been kept unchanged. Firstly, the position of the image plane of the long focal length lens, L, is unchanged and remains at the mask. Secondly, the distance between the PAVO field lens, L1 (f=2000mm), and the lenslet array is preserved at ∼2m because the same lens is used. Last but not least, the distance between the focusing lens, L, and the lenslet array via the M15 filters is kept unchanged in order to keep the image plane of the tip-tilt beams at the lenslet array because the PAVO camera is used for the tip-tilt correction system and as well as science.

3.2 MUSCA

The Microarcsecond University of Sydney Companion Astrometry (MUSCA) beam combiner was assembled and obtained its first stellar fringes in January 2011. MUSCA is a coaxially aligned pupil plane Michelson interferometer which operates at wavelengths between 0.77μm and 0.91μm. It forms temporal fringes by modulating the optical path length of one arm.

General optics

Fig. 3.3 shows the optical path and components of MUSCA. Incoming converging light beams from the top of the figure are transmitted through the M15 mirrors in Fig. 3.2(b). The M15 mirrors are the last optical components which are common to both PAVO and MUSCA. The main mirrors in MUSCA (M17M-M19M) are from Thorlabs and they are 25mm in diameter, gold and anti-reflection coated. The coatings are optimized for usage at wavelength of 0.633μm and have optical surface flatness of λ/20 (M17M) and λ/10 (M18M, M19M).

[1] `http://www.andor.com`

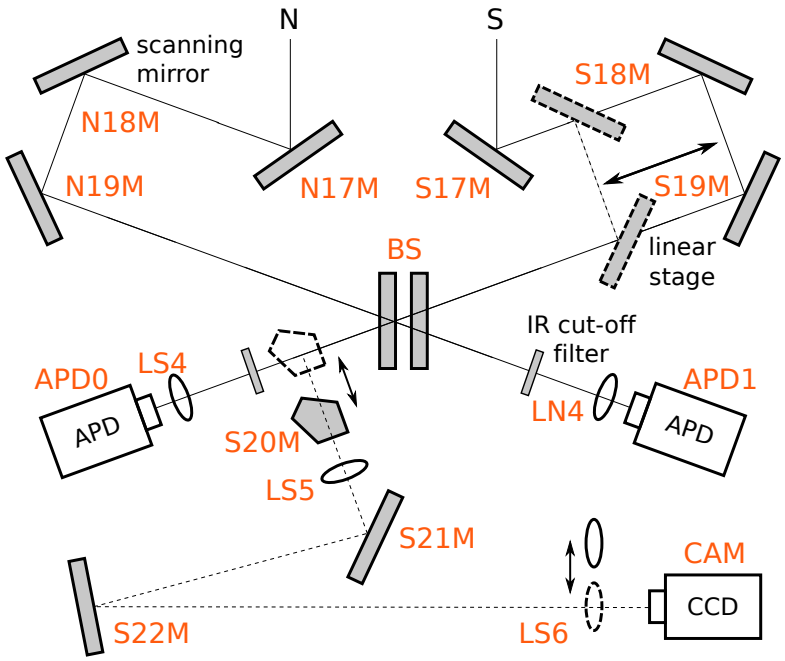

(a)

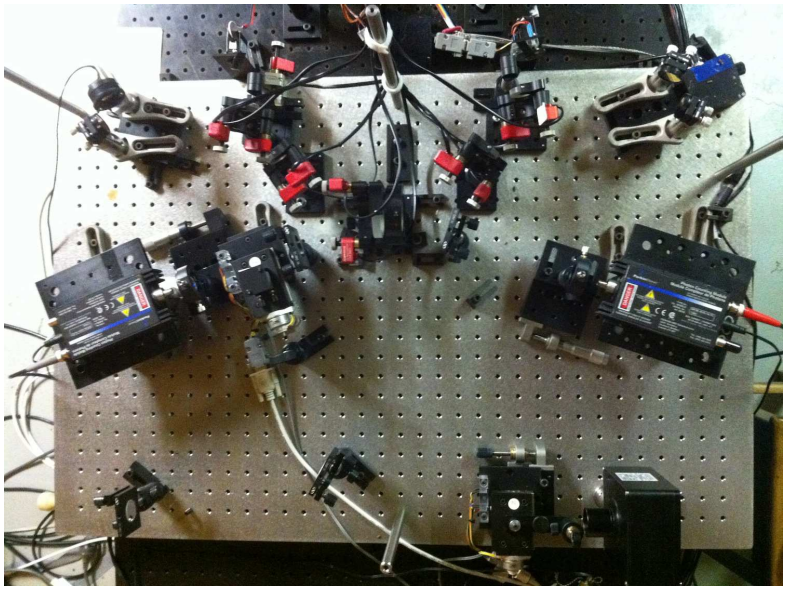

(b)

Figure 3.3: A schematic diagram and a photograph of the optical setup of MUSCA.

Scanning mirror and electronics

A scanning mirror N18M is used to modulate the optical path length of the North arm of MUSCA. It is attached to a piezoelectric transducer (PZT) which converts voltage to physical displacement. The transducer was originally used in the *red table* beam combiner for a similar purpose but is now mounted on a custom-made bracket and on a standard post for MUSCA. The motion of the mirror is controlled by a computer via the transducer. The electronics from the *red table* (Lucas, 2004) was replaced with a new PCI-based data acquisition and analog output card (DAQ-2502) from Adlink Technology. The analog output of the card is used to drive the transducer. Voltage is applied in small steps and at an interval of about 0.2–0.3ms per step. The value to be applied at each step is obtained from a software look-up table (LUT). The values in the LUT are pre-characterized and are used to linearize and eliminate hysteresis from the non-ideal PZT motion. In order to avoid excitation of unwanted mechanical resonance, the analog output of the card is passed through a 1ms low-pass RC filter before it is fed to the transducer (Ireland, 2006). The maximum path length modulation attainable from the transducer is $\sim 140\mu$m (maximum throw of the PZT is $\sim 100\mu$m in a folded optical path) but a typical value used for MUSCA is $\sim 25\mu$m. This range is chosen for MUSCA because (1) it matches with the PAVO group delay tracking window and (2) it is $\sim 2\times$ larger than the expected width of the MUSCA fringe packet. Making the range larger is undesirable because the PAVO group delay estimates are unreliable beyond its tracking window and therefore phase-referencing is futile at that range.

Differential delay line

A linear translational stage (T-LS28 from Zaber Technologies) and 2 mirrors (S18M and S19M) on the South arm of MUSCA form the DDL for the beam combiner. The stage is computer controlled via a serial port interface. It is used for fringe finding by equalizing the optical path length between the North and South arms. The fiducial location where OPD between the arms is defined as zero is chosen at the middle of the scan range of the scanning mirror. As fringe packets from two different stars are separated in optical path length the DDL must alternate between two positions in order to place either one of the fringe packets into the scan window. Effectively the DDL is used to 'select' one fringe packet for observation at any one time.

The stage is stepper-motor driven and has a built-in open loop position control system. The stepper motor converts rotary motion to linear motion via a

leadscrew. The total travel distance of the stage is more than 8mm, which is the required span to observe binary star separations as wide as 10″ using a 160m baseline. At an average slew speed of ∼2mm/s, it takes the stage less than 5 seconds to cover that distance. The stage also has built-in anti-stiction and anti-backslash features to overcome the two most common undesirable properties associated with a mechanical motion control system. The features ensure the stage (1) is always far enough away from a final destination it is programmed to go to before attempting its final move and (2) always approaches a destination from the same direction.

The leadscrew based open loop position control system of the stage, which has a nominal accuracy of 12μm and a repeatability of <0.4μm, is not the only mechanism put in place to measure the position of the stage for MUSCA's astrometric application. It is also being measured by a dual laser metrology system which has a precision better than 5nm. The metrology system works hand in hand with the open loop position control system and is discussed in detail in Section 5.3.

Detectors

The beams are combined co-axially at their common pupil plane at the beamsplitter, BS. The intensity variation of the combined beams as a result of the optical path length modulation by the scanning mirror is recorded as temporal fringes using a pair of SPCM-AQR-14-FC self-contained single photon-counting avalanche photodiode (APD) modules by PerkinElmer. Each module produces a 15ns TTL (transistor-transistor logic) output per photon. The signal is fed into a 16-bit digital counter on the same DAQ-2502 data acquisition card mentioned earlier. Read out of the counter is synchronized with the output voltage applied to the PZT of the scanning mirror so that the counts correspond to the number of photons detected at each optical path modulation step.

The role of each field lens, LN4 and LS4 (f=35mm), placed in the image plane of the beams, is to ensure that the pupil of any off axis star (in MUSCA's case, the secondary component of a binary system) is formed within the active (photosensitive) region of an APD. The size of the detector region is 180μm while the image scale formed at the image plane is about 500μm per arcsecond. Without the field lens, MUSCA would not be able to detect fringes from stars further than 0.2″ from the on-axis reference star. But with the field lens, the maximum binary separation without vignetting is limited by the semi-diameter of the field lens and is estimated to be <25″.

Beam splitter and filters

The beam splitter, BS, was previously used in an older beam combiner and it has a transmissivity to reflectivity ratio of 60:40 at MUSCA's operating wavelengths. In spite of the unbalanced ratio the loss in fringe visibility is less than 3%. Fringe visibility is not a strict design parameter for MUSCA because the main observable of MUSCA is the fringe phase which is not affected by the transmissivity to reflectivity ratio.

The IR cut-off filters in front of each APD are intended to reduce the number of background photon counts originating from an IR metrology laser ($\lambda = 1.15291\mu$m) which is used with the main delay line at SUSI. The filter cut-off wavelength is about 1μm.

Software controllers

The software for controlling MUSCA is written in C language utilizing the standard SUSI libraries. A program that controls a piece or a group of hardware items to do some specific functions is often called a *server* in SUSI because it allows users to control the hardware from any network connected computer. A *server* is written to control each of the following subsystems:

- the scanning mirror, the photon counting modules and the differential delay line –`fringecon`
- the alignment camera (discussed in the next section) –`sbigserver`
- mirror actuators, shutters and slides

The `fringecon` server is not inherited from the one for the *red table*. It was completely re-written for MUSCA because the hardware it controls as well as the approach to photon counting routine and the communication handshaking with its clients are different.

Among the subsystems within MUSCA, the tasks performed by the scanning mirror and the photon counting modules are time critical. The timing of the photon counting routine was controlled by an external hardware-driven interrupt in the original *red table* setup. A 10kHz GPS clock signal was sent to the electronics and the computer as a time-resolution reference signal (Lucas, 2004). Now in MUSCA, the external clock source is replaced with the computer's system clock which is synchronized with a GPS (Stratum 1) clock via the Network Time Protocol (NTP). Using a real time kernel based Linux operating system, a software interrupt is used to pre-empt the kernel to run the photon counting routine at

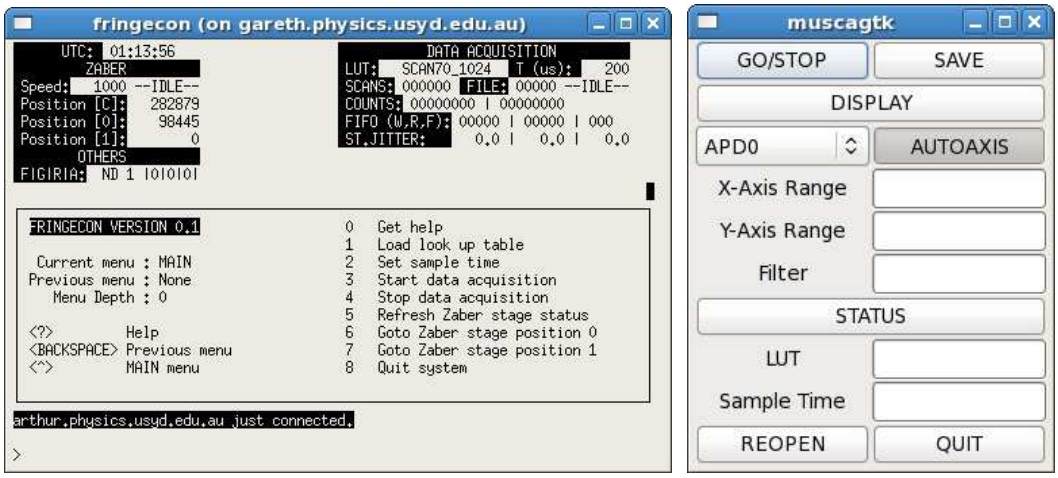

(a) (b)

Figure 3.4: A screenshot of (a) the `fringecon` server and (b) its client.

a constant time interval. The actual sampling time of the routine was measured by counting the number of software clock ticks (which has a time resolution of $\sim$1ns) that have elapsed since the last iteration of the routine. The jitter of the kernel based timing, which is the difference between the actual and the expected sampling time, is typically $\lesssim$10 but can reach up to $\sim 30\mu$s depending on the load of the operating system.

Most of the *client* software modules that connect to the *server*s via TCP/IP protocol use the GTK+ library for building their graphical user interfaces (GUI). However, clients for `fringecon` and `sbigserver` were written in Octave (a MATLAB compatible open-source programming language) and use `gtk-server`[2] for their GUI. This solution combines the quick prototyping time and platform-independent feature of an interpreted language with the user-friendliness of a GUI. Fig. 3.4 shows screenshots of the `fringecon` server and its client.

3.3 Optical alignment

The optical setup for PAVO and MUSCA also includes tools for carrying out optical alignment for the beam combiners as well as the whole interferometer.

[2] `http://www.gtk-server.org/`

3.3.1 Alignment tools

Alignment light sources in SUSI can be divided into 2 sets according to their function. The first set consists of a green 1mW He-Ne laser and a Mini-Maglite 3V tungsten bulb. They are used for general optical alignment and internal fringe searching respectively. They are injected into the optical path from an entry point in front of PAVO (see Fig. 3.2) and trace the path common to both beam combiners in reverse towards the siderostats. Most of the light is reflected towards the siderostats but a small portion is reflected back into the beam combiners for auto-collimation purposes. The second set consists of LEDs and they are attached precisely in the center of the back of the mirror mount at every siderostat. They are used to align the narrow-angle baseline of MUSCA with the wide-angle baseline of SUSI.

Auto-collimation mirrors

Two pairs of auto-collimation mirrors, NAC/SAC and NTA/STA (see Fig. 3.3(a)), are used to reflect light back into PAVO and MUSCA. Although they are located behind dichroic filters which are neither designed to operate at the laser nor the white light source wavelengths, about 2–4% of the laser intensity and a fraction of the white light source intensity are transmitted into PAVO by reflecting off the two pairs of mirrors and into MUSCA by reflecting off NAC/SAC. This setup took advantage of the imperfection in the filter fabrication and the finite slope of the filter profile at the cut-off wavelengths.

The auto-collimation mirrors, NAC and SAC, are implemented as mirrors instead of retroreflectors because the reflected beams of the latter are not necessary co-axially aligned with the incident beams despite being parallel to each other. Unless the beams are precisely aligned to the center of the retroreflectors, there would be a displacement in the pupil of alignment sources with respect to the starlight pupil. Since the laser is also used as a light source for a metrology system to measure optical path length, the pupil displacement would contribute to the non-common path error in the measurement. Therefore fine adjustment in the retroreflectors' position and angle would have to be made in order to precisely align the beams to the center of the retroreflectors each time the incident angle is changed. However, with mirrors, auto-collimated beams are always co-axially aligned with the incident beams.

Nevertheless, retroreflectors are used for ND1 and SD1 because the position of the auto-collimated beams are not as critical and the laser beams are only used for aligning the tip-tilt beams in this part of the optical path.

Remotely controllable mounts, shutters and stages

The auto-collimation mirrors, NAC and SAC, are mounted on mounts fitted with Picomotor piezo-electric linear actuators from Newport[3] which can be operated remotely over the Internet using TCP/IP protocol. Other than that, mirror NTT and STT in Fig. 3.2(b), retroreflector PUPIL in Fig. 3.2(a) as well as mirror M17M and beam splitter BS in Fig. 3.3 are remotely controllable by the same means. In addition, closing and opening shutters, selection of neutral density (ND) filters, adding and removing optics into the optical path via translational stages (e.g. IR LED in Fig. 3.2(a), S19M and LS6 in Fig. 3.3) can all be remotely operated. By having these optical and mechanical components put under computer control, the fine alignment of the optics can be carried out remotely and conveniently before observation.

MUSCA alignment camera

PAVO uses its EMCCD camera for optical alignment but MUSCA uses a separate ST-402ME CCD camera from Santa Barbara Instrument Group (SBIG) specifically for the same purpose. In order to use the latter, a pentaprism, S20M, is slid into the optical path only during alignment and is removed during observation. Images observed with the camera are a magnified version of the pupil or the image of the beams propagating into MUSCA. If an additional focusing lens, LS6, is slid into the optical path then the camera observes the image plane otherwise the camera observes the pupil plane of the beams. Therefore in order to refine the co-axial alignment of MUSCA with this setup, the lens LS6 is slid in and out of the optical path as the tilt angle of beam splitter, BS, and the mirror N17M are adjusted respectively. The goal is to overlap the beams in both the pupil and the image planes.

3.3.2 Internal fringes

Acquiring internal fringes is a procedure that is carried out before an observation. This procedure, which can only be done once the beam combiners are aligned, is mainly to ensure that optical paths non-common to PAVO and MUSCA have approximately zero OPD. In this way, MUSCA is able to acquire stellar fringes as soon as PAVO acquires and tracks them.

[3] `http://www.newport.com`

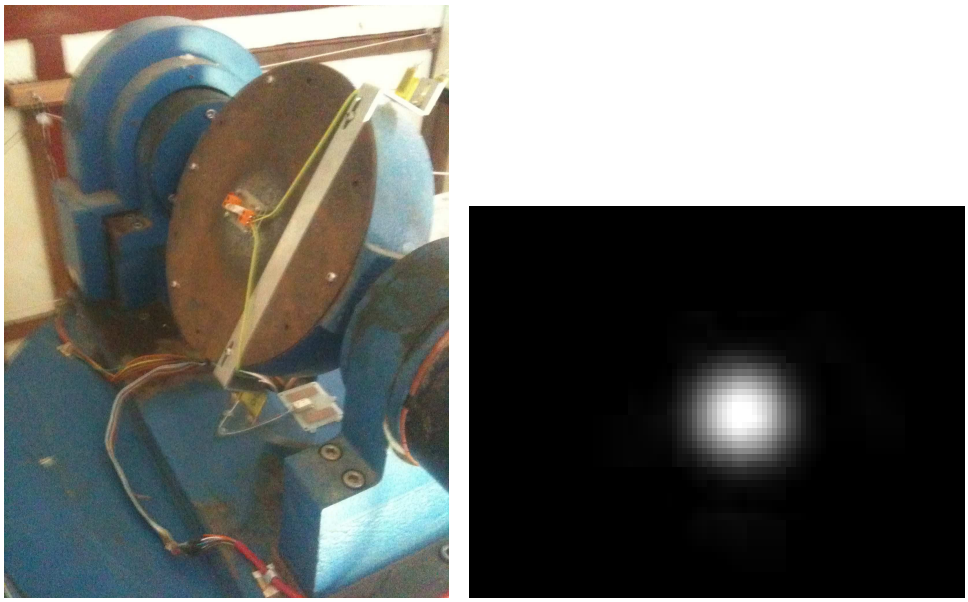

(a) (b)

Figure 3.5: Mounting of an IR LED at a siderostat and its image as seen with the MUSCA alignment CCD camera.

The white light source is used for this procedure. The position of NAC is adjusted in the direction of the beam propagation in order to acquire the fringes on PAVO. Similarly, in order to acquire fringes on MUSCA, the position of the DDL is adjusted. The optical path length within the laboratory can drift by $\sim 1\mu$m ($\sim$1–2λ) in one night. Therefore, once the internal fringes are acquired simultaneously on both beam combiners only minor tweaks are required to keep them within the field of view of the instruments.

3.3.3 Narrow-angle baseline

The alignment of MUSCA's narrow-angle baseline is crucial because it defines the uncertainty of the baseline in use when measuring the optical path difference between two stellar fringe packets. Aligning the images of LEDs at any two siderostats in use with the MUSCA camera addresses the challenge set out in Section 2.4.2. Fig. 3.5(a) shows the LED mounting on the back of the siderostat.

During alignment, the siderostats are turned so that the side with the LEDs faces the periscopes in use. The image of an LED as seen with the MUSCA camera has a size of about 12 pixels, where $\sim$1 camera pixel in the image plane corresponds to a dimension of 1mm at the siderostats. Therefore in order to meet

Table 3.1: Comparison between PAVO+MUSCA and PHASES at PTI

Specification	PAVO+MUSCA	PHASES
Operating wavelengths	Visible	Near IR
Science channel	0.77–0.91μm	K band
Fringe-tracking channel	0.54–0.79μm	K band
Phase-referencing	in post-processing	in real time
OPD modulation range	$\sim$25μm	$\sim$100μm
Field of view	$< 2''$	$< 1''$
Limiting magnitude	4–5 (V)	4.5–5 (K)

the baseline uncertainty requirement the centroid of the LED images from a North and a South siderostats must be aligned to within 1 pixel. The centroid of an LED image is computed by fitting a 2D Gaussian model to the image in real time while mirrors are being adjusted for alignment. Fig. 3.5(b) shows a snapshot of the LED as captured by the MUSCA camera. At the same time, the LED images are also aligned onto the fiducial center of the tip-tilt system in PAVO so the tip-tilt beams have the same optical axis as the MUSCA science beams.

3.4 Comparison with PHASES

The PAVO+MUSCA optical setup is similar to PHASES where both beam combiners receive the same pair of starlight beams from the siderostats and observe the same field of view ($<2''$). However in many other ways it is different. Firstly, PAVO and MUSCA operate in the visible wavelengths. At the time of writing, it is the first phase-referencing instrument in this wavelength range. Secondly, each beam combiner operates at a different wavelength band compared to the other. Thirdly, the phase-referencing of stellar fringes is carried out in post-processing which eliminates the need for a feedback servo loop in MUSCA. Lastly, MUSCA observes only one stellar fringe packet at a time but can switch between a pair of fringe packets of a binary star during observation. Table 3.1 summarizes the comparison between PAVO+MUSCA and PHASES (Muterspaugh et al., 2010b).

3.5 Discussion and summary

The optical setup of MUSCA and the supporting hardware and software tools follow the reusability and simplicity design approach, introduced in Chapter 1.2. It kept the development cost and time to its minimum.

Chapter 4

Computer simulation of PAVO+MUSCA operation

A computer simulation framework was developed to simulate the feasibility and to estimate the performance of the visible wavelength phase-referencing operation of PAVO and MUSCA. The simulation framework also provided great assistance to the development of a new data reduction pipeline for the dual beam combiner configuration. This chapter describes the development of the framework, its usage and some simulation examples showing estimated performance of the instruments.

Most of the content of this chapter is reproduced from the following paper: "Simulating a dual beam combiner at SUSI for narrow-angle astrometry", which has been published in the Experimental Astronomy journal (Kok et al., 2013b).

4.1 Simulation framework

At a glance, the framework consists of two simulators or computer models, one for each of the PAVO and MUSCA beam combiners, which were developed to generate a set of simulated interferograms of each beam combiner based on a given set of user-specified input. The simulators were written in the Interactive Data Language (IDL) but the design concepts and algorithms described here can be implemented in any other language. Both simulators can read the same set of user-specified inputs and by doing so allow users to simulate a dual beam combiner operation in which stellar fringes are recorded by the actual instruments simultaneously in real time. The simulated interferograms can then be used to test the fringe visibility squared (V^2) estimation and the phase-referencing algorithm of the new data

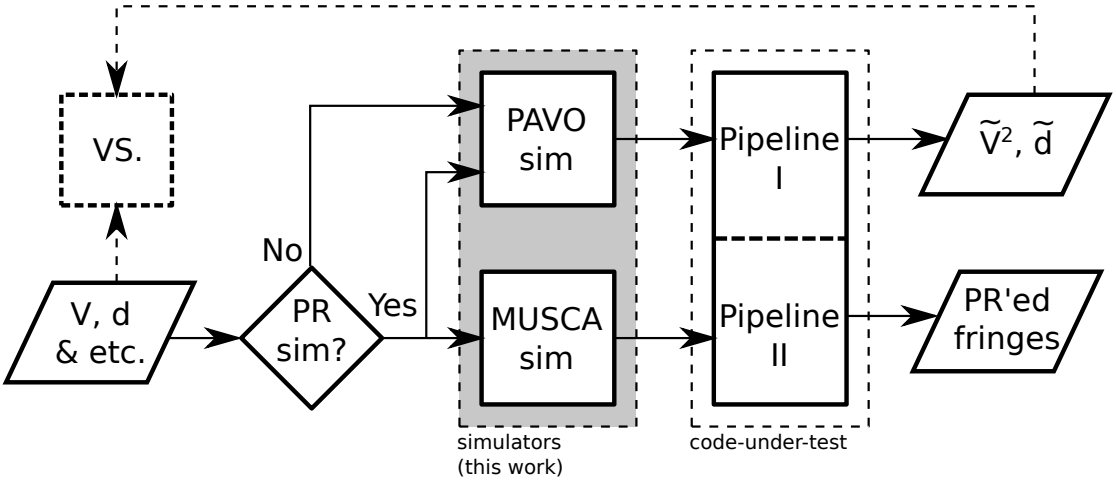

Figure 4.1: Logical flow diagram of the data reduction pipeline testbench. The symbol V and d in the diagram represent the visibility and the phase delay of the fringes to be simulated. The processes with the PR abbreviation are phase-referencing related process while the VS process compares the output of a simulation with the input fed into the simulators.

reduction pipeline (Chapter 6). The simulators are mainly used (1) to assess the accuracy of the pipeline in estimating important parameters (e.g. phase delay and V^2 from PAVO fringes) by comparing the user-specified inputs and the simulated output and (2) to estimate the performance of the dual beam combiner setup by running the simulated output through the new data reduction pipeline. Fig. 4.1 illustrates the data reduction pipeline test bench which shows the usage of the two simulators developed in this work.

The overall logical flow of both simulators is illustrated in Fig. 4.2. Simulation begins with a generic model of two or more pupils. They are then customized according to the optics of the individual beam combiner. Additional and optional phase noise to simulate the effect of atmospheric turbulence (near field approximation only) can be included before the customization of the pupils. Then user-specified inputs are processed, e.g. to determine the number of interferograms (referred to as frames in the flow diagram) to be generated or the visibility and phase delay of the fringes to be simulated. After generating the required frame either by coherent or incoherent combination of the pupils, depending on the type of frame (refer Section 4.2.3), e.g. science (S-), foreground (F-), ratio (R-) or dark (D-) frame, the amplitude of the combined pupil is converted into photon counts and subsequently into the detector read-out units or commonly known as the Analog-to-Digital Units (ADU). The detector read-out noise is also included into the simulator output. The simulated data is then saved into a file of appropriate

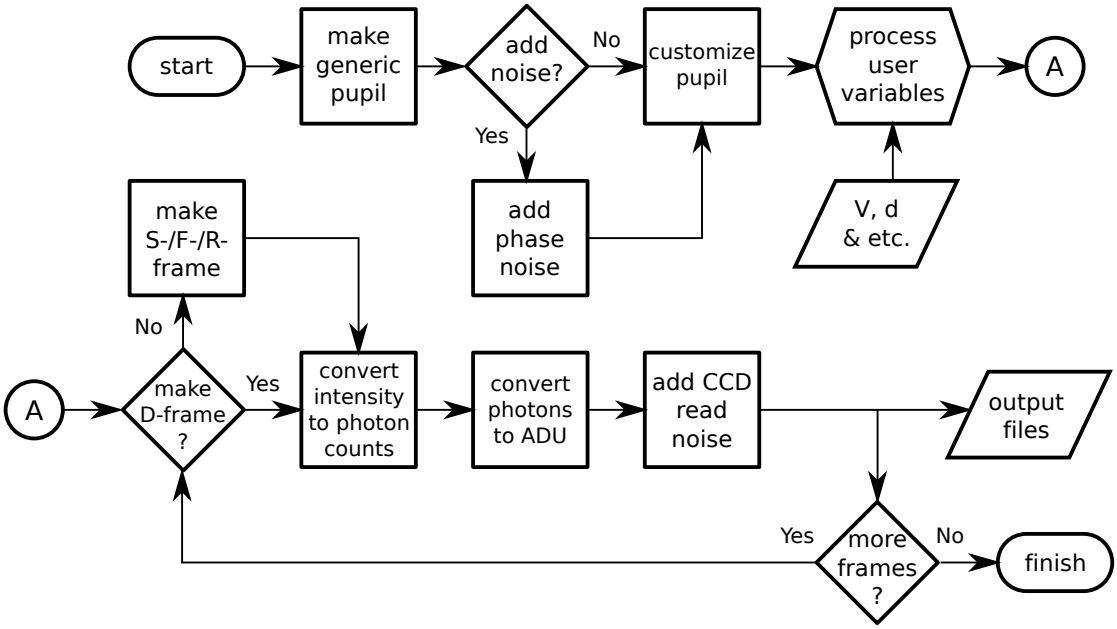

Figure 4.2: Logical flow diagram of the PAVO and MUSCA simulators. The symbol V and d in the diagram represent the visibility and the phase delay of the fringes to be simulated. The S-, F-, R- and D-frame are types of frames recorded during a PAVO observation (see Section 4.2.3).

format. The simulation finishes when all the required frames are generated. The details of each stage of the logical flow are discussed in the subsequent sections.

4.2 The PAVO simulator

The PAVO beam combiner is a multi-axially aligned Fizeau-type interferometer. Its optical setup has been discussed in detail in Section 3.1. Although PAVO at SUSI combines starlight beams from any 2 of the 11 siderostats at any one time the PAVO simulator developed in this work is able to simulate higher order beam combination (i.e. 3 or more beams simultaneously) because PAVO at SUSI has a twin instrument at the CHARA array on Mount Wilson, California (McAlister et al., 2005), which has the capability of combining starlight beams from up to 3 telescopes. The simulator can be used for either of these designs depending on its input.

4.2.1 Input and output of the simulator

There are more than 20 input parameters to the PAVO simulator with the more critical ones listed in Table 4.1. Some input parameters are common to the MUSCA simulator which will be described in Section 4.3. The main output of the simulator is a set of FITS[1] formatted files which contain images of simulated interferograms, hereinafter referred to as frames, as well as header information (e.g. timestamp, fringe lock status, etc) as would be recorded by the PAVO camera. There are four different types of frames recorded by the camera during actual observations. There are the science, ratio, foreground and dark frames. Examples of each of these frames are shown in Fig. 4.3. Each frame, except the dark, contains images of the spectrally dispersed (horizontally in the figure) pupil as sampled by an array of lenslets. The number of lenslets, N_{LL}, is different between PAVO at SUSI and at CHARA. The example shown in Fig. 4.3 is of the former which has 4 lenslets per pupil. The left pupil is for science while the middle and right pupils are used for tip-tilt correction and therefore are not generated in the simulation. The effect of tip-tilt correction, however, is still included in the simulation and is discussed in the Section 4.5. Frames of PAVO at CHARA contains only the science pupil which has 16 lenslets per pupil.

4.2.2 Model pupil

Before the pupils are combined to form fringes, they are first spatially filtered in the image plane with the PAVO mask, one for each beam, to remove high spatial frequency noise arising as a consequence of atmospheric turbulence and optical aberration. A pupil from a telescope is modeled by a square matrix, $\tilde{\mathbf{P}}$, of size $N_{\mathrm{FFT}} \times N_{\mathrm{FFT}}$,

$$\tilde{\mathbf{P}} = \begin{cases} \mathbf{J}_{\mathbf{N}_{\mathrm{FFT}},\mathbf{N}_{\mathrm{FFT}}} & ;\text{perfect wavefront} \\ \mathbf{J}_{\mathbf{N}_{\mathrm{FFT}},\mathbf{N}_{\mathrm{FFT}}} \circ \exp\left(i\boldsymbol{\varphi}\right) & ;\text{corrugated wavefront} \end{cases}, \tag{4.1}$$

where $\mathbf{J}$ represents a unit matrix consisting of all 1s of size (row×column) indicated by its subscript and the phase component is either zero or $\boldsymbol{\varphi}$ in order to represent a perfect or corrugated wavefront. A corrugated wavefront due to atmospheric turbulence will be elaborated in Section 4.5. The notation $\circ$ is the Hadamard or the element-by-element multiplication operator of two matrices. The model of a spatially filtered pupil, $\mathbf{P}'$, is then,

$$\mathbf{P}' = \mathcal{FT}^{-1}\left\{\square \circ \mathcal{FT}\left\{\bigcirc \circ \tilde{\mathbf{P}}\right\}\right\}, \tag{4.2}$$

[1] `http://fits.gsfc.nasa.gov`

Table 4.1: Input parameters for the PAVO (P) and MUSCA (M) simulators

Name	Simulators	Description
t_{START}	P,M	Start of simulation in Julian date
t_{STEP}	P,M	Exposure time of camera/photodetector
$N_{\mathrm{S-FITS}}$	P	Number of science type FITS to generate
$N_{\mathrm{R-FITS}}$	P	Number of ratio type FITS to generate
$N_{\mathrm{F-FITS}}$	P	Number of foreground type FITS to generate
$N_{\mathrm{D-FITS}}$	P	Number of dark type FITS to generate
N_{MED}	P,M	Number and types of optical media
$\boldsymbol{\zeta}$	P,M	Astrometric OPD in m
N_{TEL}	P,M	Number of telescopes
$\mathbf{B}$	P,M	Details of telescopes (e.g. baselines) to be used
m_V	P,M	Magnitude of source in V band
$\mathbf{V}$	P,M	Model complex visibility of source
$\mathbf{D}, \mathbf{d}$	P,M	Offset of $\boldsymbol{\zeta}$ in m
r_0	P,M	Fried parameter in m
$\sigma_{r_0}^{-1}$	P,M	Wavelength in which r_0 is specified (μm)
t_0	P,M	Coherence time in milliseconds
L_0	P,M	Outer scale of atmospheric turbulence in m
t_{STEP}	M	Time interval between steps
N_{STEP}	M	Number of steps of piezo driven mirror per scan
N_{SCAN}	M	Number of scans to simulate
L_{SCAN}	M	Length of a scan in μm

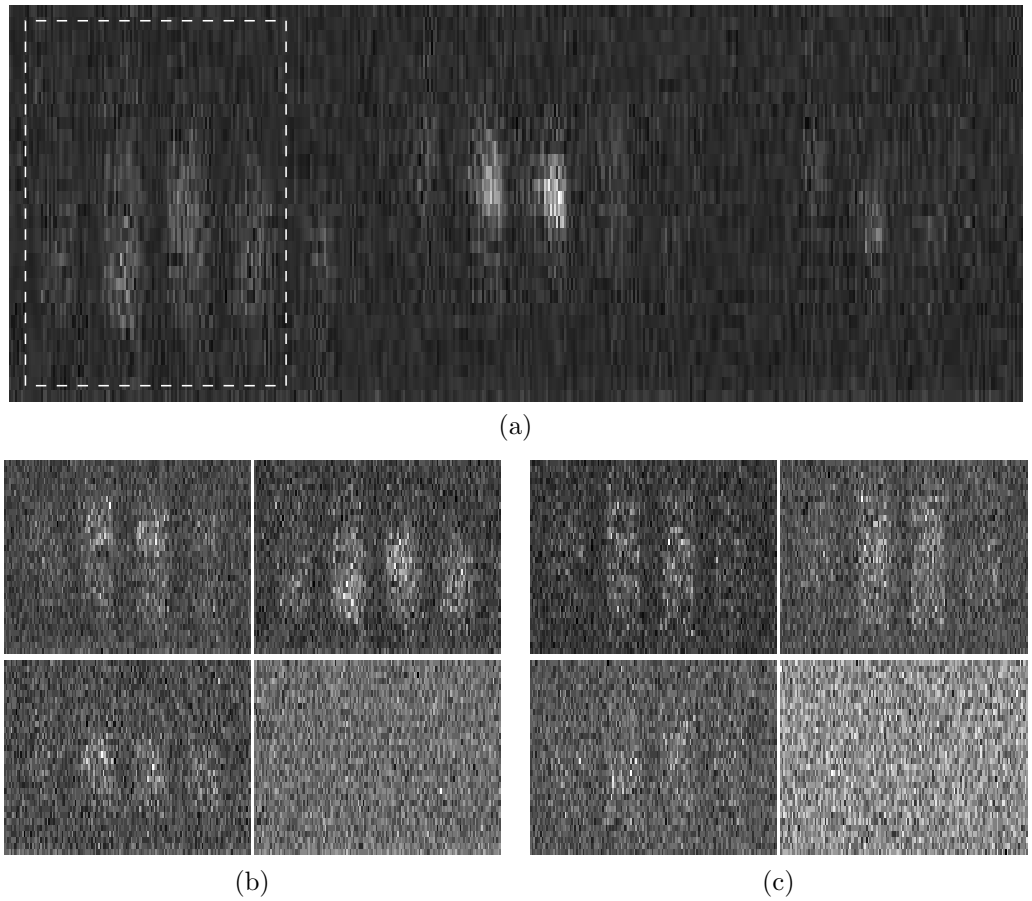

(a)

(b) (c)

Figure 4.3: (a) An example of real on-sky data of α Gru recorded by the PAVO camera. It contains images of spectrally dispersed (horizontally) pupils as sampled by an array of 4 lenslets. The science pupil on the left (indicated by the dotted box) of the frame is where fringes are formed by a pair of overlapped pupils. The pupils in the middle and right of the frame are used for tip-tilt control. They are ignored and will not be generated during simulation. The images of the science pupil for different frame types are shown in (b) and (c). The images, from left to right and top to bottom, belong to four different types of frames, namely science, foreground, ratio and dark respectively. The images in (b) are recorded by the camera while those in (c) are generated by the simulator. The convention adopted by the mathematics in this paper takes the *vertical* axis, which is the fringes direction, as the x-axis and the *horizontal* axis, which is the spectral channel direction, as the y-axis.

where $\bigcirc$ and $\square$ are square matrices of the same size which define a circular pupil and the spatial filter respectively. The notations $\mathcal{FT}\{\}$ and $\mathcal{FT}^{-1}\{\}$ represent the Fourier transform and the inverse Fourier transform of the function within the curly brackets. Each element in the matrices is defined as,

$$\begin{aligned} \bigcirc_{u,v} &= \begin{cases} 1 & ;\text{if } \sqrt{(u - N_{\mathrm{FFT}}/2)^2 + (v - N_{\mathrm{FFT}}/2)^2)} \leqslant N_{\mathrm{DIA}}/2 \\ 0 & ;\text{otherwise} \end{cases} \\ \square_{x,y} &= \begin{cases} 1 & ;\text{if } |x - N_{\mathrm{FFT}}/2| \leqslant N_{\mathrm{MASK}}/2 \text{ and } |y - N_{\mathrm{FFT}}/2| \leqslant N_{\mathrm{MASK}}/2 \\ 0 & ;\text{otherwise} \end{cases} \end{aligned} , \tag{4.3}$$

where N_{DIA} and N_{MASK} are relative sizes of the diameter of the telescopes and the width of the PAVO mask respectively. N_{FFT}, N_{DIA} and N_{MASK} take only integer values. The ratio of the width of the mask to the size of the image varies with the wavelength of light and is defined as,

$$\frac{N_{\mathrm{MASK}}}{N_{\mathrm{FFT}}/N_{\mathrm{DIA}}} \approx \begin{cases} 1.7\sigma_j & ;\text{SUSI} \\ 8.5\sigma_j & ;\text{CHARA} \end{cases} . \tag{4.4}$$

The wavelength corresponding to each PAVO spectral channel is represented by its reciprocal, or wavenumber, σ or σ_j, where j is the index of vector $\boldsymbol{\sigma}$. The vector $\boldsymbol{\sigma}$ represents the range of wavenumbers applicable to the PAVO spectrograph. The wavelength scaling factor in Eq. (4.4) is derived based on the f-ratio of the beam and the distance of the PAVO mask from the pupil plane. The different values for PAVO at SUSI and CHARA mean the optical setups at the two interferometers are not exactly the same. The simulator keeps the denominator of the left-hand side (LHS) of Eq. (4.4) constant and varies N_{MASK} at different wavelengths of light to satisfy the equation. By doing this, the size of the pupil can be kept the same before and after the simulated spatial filtering process. With N_{FFT} and N_{DIA} typically set to 256 and 114 respectively, the range of values of N_{MASK} is 5–7 for SUSI and 22–30 for CHARA.

Before a model pupil is used to form fringes, it is down-sampled to the size of an actual image taken by the PAVO camera, which is $N_{\mathrm{X}} \times N_{\mathrm{LL}}$, where N_{X} is the number of pixels in the x-axis and N_{LL} is the number of lenslets in the y-axis. The values of each parameter are listed in Table 4.2. As a result, the model pupil becomes,

$$\mathbf{P} = \frac{1}{N_{\mathrm{X}} N_{\mathrm{LL}}} \boldsymbol{\mathcal{I}}^{\mathbf{T}}_{\mathbf{N}_{\mathrm{FFT}},\mathbf{N}_{\mathrm{X}}} \, \mathbf{P}' \, \boldsymbol{\mathcal{I}}_{\mathbf{N}_{\mathrm{FFT}},\mathbf{N}_{\mathrm{LL}}} , \tag{4.5}$$

Table 4.2: Specifications of PAVO

Parameter	Notation	CHARA	SUSI
Number of spectral channels	N_σ	19	21
Spectral range (μm^{-1})	$\boldsymbol{\sigma}$	1/0.88–1/0.63	1/0.80–1/0.53
Number of lenslets	$N_{\rm LL}$	16	4
Number of pixels in x-axis	$N_{\rm X}$	128	32
FOV† to pupil size ratio	$\tilde{R}$	5.8	1.8

†the physical size of the active CCD area used

where $\boldsymbol{\mathcal{I}}_{\mathbf{M,N}}$ is a M×N matrix,

$$\boldsymbol{\mathcal{I}}_{\mathbf{M,N}} = \begin{bmatrix} \mathbf{J_{M/N,1}} & 0 & \cdots & 0 \\ 0 & \mathbf{J_{M/N,1}} & \cdots & 0 \\ \vdots & \vdots & \ddots & \vdots \\ 0 & 0 & \cdots & \mathbf{J_{M/N,1}} \end{bmatrix}, \tag{4.6}$$

and $\mathbf{J_{M/N,1}}$ is a $M/N \times 1$ unit matrix consisting of all 1s. This simple down-sampling only works if M is an integer multiple of N. For example, to down-sample a 6×6 matrix $\mathbf{P'}$ to a 2×3 matrix $\mathbf{P}$, the following operation can be applied,

$$\mathbf{P} = \frac{1}{6} \begin{bmatrix} 1 & 0 \\ 1 & 0 \\ 1 & 0 \\ 0 & 1 \\ 0 & 1 \\ 0 & 1 \end{bmatrix}^{\mathbf{T}} \begin{bmatrix} P'_{1,1} & P'_{1,2} & \cdots & P'_{1,6} \\ P'_{2,1} & P'_{2,2} & \cdots & P'_{2,6} \\ \vdots & \vdots & \ddots & \vdots \\ P'_{6,1} & P'_{6,2} & \cdots & P'_{6,6} \end{bmatrix} \begin{bmatrix} 1 & 0 & 0 \\ 1 & 0 & 0 \\ 0 & 1 & 0 \\ 0 & 1 & 0 \\ 0 & 0 & 1 \\ 0 & 0 & 1 \end{bmatrix}, \tag{4.7}$$

where the first and the last matrices on the right-hand side (RHS) are $\boldsymbol{\mathcal{I}}_{\mathbf{6,2}}$ and $\boldsymbol{\mathcal{I}}_{\mathbf{6,3}}$ respectively.

The values of the physical parameters in Eq. (4.4), Eq. (4.5) and other equations in this section are listed in Table 4.2.

4.2.3 Simulating various types of frames

Different types of frames are generated using different combinations of model pupils described in Section 4.2.2. Sets of 50 frames are saved into a FITS file. Each FITS file has a timestamp of,

$$t_\alpha = t_{\rm START} + 50 \times \alpha t_{\rm STEP}, \tag{4.8}$$

where α is the number of FITS files already generated before the current one. The typical value of t_{STEP} for PAVO at SUSI and CHARA is 5ms and 8ms respectively. The number of files to be generated for each type of frame is determined by the user.

Science frames

The science frames are generated using two or more pupils, depending on the number of telescopes in use. Simulation of PAVO at CHARA can use up to three. In reality the pupils are aligned to overlap each other and combined to produce spatially modulated fringes across the pupils. The analytic signal of the model intensity across the overlapped pupils at one particular wavelength is given as,

$$\mathbf{F} = w_j \sum_{\theta=1}^{N_{\mathrm{TEL}}} \sum_{\tilde{\theta}=1}^{N_{\mathrm{TEL}}} V_{\theta,\tilde{\theta}}\, a_\theta \mathbf{P}^{(\theta)} \circ a_{\tilde{\theta}} \overline{\mathbf{P}}^{(\tilde{\theta})} \circ \exp\left(i\mathbf{\Phi}^{(\theta,\tilde{\theta})}\right) \quad ; \begin{array}{l} \mathbf{\Phi}^{(\tilde{\theta},\theta)} = -\mathbf{\Phi}^{(\theta,\tilde{\theta})} \\ \mathbf{\Phi}^{(\theta,\theta)} = 0 \end{array} , \tag{4.9}$$

where the notation $\overline{\mathbf{P}}$ represents the complex conjugate of the variable $\mathbf{P}$. The indices θ and $\tilde{\theta}$ denote one of the several pairs of telescopes used in the simulation (N_{TEL}) while a_θ denotes the weighted amplitude of $\mathbf{P}^{(\theta)}$ such that,

$$a_1^2 + a_2^2 + \cdots + a_{N_{\mathrm{TEL}}}^2 = 1. \tag{4.10}$$

This condition is not physical requirement but is imposed for the convenience of scaling the normalized intensity to the correct photon rate in Section 4.4. The term w_j states the relative intensity of the summation in Eq. (4.9) at one wavelength while the vector $\mathbf{w}$ which w_j is a part of describes the spectrum of the light source and the bandpass profile of PAVO,

$$\mathbf{w} = \begin{bmatrix} w_1 & w_2 & \cdots & w_{N_\sigma} \end{bmatrix} \; ; \text{where } \mathbf{w}\mathbf{J}_{\mathbf{N}_\sigma,\mathbf{1}} = 1. \tag{4.11}$$

This term can easily be customized by user according to the need of a simulation. However, the results shown in Section 4.6 were simulated with a smooth-edged top hat function for $\mathbf{w}$. The model of fringes, $\mathbf{F}$, is expressed in this form in order to allow a model of complex fringe visibility, $V_{\theta,\tilde{\theta}}$, to be applied to the pairs of pupils. The complex fringe visibility matrix, which is a user-supplied input, is defined as,

$$\mathbf{V} = \begin{bmatrix} 1 & V(\sigma_j B_{1,2}) & \cdots & V(\sigma_j B_{1,N_{\mathrm{TEL}}}) \\ \overline{V}(\sigma_j B_{1,2}) & 1 & \cdots & V(\sigma_j B_{2,N_{\mathrm{TEL}}}) \\ \vdots & \vdots & \ddots & \vdots \\ \overline{V}(\sigma_j B_{1,N_{\mathrm{TEL}}}) & \overline{V}(\sigma_j B_{2,N_{\mathrm{TEL}}}) & \cdots & 1 \end{bmatrix}, \tag{4.12}$$

where each off-diagonal element represents the fringe visibility of a model light source at a given wavelength and baseline. The term $B_{\theta,\tilde{\theta}}$ is the magnitude of a baseline vector $\vec{B}_{\theta,\tilde{\theta}}$ formed by a pair of telescopes θ and $\tilde{\theta}$. Lastly the matrix below, $\mathbf{\Phi}$, represents an additional phase difference between the two pupils and it is used to model the difference in piston and tilt in the wavefront of the pupils:

$$\mathbf{\Phi}^{(\theta,\tilde{\theta})} = 2\pi\sigma_j \left(\zeta_{\theta,\tilde{\theta}} + [\mathbf{N}]_{j,*}\mathbf{z}^{(\theta,\tilde{\theta})} + D_{\theta,\tilde{\theta}} + N_{j,1}S_{\theta,\tilde{\theta}}\tilde{R}\mathbf{x}\mathbf{J}_{\mathbf{1},\mathbf{N}_{\mathrm{LL}}}\right). \tag{4.13}$$

The first three terms in Eq. (4.13) represent the piston term. The first term, $\zeta_{\theta,\tilde{\theta}}$, is the astrometric OPD due to the position of the target star with respect to the baseline $B_{\theta,\tilde{\theta}}$ while the second term $[\mathbf{N}]_{j,*}\mathbf{z}^{(\theta,\tilde{\theta})}$ is the optical path of the delay line used to compensate the astrometric OPD. The former is defined as:

$$\boldsymbol{\zeta} = \begin{bmatrix} 0 & \hat{s}\cdot\vec{B}_{1,2} & \cdots & \hat{s}\cdot\vec{B}_{1,N_{\mathrm{TEL}}} \\ -\hat{s}\cdot\vec{B}_{1,2} & 0 & \cdots & \hat{s}\cdot\vec{B}_{2,N_{\mathrm{TEL}}} \\ \vdots & \vdots & \ddots & \vdots \\ -\hat{s}\cdot\vec{B}_{1,N_{\mathrm{TEL}}} & -\hat{s}\cdot\vec{B}_{2,N_{\mathrm{TEL}}} & \cdots & 0 \end{bmatrix}. \tag{4.14}$$

The optical delay line can comprise various optical media. The types of optical media are specified by the user but practically it is usually not more than 4 different types (e.g. vacuum, air and two types of glass, BK7 or F7). The refractive indices for each medium at the wavenumbers of PAVO are calculated using values and constants obtained from Tango (1990). The notation $[\mathbf{N}]_{j,*}$ represents the j-th row of the refractive indices matrix, $\mathbf{N}$, where,

$$\mathbf{N} = \begin{bmatrix} n_1(\sigma_1) & n_2(\sigma_1) & \cdots & n_{N_{\mathrm{MED}}}(\sigma_1) \\ n_1(\sigma_2) & n_2(\sigma_2) & \cdots & n_{N_{\mathrm{MED}}}(\sigma_2) \\ \vdots & \vdots & \ddots & \vdots \\ n_1(\sigma_{N_\sigma}) & n_2(\sigma_{N_\sigma}) & \cdots & n_{N_{\mathrm{MED}}}(\sigma_{N_\sigma}) \end{bmatrix}, \tag{4.15}$$

and n_i is the refractive index of the i-th optical medium. In order to set a convention, the first medium ($i = 1$) is air. Each element in the column vector $\mathbf{z}$ represents the optical path length of each medium and to optimally compensate a given astrometric OPD the values of $\mathbf{z}$ are calculated using the method described by Tango (1990). The third term in Eq. (4.13) is an offset term to allow users to simulate a non-optimally compensated astrometric OPD. The user input matrix $\mathbf{D}$ is defined as,

$$\mathbf{D} = \begin{bmatrix} 0 & d_{1,2} & \cdots & d_{1,N_{\mathrm{TEL}}} \\ -d_{1,2} & 0 & \cdots & d_{2,N_{\mathrm{TEL}}} \\ \vdots & \vdots & \ddots & \vdots \\ -d_{1,N_{\mathrm{TEL}}} & -d_{2,N_{\mathrm{TEL}}} & \cdots & 0 \end{bmatrix}, \tag{4.16}$$

where $d_{1,2}$ for example is the OPD offset for baseline $B_{1,2}$.

The last term in Eq. (4.13) is the OPD caused by the differential wavefront tilt between a pair of pupils at the pupil plane. It is proportional to the separation of the apertures on the PAVO mask and inversely proportional to the distance of the pupil plane from the mask. $S_{\theta,\tilde{\theta}}$ is the ratio of the separation of the apertures on the PAVO mask to the width of each aperture and is defined as,

$$S_{\theta,\tilde{\theta}} = 2(\theta - \tilde{\theta}). \tag{4.17}$$

$\tilde{R}$ is the ratio of the field of view (FOV) of the PAVO camera to the diameter of one pupil at $\sigma = 1\mu m^{-1}$ and its value is given in Table 4.2. Lastly, $\mathbf{x} \in \mathbb{R} : -1/2 \leqslant x_i \leqslant 1/2$ is a column vector of length N_{X} which represents the pixels across the field of view of the camera along the direction of the tilt. This direction is also the axis where interference fringes are formed across the camera and is referred to as the x-axis by convention.

Now, $\mathbf{F}$ is defined at just one wavelength. In reality, the combined pupils are spectrally dispersed by a prism. In order to model this, $\mathbf{F}$ is evaluated N_σ times, each time at a different wavelength within the PAVO spectral bandwidth. Multiple $\mathbf{F}$ matrices are then rearranged in the following order to mimic the actual interferogram recorded by the camera using only their real parts (as denoted by the notation $\Re$),

$$\begin{aligned}\boldsymbol{\mathcal{F}} = {} & N_{\mathrm{PHOTONS}} \\ & \times \Re\left\{\left[\mathbf{0}\, F^{(1)}_{*,0} F^{(2)}_{*,0} \cdots F^{(N_\sigma)}_{*,0}\, \mathbf{0}\, F^{(1)}_{*,1} \cdots F^{(N_\sigma)}_{*,1}\, \mathbf{0}\, F^{(1)}_{*,N_{\mathrm{LL}}} \cdots F^{(N_\sigma)}_{*,N_{\mathrm{LL}}}\, \mathbf{0}\right]\right\} \\ & + \boldsymbol{\epsilon}.\end{aligned} \tag{4.18}$$

The superscripts in parentheses represent the matrices evaluated at different wavelengths within the spectral bandwidth. The interferogram, $\boldsymbol{\mathcal{F}}$, which takes only the real part of the $\mathbf{F}$, is padded with columns of zeros, $\mathbf{0}$, according to a PAVO parameter definition file. The file describes the pixel locations of a spectral channel within the camera's field of view which was determined through calibration with up to two lasers. The final size of $\boldsymbol{\mathcal{F}}$ is N_{X} by 512 elements because the latter is the maximum width (y-axis) of the active region of the EMCCD camera. The scaling factor, N_{PHOTONS}, in Eq. (4.18) converts intensity to energy in terms of number of photons. This factor is proportional to the brightness of the target star, number of telescopes used and the exposure time, all given by the user. A noise term, $\boldsymbol{\epsilon}$, is added to the interferogram to simulate photon noise, multiplication noise and read noise of the EMCCD camera. It is not purely an additive term as suggested because the expression for the noise term in Eq. (4.18) is simplistic. Physical models are used in the simulation to generate the photon and multiplication noise components based on the number of photons.

Foreground frames

Foreground frames are generated in a very similar way to the science frames. Instead of setting $\mathbf{D}$ to values within the coherent length of the PAVO spectral bandwidth, it is set to a very large number (e.g. 1m) so that no fringes are formed across the pupils. Furthermore the visibility of the fringes is set to zero. In the actual beam combiner, foreground frames are recorded by giving the optical delay line a large offset from its last position where fringes were found.

Ratio frames

Ratio frames are generated using only one pupil at a time. In the actual beam combiner, such frames are recorded when only one of the many beams is allowed from reaching the camera. This type of frame is used by the data reduction pipeline to determine the intensity of the pupil from each telescope and the maximum expected fringe visibility of a point source set by the intensity ratio of two beams producing the interference, hence the name 'ratio' frames. With only one pupil, the $\mathbf{F}$ matrix becomes,

$$\mathbf{F} = a_\theta \mathbf{P}^{(\theta)}. \tag{4.19}$$

Dark frames

Unlike previous types, dark frames are generated without any pupil. In the actual beam combiner, dark frames are recorded when all the beams are blocked from reaching the camera. The interferogram contains only the noise term which in this case made up of only the read noise of the camera. This type of frame is used by the data reduction pipeline to subtract the noise floor in the interferogram. The simulated interferogram to represent a dark frame is given as,

$$\boldsymbol{\mathcal{F}} = \boldsymbol{\epsilon}. \tag{4.20}$$

4.3 The MUSCA simulator

The MUSCA beam combiner is a co-axially aligned pupil-plane Michelson interferometer. It combines only two beams at one time, each from one siderostat. Its optical setup has been discussed in detail in Section 3.2. A summary of physical parameters related to the scanning mirror and the operational spectral range of MUSCA are listed in Table 4.3.

Table 4.3: Specification of MUSCA

Parameter	Notation	Typical values
Spectral range (μm^{-1})	$\boldsymbol{\sigma}$	1.1 –1.3
Scan range (μm)	L_{SCAN}	30
Number of steps per scan	N_{STEP}	256
Time interval between steps (ms)	t_{STEP}	0.3

4.3.1 Input and output of the simulator

The format of the input to the MUSCA simulator is exactly the same as the input to the PAVO simulator. Some input parameters are common to both simulators but there are some parameters which are applicable only to the MUSCA simulator. The parameters are listed in Table 4.1.

Instead of FITS, however, the output of the MUSCA simulator is an ASCII text file, which has the same format as one generated by the actual beam combiner. The file contains a time series of photon counts recorded by the APDs in the image plane as the scanning mirror periodically scans through a predetermined scan range. Each photon count has a timestamp with a precision of 10μs. Fig. 4.4 shows an example of the photon counts recorded by the actual instrument as well as a set generated by the simulator.

4.3.2 Model pupil

The model of a pupil in MUSCA is straightforward because there is no spatial filter. Suppose the model pupil is represented again by the matrix $\mathbf{P}$ of size $N_{\mathrm{FFT}} \times N_{\mathrm{FFT}}$, then,

$$\mathbf{P} = \bigcirc \circ \tilde{\mathbf{P}}, \tag{4.21}$$

where $\tilde{\mathbf{P}}$ and $\bigcirc$ are defined earlier in Eq. (4.1) and Eq. (4.3) respectively.

4.3.3 Simulating the photon counts in a scan

The temporal fringes in MUSCA are generated using a pair of pupils, $\mathbf{P}^{(1)}$ and $\mathbf{P}^{(2)}$. In the physical instrument the pupils are aligned and combined coaxially at

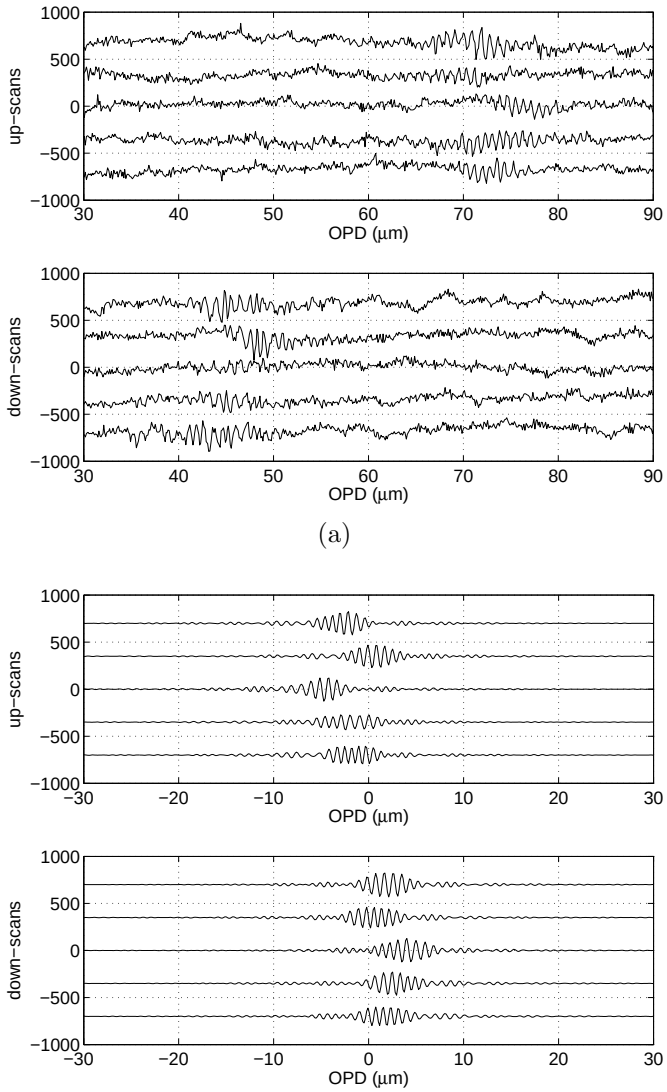

(a)

(b)

Figure 4.4: An example of two sets of time series of photon counts (a) recorded by the actual MUSCA beam combiner and (b) generated by the simulator plotted as separate scans. The simulated fringes in (b) have photodetector noise and atmospheric phase noise included. Note the distortion in the fringe phases. Low frequency fluctuation in total photon counts due to scintillation is absent because a near-field approximation in the simulated atmospheric turbulence is applied. Each scan is plotted with an offset for visualization. The x-axis shows the relative OPD within the scan range of the scanning mirror. The top and bottom plots are scans in different directions of the scanning mirror.

a beamsplitter to produce two sets of output pupils. In the simulator the output pupils are modeled as two $N_\sigma \times N_{\mathrm{STEP}}$ matrices,

$$\begin{aligned}\mathbf{F}^{(L)} &= 1 + 2a_1a_2\Re\left\{((\mathbf{w}\cdot\mathbf{v})^{\mathbf{T}}\mathbf{J}_{\mathbf{1},\mathbf{N}_{\mathrm{STEP}}}) \circ \mathbf{Q} \circ \exp\left(i\mathbf{\Phi}\right)\right\} \\ \mathbf{F}^{(R)} &= 1 - 2a_1a_2\Re\left\{((\mathbf{w}\cdot\mathbf{v})^{\mathbf{T}}\mathbf{J}_{\mathbf{1},\mathbf{N}_{\mathrm{STEP}}}) \circ \mathbf{Q} \circ \exp\left(i\mathbf{\Phi}\right)\right\}\end{aligned} . \tag{4.22}$$

The matrices and their superscripts (L) and (R) represent the intensity of the output pupil on the left and right side of the beamsplitter. The variables a_1, a_2 and $\mathbf{w}$ are previously defined in Eq. (4.10) and Eq. (4.11). The vector $\mathbf{v}$, which is similar to the matrix $\mathbf{V}$ in Eq. (4.12), is the model fringe visibility of the source for the baseline defined by telescopes of pupil $\mathbf{P}^{(1)}$ and $\mathbf{P}^{(2)}$:

$$\mathbf{v} = \begin{bmatrix} V(\sigma_1 B_{1,2}) & V(\sigma_2 B_{1,2}) & \cdots & V(\sigma_{N_\sigma} B_{1,2}) \end{bmatrix}. \tag{4.23}$$

Each element of $\mathbf{Q}$ is,

$$Q_{j,k} = \frac{\sum_{u=1}^{N_{\mathrm{FFT}}}\sum_{v=1}^{N_{\mathrm{FFT}}} P_{u,v}^{(1,j,k)}\overline{P_{u,v}^{(2,j,k)}}}{\text{Area of circular aperture in } \bigcirc}. \tag{4.24}$$

The real part of Eq. (4.24), $\Re\{Q_{j,k}\}$, represents the normalized intensity at wavenumber σ_j due to the sum of pupils $\mathbf{P}^{(1)}$ and $\mathbf{P}^{(2)}$ at k-th step of a scan. $\mathbf{\Phi}$ is the additional phase difference between two telescope pupils at various wavelengths,

$$\mathbf{\Phi} = 2\pi\left(\boldsymbol{\sigma}^{\mathbf{T}}\boldsymbol{\zeta} + \mathbf{J}_{\mathbf{N},\mathbf{1}}\boldsymbol{\sigma}\mathbf{N}\mathbf{Z} + \boldsymbol{\sigma}^{\mathbf{T}}\mathbf{d}\right), \tag{4.25}$$

and it is used to model the difference in piston between the pupils at each step of a scan.

The structure of Eq. (4.25) is very similar to Eq. (4.13). The first term in Eq. (4.25), $\boldsymbol{\zeta}$, is the astrometric OPD per scan of the baseline $\mathbf{B}_{1,2}$. Each element, ζ_k, is evaluated at time $t_{\alpha,k}$,

$$\zeta_k = \left|\hat{s}\cdot\mathbf{B}_{1,2}\right|_{t=t_{\alpha,k}}, \tag{4.26}$$

where,

$$t_{\alpha,k} = t_{\mathrm{START}} + t_{\mathrm{STEP}}\left(\alpha N_{\mathrm{STEP}} + k\right), \tag{4.27}$$

and α is the number of elapsed scans before the current one and k is the index of a step within a scan. The typical value of t_{STEP} for MUSCA is 0.3ms. The second term in Eq. (4.25), $\mathbf{NZ}$, is the optical path of the delay line used to compensate the astrometric OPD. The matrix, $\mathbf{N}$, previously defined in Eq. (4.15), denotes the

refractive indices of each optical medium in the path while the matrix, $\mathbf{Z}$, denotes the path length of each medium at every step in a scan:

$$\mathbf{Z} = \begin{bmatrix} z_1(t_{\alpha,1}) & z_1(t_{\alpha,2}) & \cdots & z_1(t_{\alpha,N_{\text{STEP}}}) \\ z_2(t_{\alpha,1}) & z_2(t_{\alpha,2}) & \cdots & z_2(t_{\alpha,N_{\text{STEP}}}) \\ \vdots & \vdots & \ddots & \vdots \\ z_{N_{\text{MED}}}(t_{\alpha,1}) & z_{N_{\text{MED}}}(t_{\alpha,2}) & \cdots & z_{N_{\text{MED}}}(t_{\alpha,N_{\text{STEP}}}) \end{bmatrix} + \begin{bmatrix} \boldsymbol{\ell} \\ \mathbf{0}_{\mathbf{1},\mathbf{N}_{\text{STEP}}} \\ \vdots \\ \mathbf{0}_{\mathbf{1},\mathbf{N}_{\text{STEP}}} \end{bmatrix}. \tag{4.28}$$

The values of elements in the first term of the RHS of Eq. (4.28) are calculated using the method described by Tango (1990). The vector $\boldsymbol{\ell}$ in Eq. (4.28) describes the relative change in the optical path length of air at every step in a scan due to the motion of the scanning mirror:

$$\begin{aligned} \boldsymbol{\ell} =& \frac{L_{\text{SCAN}}}{N_{\text{STEP}} - 1} \times \\ & \left[-N_{\text{STEP}}/2 \quad -N_{\text{STEP}}/2 + 1 \quad \cdots \quad -1 \quad 0 \quad 1 \quad \cdots \quad N_{\text{STEP}}/2 - 1 \right]. \end{aligned} \tag{4.29}$$

Elements in the same column of $\mathbf{Z}$ have the same timestamp as an element with the same index in $\boldsymbol{\zeta}$. The last term in Eq. (4.25), $\mathbf{d}$, is the user-specified offset at each step to simulate a non-optimally compensated astrometric OPD:

$$\mathbf{d} = \begin{bmatrix} d_1 & d_2 & \cdots & d_{N_{\text{STEP}}} \end{bmatrix}. \tag{4.30}$$

After the pupils are combined and have formed fringes, it is assumed that the entire image of the pupil falls within the active area of the photodiodes and all photons are detected. The photodetectors in MUSCA have only one pixel and are unable to resolve any spatial variation in intensity at the image plane. Therefore only an average intensity is recorded, hence the term $\mathbf{Q}$ in Eq. (4.22). In addition to that the photodetectors in MUSCA are unable to resolve intensity variation across wavelengths. Therefore the number of photon counts recorded by the photodetectors is the sum of photons across the entire MUSCA operating bandwidth,

$$\boldsymbol{\mathcal{F}} = N_{\text{PHOTONS}} \times \mathbf{J}_{\mathbf{1},\mathbf{N}_\sigma} \mathbf{F} + \boldsymbol{\epsilon}. \tag{4.31}$$

Similar to Eq. (4.18), N_{PHOTONS} is a scaling factor that converts the intensity of the output pupil to the number of photons expected from the source given its brightness in magnitude scale and $\boldsymbol{\epsilon}$ is a noise term included to simulate photon noise and the dark count noise of the detector.

Table 4.4: Absolute flux calibration of α Lyrae (Bessell, 1979)

Filter band	λ_{eff} (μm)	$\Delta\lambda$ (μm)	Flux density, F_ν ($\times 10^{-23}$ W m^{-2} Hz^{-1})
U	0.36	0.076*	1.81
B	0.44	0.094*	4.26
V	0.55	0.088*	3.64
R_C	0.64	0.57-0.72	3.08
I_C	0.79	0.725-0.875	2.55

*`http://www.astro.umd.edu/~ssm/ASTR620/mags.html`

4.4 Magnitude to photon rate

The scaling factor N_{PHOTONS} in Section 4.2 and Section 4.3 is estimated based on the expected throughput of the beam combiner to be simulated, the efficiency (Q.E.) of the APDs and a calibrated magnitude-to-flux scaling factor, F_ν, by Bessell (1979). The first two factors collectively describe the efficiency of the instrument, η, which is found to be $\sim$3% for PAVO and $\sim$1% for MUSCA. The lower efficiency in MUSCA is possibly due to the aluminium coated mirrors used in SUSI and a silvered beamsplitter in MUSCA. The values of F_ν at different photometric bands are listed in Table 4.4, which is reproduced from Bessell (1979). From F_ν, the number of photons from a m_V magnitude star collected by a telescope with an area of A_{tel} m^2 in Δt seconds can be estimated. Putting the factors together,

$$N_{\text{PHOTONS}} \simeq \eta \times 1.51 \times 10^{10} \times 10^{-m_V/2.5} \times F_\nu \frac{\Delta(1/\sigma)}{\Delta\lambda} A_{\text{tel}}\, \Delta t, \tag{4.32}$$

where the $\Delta(1/\sigma)$ is the bandwidth of the beam combiner and $\Delta\lambda$ is the bandwidth referred from Table 4.4 which has an effective wavelength close to that of the beam combiner. As an example, in the case of the MUSCA beam combiner, $\Delta(1/\sigma) \simeq 0.29\mu$m, $\Delta\lambda = 0.15\mu$m, $\lambda_{\text{eff}} = 0.79$, $A_{\text{tel}} = 7 \times 10^{-3}$m^2 and $\Delta t \simeq 80$ms (256$\times$0.3ms).

4.5 Simulating the effect of turbulent atmosphere

A turbulent atmosphere introduces amplitude and phase fluctuation to an otherwise plane wavefront of light from a distant star. Although amplitude fluctuation can be simulated, both PAVO and MUSCA simulators make the assumption that

the atmospheric turbulence only gives rise to perturbation in the phase of a wavefront. This approximation of discarding the amplitude (scintillation) term, also known as the near-field approximation, holds very well for optical long baseline interferometry because the phase fluctuation due to scintillation is weak and negligible at low spatial frequency (Roddier, 1981).

The phase fluctuation in the atmosphere is simulated using a large ($N_{\mathrm{ATM}} \times N_{\mathrm{ATM}}$) two-dimensional array of random phasor, $\boldsymbol{\phi}$, which has a power spectrum given as,

$$\left|\hat{\phi}_{u,v}\right|^2 = C\left(L_0^{-2} + (u^2+v^2)\right)^{-11/6}. \tag{4.33}$$

This is slightly different from the power spectrum given in Eq. (2.7) because the power level at frequencies lower than L_0 is attenuated and finite. This power spectrum is based on the von Karman model of the atmospheric turbulence (Ishimaru, 1997). The parameter L_0 is known as the outer scale of the turbulent structure. L_0 is set to a very large number in the simulation so that the power spectrum approximates the Kolmogorov model. The notation $\hat{\phi}$ denotes the Fourier transform of ϕ while u and v denote the indices of the 2D array. The phase fluctuation is computed by taking the inverse Fourier transform of $\left|\hat{\phi}_{u,v}\right| \exp(i\varepsilon)$ where ε is the phase of the Fourier transform and is a random variable. The randomness of the generated phase fluctuation, ϕ, is controlled by adjusting the scaling factor, C. It is tweaked so that the structure function of ϕ,

$$\left\langle |\phi_{u,v} - \phi_{u+r_u,v+r_v}|^2 \right\rangle = 6.88\left(\frac{\sqrt{r_u^2+r_v^2}}{r_0}\right)^{5/3}, \tag{4.34}$$

has its characteristic Fried parameter, r_0, set to the value specified by the user. Fig. 4.5(a) shows an image of the random phases generated using this method.

On the other hand the phase fluctuation of a wavefront across a telescope, or $\boldsymbol{\varphi}$ in Eq. (4.1) and Eq. (4.21), is simulated by extracting a small portion ($\sim$100$\times$100) of the much larger $\boldsymbol{\phi}$ array. The typical size of the $\boldsymbol{\phi}$ array is 2048$\times$2048. Since r_0 is specified at a certain wavelength, $\sigma_{r_0}^{-1}$, and the phase fluctuation in $\boldsymbol{\phi}$ is generated according to r_0, the value extracted from the larger array must be scaled by a factor of σ_j/σ_{r_0}, where σ_j is the desired wavenumber for simulation, before applying it to the model pupils in Eq. (4.1) and Eq. (4.21). The position of this small sampling window is displaced across the larger array after every time step of the simulation. This simulates the effect of Taylor's (1938) hypothesis of a frozen atmosphere drifting across the aperture of the telescope. The rate of displacement of the sampling window depends on the effective wind speed and the time step of

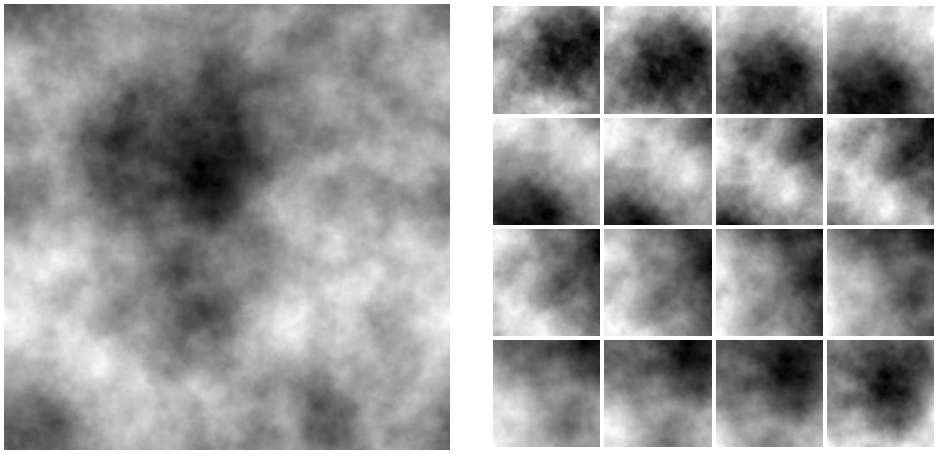

(a) (b)

Figure 4.5: (a) An array of random phases generated with the inverse Fourier transform method. The value of the phases is indicated by the shades of gray in the images. (b) Small portions of the larger array in (a) sampled at slightly different positions at each time step showing the progress through time. Time increases from left to right and top to bottom.

the simulation, t_{STEP}. The effective wind speed is estimated from,

$$\bar{v} = 0.314\frac{r_0}{t_0}, \tag{4.35}$$

where t_0 is the atmospheric coherence time of the phase fluctuation. Both parameters are specified by the user. In this context, it is not important to argue about the appropriate definition of the atmospheric coherence time (as discussed in Section 2.2) because it is only used to estimate $\bar{v}$ in the simulation. It is up to the user to convert the value of the atmospheric coherence time to be used, if necessary, according to Eq. (4.35). The direction of the displacement is random but remains constant throughout the simulation. Fig. 4.5(b) shows several snapshots of phase variation over a small portion of a larger array drifting across the sampling window.

A separate array of $\boldsymbol{\phi}$ is generated for each telescope. By doing this, it is assumed that the phase fluctuations over individual telescopes are uncorrelated. As a result, the low-frequency phase fluctuations do not increase with baseline in the simulation. In practice this scenario is true if the baseline is longer than the outer scale of turbulence, L_0, which is in the order of 100m (Davis et al., 1995). Therefore this approach of having a separate array of $\boldsymbol{\phi}$ for each telescope does not realistically simulate the piston term of an aberrated pupil due to atmospheric turbulence. In order to address this shortcoming in the PAVO and MUSCA sim-

ulator, the input variable, **D** or **d** (refer Table 4.1), can be used to add an extra differential piston between pupils from two apertures.

Another shortcoming of this method in simulating the phase variation across a turbulent atmosphere is a structure function that deviates from its theoretical value at large distances. Fig. 4.6 shows comparison between a theoretical structure function and one calculated from the $\boldsymbol{\phi}$. The plots in the figure are $(D_\phi/6.88)^{3/5}$ versus r and normalized to the size of the array, N_{ATM}. The theoretical Kolmogorov (KM) model curve is a straight line with unity slope ($r_0 = 1$). The deviation from the theoretical value is very pronounced especially at large distances. This is not surprising because the power spectrum, $|\hat{\phi}|^2$, is undersampled at low frequencies, where most of the energy resides. A practical solution to this problem, which is the approach implemented in this work, is to sub-sample the phase fluctuation from a much larger array (Lane et al., 1992; McGlamery, 1976; Shaklan, 1989). With a telescope aperture model of ∼5% of the size of the larger phase array, such approximation produces a phase fluctuation that is at most 20% off the theoretical KM model. This is shown in Fig. 4.6. Also shown in the figure is a theoretical von Karman (VK) model which has a structure function very similar to that of the generated phase fluctuation. The outer scale of turbulence of the model is ∼44% of N_{ATM} and at this outer scale of turbulence, given the telescope aperture used in the simulation model, the variance of the tip-tilt angle of an image formed with the phase fluctuation is reduced by ∼40% from its expected value based on a KM model which has an infinite outer scale (Sasiela & Shelton, 1993). This reduction in tip-tilt fluctuation simulates the active tip-tilt correction at SUSI which stabilizes the image of a star.

4.6 Simulation testcases

The main objective of this simulation framework is to test the data reduction pipeline of the beam combiners. It is also a good tool to investigate software bugs in a data reduction pipeline during its development stage. The following sections discuss some testcases using the simulators.

Several testcases were carried out to demonstrate the functionality of the simulator and at the same time the accuracy of the data reduction pipeline for both PAVO and MUSCA. Testcase I is carried out to verify the extraction of visibility squared, V^2, of a set of fringes by the PAVO pipeline. Testcase II-IV were carried out to probe the lower bound phase error of the phase-referenced fringes constructed by the PAVO and MUSCA phase-referencing pipeline. On top of that they are also used to verify the PAVO V^2 pipeline. Table 4.5 shows the input for

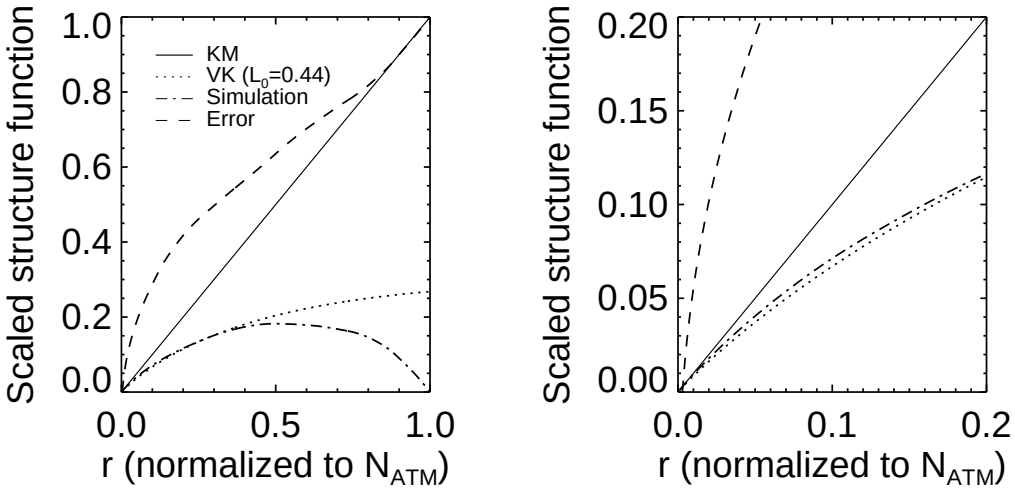

Figure 4.6: Plots of $(D_\phi/6.88)^{3/5}$ against r where D_ϕ is either a theoretical, based on a Kolmogorov (KM) model, Eq. (4.34), or a von Karman (VK) model (Valley, 1979)), or a simulated structure function. Both axes are normalized to the size of the random phases array. The dashed lines (Error) in the plots are the difference between the solid (KM) and dash dot (Simulation) lines relative to the former. If the simulated structure function is exactly the same as the theoretical structure function then the dash lines will be horizontal at 0. The right plot is the zoomed in version of the left.

each testcase. All input parameters for Testcase II-IV are kept the same except for the fringe visibility parameter.

4.6.1 To verify the V^2 reduction pipeline

Testcases I-IV were used to verify the V^2 reduction pipeline of PAVO at SUSI. In these testcases the PAVO simulator was used to investigate the pipeline's ability to reproduce the square of the visibility of a given model. The input fringe visibility for Testcase I is a sinusoidal function which models a binary star system with the primary and secondary stars almost equal in brightness (contrast ratio of $\sim$0.95) and having a projected separation of $\sim 0.04''$ using a 15m baseline. On the other hand, the input fringe visibilities for Testcase II-IV are constant to model an unresolved single star but have different values of instrument visibilities. Since PAVO at SUSI uses only two telescopes at any one time, $\boldsymbol{\zeta}$ and $\mathbf{D}$ each reduce to a 2×2 square matrix. The values of off-diagonal elements of the matrices, $\zeta_{1,2}$ and $d_{1,2}$, are shown in Fig. 4.7. All testcases have 3 sub-cases (A, B and C) where the photon rate is varied to simulate an observation of a zeroth, 2nd or 4th magnitude star. The number of photons in a generated PAVO frame is adjusted to match the number in an actual frame recorded by the PAVO camera at a gain of 5^2, for a star of magnitude $m_V = 0.0$ and $m_V = 2.0$, and 25, for a star of magnitude $m_V = 4.0$.

The four types of frames generated by the PAVO simulator are similar to those shown in Fig. 4.3(c) and therefore will not be shown again in this section. The estimated V^2 of each simulated data set extracted by the PAVO pipeline are plotted against the models fed into the simulator in Fig. 4.8. This is the main goal of the simulation, to be able to compare the output of the data reduction pipeline with the input of the simulator and to verify the accuracy of the former. Also plotted for comparison, in Fig. 4.9, are the estimated V^2 of Testcases II-IV. Both figures show that the estimated values are consistent with the model, but are biased low when atmospheric phase noise is present. The expected reduction in visibility of the fringes, which is more pronounced at higher spatial frequencies (right half of the graphs), is due to the atmospheric phase noise. The observed trend in Fig. 4.9(b), is due to a wavelength-dependent scaling factor in the order of unity which is in turn caused by the shape of a Fourier domain windowing function used in the data reduction pipeline. This scaling factor and the biased value can be calibrated out because it is identical regardless of the visibility function, as seen in Fig. 4.8(b) which plots the ratios between the estimated and the model V^2 across spatial frequency (a form of a transfer function of the data reduction pipeline). Data points in the plot significantly larger than 1 are an effect of calculating a ratio

[2]This is an instrumental gain factor of the EMCCD camera

Table 4.5: Input parameters for all testcases

Testcases → Names ↓	I	II	III	IV
Section	Section 4.6.1	Section 4.6.1 & 4.6.2		
t_{START}	2455848.5			
t_{STEP}	PAVO: 5.0ms MUSCA: 0.2ms			
$N_{\mathrm{S-FITS}}$	150			
$N_{\mathrm{R-FITS}}$	20			
$N_{\mathrm{F-FITS}}$	20			
$N_{\mathrm{D-FITS}}$	20			
N_{STEP}	–	1024		
N_{SCAN}	–	150		
L_{SCAN}	–	140μm		
N_{MED}	3 (air, BK7, F7)			
$\boldsymbol{\zeta}$	See Fig. 4.7			
N_{TEL}	2 (N3, S1)			
$\mathbf{B}$	$\lvert B_{1,2}\rvert$ ∼15m			
m_V	Sub-case A: 0.0 Sub-case B: 2.0 Sub-case C: 4.0			
$\mathbf{V}^2$	0.01–0.36	0.25	0.10	0.01
$\mathbf{D}, \mathbf{d}$	See Fig. 4.7			
r_0	10cm			
$\sigma_{r_0}^{-1}$	0.5μm			
t_0	1ms			
L_0	100m			

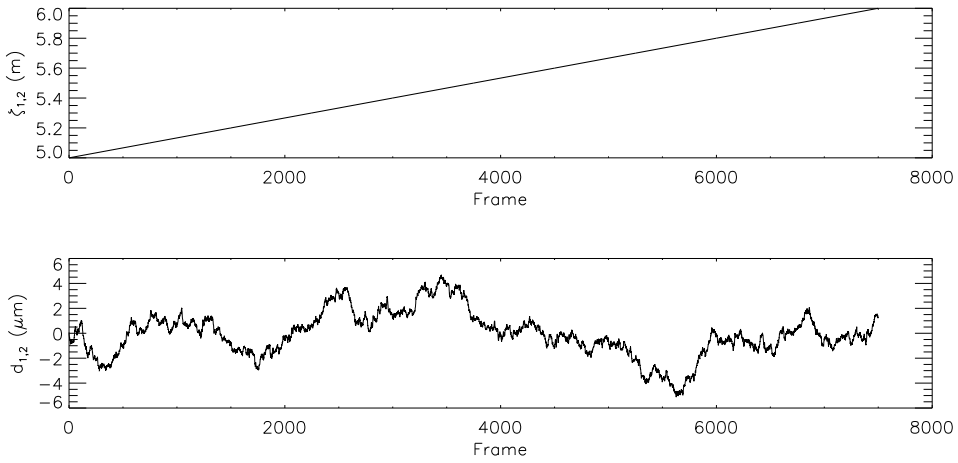

Figure 4.7: The value of $\zeta_{1,2}$ and $d_{1,2}$ used in the simulation versus the frame number. The latter is a pseudo-random variable where the difference in value between each step has a normal distribution of zero mean and a standard deviation of 10nm.

with the denominator that has a very small value. Calibrating fringe visibility of a target with respect to the fringe visibility of a calibration source (e.g. an unresolved single star) yielding the target's true fringe visibility from the instrument's transfer function is a standard practice in stellar interferometric data analysis (see Eq. 2.4).

In summary, these testcases show that the V^2 reduction pipeline has some dependence on the seeing condition, which can be calibrated out, but no measurable bias as a function of target brightness or the square of the visibility of the fringes.

4.6.2 To verify the phase-referencing pipeline

In addition to the goal mentioned in the previous section, the main aim of Testcases II-IV is to test a newly written PAVO and MUSCA phase-referencing pipeline and to probe the lower bound phase error of the phase-referenced fringes. Both simulators were fed with the same input for this purpose. Some inputs which are common to both simulators, e.g. $\boldsymbol{\zeta}$ and $\mathbf{D}$ for PAVO, are resampled at a different rate for MUSCA because the time steps of the two simulators are different. Inputs which are not common to both inputs, e.g. $N_{\mathrm{S-FITS}}$ and N_{STEP}, are defined separately.

The role of the PAVO data reduction pipeline in these testcases is to provide estimates of the group and phase delay of the fringes. The group delay of the

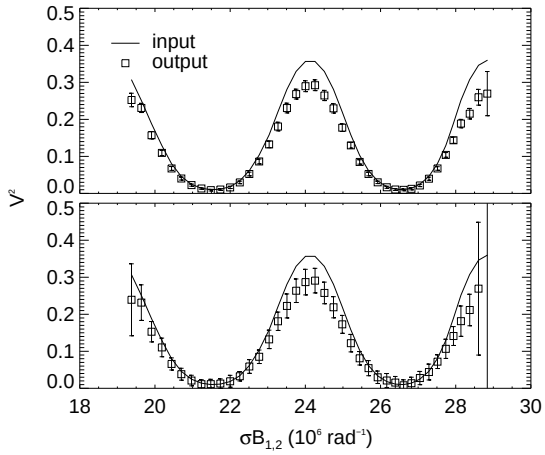

(a)

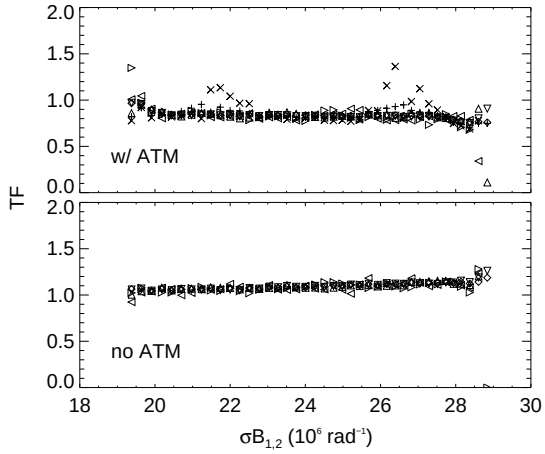

(b)

Figure 4.8: A comparison between user-specified models of V^2 (solid line) and the estimated V^2 produced by the PAVO V^2 reduction pipeline. The top plot of (a) shows the comparison between a wavelength-dependent V^2 model (input) and the (output) values estimated by the pipeline at high photon rate (sub-case A) while the bottom plot of (a) represents a similar comparison at lower photon rate (sub-case B). The ratio of estimated to model V^2 for Testcase I (+, ×), II ($\diamond$,$\triangle$), III ($\triangledown$,$\triangleright$) and IVB ($\triangleleft$) are plotted against spatial frequency in (b). The plot in (b) shows the transfer function (TF) of the data reduction pipeline. Each pair of symbols in the parentheses except for Testcase IV represents sub-cases A and B respectively. Also in (b), the ratios are shown when atmospheric phase noise was excluded in the simulation (no ATM).

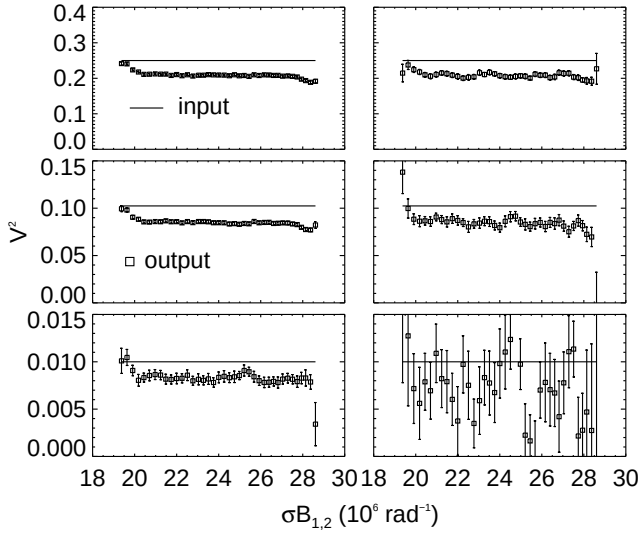

(a)

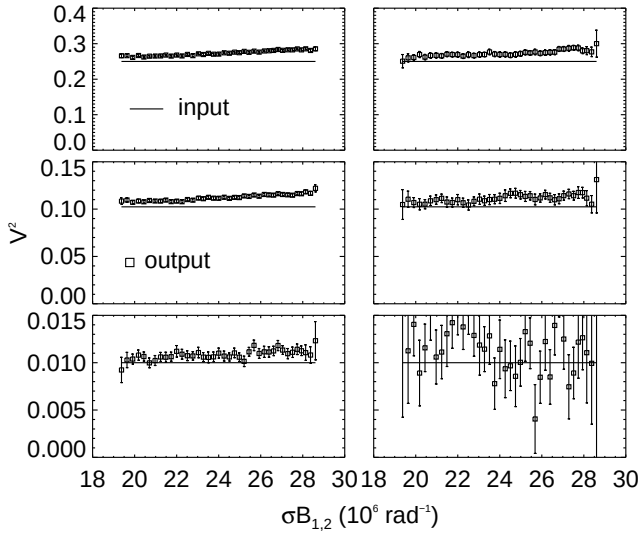

(b)

Figure 4.9: Similar to Fig. 4.8(a), the top, middle and bottom plots of (a) and (b) show the comparison between a constant V^2 model (input) and the estimated (output) of the pipeline for Testcase II, III and IV respectively. The plots on the left column are from sub-case A where the photon rate is higher than sub-case B which plots are on the right column. The estimated V^2 values of sub-case B of Testcase IV are very noisy but are still unbiased. The plots in (a) are simulated with the presence of atmospheric phase noise while plots in (b) are simulated without.

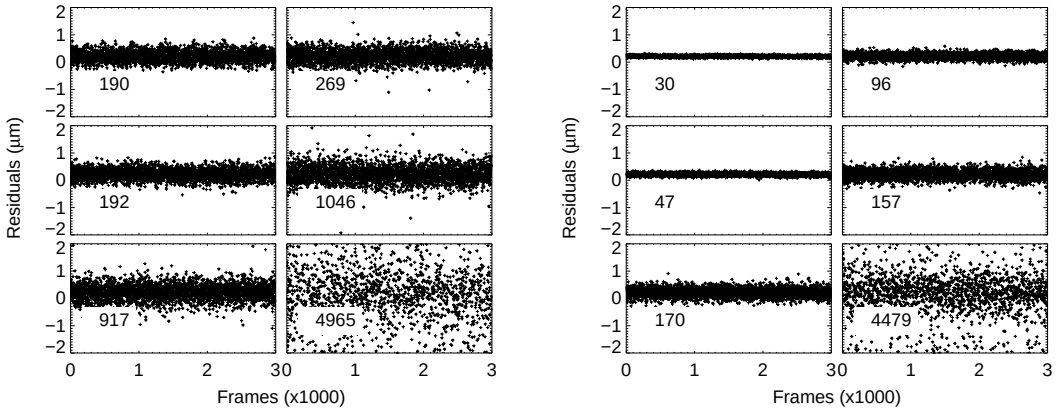

(a) (b)

Figure 4.10: The residuals of group delay estimates obtained from the PAVO reduction pipeline for Testcases II-IV (from top to bottom) after subtracting off a value equal to the input OPD from the estimates. The left and right columns are residuals for sub-cases A and B respectively. The root of mean squared of the residuals (rms), in unit of nanometers, are stated in the plots. The data for the plots in (a) and (b) are obtained with and without atmospheric phase noise in the simulations.

fringes is defined by the user-specified input variables, **D** and **d**. The errors of the group delay estimates are shown in Fig. 4.10. The standard deviation of the error of the group delay estimates increases as the visibility of the fringes and the photon rate decrease. This is expected as the signal becomes weaker than the photon noise and read noise of the camera. Since the phase delay of the fringes is estimated from the group delay estimate, residuals of group delay errors which are larger than one wavelength of the fringes produce unreliable phase delay estimates. Only reliable estimates of phase delay are chosen and applied to stabilize the position of a fringe packet generated by the MUSCA simulator. The percentage of reliable estimates within an observation is a function of atmospheric seeing, brightness of the target star and the visibility of the stellar fringes.

Waterfall plots in Fig. 4.11 show the position of the fringe packet through time. They clearly show that the fringe packet has a continuously changing position before the phase delay estimates are applied and a relatively constant position after they are applied. The phase variation of the phase-referenced fringes across multiple scans, as seen in the plot, can be estimated from the $\langle |C|^2 \rangle$ metric, which

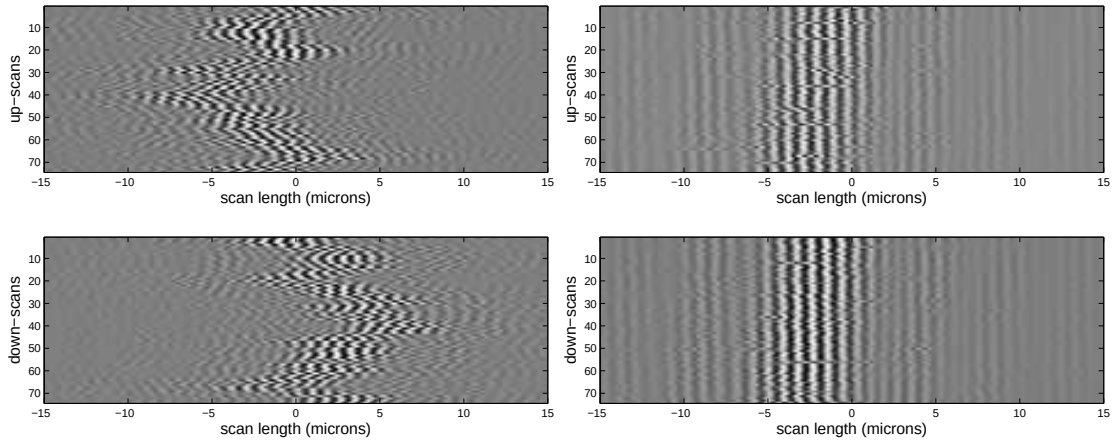

Figure 4.11: Simulated MUSCA fringes in a waterfall plot format showing the effect of (a) without and (b) with phase-referencing. The vertical axis is time and the horizontal axis is the optical delay. The top and bottom plots are of different scan direction.

is a measure of the coherence of the fringes (see Eq. 6.16), and is given as,

$$s_x^2 \approx -2 \ln \langle |C^2| \rangle \frac{N_{\rm SC}}{N_{\rm SC} - 1} \left(\frac{1}{2\pi \tilde{\sigma}_{\rm M}} \right)^2, \tag{4.36}$$

where $N_{\rm SC}$ is the number of good scans used in the estimation and $\tilde{\sigma}_{\rm M}$ is the mean wavenumber of MUSCA fringes, which has a typical value of $1.2\mu{\rm m}^{-1}$. The factor $\frac{N_{\rm SC}}{N_{\rm SC}-1}$ is used to obtain an unbiased estimate of the sample variance. Table 4.6 shows the value of $\langle |C|^2 \rangle$, $N_{\rm SC}$ and s_x for all testcases.

For a scan to be considered good, there must be a continuously reliable phase delay estimate throughout at least $\frac{3}{4}$ of the time to make the scan. The number of good scans as well as the value of $\langle |C|^2 \rangle$ decrease in the same trend as the standard deviation of the errors of the group delay estimates increases because residuals of the errors which are larger than one wavelength of the fringes produce unreliable phase delay estimates. Testcase IVB is an example of an extreme case as there are no good scans found.

The summation of the phase-referenced fringes in all good scans reproduces the fringe packet without the distortion introduced by the atmospheric phase noise. The effect of coherent summation of the fringes is shown in Fig. 4.12. The position of the fringe packet within the scan range of the scanning mirror can be determined to an uncertainty defined by $s_x/\sqrt{N_{\rm SC}}$. For example, in order to determine the

Table 4.6: Results from PAVO and MUSCA phase-referencing algorithm

		with ATM			without ATM		
Testcases ↓	m_V →	0.0	2.0	4.0	0.0	2.0	4.0
II ($V^2 = 0.25$)	N_{SC}	74	74	72	74	74	74
	$\langle\|C\|^2\rangle$	0.6407	0.3740	0.4112	0.8236	0.5678	0.5067
	s_x (nm)	126	188	179	84	143	156
III ($V^2 = 0.10$)	N_{SC}	74	58	21	74	74	74
	$\langle\|C\|^2\rangle$	0.6387	0.2630	0.1352	0.7582	0.3752	0.3708
	s_x (nm)	127	220	275	100	188	189
IV ($V^2 = 0.01$)	N_{SC}	58	0	0	74	0	0
	$\langle\|C\|^2\rangle$	0.2684	N/A	N/A	0.3346	N/A	N/A
	s_x (nm)	218	N/A	N/A	198	N/A	N/A

fringe packet position to an uncertainty of 5nm, which translates to an astrometric uncertainty of 10μas with 100m baseline, in Testcase IIIB, at least 1900 good scans are required. This number is not impractical as a period of good seeing at SUSI can produce over 1000 good scans in about 10 minutes of observation (a total of 3600 scans) with β Cru, which has a V magnitude of 1.3 and an uncalibrated V^2 range of 0.02–0.20 as measured by PAVO.

Although the results in Table 4.6 were simulated for the setup at SUSI, they can be extrapolated to estimate the performance of a similar setup at different observation sites. For example, the scenario in Testcase IIC (4th magnitude star, seeing condition of $\sim 1''$ and diameter of light collecting aperture of 14cm) is equivalent to observing a $\sim$6th magnitude star at a site with $\sim 0.5''$ seeing (e.g. at NPOI[3] or in Antarctica) but with twice the aperture size (28cm). In such a scenario, at least 1000 good scans are required to achieve a phase uncertainty of 5nm, which is equivalent to an astrometric precision of 10μas with a 100m baseline. The phase-referencing performances in Testcase IIB and IIC are similar because a higher EMCCD gain was used to compensate the lower flux in the latter.

4.7 Discussion and summary

The simulators developed in this work not only have been a very useful tool to test the data reduction pipeline developed for the new configuration and observational

[3]Navy Precision Optical Interferometer

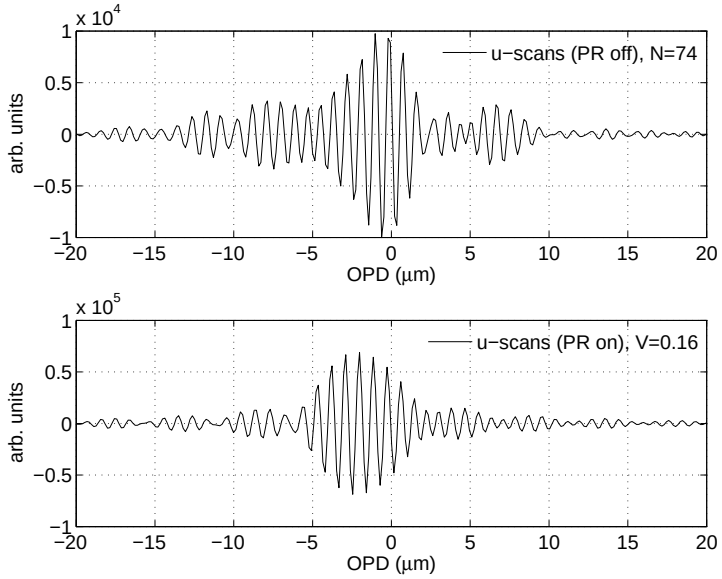

(a)

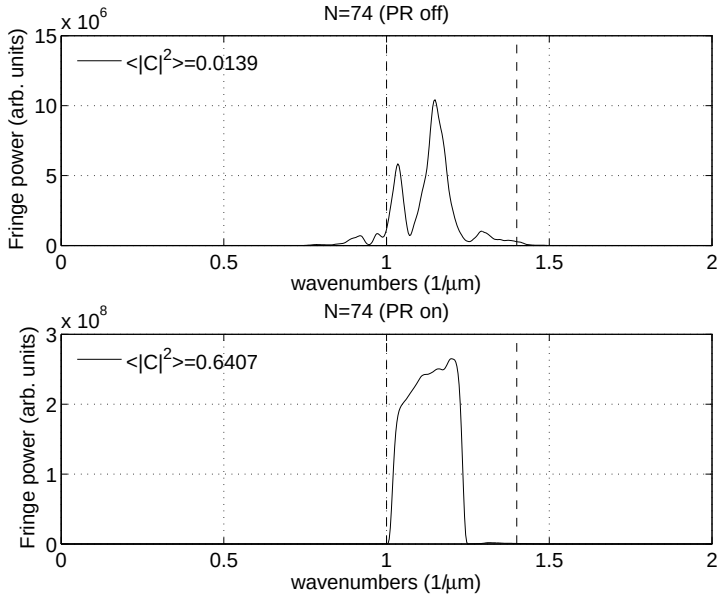

(b)

Figure 4.12: The top and bottom plots of (a) show the result of summation of multiple scans of incoherent and coherent fringes respectively. Note the difference in the vertical scale, showing a much larger signal when phase-referencing (PR) is applied. Similarly the top and bottom plots of (b) show the huge (about an order of magnitude) difference in the power spectrum of the incoherently (PR off) and coherently (PR on) summed fringe packets respectively. The number of scans used for the summation and the $\langle |C|^2 \rangle$ metric are indicated in (b).

technique at SUSI but have also shown the feasibility of visible wavelength phase-referencing at sub-wavelength OPD uncertainty. The PAVO+MUSCA setup at SUSI can determine the position of a fringe packet of a 2-4th magnitude star to an accuracy of 5nm by coherently integrating 1000-2000 good fringe packet scans. The simulated performance of the dual beam combiner can be extrapolated to estimate performance of a similar setup at future possible sites (e.g. NPOI and Antarctica). In addition to that, due to the selection of input parameters the simulators were designed to accept they could also be used to perform simulation for many other functions (e.g. to explore the option of expanding the capability of PAVO at CHARA from a 3-telescope to a 4-telescope beam combiner or to investigate the effect of optical aberration of lenses on the performance of the beam combiners) which is beyond its main role described in this paper.

Despite having shown the feasibility of phase-referencing between PAVO and MUSCA, the simulation framework assumed that the OPDs of non-common paths between PAVO and MUSCA are stable and do not vary with time. However, this is not the case in the laboratory. A network of metrology systems are used to measure OPD between the two beam combiners so that any OPD variations not measured by PAVO are taken into account and included into the phase-referencing data analysis.

Chapter 5

Metrology systems

The content of this chapter is reproduced from the following papers: "Phase-referenced interferometry and towards narrow-angle astrometry with SUSI", which has been accepted for publication in the Journal of Astronomical Instrumentation, and "Low-cost scheme for high-precision dual-wavelength laser metrology", which has been published in the Applied Optics journal (Kok et al., 2013a).

A combination of 3 new interferometer-based metrology systems are installed in SUSI for phase-referenced narrow-angle astrometric observations. Other than additional light sources, which consist partly of those shown in Fig. 3.1(a), the metrology systems do not require any extra hardware or optical components. The systems are made up of a white-light (WL) metrology, a single-laser (SL) metrology and a dual-laser (DL) metrology. Together they form a two-prong approach to measuring the optical path length between fringe packets of binary stars. First, the WL and the SL metrology systems are used to measure the OPD of every optical path non-common to PAVO and MUSCA. The objective is to ensure that any change in the position of a MUSCA phase-referenced fringe packet is caused by the DDL within the beam combiner. Second, the DL metrology system is used to measure the displacement of the DDL.

A schematic diagram of the optical paths of SUSI is shown in Fig. 5.1. The labels in bold in the figure represent the different parts of SUSI. The labels in regular type font are optical components which can be cross-referenced back to Fig. 3.2 and 3.3. The non-common paths between PAVO and MUSCA are labeled as **P** and **M** in Fig. 5.1. In the first prong of the approach, the phase delay of interference signals in MUSCA, m, is estimated using phase delays of interference signals measured by PAVO, z, and the OPDs of the non-common paths measured by the metrology systems. m is a measure of the OPD between the North and

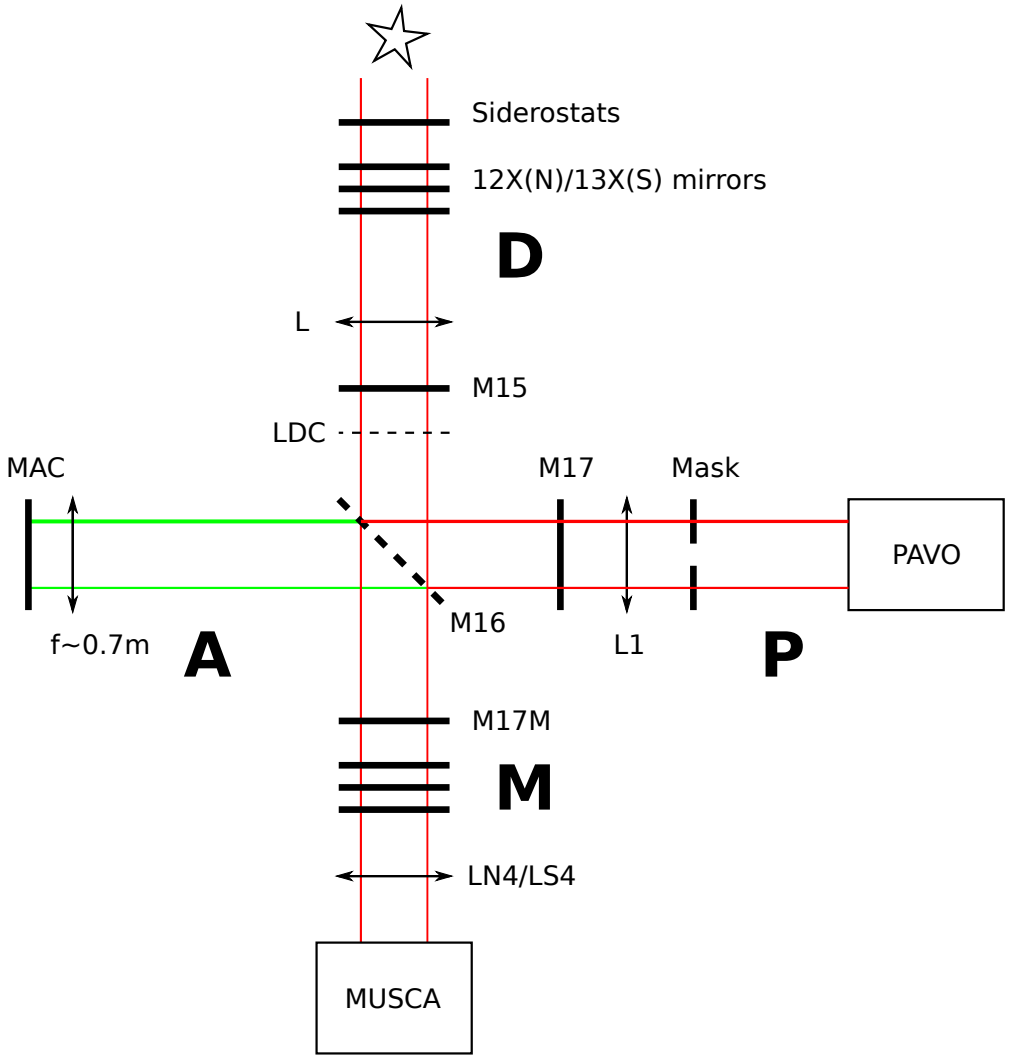

Figure 5.1: Schematic of beam combiners at SUSI. Part D includes all the optical components from the siderostat until M16 (a collective term for N16 and S16). Part P consists of all optical components from M16 to the PAVO camera. Part A consists the MAC (collective term for NAC and SAC), LS3 and LN3. Part M consists of all the optical components from M16 to the MUSCA APDs.

South arm of SUSI and is given as,

$$\begin{aligned} m &= \mathrm{OPD_D} + \mathrm{OPD_M} \\ &= z + (\mathrm{OPD_M} - \mathrm{OPD_P})\,, \end{aligned} \tag{5.1}$$

where,

$$z = \mathrm{OPD_D} + \mathrm{OPD_P}, \tag{5.2}$$

and the subscripts in the equations represent different parts of the SUSI optical paths as illustrated in Fig. 5.1. By convention, a positive value of m indicates the North arm of the interferometer is optically longer than the South arm. Then in the second prong of the approach, the true phase delay difference between two MUSCA fringe packets, S, is estimated by correcting the apparent phase delay difference with the change in the OPD within MUSCA, $\Delta\mathrm{OPD_M}$, which is attributed to a displacement of the differential delay line (DDL). This is given as,

$$S = (m_2 - m_1) + \Delta\mathrm{OPD_M}, \tag{5.3}$$

where m_i is the phase delay of either fringe packet.

The fiducial location where OPD is defined as zero for MUSCA is in the middle of the scan range of the scanning mirror while for PAVO it is in the center of the FOV of the EMCCD camera. The fiducial locations for computing the remaining OPD terms in Eq. (5.1) and (5.2) are not important because they are not measured independently.

5.1 White-light (WL) metrology

The light source for this metrology is an IR LED (TSAL6100 from Vishay Semiconductors) which emits light at a peak wavelength of $\lambda_\mathrm{I} = \sigma_\mathrm{I}^{-1} = 0.940\mu$m. It is injected into the SUSI optical path in front of PAVO with a pellicle beam-splitter (see Fig. 3.2(a)). It then propagates to a pair of retro-reflecting mirrors, NAC and SAC, and back to PAVO. This optical setup constitutes a Fizeau interferometer. Less than 5% of the total light from the LED is reflected into MUSCA because the dichroic mirrors (M16) are only highly reflective at wavelengths shorter than 0.79μm. This increases the background photon count for MUSCA but has minimal effect on the phase-referencing performance.

The optical path of the metrology is coaxially aligned with the incoming starlight path in order to minimize the non-common path error in the measurement. The interference fringes formed by the IR LED are recorded simultaneously with the

stellar fringes during observation with the same PAVO camera for the same purpose. The lower quantum efficiency of the camera at the metrology wavelength (∼25-30%) enables PAVO to observe fringes of a star and the metrology simultaneously.

Suppose w represents the phase delay of the fringes formed by this metrology, then w is the sum of OPDs along the propagation path of the metrology, i.e.,

$$w = 2\mathrm{OPD_P} + 2\mathrm{OPD_A}. \tag{5.4}$$

There is a factor of 2 in the equation above because the metrology probes the OPDs in double pass. However, the factor of 2 in the first term of the equation, $\mathrm{OPD_P}$, denotes a simplification in the optical path. It assumes the light source for the metrology is located at the location where fringes are formed (i.e. at the lenslet array, see Fig. 3.2(b)). In actual case, the light source originates from a nearby pinhole. Any variation in the OPD between the 2 arms of the interferometer from the pinhole to the pellicle beam-splitter, where the light source is injected into the science path, is also probed by the SL metrology and hence will be cancelled out in the data reduction pipeline.

5.1.1 Principle of metrology

The phase delay of the fringes at the LED emitted peak wavelength is a measure of the OPD between two arms of the interferometer. However, the phase measurement is modulo 2π. Therefore the range where the measurement is not ambiguous, commonly known as the non-ambiguous range (NAR) is equal to one wavelength of the LED light. Despite the short range, it is adequate because fringes are recorded by the PAVO camera at a rate of one frame per ∼5ms and the OPD measured by w is not expected to change by more than one wavelength within this time. The OPD has been measured to drift, mainly due to mechanical factors, by $\sim 0.1\mu$m per hour. This value has been corrected for the double pass optical path of the metrology.

Over longer timescales of several hours and during poor internal laboratory seeing, the range of the OPD variation measured by w can exceed one wavelength of light. This is not a concern because the PAVO spectrograph disperses the metrology fringes into narrow bands so that the coherence length of the fringe packet is $\sim 30\mu$m. The sum of $\mathrm{OPD_P}$ and $\mathrm{OPD_A}$ is not expected to vary beyond 30μm in one night because there are no moving parts along the optical path. Fig. 5.2 shows a typical laboratory condition at SUSI. The ambient temperature near the beam combiners (labeled as CEN in the figure) does not vary by more than 1°C over the course of 24 hours.

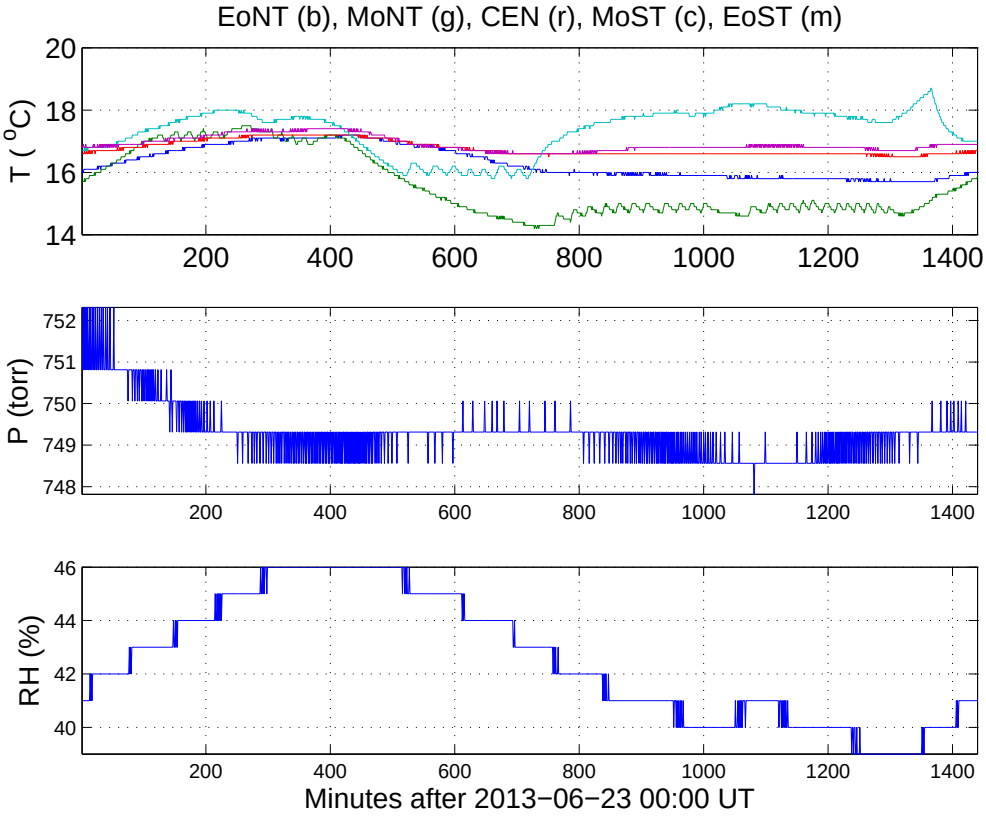

Figure 5.2: Typical temperature (upper panel), atmospheric pressure (middle panel) and relative humidity (lower panel) inside the laboratory where PAVO and MUSCA are housed. The temperature in various locations: end of North tunnel (EoNT), middle of North tunnel (MoNT), center (CEN), middle of South tunnel (MoST) and end of South tunnel (EoST), are shown in the upper panel as blue, green, red, cyan and magenta lines.

The WL metrology measures only the relative OPD. The reference OPD is taken to be the OPD at the start of an observation session. The value is near to zero (within $\pm 10\mu$m approximately). The absolute value of the reference OPD is not important nor does it need to be precisely at zero because it will be cancelled out in the data analysis.

5.1.2 Uncertainty of measurement

The uncertainty of the OPD measurement depends on the uncertainty of measuring the fringe phase and the uncertainty of the wavelength. It is given as,

$$\delta w = \sqrt{\left(\frac{\delta\phi_{\mathrm{I}}}{2\pi\sigma_{\mathrm{I}}}\right)^2 + \left(\frac{\delta\sigma_{\mathrm{I}}}{\sigma_{\mathrm{I}}}w\right)^2}, \tag{5.5}$$

where $\delta(\cdot)$ denotes the uncertainty of a measured quantity and ϕ_{I} is the phase of the metrology fringes. The fringe phase error depends on the SNR and visibility of the fringes as well as the brightness of the source (Walkup & Goodman, 1973). Based on typical numbers extracted from actual measurements, the fringe phase error is estimated to be less than 0.5 radians. On the other hand, the uncertainty of the wavelength is defined by the wavelength scale and the bandwidth of each spectral channel of the PAVO spectrograph, which is calibrated regularly. Since the mean coherence length of one spectral channel is $\sim 30\mu$m, then $\delta\sigma_{\mathrm{I}}$ is estimated to be $\sim 0.030\mu\mathrm{m}^{-1}$. With $w \lesssim \sigma_{\mathrm{I}}$, the uncertainty of the OPD measurement is estimated to be less than 80nm.

Other factors that affect the uncertainty of the OPD measurement are imperfect alignment of the metrology light source with starlight which leads to an inaccurately measured OPD and variation in the difference of refractive index of air at the metrology and science wavelengths. Since the OPD variation along the optical path measured by w is $\ll 1\mu$m, errors due to these factors are negligible.

Despite having an estimated measurement uncertainty of 80nm or less, this value does not translate directly into astrometric error. The error in determining the relative position of the phase-referenced fringe packet can be averaged over many MUSCA scans to reduce the error by a factor of $\sqrt{N_{\mathrm{SC}}}$, where N_{SC} is the number of good scans used in the integration, because photon noise is uncorrelated between one PAVO frame and another. It does however affect the overall integration time because more scans are required to average out larger uncertainties.

5.2 Single-laser (SL) metrology

The light source for this metrology is a green He-Ne laser (from Laserdyne) which emits light at a peak wavelength of $\lambda_G = \sigma_G^{-1} = 0.5435161\mu$m. This laser also serves a dual purpose for optical alignment. The metrology laser is injected into the SUSI optical path in the same way as the IR LED but it propagates past the pair of retro-reflecting NAC and SAC mirrors and into the MUSCA beam combiner. The intensity of the metrology laser is controlled by the selection of neutral density filters at the source (see Fig. 3.2(a)) so that it does not blind the APDs when observing faint stars. This optical setup constitutes a Mach-Zehnder interferometer.

Like the WL metrology, the optical path of the SL metrology is also coaxially aligned with the starlight path in order to minimize the non-common path error in the measurement. For the same reason, the interference fringes formed by the laser at the MUSCA beam-splitter are recorded by the MUSCA APDs simultaneously with the stellar fringes during observation. Suppose x represents the phase delay of the fringes formed by this metrology, then the OPDs probed by x which can be traced out from Fig. 5.1 is,

$$x = \mathrm{OPD_P} + 2\mathrm{OPD_A} + \mathrm{OPD_M}. \tag{5.6}$$

Consistent with Eq. (5.4) for the WL metrology, the term $\mathrm{OPD_P}$ in the above equation includes the OPD between the 2 arms of the interferometer from the pinhole to the pellicle beam-splitter, which will be cancelled out in the data reduction pipeline.

5.2.1 Principle of metrology

Similar to the WL metrology, the phase of the SL metrology fringes is a measurement of the OPD between the two arms of the interferometer. Although the phase measurement is modulo 2π, the range where measurement is not ambiguous is adequate because the scanning mirror makes one up and down scan (one period) per 150ms and the OPD measured by x is not expected to change by more than one laser wavelength within this time interval. The OPD has been measured to drift by $\sim 0.3\mu$m per hour. This value has been corrected for the double pass optical path of the metrology and is slightly larger than the value measured by the WL metrology. This is expected because the position of the DDL is affected by the heat generated by its motor drive and electronics when the DDL is slewed from one position to another (Zaber, 2006). Over longer timescales of several hours and

during unstable laboratory conditions, the OPD variation measured by x can exceed one laser wavelength, but is still negligible compared to the coherence length of the laser.

The SL metrology measures the relative OPD between two arms of the interferometer. The OPD measured at the start of an observation session is set as the reference OPD. It is also not necessary for the reference OPD to be precisely zero although it is set to be near zero (within $\pm 5\mu$m approximately) by adjusting the MUSCA DDL before the start of an observation. The absolute value of the reference OPD is not important because it will be cancelled out in the data analysis.

5.2.2 Uncertainty of measurement

Similar to the WL metrology, the uncertainty of the OPD measurement with the SL metrology also depends on the uncertainty in measuring the fringe phase and the uncertainty of the laser wavelength. The uncertainty is,

$$\delta x = \sqrt{\left(\frac{\delta\phi_{\mathrm{G}}}{2\pi\sigma_{\mathrm{G}}}\right)^2 + \left(\frac{\delta\sigma_{\mathrm{G}}}{\sigma_{\mathrm{G}}}x\right)^2} \approx \left|\frac{\delta\phi_{\mathrm{G}}}{2\pi\sigma_{\mathrm{G}}}\right|, \tag{5.7}$$

where ϕ_{G} is the phase of the metrology fringes which depends on the SNR and the visibility of the fringes and the brightness of the laser. Based on typical numbers extracted from actual measurements, the fringe phase error is estimated to be less than 0.3 radians. On the other hand, the relative uncertainty of the laser wavelength is computed from the theoretical full width half maximum of the laser gain profile (1.5GHz (Svelto, 1998)) to be better than 3×10^{-7}, which is typical for a standard He-Ne laser without frequency-stabilization. The uncertainty of the OPD measurement is therefore estimated to be better than 25nm. This value does not translate directly into an astrometric error because the error in determining the relative position of the phase-referenced fringe packet is averaged over many MUSCA scans and is reduced by a factor of $\sqrt{N_{\mathrm{SC}}}$ where N_{SC} is the number of good MUSCA scans integrated.

5.3 Dual-laser (DL) metrology

The objective of this metrology system is to measure with high precision the change in OPD within MUSCA brought about by a displacement of its DDL. In order to achieve its objective, the metrology system must meet the following criteria.

- Have a non-ambiguous range (NAR) of up to 2mm
  The displacement of the MUSCA DDL is expected to reach 2mm because a pair of stellar fringe packets separated at this distance corresponds to a separation of 2″ (current FOV limit) in the sky if they are observed with a 160m baseline (current longest available baseline).

- Be able to measure an OPD to a precision better than 5nm
  Unlike the previous two metrology systems, measurements from this metrology system are not used for phase-referencing MUSCA fringes and therefore uncertainties in the measurements are not averaged down by coherent integration.

- Be able to complete a measurement quickly (∼1min)
  The cost of spending more time on metrology is the time lost to observe science targets. Therefore a system that can acquire measurements quickly is always preferred.

Conventionally, two laser wavelengths are used to obtain a long synthetic optical wavelength by means of heterodyne interferometry (Daendliker et al., 1988; Schuhler et al., 2006) and extend the NAR of a single wavelength metrology. However, instead of using the heterodyne detection technique which requires specialized optical elements and hence has higher cost, the dual-wavelength metrology described here employs a simple homodyne fringe counting detection scheme together with a (relatively) less precise stepper motor open-loop position control system to extend the range of distance the metrology can accurately measure.

5.3.1 Principle of metrology

The underlying principle of this metrology is to first measure phases of interference fringes of two lasers, operating at wavelengths whose ratio is not a rational number, at two different delay line positions and then determine the number of fringe cycles that have evolved as a result of the displacement. The phase measurement is key in this classical two-wavelength approach to displacement metrology. The novel aspect of the metrology described here is the use of optical path modulation to measure the phases of the fringes of the two lasers simultaneously. In an idealized case where the laser wavelengths are perfectly stable and the measurements of the phases are noiseless, one measurement at each delay line position would be enough to uniquely resolve the length of the optical path between the two positions. However, in the real world, due to uncertainties in the phase measurements and laser wavelengths, there are a series of plausible solutions for the optical path length. The span between these plausible solutions is the non-ambiguity range

(NAR) of the metrology and is elaborated in Section 5.3.3. In order to extend the range of distance the metrology can measure an open loop stepper motor position control system is exploited to narrow down the plausible solutions to a single best fit, thereby yielding the displaced optical path length measurement at interferometric precision. The basic requirement for this two-prong approach is that the NAR arising from fringe phase measurement must be larger than the uncertainty of the stepper motor positioning system. Since the stepper motor positioning system can determine the position of the delay line unambiguously over a large distance range (in the case of T-LS28M, 28mm), the delay line can be moved quickly (∼2mm/s) from one position to another and fringe phase measurement does not have to be done on the fly but before and after a move.

In order to explain the method in more detail, first, let the distance between a position of the delay line and an arbitrary reference position be expressed in terms of two laser wavenumbers (σ_{R} and σ_{G}) as follows,

$$d_i = \frac{1}{n_{\mathrm{R}}\sigma_{\mathrm{R}}}\left(N_{\mathrm{R}i} + \frac{\phi_{\mathrm{R}i}}{2\pi}\right) = \frac{1}{n_{\mathrm{G}}\sigma_{\mathrm{G}}}\left(N_{\mathrm{G}i} + \frac{\phi_{\mathrm{G}i}}{2\pi}\right). \tag{5.8}$$

n_{R} and n_{G} are the refractive indices of air at the respective wavenumbers while $N_{\mathrm{R}i}$ and $\phi_{\mathrm{R}i}/2\pi$ or $N_{\mathrm{G}i}$ and $\phi_{\mathrm{G}i}/2\pi$ are the number of full (integer) and fractional wavelengths that fit within this distance. The subscript i represents one position of the delay line and if two different positions are considered, then, from Eq. (5.8),

$$\begin{aligned} d &= d_1 - d_0 \\ &= \frac{\left(\Delta\varphi_1 - \Delta\varphi_0\right)/2\pi + \Delta N}{n_{\mathrm{R}}\sigma_{\mathrm{R}} - n_{\mathrm{G}}\sigma_{\mathrm{G}}}, \end{aligned} \tag{5.9}$$

where d represents the displacement of the delay line between the two positions while $\Delta\varphi_i = \phi_{\mathrm{R}i} - \phi_{\mathrm{G}i}$, $\Delta N = \Delta N_{\mathrm{R}} - \Delta N_{\mathrm{G}}$, $\Delta N_{\mathrm{R}} = N_{\mathrm{R}1} - N_{\mathrm{R}0}$ and $\Delta N_{\mathrm{G}} = N_{\mathrm{G}1} - N_{\mathrm{G}0}$. The phases of the laser fringes, $\phi_{\mathrm{R}i}$ and $\phi_{\mathrm{G}i}$, and their difference, $\Delta\varphi_i$, can be obtained from the photon counts recorded by the APDs. ΔN_{R} and ΔN_{G}, on the other hand, cannot be directly determined but can be inferred from the following equality,

$$\Delta N_{\mathrm{G}} - \alpha\Delta N_{\mathrm{R}} = (\Delta\psi_1 - \Delta\psi_0)/2\pi, \tag{5.10}$$

where $\alpha = \frac{n_{\mathrm{G}}\sigma_{\mathrm{G}}}{n_{\mathrm{R}}\sigma_{\mathrm{R}}}$ and $\Delta\psi_i = \alpha\phi_{\mathrm{R}i} - \phi_{\mathrm{G}i}$. Therefore the main observables for the metrology at each delay line position are $\phi_{\mathrm{R}i}$, $\phi_{\mathrm{G}i}$, $\Delta\varphi_i$ and $\Delta\psi_i$.

The values of ΔN_{G} and ΔN_{R} are determined through a model-fitting method based on Eq. (5.10). First, a range of guess values are generated based on the optical path length estimated from the stepper motor positioning system, d_{zaber}, and the NAR of the metrology to evaluate the LHS of Eq. (5.10). Next the

result is compared with the RHS of Eq.(5.10) which is obtained from the phase measurement. Theoretically, there is a unique set of $\Delta N_{\rm G}$ and $\Delta N_{\rm R}$ values that satisfy the equation because α is an irrational number. However, due to uncertainty in the phase measurement this is not the case in practice. Instead, the set of $\Delta N_{\rm G}$ and $\Delta N_{\rm R}$ that minimizes the error between the RHS and LHS of the equation is the set of values to be used for distance determination in Eq. (5.9). Therefore, the estimated position of the delay line from its built-in stepper motor positioning system is the key to obtaining the right d value from the selected $\Delta N_{\rm G}$ and $\Delta N_{\rm R}$ values.

5.3.2 Optical setup

The diagram in Fig. 5.3 shows a simplified version of the narrow-angle astrometric beam combiner (MUSCA) in SUSI. Instead of depicting the entire SUSI facility for which schematic diagrams can be obtained from Robertson et al. (2012), the diagram shows only the optical path relevant to the metrology and the beam combiner which is a pupil-plane Michelson interferometer. The light sources for the metrology are two He-Ne lasers; one emits at peak wavelength of $\lambda_{\rm R} = \sigma_{\rm R}^{-1} = 0.6329915\mu$m and the other at peak wavelength of $\lambda_{\rm G} = \sigma_{\rm G}^{-1} = 0.5435161\mu$m (Edlén, 1966; Kurucz, 2012, converted from wavelengths in standard (760 torr, 15°C) dry air). The quoted values are wavelengths in vacuum but the two lasers are operated in air. Both laser beams are first spatially filtered by pinholes, then collimated and finally refocused into the interferometer. Each refocused beam forms an image at a field lens in front of an avalanche photodiode (APD). The optical path along the left arm of the interferometer (as seen in Fig. 5.3) is periodically modulated by a piezo-electrically actuated mirror (scanning mirror) to produce temporal fringes, which are then recorded by the pair of APDs as a time series of photon counts. The scanning mirror modulates the optical path in 256 discrete steps in about 70ms per scan period per scan direction. On the right arm of the interferometer, the length of the optical path can be changed by a movable delay line. The leadscrew based built-in open loop position control system of the delay line has a nominal accuracy of 15μm.

It is important to note that, apart from the lasers and their injection optics, all components in Fig. 5.3 were pre-existing and required for the science goal of the PAVO beam combiner. During astronomical observations, the same pair of APDs are used to record both the stellar and the metrology fringes. The optical path of the metrology lasers is designed to trace the optical path of the starlight beams in the beam combiner, which propagates into the instrument from the top as seen in Fig. 5.3 through a pair of dichroic filters. In this way, the optical path probed

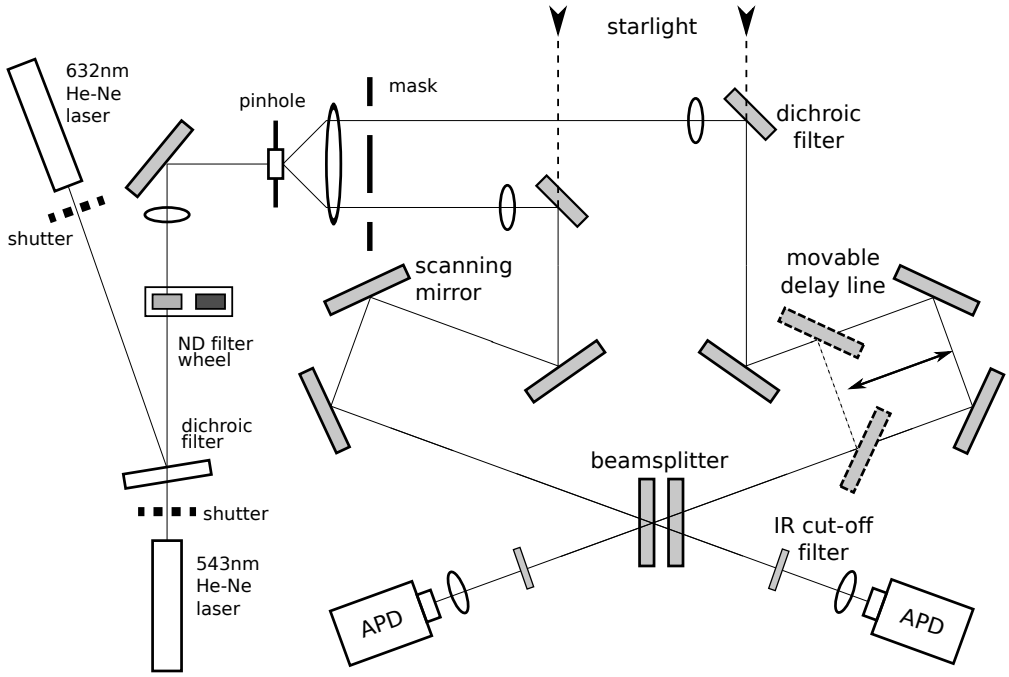

Figure 5.3: Optical setup of the dual-wavelength metrology and the astrometric beam combiner in SUSI.

by the metrology is nearly identical to the optical path of the starlight and the small difference in optical delay (due to the difference in wavelengths) is invariant under the controlled atmospheric condition in the laboratory in which the optics are housed (Erickson, 1962).

5.3.3 Non-ambiguity range

As previously described, the metrology measures the length of an optical path by calculating the number of laser wavelengths that can be fitted into it. However, since the ratio of the laser wavenumbers, $\alpha = 1.164644$, can be approximated by a ratio of two integers, e.g. $\alpha \approx \frac{7}{6}$ or $\alpha \approx \frac{92}{79}$, the phases of the laser fringes will appear (depending on the uncertainty of the phase measurement) to realign after several wavelengths as suggested by the numerator and denominator of the fraction. This means that the phase differences between the laser fringes will repeat and become indistinguishable from the previous phase realignment if the optical path length is larger than the distance suggested by the wavelength range. Therefore the metrology can only determine the accurate length of the optical path if it is within this range, which is the non-ambiguity range (NAR) of the metrology.

The parameters, ΔN_{R} and ΔN_{G}, can take any integer value but in order to determine the value of NAR of the metrology, suppose $0 \leqslant \Delta N_{\mathrm{R}} \leqslant \Delta N_{\mathrm{R,max}}$ and $0 \leqslant \Delta N_{\mathrm{G}} \leqslant \Delta N_{\mathrm{G,max}}$. Then the NAR is defined as,

$$\mathrm{NAR} = \min\left(\Delta N_{\mathrm{R,max}}/\sigma_{\mathrm{R}},\ \Delta N_{\mathrm{G,max}}/\sigma_{\mathrm{G}}\right), \tag{5.11}$$

provided that the following inequalities are satisfied for all values of ΔN_{G} and ΔN_{G},

$$\begin{aligned} |\alpha\Delta N_{\mathrm{R}} - [\alpha\Delta N_{\mathrm{R}}]| &> \delta(\Delta\psi)/2\pi, \\ |\Delta N_{\mathrm{G}}/\alpha - [\Delta N_{\mathrm{G}}/\alpha]| &> \delta(\Delta\psi)/2\pi, \end{aligned} \tag{5.12}$$

which is derived from the LHS of Eq. (5.10) when the phases of the laser fringes are aligned, hence the RHS is zero. The notation $[\cdot]$ denotes the nearest integer of the real number within the brackets and $\delta(\Delta\psi)$ is the standard error of mean of $\Delta\psi = \Delta\psi_1 - \Delta\psi_0$.

5.3.4 Implementation

The photon counts recorded from the setup in Fig. 5.3 are reduced with a program written in MATLAB/Octave[1] to determine optical path differences based on the model presented in the previous sections. For each set of laser fringes recorded at one position of the delay line the phases of the fringes (relative to the middle of the scan length), namely $\phi_{\mathrm{R}i}$, $\phi_{\mathrm{G}i}$, $\Delta\varphi_i$ and $\Delta\psi_i$, are extracted using a Fast Fourier Transform (FFT) routine. Fig. 5.4 shows an example of the laser fringes and the phases extracted from them. Because the implementation is numerical and the FFT routine expresses phases in the range of $-\pi$ to π, a minor tweak to the value of ΔN in Eq. (5.9) may be required to obtained an accurate value of d. As a result, the term should be replaced with $\Delta N'$, where,

$$\Delta N' = \Delta N + \delta(\Delta N). \tag{5.13}$$

The adjustment, $\delta(\Delta N)$, which value is obtained from computer simulation, consists of two parts and is summarized below as,

$$\begin{aligned} \delta(\Delta N) = \delta(\Delta N)_0 & \\ + \begin{cases} -1 & \text{if } \Delta\phi_{\mathrm{R}} < 0, \Delta\phi_{\mathrm{G}} \geqslant 0; \\ 0 & \text{if } \Delta\phi_{\mathrm{R}} < 0, \Delta\phi_{\mathrm{G}} < 0; \text{or} \\ & \quad \Delta\phi_{\mathrm{R}} \geqslant 0, \Delta\phi_{\mathrm{G}} \geqslant 0; \\ 1 & \text{if } \Delta\phi_{\mathrm{R}} \geqslant 0, \Delta\phi_{\mathrm{G}} < 0. \end{cases} , \end{aligned} \tag{5.14}$$

[1] `http://www.gnu.org/software/octave`

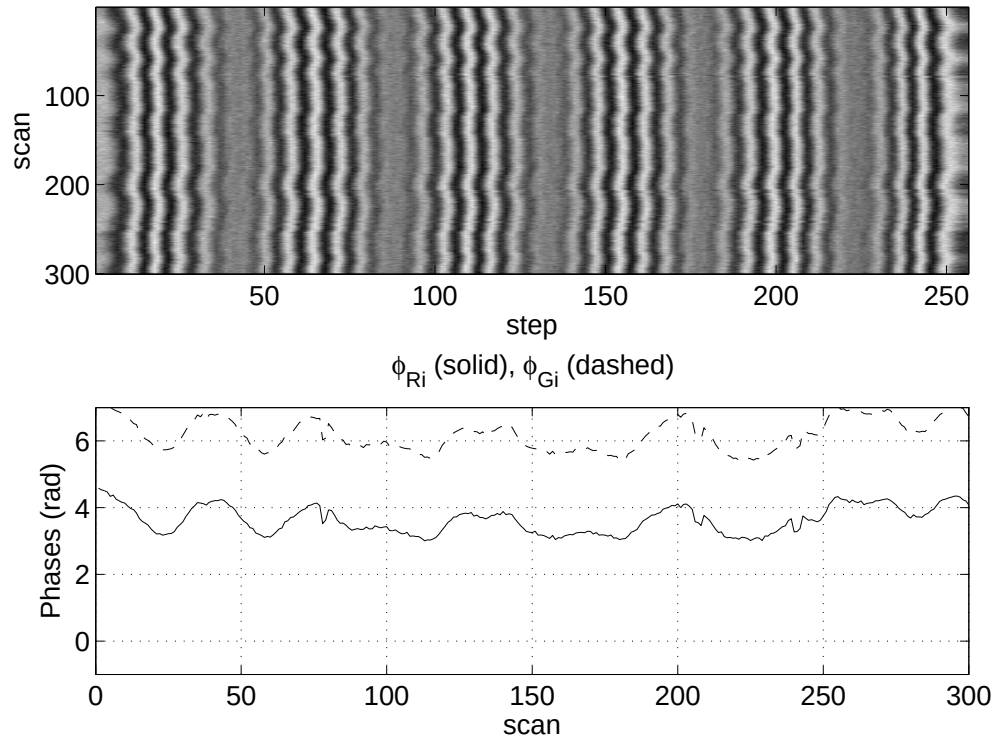

Figure 5.4: Consecutive scans of laser fringes (top) and the phases (bottom), $\phi_{\mathrm{R}i}$ and $\phi_{\mathrm{R}i}$, extracted from each scan. The internal laboratory seeing was moderate at the time of measurement.

where $\Delta\phi_{\mathrm{R}} = \phi_{\mathrm{R}1} - \phi_{\mathrm{R}0}$ and $\Delta\phi_{\mathrm{G}} = \phi_{\mathrm{G}1} - \phi_{\mathrm{G}0}$. The value of $\delta(\Delta N)_0$ is given in Table 5.1 if all the expressions in the first five columns in the table are satisfied, otherwise $\delta(\Delta N)_0$ is zero. For example, according to the first row of Table 5.1, if $\Delta\varphi_1 \geqslant \Delta\varphi_0$, $\Delta\phi_{\mathrm{R}} \geqslant 0$, $\Delta\phi_{\mathrm{G}} \geqslant 0$, $|\Delta\phi_{\mathrm{R}}| \leqslant \pi$ and $|\Delta\phi_{\mathrm{G}} > \pi$, then $\delta(\Delta N)_0 = -1$. The differences of phases in Eq. (5.14) and Table 5.1 are computed by first expressing the phases in the range of 0 to 2π.

The measurement of the phases of the lasers fringes are carried out before and after the delay line is moved for astronomical observation. The displacement of the delay line brings one of the two stellar fringe packets[2] into the scan range of the scanning mirror. By measuring the displacement of the delay line and the position of the fringe packets, the optical delay between them, which is the main science observable of MUSCA, can be measured. MUSCA spends about 15–30 minutes, depending on seeing conditions, integrating on each fringe packet while the metrology takes about 2–3 minutes in total to measure phases of the lasers

[2]Interference fringes localized in delay space due to limited coherence length of the source

Table 5.1: Look-up-table for $\delta(\Delta N)_0$ in Eq. (5.14). By default, $\delta(\Delta N)_0$ is 0.

$\Delta\varphi_1 < \Delta\varphi_0$	$\Delta\phi_\mathrm{R} < 0$	$\Delta\phi_\mathrm{G} < 0$	$\lvert\Delta\phi_\mathrm{R}\rvert > \pi$	$\lvert\Delta\phi_\mathrm{G}\rvert > \pi$	$\delta(\Delta N)_0$
F	F	F	F	T	-1
F	F	T	F	F	-1
F	T	F	T	T	-1
F	T	T	T	F	-1
T	F	F	T	F	1
T	F	T	T	T	1
T	T	F	F	F	1
T	T	T	F	T	1

F ≡ FALSE; T ≡ TRUE

fringes. The time spent by the metrology includes moving the delay line from one position to another. This sequence of astronomical and metrology measurements is repeated at least 3 times for each science target.

5.3.5 Sources of error

The precision of the measurement by the dual-wavelength metrology depends on several factors which will be elaborated individually in this section.

Phase error

This is the main source of error affecting the precision of the metrology. Errors in measuring $\Delta\psi_i$ and $\Delta\varphi_i$ determine the uncertainty in choosing the right value for ΔN_R and ΔN_G and the uncertainty of d respectively. The physical processes contributing to this error are photon noise and internal laboratory seeing. At high photon count rates (about 10^6 counts per second in the SUSI setup), the uncertainty of the phase information obtained from a FFT (or more generally a Discrete Fourier Transform) routine is negligible (i.e. in the order of 10^{-5} radians) (Walkup & Goodman, 1973). Therefore, internal laboratory seeing is the dominant factor. Fig. 5.5 shows the standard error of the mean of typical measurements of $\Delta\psi_i$ and $\Delta\varphi_i$. The errors decrease with increasing number of scans. If the uncertainty of $\Delta\psi_i$ is less than 0.002 radian (with $\gtrsim$500 scans), then the NAR of this metrology is estimated to be $\sim 460\mu$m ($\Delta N_{\mathrm{R,max}} = 735$).

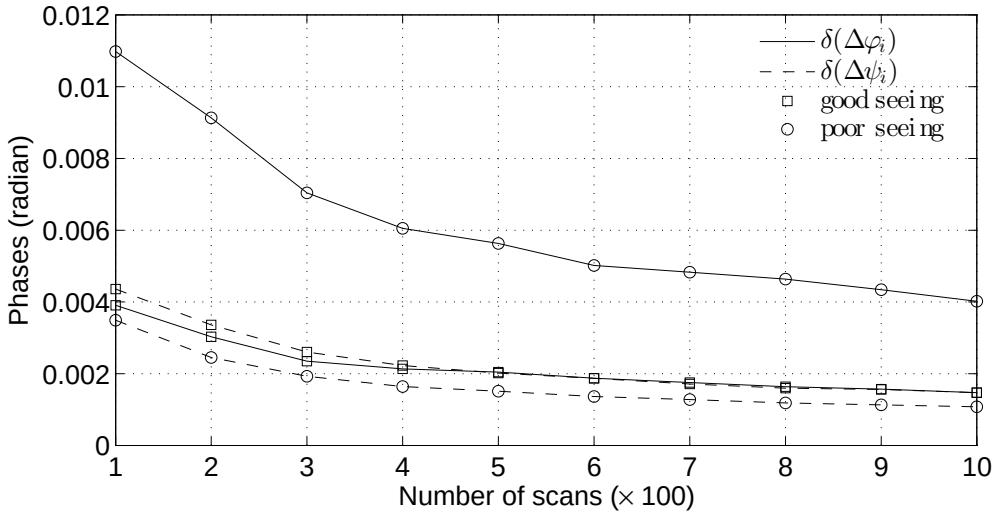

Figure 5.5: The uncertainty of $\Delta\psi_i$ and $\Delta\varphi_i$ measured with different number of scans of laser fringes. The measurement of the latter is more susceptible to internal seeing condition in the lab.

Instrumental error

Given an NAR of $\sim$460μm the difference between an initial guess optical path length, d_{zaber}, and its true value must be less than the NAR value. The initial guess value is obtained from the stepper motor positioning system. The characterization of the precision of the system is shown in Fig. 5.6. The plot in the figure shows the difference between the position of the delay line indicated by the stepper motor positioning system and the position measured by the dual-laser metrology. The cyclical error as seen from the plot is typical for a leadscrew based linear translation stage (Zaber, 2006). Being able to reproduce such a cyclical pattern verifies the accuracy of the dual-laser metrology especially the accuracy of $\Delta N'$. Instead of the specified 15μm accuracy Fig. 5.6 shows that the leadscrew has a precision of $\sim$20μm which is still well within the NAR requirement. This requirement is satisfied even though the optical path length change induced by the delay line is twice its actual physical change in position (refer to Fig. 5.3).

Laser wavelength error

Based on the longitudinal mode spacing specification of the laser (438MHz for the red and $\sim$350MHz for the green laser) and the theoretical full width half maximum (FWHM) of the gain profile at the laser wavelengths (1.8GHz for the

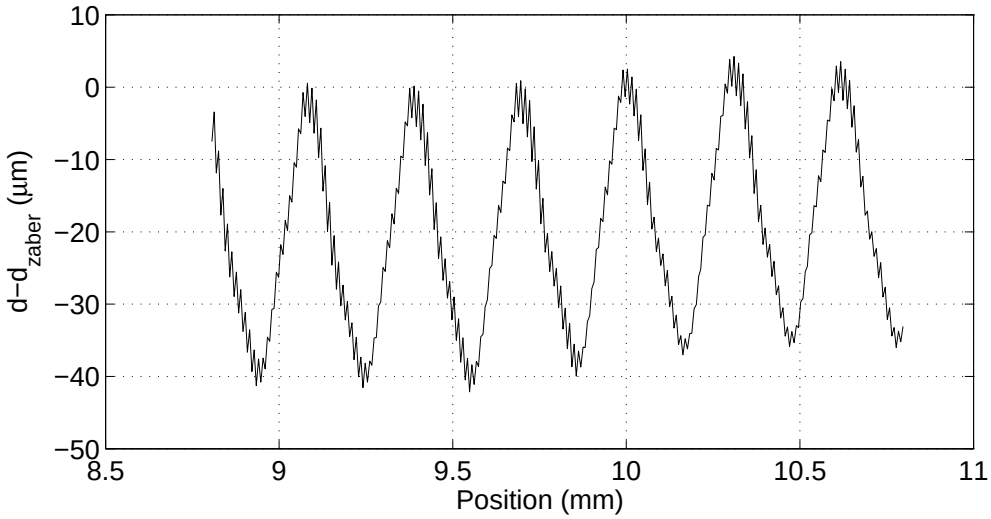

Figure 5.6: The difference between the OPD measured by the dual-laser metrology described in this section, d, and the OPD estimated with the stepper motor metrology of the Zaber stage, d_{zaber}, at different stage position.

red and 1.5GHz for the green laser (Svelto, 1998)), the relative uncertainty of the wavelength, $\frac{\delta\sigma_{\mathrm{R}}}{\sigma_{\mathrm{R}}}$ and $\frac{\delta\sigma_{\mathrm{G}}}{\sigma_{\mathrm{G}}}$, of individual lasers is better than 3×10^{-7}. Here the notation $\delta(\cdot)$ means one standard deviation of the wavenumber variation. If $\Delta\sigma_{\mathrm{RG}} = n_{\mathrm{R}}\sigma_{\mathrm{R}} - n_{\mathrm{G}}\sigma_{\mathrm{G}}$, then,

$$\frac{\delta(\Delta\sigma_{\mathrm{RG}})}{\Delta\sigma_{\mathrm{RG}}} \approx 3.6 \times 10^{-6}, \tag{5.15}$$

because the refractive indices are similar ($n_{\mathrm{R}} - n_{\mathrm{G}} \approx 1 \times 10^{-6}$) and approximately constant (Erickson, 1962) between the time when the laser fringes are recorded at the two delay line positions. In the case of SUSI, this condition is true because the fluctuations of ambient temperature in the laboratory are designed to be small within a typical duration of an astronomical observation (Davis et al., 1999). Laser wavelength error of this magnitude is not significant when measuring a short optical path length but can lead to substantial error in optical path length measurement if the optical path is long. This and the effect of using frequency-stabilized lasers will be discussed in Section 5.3.6.

Non-common-path error

Other than being used as light sources for the metrology, the lasers are also used for optical alignment for MUSCA and the rest of the optical setup at SUSI. In the

case of MUSCA the alignment between the lasers and starlight beams is critical in order to minimize the non-common-path between the metrology and the science channel. Several other optical elements in the full optical setup at SUSI which also play a role in assisting the alignment process (e.g. retro-reflecting mirrors, lenses, a camera in SUSI's main beam combiner, etc.) are not included in the simplified version the setup in Fig. 5.3 but can be referred from (Robertson et al., 2012). The optics put the pupil and the image of the pinhole and a star on the same respective planes through the aperture of the mask. The lasers and starlight beams should ideally be coaxially aligned in order to minimize the non-common-path between them. However, in the actual optical setup there can be a maximum misalignment of 0.5mm between the pinhole and the image of the star over a distance of about 2m. This translates to a maximum of 0.3 milliradians of misalignment or $\sim 3 \times 10^{-8}$ of relative metrology error. In absolute terms, this error is negligible ($\ll$1nm) for short ($<$ 10mm) optical path length measurement. However, a more precise alignment is necessary for measurement of longer optical paths.

5.3.6 Uncertainty of measurement

The uncertainty of the optical path length measurement, δd, can be derived from Eq. (5.9). The precision of the stepper motor positioning system (well within the NAR) ensured that the uncertainty of $\Delta N'$ is always zero. The characterization of the delay line in Fig. 5.6 verified this in practice. Therefore the uncertainty of the optical path length measurement, given below, depends only on the uncertainty of the phase measurements and the laser wavenumbers. In order to simplify the equation, let $\Delta\varphi = \Delta\varphi_1 - \Delta\varphi_0$, so that,

$$\begin{aligned} \delta d &= \sqrt{\left(\frac{\delta(\Delta\varphi)}{2\pi\Delta\sigma_{\mathrm{RG}}}\right)^2 + \left(\frac{\delta(\Delta\sigma_{\mathrm{RG}})}{\Delta\sigma_{\mathrm{RG}}}\, d\right)^2} \\ &\approx \left|\frac{\delta(\Delta\varphi)}{2\pi\Delta\sigma_{\mathrm{RG}}}\right|, \quad (\delta(\Delta\varphi) > 0.001, d < 0.5\mathrm{mm}). \end{aligned} \tag{5.16}$$

If the phase error, $\delta(\Delta\varphi)$, is more than 1 milliradian, which is typical for this metrology setup then it can be shown that the contribution of the wavenumber error is negligible at short optical path ($d < 0.5$mm). This value is similar to the separation of two fringe packets of two stars with a projected separation of about $0\farcs6$ in the sky observed with a 160m baseline interferometer. The plot in Fig. 5.5 shows that a phase error, $\delta(\Delta\varphi_i)$, of $\sim$5 milliradians can be achieved with just 100 scans or more than 500 scans in poor internal (laboratory) seeing conditions.

With such magnitude of phase error and according to Eq. (5.16), the uncertainty of an optical path length measurement is in the order of 5nm or less.

The range of optical path where the contribution of $\frac{\delta(\Delta\sigma_{\mathrm{RG}})}{\Delta\sigma_{\mathrm{RG}}}$ to the overall error is negligible can be extended if frequency-stabilized lasers are used. Such lasers usually have wavelengths accurate to $1 \times 10^{-9}\mu$m or $\sim 1 \times 10^{-9}$ or smaller in relative error and cost about 3–4 times the price of a regular He-Ne laser. At that precision, δd is not dependent on the optical path length until about 1m which is well beyond the required optical delay for narrow-angle astrometry. However, the extension of the optical path range may also incur other technical costs, which involve improving the precision of optical alignment and increasing the range and speed of the delay line. Therefore, an upgrade to the metrology system described here should take all these factors into consideration.

5.4 Discussion and summary

All three metrology systems discussed in this chapter share several common but vital features. Firstly, all the light sources are propagated along optical paths and recorded by detectors which are identical to those of the science beams, thereby eliminating non-common path errors. Secondly, all the metrology systems used pre-existing hardware, do not require additional specialized optics (e.g. an acoustic-optoelectronic modulator (AOM)) or electronics (e.g. a digital phasemeter) and have relaxed requirements on the accuracy and stability of the laser wavelengths which kept the cost to a minimum. Lastly, all OPD measurements are carried out at wavelengths slightly different from the science bandpass. By doing so, the OPD measurement incurs some error because the optical media (air and glass) within and between MUSCA and PAVO are dispersive. However, the magnitude of the dispersion induced OPD error is negligible ($<$1nm) because the variation in OPD due to internal laboratory seeing ($\ll 1\mu$m) and the MUSCA DDL ($<$2mm) is short and insignificant.

Chapter 6

Data reduction and analysis

The content of this chapter is partially reproduced from the paper: "Phase-referenced interferometry and towards narrow-angle astrometry with SUSI", which has been accepted for publication in the Journal of Astronomical Instrumentation

Raw data from a PAVO+MUSCA observation, in the form of interferograms, are reduced in two stages to produce their primary observable, i.e. the fringe packet separation of a binary star or the variable S in Eq. (2.13). The first stage of the data reduction pipeline computes the phase delay of the MUSCA fringes, m in Eq. (5.1), using the estimated phase delay of fringes of PAVO, z in Eq. (5.1), the WL metrology, w in Eq. (5.4), and the SL metrology, x in Eq. (5.6), while the second stage computes the fringe packet separation, S, using the estimated displacement of the differential delay line (DDL), d in Eq. (5.9).

The PAVO interferograms (see Fig. 4.3(a)) are 32 by 512 pixels images recorded in 4.2ms of exposure time. They contain images of three pupils, one to be used for fringe-tracking (left in the figure) and two to be used for tip-tilt correction (middle and right in the figure). Each pupil is imaged by 4 lenslets and spectrally dispersed by a prism. Each dispersed segment of a pupil is 33-pixel wide, which represents individual spectral channels of the PAVO spectrograph. The PAVO interferograms are stored as FITS files with headers that contain various information such as the status of the fringe lock, timestamp, etc.

The MUSCA interferograms are time series of photon counts recorded by a pair of APDs as the scanning mirror scans through a predetermined range periodically. The photon counts are stored as ASCII text files and each count has a timestamp for synchronization with post-processed data from PAVO in the pipeline. The temporal fringes recorded by the two APDs have a phase difference of π radian due to the beam-splitter. Fig. 6.1 shows several scans of MUSCA interferograms with

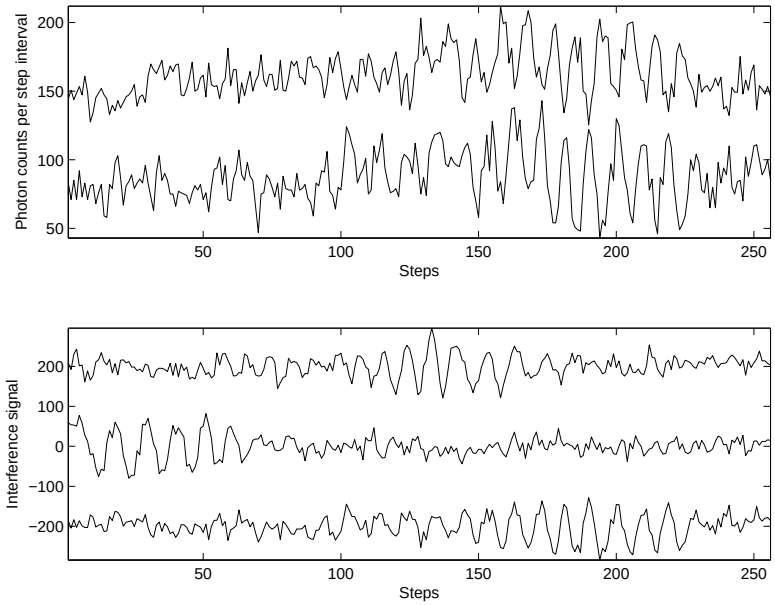

Figure 6.1: Interferograms of β Cru recorded by MUSCA. The top plots are photon counts recorded by the pair of APDs, one on each output port of the beam-splitter, hence the π radian phase difference for the interference signals. The bottom plots show the difference of photon counts recorded by the APDs. Three separate sweeps through the fringe packet are depicted, illustrating the varying position of the fringes at different times. Vertical offsets have been added to individual scans for clarity.

the upper panel illustrating the out-of-phase relationship between signals from two APDs. Let the *interference* signal of the time series be defined as the difference between the photon counts recorded by APD0 and APD1 and the *photometry* signal of the series be defined as the sum of the photon counts recorded by the APDs. The interference signal of the same scan in the upper panel of Fig. 6.1 is the lowest line in the lower panel in the same figure. Also plotted in the bottom plot are interference signals of two other scans at different times which show the position of stellar fringe packets vary with time due to atmospheric turbulence.

6.1 Stage I

The main goal of the first stage of the pipeline is to produce a phase-referenced fringe packet that has an average phase uncertainty better than 5nm. This stage is implemented in two parts, one for each type of interferogram. The PAVO part of

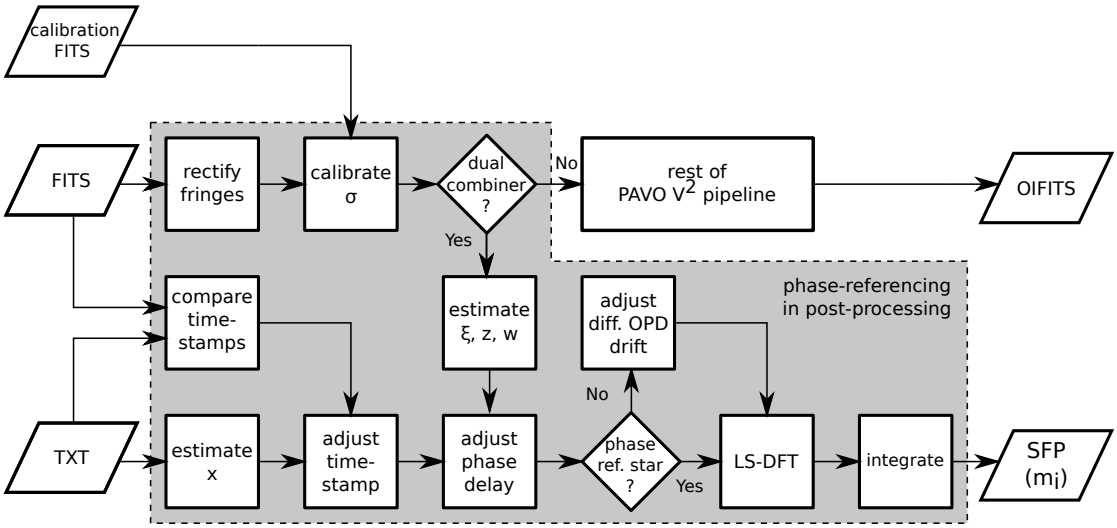

Figure 6.2: The logical flow of Stage I of the PAVO+MUSCA pipeline. Subprocesses within the shaded region are the phase-referencing part of the pipeline. The main inputs to the pipeline are the PAVO (FITS) and MUSCA (TXT) interferograms. If necessary, calibration FITS files which contain PAVO interferograms of metrology light sources are also included to calibrate the PAVO spectrograph. The output is a phase-referenced separated fringe packet (SFP).

the pipeline is modified from an existing V^2 pipeline developed for PAVO V^2 science observation (Ireland et al., 2013, in prep.). It is written in IDL programming language. On the other hand, the MUSCA part of the pipeline was developed from scratch and is written in MATLAB. A diagram showing the interdependency between the PAVO and the MUSCA parts in this stage of the pipeline and the summary of their various subprocesses is shown in Fig. 6.2. Only subprocesses within the shaded region in the figure are related to the phase-referencing part of the PAVO+MUSCA pipeline. The following subsections describe some of the more important subprocesses in the figure in the context of phase-referencing.

6.1.1 Wavelength scale calibration

The main goal of this calibration step is to determine the wavelength scale of the PAVO spectrograph. The accuracy of the wavelength scale determines the accuracy of the group delay and phase delay estimation derived from the analysis of the PAVO fringes. For example, in order not to exceed an uncertainty of 1μm in the group delay estimation the uncertainty of the wavelength scale of a pixel and the uncertainty of the difference of the wavelength scale between adjacent pixels

must not exceed 120nm and 5nm respectively. In order to obtain a more accurate wavelength scale, the wavelength calibration for PAVO+MUSCA phase-referencing is carried out slightly differently compared to the original PAVO pipeline for V^2 science.

Previously, a PAVO calibration frame was taken after a major optical realignment with one He-Ne laser source and the presence of fringes was not required. It is used to calibrate the wavelength value of each spectral channel in the PAVO spectrograph. Since more than one set of spectra are recorded at the same time (each lenslet produces a spectrum of the source), the mean wavelength of a spectral channel (a column of pixels in the interferogram in Fig. 4.3(b)) can be calculated by extrapolating the location of laser lines to each channel. The mean wavelengths of the spectral channels, also known as the wavelength scale, are then stored in an ASCII text file for future reference. In order to account for long term drifts in the optical alignment the wavelength scale is adjusted for offset using the stellar spectra obtained during astronomical observations. This is done by aligning one of the two edges of the stellar spectra (defined by the bandpass created by a series of dichroic filters in SUSI) to a wavelength channel of known value before further processing. This method is described by Maestro et al. (2012) for PAVO at CHARA but is very similar to the method described here for PAVO at SUSI.

As for the PAVO+MUSCA phase-referencing observation, a calibration frame is recorded before or after every observation season (or every night depending on the requirement of the observer). Instead of one, two He-Ne lasers and an IR LED are used as light sources for the calibration. They are the same light sources used for optical alignment and metrology discussed in earlier chapters. By using more sources, a more accurate wavelength scale, especially for those spectral channels at the extreme red end of the PAVO bandwidth, can be obtained. By recording calibration frames for every PAVO+MUSCA observation the calibrated wavelength scale is directly applicable to the PAVO interferograms recorded on the same night and does not have to be subjected to adjustment based on stellar spectra. This eliminates the need to observe bright blue stars before the start of any science observation.

The details of the data analysis and mathematics of the wavelength calibration is presented in Appendix D.

6.1.2 Estimation of z, the phase delay of PAVO fringes

Only PAVO interferograms with stellar fringes are selected for further processing. First, the interferograms are pre-processed to retain only the relevant parts of the

image (i.e. the spectrum of the science pupil) and to correct for a small distortion in the spectrum (which is due to a curvature aberration in the direction of the x-axis of the image or the spatial fringes direction) which is caused by the glass prism and lenses system of the spectrograph. Then the spatially modulated fringes are rectified by treating the fringes in each spectral channel as an analytic signal and removing the carrier frequency through a series of forward and inverse Fourier transform operations and data manipulation in the Fourier domain. The outcome of the rectification is a complex function that describes the envelope of the fringes in each spectral channel, which is modeled as,

$$\rho_{j,k} = \Omega_{j,k}\, e^{-i\phi_{j,k}}, \tag{6.1}$$

where j and k are indices of a pixel in the y- and x-axis respectively while $\Omega_{j,k}$ is the function of the fringe envelope and $\phi_{j,k}$ is a phase term attributed to the OPD of the combining beams. The index j refers to one of the 33 spectral channels while k refers to one of the 4 lenslets in PAVO. Only the first 21 channels are within the PAVO science bandwidth and used for estimating z. Suppose σ_j represents the wavenumber of a spectral channel and $z(\sigma_j)$ or z_j is the OPD between two arms of SUSI at a particular wavenumber, then, according to Tango (1990),

$$\sigma_j z_j = \bar{\sigma} z(\bar{\sigma}) + \xi(\sigma_j - \bar{\sigma}) + \psi_j, \tag{6.2}$$

where $\bar{\sigma}$ is the mean of the wavenumbers of all the spectral channels, ξ is the group delay of the fringes at $\bar{\sigma}$ and ψ_j or $\psi(\sigma_j - \bar{\sigma})$ is the higher order terms of the Taylor's expansion of $\sigma_j z_j$. With an additional noise term, $\varepsilon_{j,k}$, to represent atmospheric phase noise or optical aberration, then the argument of $\rho_{j,k}$ in Eq. (6.1) is,

$$\phi_{j,k} = 2\pi\sigma_j z_j + \varepsilon_{j,k}. \tag{6.3}$$

The first step in estimating z_j is to estimate the group delay of the fringes. This is done as follows. First, the autocorrelation of the phasor, p_j, is calculated. The phasor, p_j, is defined as,

$$p_j = \sum_k \rho_{j,k} = \bar{\Omega}_j\, e^{-i\bar{\phi}_j} = \bar{\Omega}_j\, e^{-i(2\pi\sigma_j z_j + \bar{\varepsilon}_j)}, \tag{6.4}$$

and its autocorrelation is,

$$\begin{aligned} q_a &= \sum_j p_j p^*_{j+a} \\ &= e^{-i2\pi a\Delta\sigma\xi} \sum_j \bar{\Omega}_j \bar{\Omega}_{j+a}\, e^{-i2\pi\Delta\psi_{j,a}}, \end{aligned} \tag{6.5}$$

where $a\Delta\sigma = \sigma_j - \sigma_{j+a}$ and $\Delta\psi_{j,a} = \psi_j + \bar{\varepsilon}_j - (\psi_{j,a} + \bar{\varepsilon}_{j+a})$. The wavenumber difference between two adjacent spectral channels, $\Delta\sigma$, is sufficiently regular across the entire spectral bandwidth to be considered constant and have negligible effect on the following analysis step.

Next, the Fourier transform of the vector $\mathbf{q}$ from Eq. (6.5) is calculated using a Fast Fourier Transform (FFT) routine. Using the notation $\hat{\mathbf{q}}$ to denote the Fourier transform of $\mathbf{q}$, then,

$$\hat{q}_b = \delta_{b-\check{b}} * \hat{\bar{\Omega}}_b = \hat{\bar{\Omega}}_{b-\check{b}}, \tag{6.6}$$

where $\delta_{b-\check{b}}$ is a delta function at index $\check{b}$ and $\check{b} = \Delta\sigma\xi N_{\mathrm{FFT}}$. The second term of the convolution in Eq. (6.6) is the power spectral density (PSD) of $\bar{\Omega}_j e^{-i(\psi_j+\bar{\varepsilon}_j)}$ and has a global maximum at the origin. As a result the group delay of the fringes can be estimated from the position of the global maximum of $\hat{q}_b$. The estimated group delay is,

$$\tilde{\xi} = \Delta\sigma^{-1}\tilde{b}/N_{\mathrm{FFT}}, \tag{6.7}$$

where $\tilde{b}$ is the location of the global maximum of $\hat{q}_b$, which may not necessarily be at $\check{b}$ as discussed in the next paragraph, and N_{FFT} is the size of the vector as input to the FFT routine. The tilde notation in Eq. (6.7) and throughout this chapter denotes estimation of a parameter. Since the coherence length of each spectral channel, $\Delta\sigma^{-1}$, is $\sim 30\mu$m, this estimate is reliable if the true group delay is within $\pm 15\mu$m.

The assumption that ψ_j is approximately constant across the bandwidth of the PAVO spectrograph is ensured by the usage of a longitudinal dispersion compensation system, or LDC (Davis et al., 1999). However the similar assumption on $\bar{\varepsilon}_j$ is only true when the atmospheric phase noise across the pupil is small (i.e. the seeing is good). If the phase noise variation is large then location of the global maximum of $\hat{q}_b$ may not be at zero. In addition, a large variation also gives rise to spurious peaks in the PSD.

In order to gauge the phase noise variation, a signal-to-noise (SNR) ratio, η, is introduced. η is defined as the ratio of the value of the dominant peak to the noise floor of the PSD and the noise floor is defined as the standard deviation of the PSD with the dominant peak removed. The value of η, which is inversely proportional to the phase noise variation, is also used to gauge the accuracy of the OPD estimate, $\tilde{z}_j$, because the requirement is that $\tilde{\xi}$ must be accurate to within one wavelength. From computer simulation, an η of 5 is acceptable while an η of 6 is good (Kok et al., 2013b).

If the optical media in which the starlight propagates to reach the beam combiners are non-dispersive then the group delay is also the OPD affecting the fringes at all wavenumbers. However, except for the optical path in the vacuum pipe near the siderostats, all optical media along the optical path of PAVO and MUSCA are dispersive.

The last step in estimating z_j is to adjust the group delay estimate by a fraction of a wavelength according to the dispersion factor, δ_ℓ, and length of the optical path propagated by the light source, L_ℓ. Suppose the value to be adjusted is α, which is defined as,

$$\begin{aligned} \alpha &= \sum_{\ell=1}^{N_{\mathrm{MED}}} \delta_\ell L_\ell, \quad \text{or,} \\ e^{i\tilde{\alpha}} &= \left\langle e^{i\bar{\phi}_j} e^{-i2\pi\sigma_j\tilde{\xi}} \right\rangle, \end{aligned} \tag{6.8}$$

where N_{MED} is the number of different optical media along the propagation path, then,

$$\tilde{z}_j = \tilde{\xi} + \frac{\tilde{\alpha}}{2\pi\sigma_j}. \tag{6.9}$$

Finally, suppose σ_{M} is the mean wavenumber of the MUSCA's operating bandwidth, which is $\sim 1.2\mu\mathrm{m}^{-1}$, then the OPD estimate at that wavelength is obtained by evaluating Eq. (6.9) at σ_{M}.

6.1.3 Estimation of w, the phase delay of WL metrology fringes

The WL LED metrology fringes are recorded at the same time and in the same way as the stellar fringes in PAVO. After undergoing the same pre-processing, the metrology fringes are used to estimate w in a slightly different way than the stellar fringes to estimate z. Since the optical paths probed by w are contained within a climate controlled environment it is not expected to vary beyond one wavelength of the metrology fringes within the one unit of a PAVO interferogram exposure time. Therefore the OPD probed by the metrology can be measured by converting the phase of the metrology fringes, which is the argument of p_j in Eq. (6.4), into distance. The estimate of w is given as,

$$\tilde{w} = \frac{2\pi N_{\sigma\mathrm{I}} + \arg(p_{\mathrm{I}})}{2\pi\sigma_{\mathrm{I}}}, \tag{6.10}$$

where the subscript I is the spectral channel at σ_{I} and $N_{\sigma\mathrm{I}}$ represents an integer number of cycles over which the fringes have wrapped around. $N_{\sigma\mathrm{I}}$ is obtained by

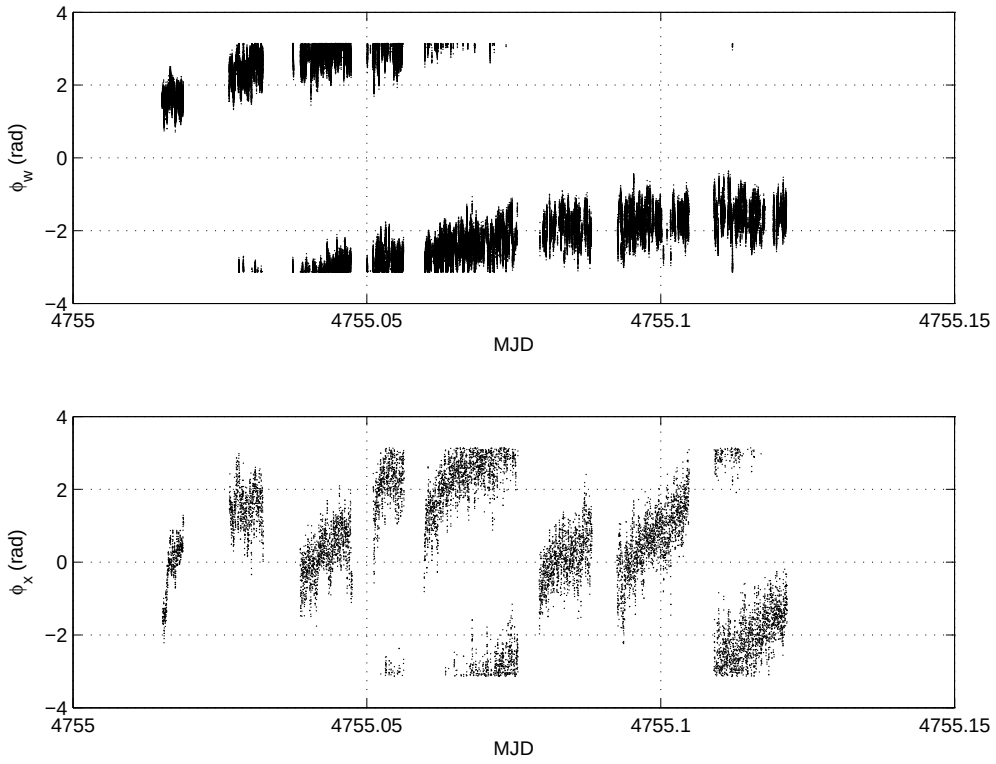

Figure 6.3: Wrapped phases of the WL (top) and the SL (bottom) metrology fringes used to estimate w and x respectively.

unwrapping the phase measurement collected throughout several sets of observations (or the entire night) because the phase measurement obtained directly from a 'single' wavelength fringes is modulo of 2π. The top plot in Fig. 6.3 shows the argument of p_{I} without taking into account phase wrapping.

6.1.4 Estimation of x, the phase delay of SL metrology fringes

The SL metrology fringes are recorded by MUSCA together with its science fringes. As a result of that, the interference signal of the metrology fringes imposes a measurement grid across the scan range of the scanning mirror. The spacing of the gridlines, which is defined by the wavelength of the metrology laser, is used to measure the change in OPD induced by the mirror. A visualization of this grid is shown in Fig. 6.4(a). Instead of using a Fourier filtering method, the faint metrology fringes are extracted by shifting a pre-recorded scan of high SNR reference

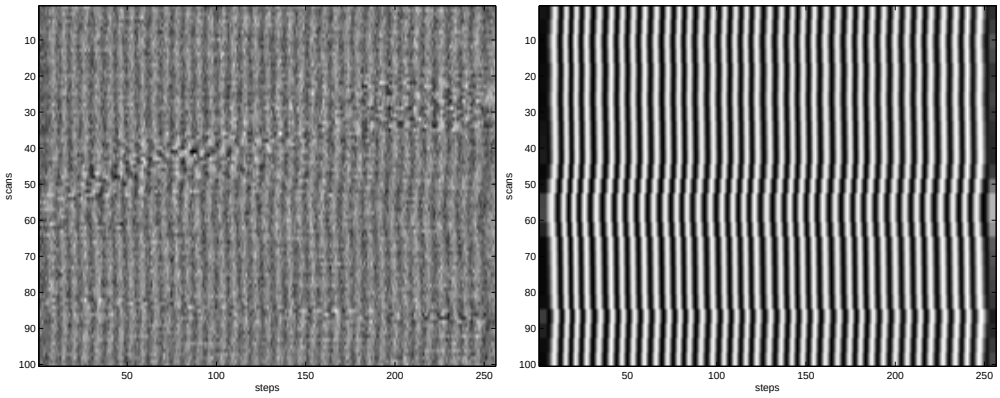

(a) (b)

Figure 6.4: Waterfall plot of (a) SL metrology and MUSCA science fringes as recorded and (b) SL metrology fringes after SNR enhancement and removal of the science fringes. The wavy 'gridlines' show the phase shifts in the metrology fringes due to internal laboratory seeing.

fringes in the spatial domain and the amount of shift to be applied is measured from the phase of the metrology fringes recorded during observation. This method assumes that the metrology fringes produced by each scan of the scanning mirror, denoted by $\ell(x)$, are a spatially shifted version of fringes produced by a reference scan, $\ell_{\mathrm{R}}(x)$. Physically, the spatial shift is caused by internal laboratory seeing which has a timescale[1] of several tens of seconds to a minute. This is very slow compared to the time taken by the scanning mirror to complete an up and down scan cycle, which is about 150ms. Therefore the assumption that path length variations are much less than one wavelength between successive scans is reasonable. Suppose $\hat{\ell}_{\mathrm{R}}(\sigma)$ represents the Fourier transform of $\ell_{\mathrm{R}}(x)$ and the $\tilde{\ell}(x)$ represents an estimate of $\ell(x)$, then,

$$\tilde{\ell}(x) = \mathcal{FT}^{-1}\left\{\hat{\ell}_{\mathrm{R}} \exp\left(i\frac{\sigma}{\sigma_{\mathrm{G}}}\phi_{\mathrm{G}}\right)\right\}, \tag{6.11}$$

where ϕ_{G} is the phase of the metrology fringes recorded during observation. A waterfall plot of a set of recovered metrology fringes (or $\tilde{\ell}$) over time is shown in Fig. 6.4(b). The phase variation of the metrology fringes in Fig. 6.4(a) is preserved in Fig. 6.4(b). However, the SNR of the fringes is greatly enhanced.

The phase delay of the fringes is then computed by inverting the function, $\tilde{\ell}(x)$.

[1]Duration over which the average phase variation is 1 radian, computed from the spectral density of the measured phase variation

Mathematically,

$$\tilde{x} = \frac{N_{\sigma \mathrm{G}}}{\sigma_{\mathrm{G}}} + \tilde{\ell}^{-1}\left(\tilde{\ell}(x)\right). \tag{6.12}$$

The function $\tilde{\ell}(x)$, which is in the form of,

$$\tilde{\ell}(x) = A\cos\left(2\pi\sigma_{\mathrm{G}}x + \phi_{\mathrm{G}}\right), \tag{6.13}$$

is not invertible by definition due to the periodic nature of a cosine function but with additional computation (e.g. the derivative of the function), $\tilde{x}$, can be recovered for the entire scan range.

The phase delay in the middle of the scan range is set to zero thereby providing a reference point for measuring positions of phase-referenced fringe packets in the next stage of the pipeline. However, like the measurement with the WL metrology, the phase measurement of the SL metrology fringes must also be corrected for phase-wrapping. The term $N_{\sigma \mathrm{G}}$ in Eq. (6.12) is added to represent an integer number of cycles that the fringe phase has wrapped around and is obtained by unwrapping the phase measurement collected throughout several sets of observations. The lower plot of Fig. 6.3 shows the phase of the SL metrology fringes before unwrapping.

6.1.5 Adjusting timestamps

The PAVO and MUSCA beam combiners are controlled by two separate computers. Although their system clocks are synchronized to a Stratum 1 network time protocol (NTP) clock source, the offsets between the time when data are recorded and saved into the filesystem of the two separate computers can be in the order of several to ten milliseconds. In order to reduce the synchronization error to below 1ms, the timestamps of the interferograms are adjusted in post-processing. Since adjusting the timestamp of the PAVO interferograms is equivalent to adjusting the timestamp of the MUSCA interferograms, only the former is implemented.

The time offset to be adjusted is obtained by cross-correlating the PAVO and MUSCA interferograms and then extracting the average time offset by locating the peak of the cross-correlation. The quantity used for the cross-correlation is the total flux recorded by photo-detecting elements in each beam combiner over a certain period of time, i.e. a time series of recorded flux. By default, the pipeline selects portions of data taken during a shutter sequence for cross-correlation because the sharp transitions from high to low flux are good reference points for checking the result of the timestamp adjustment. A shutter sequence is a routine that toggles a pair of shutters in the optical path common to both PAVO and

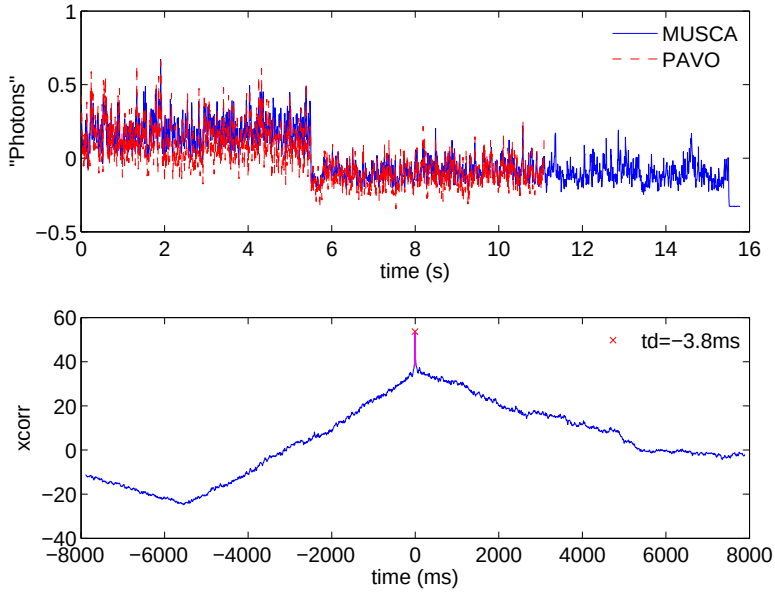

Figure 6.5: (top panel) Recorded flux by PAVO and MUSCA versus time. (bottom panel) Cross-correlation of the two time series in the top panel where the position of the peak indicates the offset in time between the two time series.

MUSCA so that PAVO can record the 4 different types of frames necessary for its V^2 science data reduction. The cross-correlation operation is carried out in the Fourier domain by computing the power spectrum of the product of the Fourier transform of the two time series. This is done because the sampling rate of the two time series are different and to avoid interpolation in the time domain.

Fig. 6.5 shows an example of the time series from PAVO and MUSCA as well as the outcome of the cross-correlation. The time offset to be adjusted to the PAVO interferograms is indicated in the bottom plot. The typical number is about 3-6ms. A negative value means PAVO's timestamps are lagging MUSCA's.

6.1.6 Estimation of m, the phase delay of MUSCA fringes

The phase delay of the MUSCA fringes can be estimated by combining phase delay measurements from PAVO and the two metrology systems and is given as,

$$\tilde{m} = \tilde{z} - \tilde{w} + \tilde{x}. \tag{6.14}$$

The values of $\tilde{z}$ and $\tilde{w}$ are linearly interpolated to simulate the same sampling rate as $\tilde{x}$ before the above equation is computed. In order to avoid confusion, the

values of $\tilde{m}$ do not represent the photon counts in the MUSCA interferograms. Instead, they represent OPD at each step in one mirror scan. If the stellar fringes are to be plotted as a graph, the photon counts are on the ordinate and values of $\tilde{m}$ are on the abscissa.

6.1.7 Coherent integration

In order to reduce the uncertainty in the phase delay estimation of $\tilde{m}$, a number of scans can be coherently integrated together. This means the photon counts are summed up with shifts according to their OPDs. However, only the photon counts with reliable estimates of m (having $\tilde{z}$ of $\eta \geqslant 5$) are integrated. Due to contribution from the other phase delays, $\tilde{m}$ does not have regular sampling. Therefore, it is easier to integrate the fringes in the Fourier domain by first computing the Fourier transform of the fringes using a discrete Fourier transform (DFT) algorithm which is capable of computing the Fourier transform of a non-uniformly sampled signal (Scargle, 1989). The computed Fourier transforms have regular frequency spacing in the Fourier domain. The algorithm also allows the frequency spacing in the Fourier domain to be appropriately specified. Furthermore, by integrating the fringes in the Fourier domain, additional phase error due to interpolation in the time domain can be avoided. Fig. 6.6 and 6.7 show the result of coherently integrated phase-referenced fringe packets. They are also the output of this first stage of the pipeline.

The phase-referenced fringe packet in Fig. 6.6 is a result of observing a target in self phase-referencing mode. This means both PAVO and MUSCA were observing the same star. The phase-referenced fringe packet in Fig. 6.7 is a result of observing a target in dual-star phase-referencing mode. In this mode, PAVO observed one component of a binary star while MUSCA observed the other. Due to their relative position in the sky, the separation between fringe packets changes with time as the pair of stars traverse the night sky. Therefore a correction term, Δz, must be added to Eq. (6.14) in order to accurately estimate the phase delay of the MUSCA fringes, otherwise the integration will yield fringes of very low or zero visibility because they are incoherently summed. Eq. (6.14) for dual-star phase-referencing becomes

$$\tilde{m} = (\tilde{z} + \Delta z) - \tilde{w} + \tilde{x}. \tag{6.15}$$

In its simplest form, Δz is a function of drift velocity and elapsed time (with respect to a chosen reference time, usually chosen to be at the start of the dual-star observation). However, the pipeline uses an astronomical model, which is based on the position angle and the on-sky separation of two stars, to compute Δz. The same model is also used for narrow-angle astrometry and is discussed

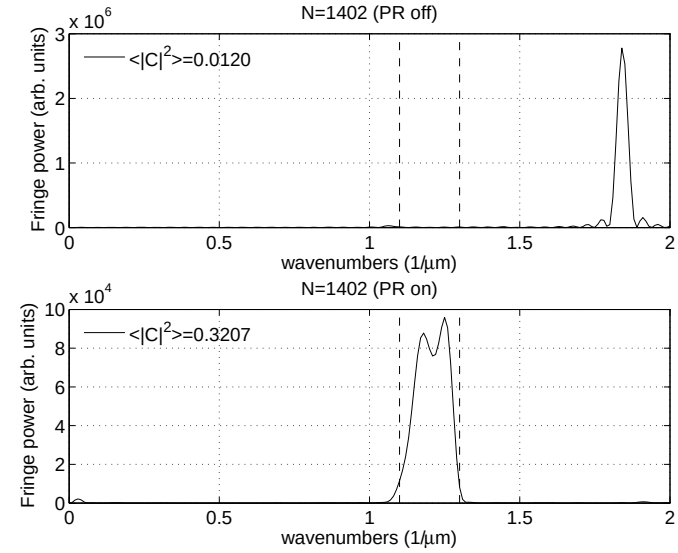

(a)

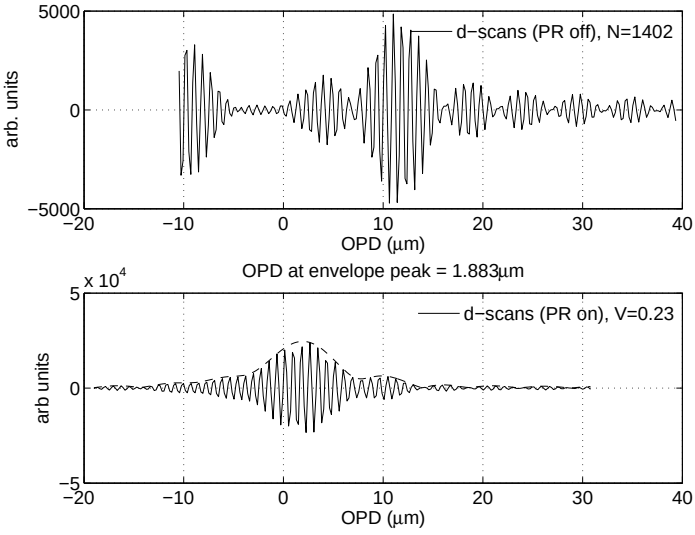

(b)

Figure 6.6: Plots in (a) show the incoherently (top) and coherently (bottom) integrated Fourier transform of a self phase-referenced fringe packet of δ Orionis Aa. The peak in the top plot of (a) belongs to the SL metrology laser because the metrology fringes are coherently integrated without phase-referencing. However, when phase-referencing is engaged the fringes are incoherently integrated and hence the absence of the metrology laser peak in the bottom plot. The signal within the two vertical dashed lines in the bottom plot of (a) belongs to the star. Plots in (b) show the inverse Fourier transform of (a) but only of the signal between the dashed lines.

in Section 6.3. Optimizing the amplitude of the coherently integrated fringes by tweaking the position angle parameter in the model does not immediately yield the astrometry of the two stars because Δz is also affected by the group delay drift effect, which is also discussed in Section 6.3.

Phase error

The coherence of fringes across multiple scans can be assessed using a metric which is defined as,

$$\langle |C|^2 \rangle = \frac{\int_0^\infty |\langle \hat{I}(\sigma) \rangle|^2 \, d\sigma}{\int_0^\infty \langle |\hat{I}(\sigma)|^2 \rangle \, d\sigma}, \tag{6.16}$$

where $\hat{I}$ is the Fourier transform of the phase-referenced fringes and the notation $\langle\rangle$ denotes an average over multiple scans. The metric measures the weighted average of the phase variation across the Fourier transform of the fringes. Similar to the Strehl ratio for measuring the performance of an adaptive optics system, this metric has a value between 0 and 1. If the fringe integration is perfectly coherent over all scans, then the metric will have a value of 1. On the other hand, if the fringes are completely out of phase then the metric will have a value of 0. If the phase variation is random and has a normal distribution of $\mathcal{N}(\mu_\varphi, \sigma_\varphi^2)$, then,

$$\langle |C|^2 \rangle \approx e^{-\sigma_\varphi^2/2}, \tag{6.17}$$

where σ_φ in this context is the standard deviation of the phase variation. The average phase variation can then be estimated from the coherence metric.

6.2 Stage II

The main goal of the second stage of the pipeline is to measure the separation of two fringe packets at high precision. This stage is executed when the previous stage has produced two or more phase-referenced fringe packets. In this stage, the apparent and true separation of a pair of phase-referenced fringe packets are computed. Fig. 6.8 illustrates the logical flow of this stage of the pipeline, which is written entirely in MATLAB.

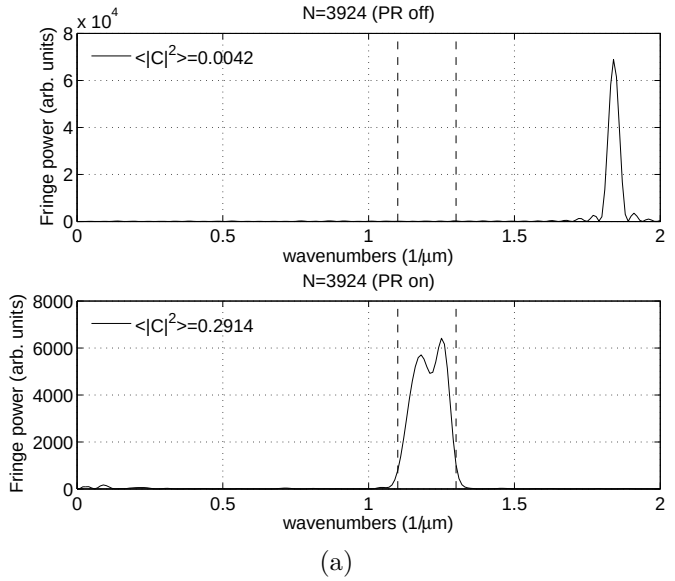

(a)

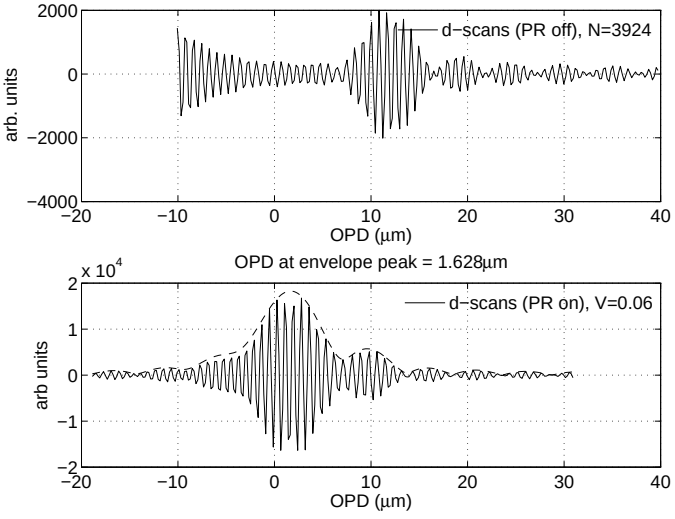

(b)

Figure 6.7: Similar to Fig. 6.6. Plots in (a) show the incoherently (top) and coherently (bottom) integrated Fourier transform of a dual phase-referenced fringe packet of δ Orionis Ab, which is separated by $\sim 0.3''$ from the reference star δ Orionis Aa. Plots in (b) show the inverse Fourier transform of (a) but only of the signal between the dashed lines.

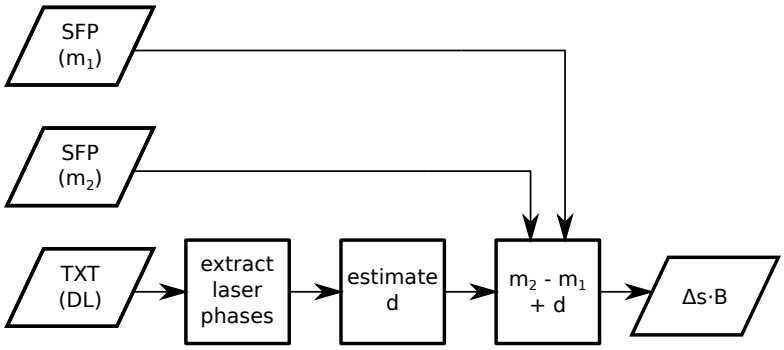

Figure 6.8: The logical flow of Stage II of the PAVO+MUSCA pipeline. The main inputs comprise the output of Stage I and a set of MUSCA interferograms containing only the DL metrology fringes. The output is the true separation of the given pair of fringe packets.

6.2.1 Estimation of d, the OPD due to the displacement of DDL

The dual-laser metrology is used to measure a change in the position of the differential delay line (DDL) in MUSCA. The DDL is static when stellar fringes are being recorded and it is only moved to alternate between different fringe packets. Therefore, $\tilde{d}$ is a one-off measurement of the DDL displacement between successive observations for which metrology fringes are recorded just before and after the DDL is moved. The estimated change in optical path is given as,

$$\tilde{d} = n_{\mathrm{M}} d \approx \frac{(\Delta\varphi_2 - \Delta\varphi_1)/2\pi + \Delta N}{\sigma_{\mathrm{R}} - \sigma_{\mathrm{G}}}, \tag{6.18}$$

where n_{M} is the refractive index of air at MUSCA mean wavenumber, $\sigma_{\mathrm{M}} = 1.2\mu m^{-1}$, while σ_{R} and σ_{G} in the denominator are the wavenumbers of the two lasers in vacuum. The terms in the numerator of the above equation (see Eq. (5.9)) describe the difference between the phases of the red and green laser fringes at two different DDL positions indicated by the subscript 1 and 2. The model of the displacement of DDL, d, and the analysis of the metrology phases to estimate its value is discussed in Section 5.3.

6.2.2 Estimation of S, the true projected separation

The apparent separation of the two fringe packets, Δm, is estimated from the phases of the product of the Fourier transform of one fringe packet and the conjugate of the Fourier transform of the other fringe packet. Examples of the modulus

amplitude and phase of the Fourier transform products are shown in the middle and lower plots of Fig. 6.9. The phase delay at the mean wavenumber is a measurement of the apparent separation of the fringe packets, $\Delta\tilde{m}$, and is estimated from a linear least squares fit. Examples of the goodness of fit, χ^2, of possible values of Δm are also plotted in Fig. 6.9. The value that has the global minimum χ^2 is usually but not always the case accepted as the value for $\Delta\tilde{m}$. The presence of severe differential dispersion (between 2 fringe packets) and an unresolved fringe packet embedded within one of the two fringe packets used in the analysis may cause the result of the fit to be ambiguous by one wavelength. Example of cases due to the latter are discussed in Chapter 7.

The true separation of a fringe packet pair, S, is finally given as,

$$\tilde{S} = \Delta\tilde{m} + \tilde{d}, \tag{6.19}$$

where $\Delta\tilde{m} = \tilde{m}_2 - \tilde{m}_1$ is the estimated apparent separation of the fringe packets. The true separations of the fringe packets in the examples in Fig. 6.9 are indicated in the top most plots.

6.3 Narrow-angle astrometry with SUSI

The data analyses described in this section compute the true on-sky separation between the primary and the secondary star of the binary using the projected fringe packet separation obtained from the pipeline.

A complete set of MUSCA measurement consists of a series of fringe packet acquisitions. Fringes of a reference (primary component of a binary) star, then a target (secondary component of a binary) star and finally back to the reference star are acquired in sequential order. This is done so that the systematic error in phase delay of the fringe packet caused by the group delay drift can be corrected.

6.3.1 Group delay drift

The group delay drift occurs because optical media used to equalize the optical path in SUSI (air and glass) are dispersive and the mean operating wavelengths of PAVO and MUSCA are not the same. The rate of the drift is proportional to the length of the optical media along the common optical path of the interfering starlight and the difference of group delays at PAVO and MUSCA operating wavelength is about 0.36μm per 1m of air path. This estimate, which used the extrapolated numbers from Tango (1990), takes into account the proportionality

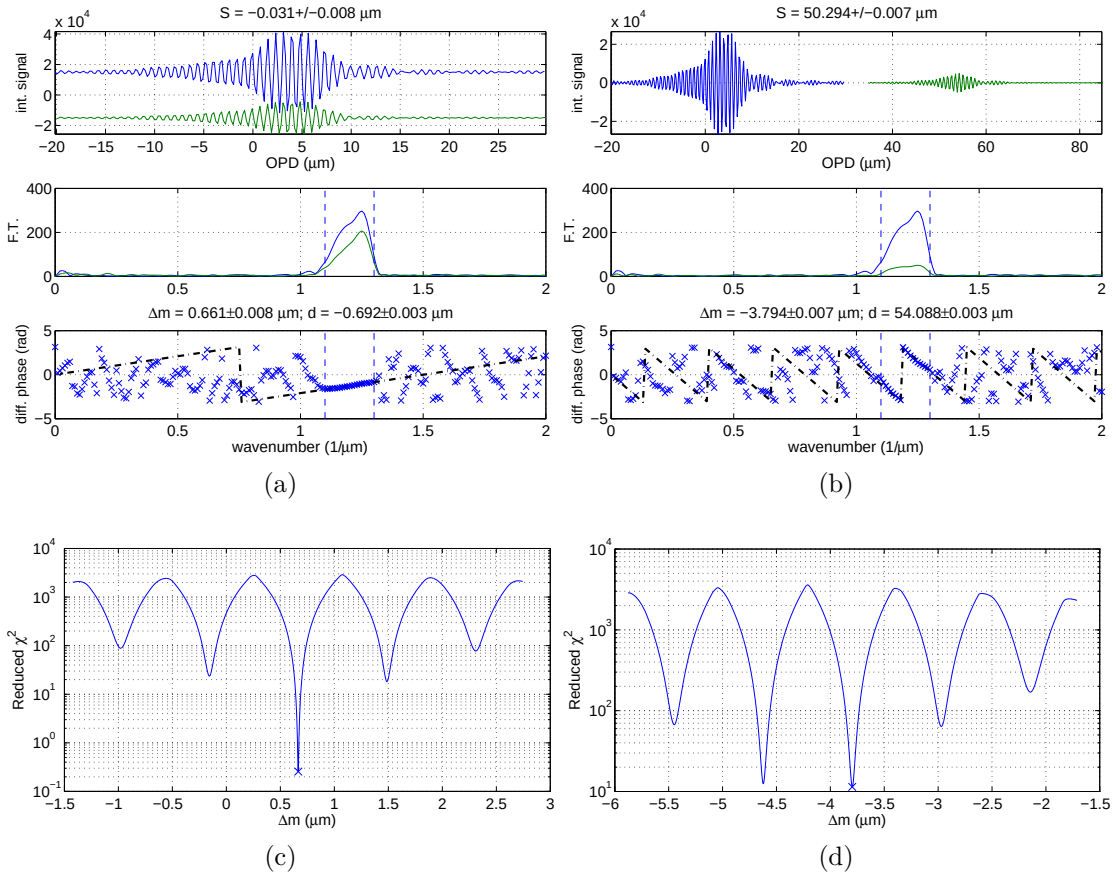

Figure 6.9: The top plot in (a) shows the phase-referenced fringe packet of δ Orionis Aa observed at two different times while (b) shows the fringe packet separation of δ Orionis Aa and Ab. The level of the interference signals in the top plot of (a) have been arbitrarily adjusted for clarity. The middle plots show the modulus amplitude of the Fourier transform of each fringe packet in the top plot. The bottom plots show the phase difference of the Fourier transform of the fringe packets (middle plots). The middle and bottom plots have the same x-axis scale. The portion of the phase signal that determines the apparent separation of the fringe packets, Δm, lies between the two vertical dashed lines. The dash-dotted lines show the least-squares fit to the phases in that region. The plots in (c) and (d) are the goodness of fit, χ^2, of possible values of Δm to the phases in (a) and (b) respectively. It is usually but not always the case that the value having the global minimum χ^2 (indicated by the symbol $\times$) is associated with the accepted value for Δm.

of optical path length in both air and glass which are used in SUSI. Fig. 6.10 plots the differential group and phase delay (at mean wavenumber) of a fringe packet as extracted from the phases of its Fourier transform. The computation is similar to the one discussed in the previous section for computing $\Delta\tilde{m}$ but the reference fringe packet in this case is a fringe packet from the same source but constructed with a different amount of air path. Essentially the group delay in the plot shows the relative position of a fringe packet of source when the amount of air path is varied. The fringe packet in the figure is simulated with the PAVO and MUSCA simulator. Although the group delay drifts according to the linear relation with the air path length, the differential phase delay of the fringe packet varies in discrete steps of about one MUSCA wavelength. This is expected because the measurement is phase sensitive and does not change unless the differential group delay changes by more than half a MUSCA wavelength from its previous value.

Due to this group delay drift effect, the separation between the primary and the secondary fringe packets must be corrected to yield a value that depends only on the projected separation of the binary star. Suppose $\xi_{S,P}$ represents the differential group delay between the primary and the secondary fringe packets which is interpolated from the slope of the phases of the Fourier transform of the cross-correlation of the two primary fringe packets (e.g. the lower plots of Fig. 6.9(a)-(b)) of a given astrometric observation, then the amount of adjustment to the fringe packet separation is,

$$\Delta S = \xi_{S,P} + \frac{1}{2\pi\sigma_{\mathrm{M}}} \arg\left(e^{-i2\pi\sigma_{\mathrm{M}}\xi_{S,P}+i\phi_{S,P}}\right), \tag{6.20}$$

where $\phi_{S,P}$ is a correction to the phase of the fringe packet due to a similar phase delay drift effect which is discussed in the next section. In most cases, ΔS is small ($\phi_{S,P}/2\pi\sigma_{\mathrm{M}}$) because the amount of air path change within the time span of one bracketed astrometric observation is usually shorter than 3m and therefore $\xi_{S,P}$ is usually less than half of one MUSCA wavelength.

6.3.2 Phase delay drift

The phase delay of the MUSCA fringes also drifts systematically in proportion to the length of the optical media along the common optical path of PAVO and MUSCA. This phenomenon occurs because the effect of higher order dispersion is not taken into account when estimating the phase delay at the mean MUSCA wavelength. The amount of systematic error is given as $\psi(\sigma_{\mathrm{M}} - \bar{\sigma})$ where the function $\psi(\sigma - \bar{\sigma})$ was first introduced in Eq. (6.2) and is explained in detail by Tango (1990). The rate of drift is very small but can become significant when

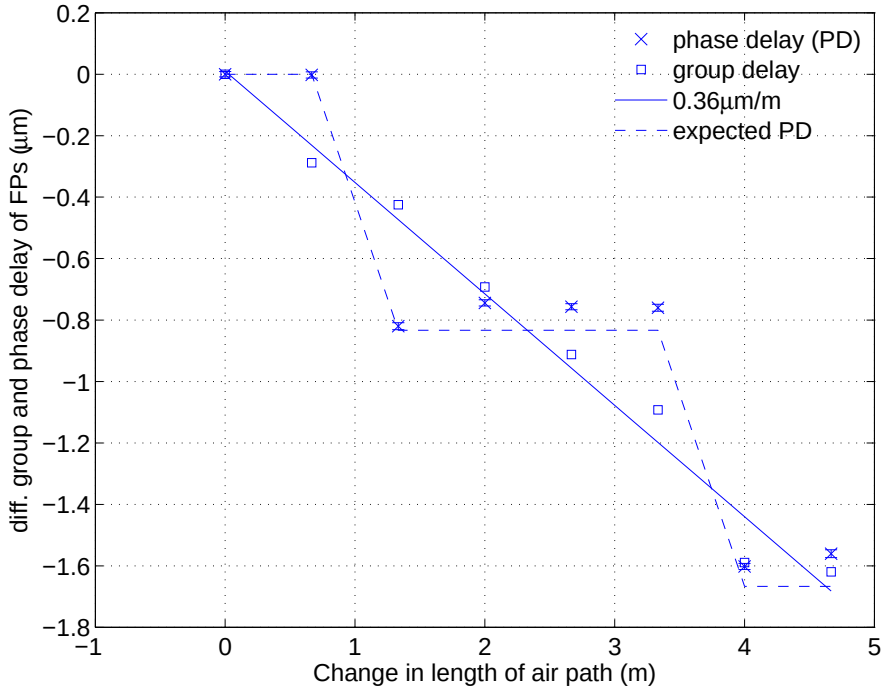

(a)

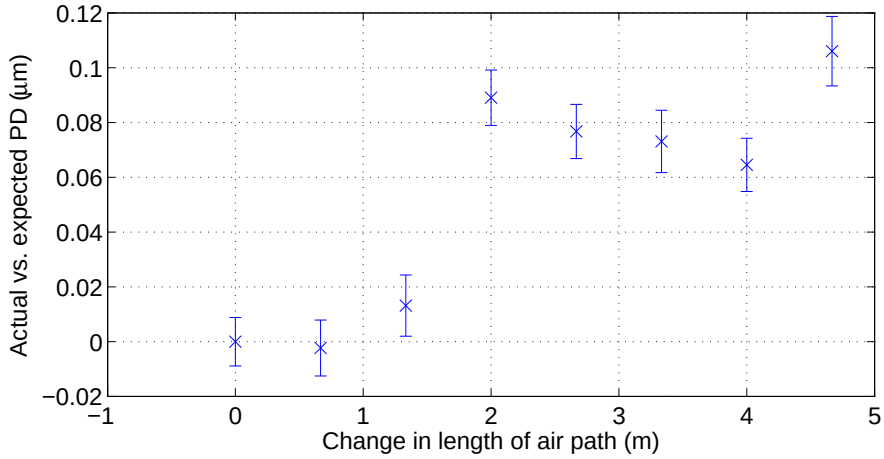

(b)

Figure 6.10: (a) Relative position (group and phase delay) of a fringe packet (FP) showing the effect of group delay drift. (b) The actual versus the expected phase delay (PD) of the FP showing the effect of phase delay drift. Both plots are derived from the PAVO and MUSCA simulators without atmospheric phase noise.

the change in the uncompensated dispersive media path length is large (∼5–10m) or the longitudinal dispersion is not well compensated. A calculation based on refractive indices and dispersion coefficients extrapolated from Tango's (1990) to MUSCA's wavelength suggests that the air and glass combination in SUSI gives rise to phase delay drift of about 0.035μm for every 1m air path of change. If uncorrected, this phase delay drift translates to about 72μas of astrometric error for every 1m air path change over a baseline of 100m. Fig. 6.10(b) shows the effect of the phase delay drifts of a simulated fringe packet. Since the difference in air path is unlikely to change by more than 10m between the time when the primary and secondary fringe packets of a binary star are recorded, this error is unlikely to cause an additional phase delay jump as seen in Fig. 6.10(a). The amount of phase delay adjustment, $\phi_{S,P}$, to be applied to the fringe separation is empirically interpolated from the measured phase delay difference between two primary fringe packets within a bracketed observation.

6.3.3 Position angle and on-sky separation

The corrected measurements of the projected separation of the primary and secondary fringe packets are then used to estimate the position angle, θ, and on-sky separation, ρ, of the binary through model-fitting.

The model used for parameter extraction is derived from Eq. (2.13)–(2.14) and is given as,

$$\begin{aligned} S &= \Delta\vec{s}\cdot\vec{B} \\ &= \begin{bmatrix} -\cos\delta_1\sin\mathrm{HA}_1 + \cos\delta_0\sin\mathrm{HA}_0 \\ \cos\phi\,(\sin\delta_1 - \sin\delta_0) - \sin\phi\,(\cos\delta_1\cos\mathrm{HA}_1 - \cos\delta_0\cos\mathrm{HA}_0) \\ \sin\phi\,(\sin\delta_1 - \sin\delta_0) + \cos\phi\,(\cos\delta_1\cos\mathrm{HA}_1 - \cos\delta_0\cos\mathrm{HA}_0) \end{bmatrix}_{xyz} \cdot \begin{bmatrix} B_x \\ B_y \\ B_z \end{bmatrix}_{xyz}, \end{aligned} \tag{6.21}$$

where S is the projected fringe packet separation of two stars, $\vec{B}$ is the vector of the chosen baseline and $\Delta\vec{s} = \hat{s}_2 - \hat{s}_1$ is the difference between pointing vectors of the target and the reference stars. Both vectors are resolved into their components in a rectangular coordinate system, taking the ground as the frame of reference. The x-axis points to the East, y-axis points to the North and z-axis points to zenith. The celestial coordinates, $(\mathrm{HA}_1, \delta_1)$ and $(\mathrm{HA}_2, \delta_2)$, define the location of the primary and secondary stars in the sky where $\delta_2 = \delta_1 + \rho\cos\theta$ and $\mathrm{HA}_2 = \mathrm{HA}_1 - \rho\sin\theta$. The symbols ρ and θ represent the on-sky separation and position angle of the two stars in a polar coordinate system. Although the uncertainty in the position of the primary star translates to an uncertainty in projected fringe packet separation, the value is extremely small and negligible. For example, through computer simulation, it was found that a standard deviation of 0.5″ in both axes of

the coordinate system produces a standard deviation of less than 1nm in projected fringe packet separation measurements, even at an unfavorable pointing angle and with a long (160m) baseline. By unfavorable pointing angle, we mean that the angle subtended by the pointing vector, $\hat{s}$, and the baseline vector, $\vec{B}$, is very small. This means the parameters extracted from fitting the model to the measured projected separation are insensitive to the absolute position of the primary star if the accuracy is better than $0.5''$. Finally the symbol ϕ in the above equation represents the geographical latitude of SUSI.

An alternative model described by Rizzuto et al. (2013, submitted) can also be used. However it may not be suitable for high-precision narrow-angle astrometry of stars separated by more than $3''$ and/or using baselines longer than 160m because the approximation in $\Delta\vec{s} \cdot \vec{B}$ may exceed 10nm. The model uses an astrometric coordinate system that takes the sky as the frame of reference. In order to differentiate the frame of reference from that used for this work, the axes of the astrometric coordinate system are labeled u, v and w. The u-axis points to the celestial East, the v-axis points to the celestial North and the w-axis points towards the sky (or towards target objects). The model is given as,

$$\begin{aligned} S &= \vec{\rho} \cdot \vec{B}_p \\ &= \begin{bmatrix} \rho \sin\theta \\ \rho \cos\theta \\ 0 \end{bmatrix}_{uvw} \cdot \begin{bmatrix} B_u \\ B_v \\ 0 \end{bmatrix}_{uvw} , \end{aligned} \tag{6.22}$$

where $\vec{\rho}$ is a vector defining the separation of two stars in the two-dimensional uv-plane of the sky and $\vec{B}_p$ is the component of $\vec{B}$ projected onto the same plane. Since $\vec{B}$ is commonly quoted in the ground (xyz) frame because it is more natural to an observer on the ground, it can be converted into the sky (uvw) frame as shown,

$$\begin{bmatrix} B_u \\ B_v \\ B_w \end{bmatrix}_{uvw} = \mathbf{T} \begin{bmatrix} B_x \\ B_y \\ B_z \end{bmatrix}_{xyz} , \tag{6.23}$$

where $\mathbf{T}$ is a matrix for coordinate transformation (Fomalont & Wright, 1974), which is given in Appendix E.

The RHS of Eq. (6.22) is an approximation of $\Delta\vec{s} \cdot \vec{B}$ and therefore the accuracy of the parameters extracted from the model could be systematically lower than the accuracy of the parameters extracted from the first model (Eq. 6.21). The calculated projected separation using Eq. (6.22) could be off by as much as 10nm under certain conditions. For example, observing a wide binary at low altitude,

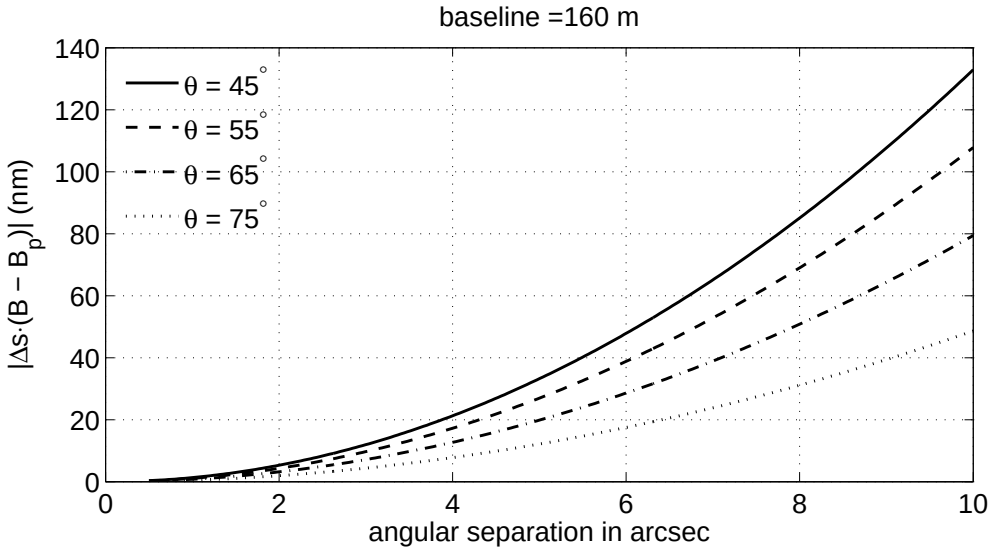

Figure 6.11: Optical path length contributed by $\Delta\vec{s}\cdot\vec{B}_p - \Delta\vec{s}\cdot\vec{B}$. The angle θ in the legend represents the angle between $\hat{s}_1$ and $\vec{B}$.

as shown in Fig. 6.11. This undesirable value translates to more than 10μas of astrometric error if the baseline of the interferometer is 100m or less. The factors affecting the approximation error are given as,

$$\begin{aligned}\Delta\vec{s}\cdot\vec{B} &= \Delta\vec{s}\cdot\vec{B}_p - 2|\hat{s}_0\cdot\vec{B}|\sin^2\frac{\Delta\theta}{2} \\ &\approx \vec{\rho}\cdot\vec{B}_p - 2|\hat{s}_0\cdot\vec{B}|\sin^2\frac{\Delta\theta}{2}\end{aligned}, \tag{6.24}$$

where $\Delta\theta$ is the angle subtended by the pointing vectors of the primary and secondary stars. In the narrow-angle regime, $\Delta\theta \approx |\Delta\vec{s}|$ and $\Delta\vec{s} \approx \vec{\rho}$. The approximation error of the latter is negligible even at long baseline (>100m). On the contrary, the plot in Fig. 6.11 shows that the approximation error of $\Delta\vec{s}\cdot\vec{B}_p \approx \Delta\vec{s}\cdot\vec{B}$ is negligible only for very closely separated stars. In summary, this alternative model is still suitable for MUSCA, which has a FOV of $<2''$, but may not be suitable for other instruments with a wider FOV.

6.4 Discussion and summary

MUSCA achieved dual-feed "first light" on January 2013 but its full suite of data reduction pipeline software for performing dual-star phase-referencing and binary

astrometry was not complete until May/June 2013. The usage of and the results from the pipeline are discussed in the next chapter.

Chapter 7

Observations

Astronomical observations were carried out with the PAVO and MUSCA beam combiners in order to test their narrow-angle astrometric performance. Not all the tests described in this chapter were carried out at the same time because different observation modes of the instrument were commissioned at different times. Observations of single stars which serve as calibrators for the instrument were made as soon as the self-phase-referencing mode of the instrument was available in January 2012. However observations of separated fringe packets of binary stars were carried out beginning in January 2013 as soon as the dual-star phase-referencing mode was available.

Observations using only the PAVO beam combiner are also included in this chapter because the capability of MUSCA to measure fringe packet separation breaks down when their projected separation becomes too small (see Section 2.4.1 for details).

7.1 PAVO+MUSCA observations

Before an observation, the optics in MUSCA are aligned with the optics in PAVO and the IR LEDs at the siderostats. The tools for optical alignment are discussed in Section 3.3 and the procedures, which may be updated occasionally, are available online[1]. The procedure on acquiring a star with PAVO and MUSCA is also available online. Then during the observation, a series of optical path length measurements are made with the metrology systems discussed in Chapter 5. The sequence of path length measurements is described in the next section.

[1] `http://pavo.wikispaces.com/`

7.1.1 Procedure

The sequence of a PAVO+MUSCA astrometric observation is briefly described in Section 6.3. First, a reference star (primary component of a binary) is acquired and its fringes are recorded with both beam combiners. At the same time, fringes of the white laser (WL) metrology are recorded with PAVO and the fringes of the single laser (SL) metrology are recorded with MUSCA. The amount of data to be recorded depends on the quality of atmospheric seeing on the night of observation. Typically, on a good seeing night about 10 minutes of data is sufficient.

Then, while PAVO tracks the reference star, the target star (secondary component of the same binary) is acquired with MUSCA. This is done by slewing the differential delay line (DDL) in MUSCA to a location where the fringe packet of the target star is expected to be. The amount of DDL displacement needed is computed from the expected separation and position angle of the binary and the baseline of the interferometer used during the observation. If the relative brightness of the secondary star with respect to the primary is high, the envelope of the secondary fringe packet may be visible in real time with MUSCAs software. This condition is useful because the position of the DDL can be tweaked so that the fringe packet is in the middle of the MUSCA scan range. However, such a condition is unnecessary because the estimated position of the fringe packet is usually about 5μm from its actual position (assuming the uncertainties of the binary separation and position angle are respectively $<1^\circ$ and $<$10mas) and this error is much smaller than the MUSCA 25μm scan range. Therefore, the secondary fringe packet should be within the scan range even if its envelope is not visible during observation. The amount of time spent recording fringes of the target star is usually longer than the time spent on the reference star by at least a factor equal to their brightness ratio so that the phase uncertainty of the fringe packets are similar. For example, in the case of a 1.35 magnitude difference binary the expected time to be spent on the secondary star is about 35 minutes.

Before the DDL is displaced from its nominal position to the position of the secondary fringe packet, the dual laser (DL) metrology is engaged to measure the displacement. The displacement of the DDL can then be converted into optical path length in the data analysis. During this period of time, the intensity of the green He-Ne laser, which is also used for the SL metrology system, is increased and the mechanical shutter controlling red He-Ne laser is opened to allow a high SNR dual laser fringes to be recorded with MUSCA. The dual laser fringes are recorded before and after the DDL is displaced. About 2–3 minutes of metrology data are recorded at each location. The metrology system is then switched from dual laser back to single laser to allow the fringes of the secondary fringe packet

to be recorded. The red He-Ne laser remains on throughout the observation and is only temporarily blocked with the mechanical shutter when it is not used. The WL metrology system also remains on throughout the observation.

Finally, in order to make a complete fringe packet separation measurement, the DDL of MUSCA is slew back to its nominal position again to acquire the reference star. The operation involving the switching between the DL and SL metrology systems is similar to that described in the previous paragraph. The entire procedure is repeated for another set of measurements. At least 3 sets of measurements are required to make one astrometric observation of a binary star.

7.1.2 Calibrators

Single unresolved stars are good targets for instrument calibration. They are used to test the stability of the reference phase of the fringes in MUSCA and consequently the intrinsic precision of the instrument and its data reduction pipeline. The intrinsic precision of the data reduction pipeline was initially evaluated with simulated data and it has been discussed in Section 6.3.1. The reference fringe phase in MUSCA can change due to instrumental and astrophysical reasons. The main instrumental cause is a change in the position of the differential delay line (DDL) in MUSCA while the main astrophysical cause is a change in the photo center of the star under observation. Single unresolved stars are suitable because they appear as point sources and therefore do not exhibit any photo center shift.

Calibration tests were carried out in two stages. In the first stage, an internal white light source was used. Then in the second stage, a known unresolved single star (for a given baseline) was used.

Internal phase stability

In the first stage, the goal of the test is to assess the ability of the DDL to slew away and then slew back to (or close to) its original position as well as the ability of the dual-laser (DL) metrology to measure the displacement of the DDL. The reason an internal white light source is used at this stage is to eliminate any astrophysical effect and to isolate the cause of phase shifts to just the DDL and the metrology. The white light source is the tungsten bulb which is also used for internal fringe searching. The optical setup for this test is similar to the setup for the DL metrology (a Mach-Zehnder interferometer). The non-common paths between the white light source and the DL metrology are negligible because these

two sources both originate from the same pin hole and are injected into the optical path by the same optical components (see Fig. 3.1(a)).

An example of fringe packets of the internal white light source recorded after every subsequent DDL slew away and back are shown in the top panel of Fig. 7.1(a). The middle and bottom panels of the figure respectively show the modulus amplitude and phase of the Fourier transform of the cross-correlation of the two fringe packets as described in Section 6.2.2. The differences in OPD or the separations (symbol S) between pairs of fringe packets (measured in μm) from several consecutive iterations of this test are shown in Fig. 7.1(b). The first fringe packet is used as the reference and therefore is plotted with a fringe packet separation of zero. Similar but slightly different measurements, the phase differences between pairs of fringe packets (measured in radians) are listed in Table 7.1. This measurement is not applicable to the first data point in Fig. 7.1(b), hence the table has one data point less that the figure. The values in the table are equivalent to 2π times the $1/\sigma_{\mathrm{M}}$ modulo of the points in the plot in Fig. 7.1(b). σ_{M} is the mean wavenumber of the fringes which in this case, $\sigma_{\mathrm{M}} \approx 1.25\mu\mathrm{m}^{-1}$ but for the actual stellar fringes $\sigma_{\mathrm{M}} = 1.2\mu\mathrm{m}^{-1}$.

The values in Table 7.1 provide a very useful metric to assess how well two fringe packets are aligned in terms of their phases. Ideally, a perfect alignment gives a zero phase difference while a less than perfect alignment gives a non-zero phase difference between $-\pi$ and π. A large phase difference indicates the presence of a large systematic error in the instrument which has a direct effect on its narrow-angle astrometric precision. Since the optical path of the interferometer was not changed during this test, the phase misalignment observed here is not due to the phase delay effect mentioned in Section 6.3.2. The range of phase differences measured with the internal white light source is between 0.1 and 0.8 radian or ∼10–100nm. The lower end of this range is good and is the level of precision required for high precision astrometry. However, the upper end of this range is poor.

On-sky phase stability

In the second stage, the goal of the test is to assess the ability of the instrument as a whole (all SUSI subsystems, PAVO and MUSCA) to maintain phase stability during a dual-star phase-referencing observation. The optical setup is not a Mach-Zehnder interferometer as in the first stage but the actual MUSCA setup described in Section 3.2 for astrometric observation. Several known single stars have been used as calibrators but only a selected few are listed in Table 7.2 together with records on nights they are observed. These selected observations either have long

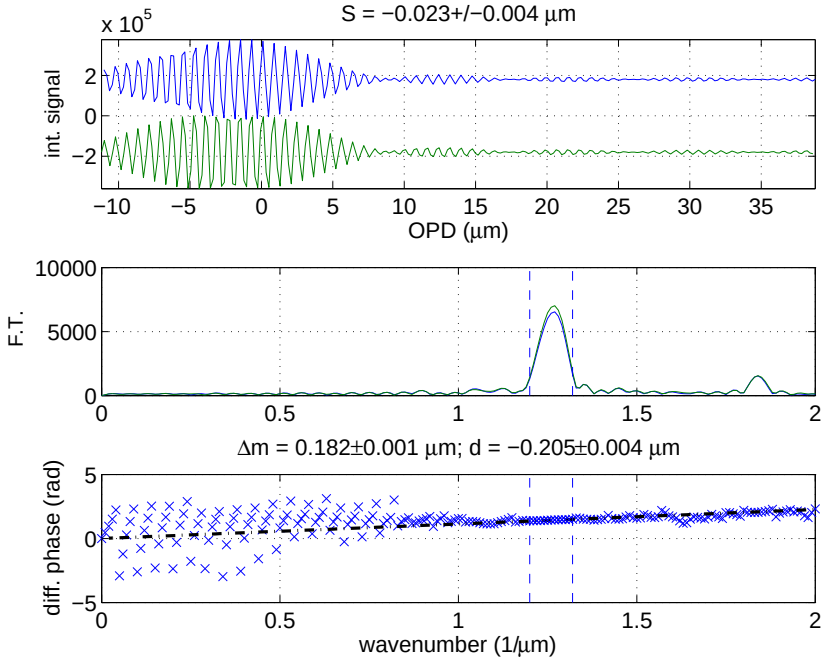

(a)

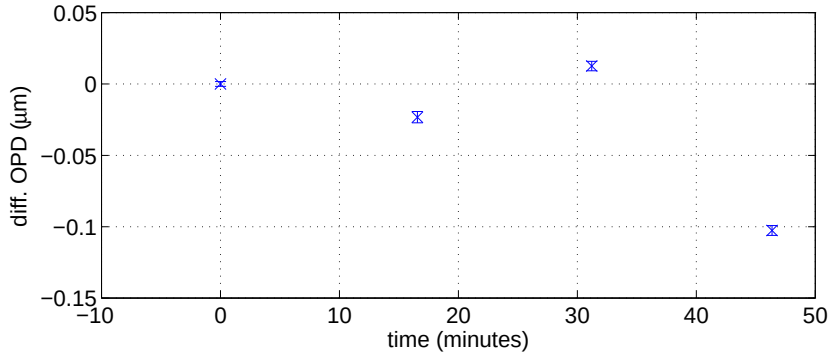

(b)

Figure 7.1: Comparison between the phases of a pair of fringe packets. In (a), the top panel shows the two fringe packets which have their mean level adjusted so that their phase alignment can be clearly seen while the middle and bottom panels show the modulus amplitude and the differential phase of the Fourier transform of the two fringe packets respectively. The displacement of the DDL in MUSCA as measured by the DL metrology is indicated above the bottom panel. In (b), the fringe separations of several pairs of fringe packets are shown. The light source of the fringe packets in this figure is the internal laboratory tungsten bulb.

Table 7.1: Phase stability of fringes in MUSCA

Light source	Related Figures	Differential Phase (rad)
Internal WL	Fig. 7.1(b)*	-0.18±0.03 0.10±0.03 -0.81±0.03
Achernar	Fig. 7.2(a)	-0.02±0.10 0.01±0.10 0.02±0.09 -0.07±0.10
	Fig. 7.4(a)-(b)*	-1.44±0.06 0.50±0.06
Bellatrix	Fig. 7.2(b)	-0.18±0.08 -0.08±0.08
β Lupi	Fig. 7.2(c)	0.04±0.12 0.17±0.13
	Fig. 7.4(c)*	-0.69±0.16
ϕ Sagittarii	Fig. 7.2(d)	-0.10±0.11 -0.07±0.10

*with DDL displacement

Table 7.2: Successful observations of calibrators

HR	Star	Baseline	Dates
472	Achernar	N3-S2	121120, 121122
1790	Bellatrix	N4-S2	130107
5571	β Lupi	N3-S3	130717, 130720
7039	ϕ Sagittarii	N4-S2	130726

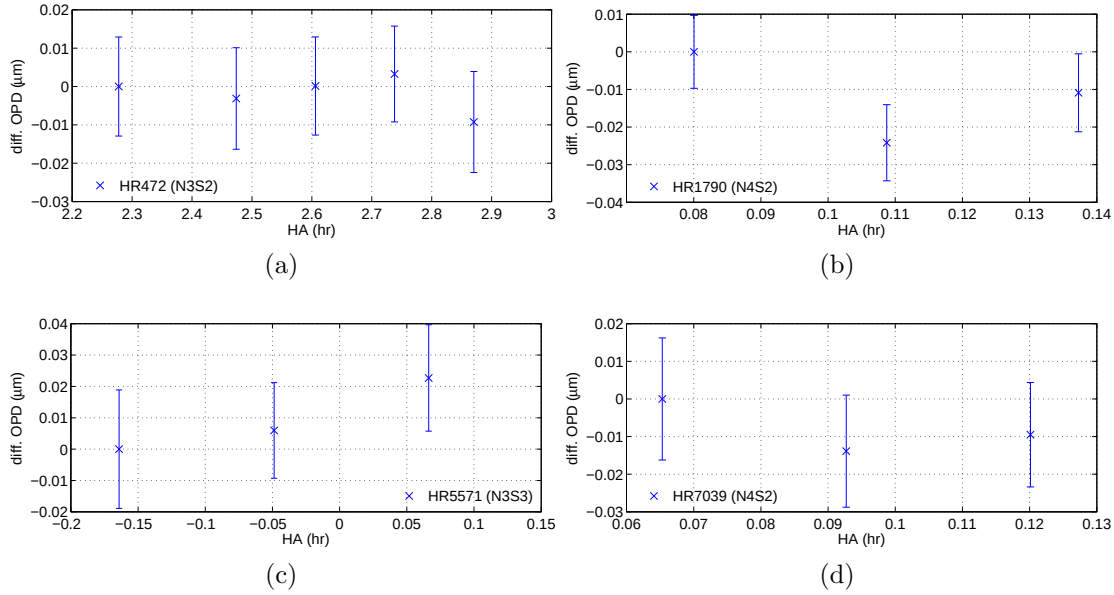

Figure 7.2: Similar to Fig. 7.1(b) but single stars (indicated in the legend of each plot) replaced the tungsten bulb as light sources. No DDL displacement took place.

enough observation time or were observed more than once in one night which allows their phase stability to be analyzed.

Similar to Fig. 7.1(b), the plots in Fig. 7.2 shows the phase sensitive relative position of fringe packets (with respect to the first data point) of Achernar, Bellatrix, β Lupi and ϕ Sagittarii. The fringe packets shown were recorded at different times but on the same nights for each star. The DDL in MUSCA was not moved during these observations. The results here show the intrinsic precision of the instrument and the data reduction pipeline without the effect of the DDL and the DL metrology. Fringe packets of Bellatrix and ϕ Sagittarii recorded at different times are plotted in Fig. 7.3 as examples. The results are discussed at the end of this section.

With the DDL in MUSCA moved away and back after one fringe packet is recorded, the separations of pairs of fringe packets are shown in Fig. 7.4. The phase differences of the fringe packets are listed in Table 7.1. The phase misalignments reported in the table are due to the intrinsic misalignment observed in the previous section as well as the phase delay drift effect because the stellar fringe packets were observed at different times and hence with different air path length. The fringe separation of the pair of β Lupi fringe packets in Fig. 7.4(c) is more than one

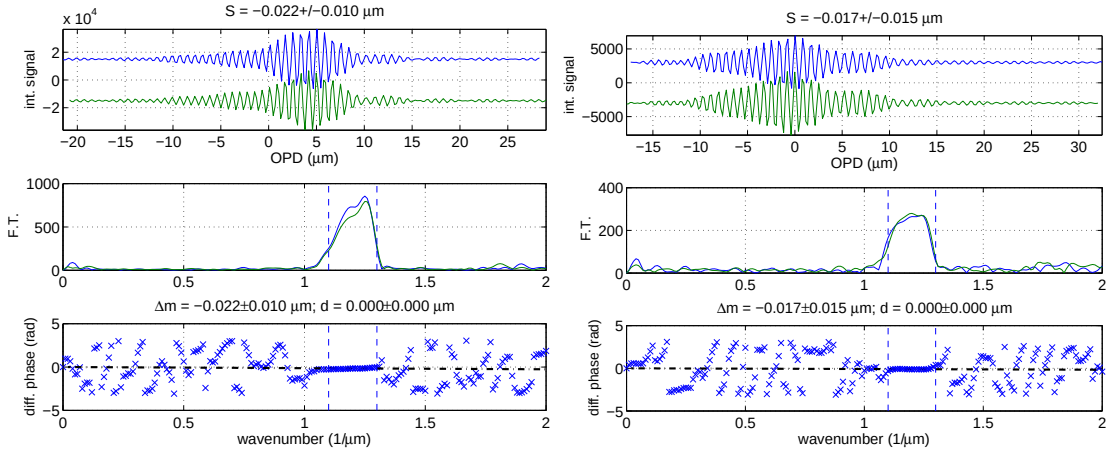

(a) Bellatrix (b) ϕ Sagittarii

Figure 7.3: Similar to Fig. 7.1(a) but single stars replaced the tungsten bulb as light sources. No DDL displacement took place.

MUSCA wavelength because of a change in the amount of air path in the main delay line as fringe packets were observed at different times in the night and the longitudinal dispersion compensator (LDC) was adjusted in between observations. Despite that, the phase alignment between the fringe packets is still less than 1/8th of the mean MUSCA wavelength (<0.8 radian).

The results from the series of calibration tests discussed in this section indicate that the intrinsic precision of the instrument and the data reduction pipeline is better than ∼20nm when the DDL in MUSCA is not displaced between observations but degrades to ∼100nm, which translates to about 0.2mas of astrometric error, when the DDL is displaced. This accuracy is not adequate for mircoarcsecond precision astrometry.

The correlation between the precision of measurement and the displacement of the DDL suggests that the accuracy of the DL metrology could be a problem despite having a precision of ∼5nm or better. However further investigation revealed that the suggestion is not definitive. Firstly, the non-common path error arising from the difference in optical path between the metrology lasers and the white light source (tungsten bulb) is negligible because both light sources originate from the same pin hole and their fringes are recorded with the same photo-detectors. Secondly, the position of the linear stage on which the DDL is mounted varies due to changes in internal (electronics) and external temperature but this variation is measured by the SL metrology system and corrected for in all the tests. The low duty cycle (<5%) motion pattern of the DDL (the ratio between the time spent

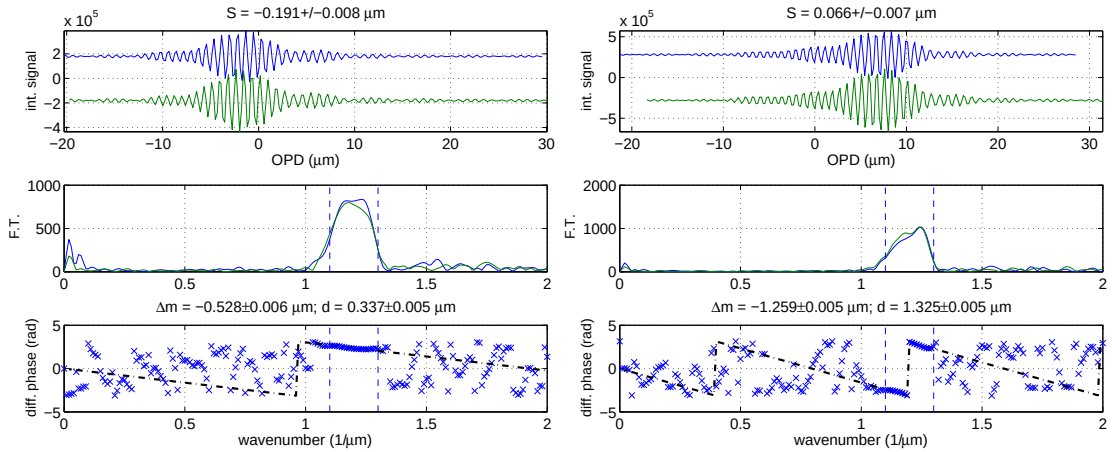

(a) Achernar

(b) Achernar

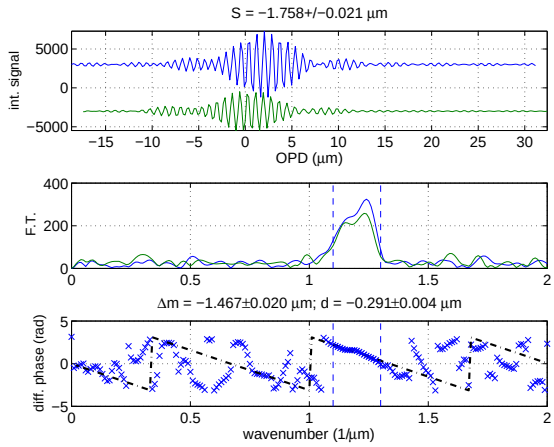

(c) β Lupi

Figure 7.4: Similar to Fig. 7.1(a) but single stars replaced the tungsten bulb as light sources. DDL in MUSCA was displaced after each fringe packet is recorded. The amount of displacement as measured by the DL metrology is indicated above the bottom panel of each sub-figure.

slewing the stage to idle) during the above tests and observations ensured no excessive heat is generated by the motor driving currents in the electronics (Zaber, 2006). Lastly, there were no obvious changes in the structure of the metrology laser pupils that could have altered the phase of the laser fringes. Images of the laser pupils as seen with the MUSCA alignment CCD camera are shown in Fig. 7.5. The structures in the pupils originate from spurious reflections off the back side of the M16 dichroic filters, which are fabricated on 6mm thick parallel glass windows (wedge angle of $\lesssim 30''$). The pupils of the green and red lasers are not identical and are labeled in the figure as "G" and "R" respectively. Neither are the pupils of the North and South beams identical. The exact cause of the observed asymmetries is uncertain but are probably due to the fabrication process. These structures are neither observed with the internal WL source, the IR LEDs at the siderostats (see Fig. 3.5(b)) nor starlight. The structures within the laser pupils are not expected to change because the spurious reflections occur before the laser beams enter into MUSCA (see Fig. 3.2(a) and 3.3(a)) and Fig. 7.5 clearly shows this. Due to the presence of such structures, the probability of unsuspectingly altering the phase of the laser fringes is not zero. The spatially modulated fringes across the laser pupils are sensitive to the differential tilt of the original and the displaced laser beam. Changes in the fringe pattern can alter the total intensity recorded by the MUSCA APDs at a given scan step and eventually the phase of the metrology fringes.

7.1.3 β Crucis

β Crucis (HR4853) is a suspected spectroscopic binary, of which a previously unresolved secondary component (β Crucis B) is thought to make a complete orbit around the primary component (β Crucis A) every 5.0 years (Aerts et al., 1998). With an estimated apastron[2] distance of $\sim$12AU (Aerts et al., 1998) and a parallax of 11.8mas (van Leeuwen, 2007), the separation between the primary and the secondary component is estimated to be less than $0.14''$ (assuming the orbital plane is face-on). On the other hand, the minimum separation of the pair is difficult to estimate because it depends on the orientation of their orbital plane with respect to the plane of the sky.

β Crucis is one of the preferred fringe-finding stars at SUSI because it is bright ($m_V \approx 1.3$) and it reaches a maximum elevation of $\sim 60^\circ$ in the sky. Fringe-finding stars are used to find the offset position (difference between the expected and the actual position) of the stellar fringes at the start of an observation session so as

[2]A phase in a Keplerian orbit where the secondary component is at its furthest distance from the primary star

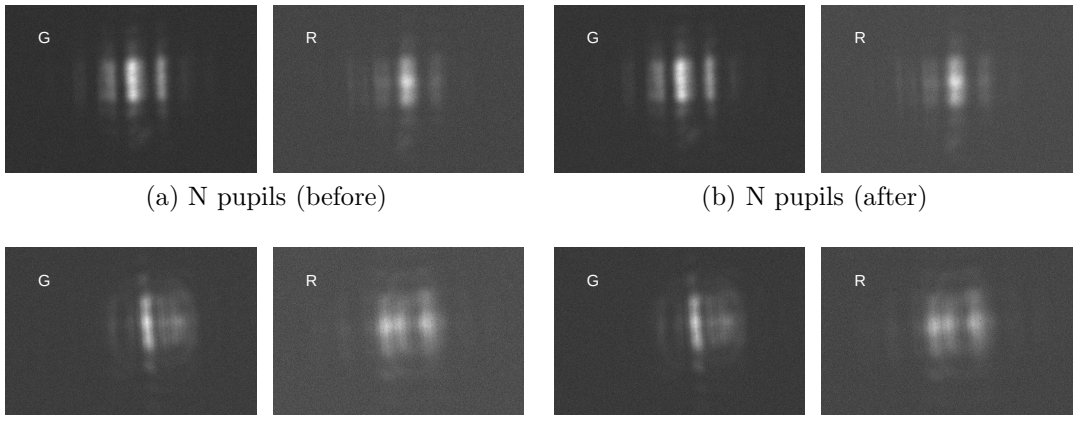

(a) N pupils (before) (b) N pupils (after)

(c) S pupils (before) (d) S pupils (after)

Figure 7.5: Images of the green (G) and red (R) laser pupils as seen with the MUSCA alignment CCD camera. The spatially modulated fringes like structures seen across the pupils are caused by overlapped and displaced pupils from spurious reflections off the back side of the M16 dichroic filters. The structures are not identical between the North (N) and the South (S) pupils because the 6mm parallel glass windows the dichroic filters were fabricated on most probably have different reflectivity profile (exact cause was not investigated). More importantly the structure within the pupils remains unchanged after the DDL is displaced and then slew back to its original position. This result is expected because the spurious reflections occur before the laser beams propagate into MUSCA and through the DDL.

Table 7.3: Successful observations of β Crucis

Date	Baseline	Range of HAs (Hr)	Calibrators
120515	N1-S2	-0.9 – -0.3	Del Cru
130529	N4-S3	-1.9 – -0.9	Del Cru
130624	N4-S3	-0.7 – 0.6	Del Cru, Lam Cru
130720	N3-S3	2.8 – 3.3	Bet Lup
130726	N4-S2	1.7 – 4.2	Del Cru

N1-S2=10m, N3-S3=40, N4-S2=60m, N4-S3=80m

to facilitate fringe-finding of fainter stars throughout the session. As a result, there are many observations of β Crucis with PAVO since 2009 taken mainly by Ireland and Rizutto but most of them are with short baselines (<40m) and none has successfully resolved the binary which reduces the estimated maximum binary separation to less than 3mas (mean wavelength of PAVO, $\sim$0.6μm, over a maximum of 40m baseline).

β Crucis was observed with MUSCA between 2012 and 2013. Table 7.3 lists some of the more successful observations of β Crucis with MUSCA as well as PAVO during this period of time. At first, it was mainly used as a target for testing the self-phase-referencing mode of the instrument and the data reduction pipeline but it later became a target for PAVO to resolve the secondary component with long baselines.

At short baselines, the phases of the β Crucis A fringe packets recorded with MUSCA show the stability performance of a single star. This is expected from an unresolved binary star. Fig. 7.6(a) shows the relative position of the fringe packet recorded with a 10m baseline over time. However, at longer baselines (e.g. 30m and above) the fringe packet registers discrete jumps of about one MUSCA wavelength in its relative position. These jumps occur within time intervals that are too short for an unresolved secondary fringe packet to drift by the same amount. Plots in Fig. 7.6(b)-(c) show the jumps at hour angles (HA) of $\sim$3.2 and $\sim$2.1 respectively. Despite the one wavelength jump the alignment of the fringe phases is still better than 1/10th of a wavelength ($\sim$0.6 radian). Table 7.4 lists the relative phase of the fringe packets whose relative positions are plotted in Fig. 7.6. Examples of the fringe phase alignment between a reference fringe packet and the fringe packet that registers the relative position jump are shown in Fig. 7.7(a) and (c). Also shown in the figure are plots of reduced χ^2 values versus possible relative fringe packet positions for respective pairs. Details regarding the reduced χ^2 value are discussed in Section 6.2.2. The relative position with the lowest χ^2 number best

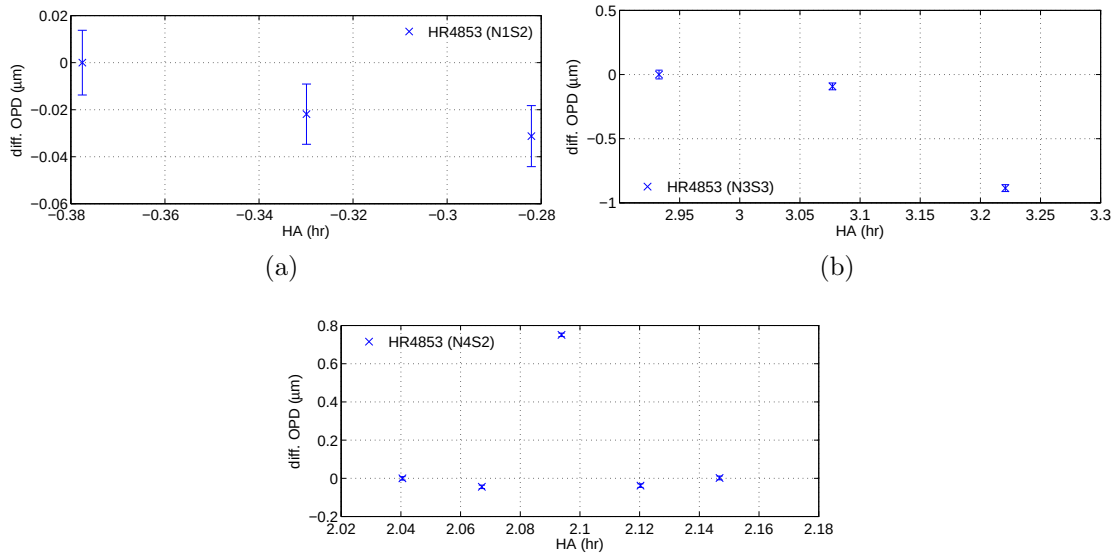

Figure 7.6: Fringe packet separations of the pairs of fringe packets of β Crucis A recorded at different times and with different baselines (indicated in parentheses in the legends of the plots). The jumps in the relative position of the fringe packet due to the presence of an unresolved secondary fringe packet are visible in (b) and (c). The nominal length of the N1S2, N3S3 and N4S2 baselines are 10m, 40m and 60m respectively.

describes the separation of the fringe packet with respect to the reference fringe packet. It is also obvious from the reduced χ^2 plots that the next best relative position is close to zero which is the expected value if the unresolved secondary fringe packet is absent.

The origin of the fringe packet position jump observed with β Crucis A can be traced back to the method the phase delay was computed from the PAVO interferograms. Phase delays are computed from group delays which in turn are estimated from the position of the peak of the Fourier transform of the complex visibility of the fringes across the PAVO bandpass. The detailed description of this algorithm is given in Section 6.1.2. A computer simulated example plot of the Fourier transform, $\hat{\mathbf{q}}$ in Eq. (6.6), is shown in the top panel of Fig. 7.8(a). In the example, the fringes are from a single star and the phase delay (indicated by the symbol z in the figure) is zero (within the uncertainty of the algorithm). When fringes from a secondary star are introduced into the simulation, the phase delay of the fringes from the primary star will be altered depending on the fringe separation and the visibility of the secondary star fringes. Similar example plots

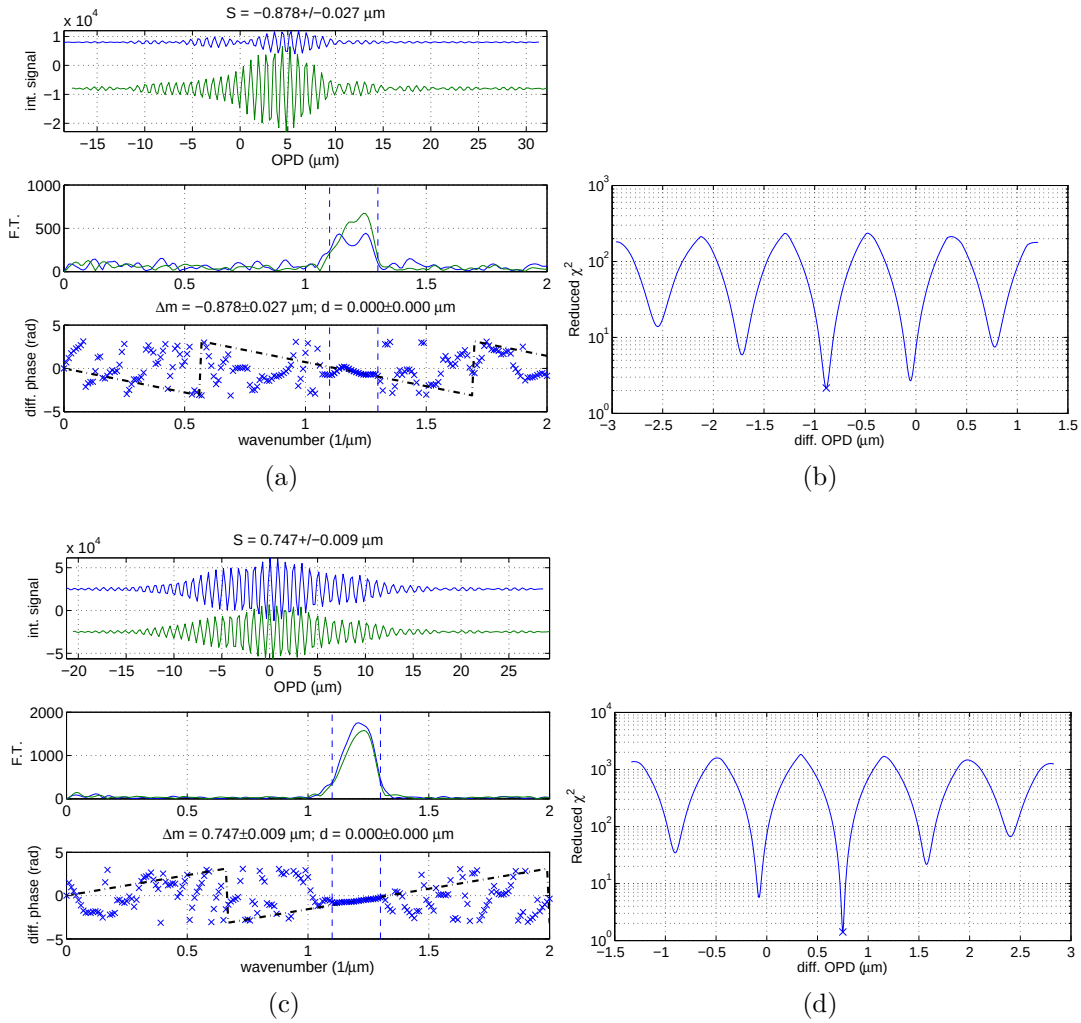

Figure 7.7: The description for plots in (a) and (c) is similar to the description for Fig. 7.1(a) but the fringe packets here are of β Crucis A. Plots in (b) and (d) are the reduced χ^2 values of various possible relative positions of the fringe packets. The relative position with the lowest χ^2 is usually but not always taken as the true value. In the case of (b) and (d), the expected true values are closer to zero.

Table 7.4: Phase stability of fringes of β Crucis A in MUSCA

Related Figures	Differential Phase (rad)
Fig. 7.6(a)	-0.17±0.10 -0.24±0.10
Fig. 7.6(b)	-0.70±0.20 -0.39±0.20
Fig. 7.6(c)	-0.34±0.07 -0.62±0.07 -0.29±0.07 0.02±0.08

of $\hat{\mathbf{q}}$ when PAVO interferograms consist of fringes from two stars are shown in the middle and bottom panels of Fig. 7.8(a). Different values of fringe separations, indicated by the symbol S in the legend, are chosen in order to illustrate the effect of additional fringes on the phase delay of the primary. The ratio of the visibility of the two sets of fringes in the plots is chosen to be 0.9. The position of the peak of $\hat{\mathbf{q}}$ in the middle panel clearly shows the phase delay deviates from zero. If the phase delay deviates by more than half of a MUSCA wavelength, then the fringe separation computed between the current and a reference MUSCA fringe packet will register a jump of one MUSCA wavelength, a phenomenon observed in Fig. 7.6. The magnitude of the jump for a range of primary-secondary fringe packet separations and visibility ratios is shown in Fig. 7.8(b) and (c). The images in the figure show various locations where phase delay jumps can occur and the grayscale of the image shows the magnitude of the jump in MUSCA wavelengths. Fig. 7.8(c) is a zoomed in version of (b). The latter also shows that the probability of a phase delay jump occurring is zero when the fringe packet separation is larger than $\sim 15\mu$m which is half of the coherence length of one PAVO spectral channel. This is expected because the fringe packets will no longer overlap each other at that separation.

In an attempt to resolve and measure the position angle of β Crucis A-B, PAVO was used to observe the fringe visibility modulation of the fringes. Only two successful observations were made with an 80m baseline (N4-S3). PAVO interferograms are reduced with the PAVO V^2 pipeline (Ireland et al., 2013, in prep.), which produces the square of the fringe visibilities across the PAVO science bandwidth over a range of observation time, $V^2(\sigma, t)$. The visibilities are then calibrated with fringe visibilities from one or several calibrator stars, which were observed before

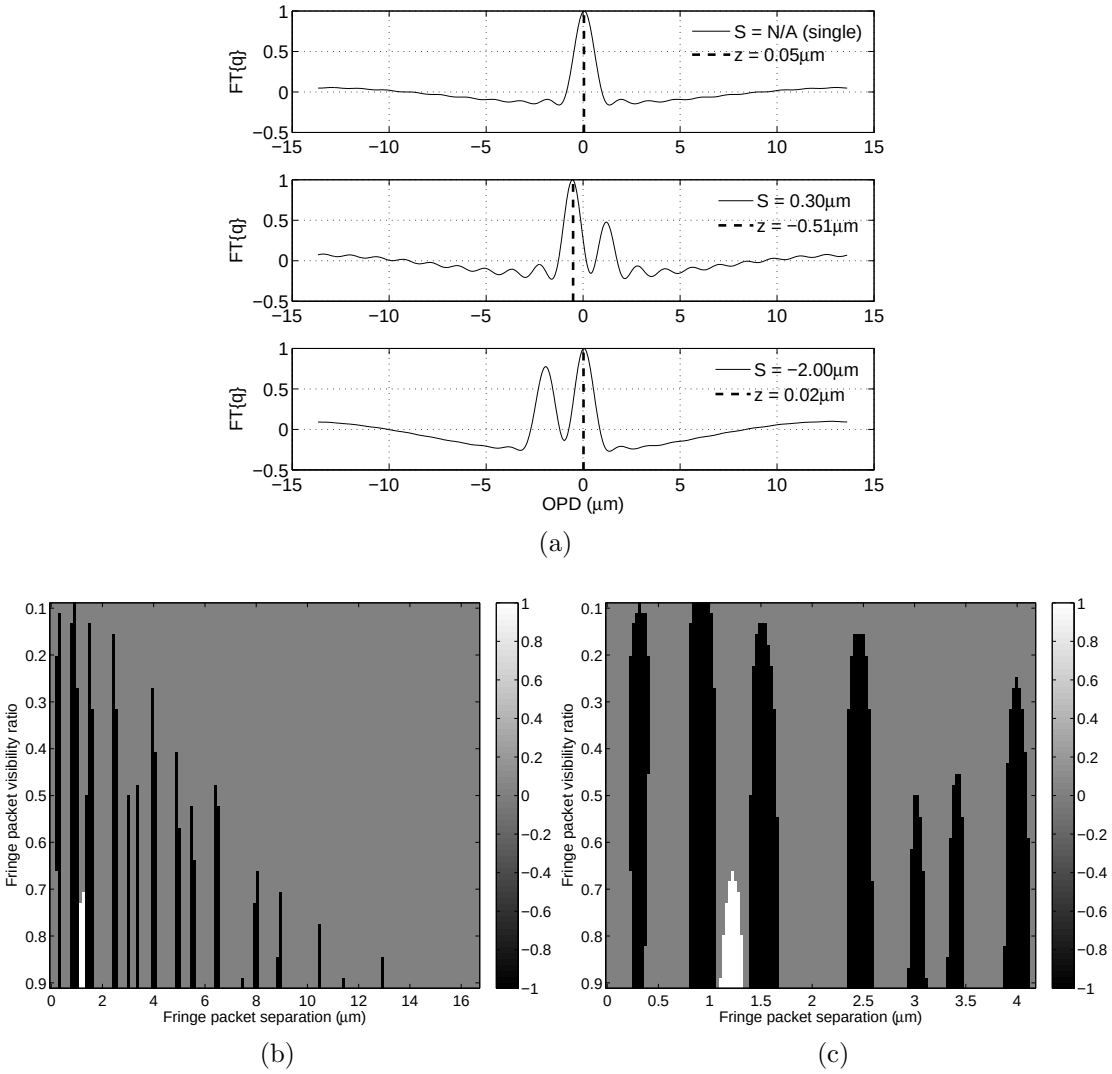

(a)

(b) (c)

Figure 7.8: The plots in (a) show the Fourier transform of the complex visibility, a variable computed in the data reduction pipeline to obtain the phase delay of a set of fringes from the location of the peak in the plots (see Eq. (6.6)). The addition of a second set of fringes at the right fringe separation can artificially shift the peak, thereby resulting in an incorrect phase delay computed for the first. Due to this error, the relative phase delay of the primary fringes between the middle and bottom panels of (a) will wrongly be computed as one MUSCA wavelength despite them being kept unchanged. Plots in (b) and (c) show the relative phase delay error in MUSCA wavelengths for various fringe separations and visibility ratios (primary vs. secondary set of fringes).

Table 7.5: Relative astrometry of β Crucis A-B

Parameter	As fitted	
Epoch	2013.4062	2013.4771
N_{V^2}	37×2	37×3
$\Delta\alpha_{\mathrm{A,B}}$ (mas)	0.29±0.34	-0.46±0.15
$\Delta\delta_{\mathrm{A,B}}$ (mas)	-1.74±0.08	-1.66±0.02
$\rho_{\mathrm{A,B}}$ (mas)	1.76±0.10	1.72±0.05
$\theta_{\mathrm{A,B}}$ ($^\circ$)	171±11	196±5
χ^2_{R}	0.8	1.8

and after the target star. The calibration step using fringe visibilities from single unresolved stars is performed to obtain the loss in visibility due to the instrument and atmosphere and to recover the fringe visibility attributed to the astrophysical source (see Section 2.1). The calibrated visibilities of the target star are used to extract the on-sky separation and position angle of the primary and secondary components by fitting the models in Eq. (2.16), (2.18) and (6.22) to the calibrated data. The brightness ratio, β, is set to 0.1 when fitting the model to the data because the estimated difference in magnitude between the primary and secondary components is ∼2.9 at a mean wavelength of 4430$\mathring{A}$ (Hanbury Brown et al., 1974; Popper, 1968). By fixing the value of β, it ensures the fitting routine does not over fit the astrometric parameters. Fig. 7.9 shows the calibrated square of the fringe visibility and the V^2 model that was fitted to the data. The relative astrometry extracted from the V^2 data is given in Table 7.5. The position angles listed in the table have an ambiguity of 180° because this method is unable to determine the position of individual fringe packets. The uncertainties of the measurements in the right ascension (RA) and declination (Dec) axes are correlated to the orientation of the projected baseline of the interferometer. In the case of the two observations in Table. 7.5, which were made shortly before and after the star transits, the projected baseline is aligned to the declination axis. Therefore, the uncertainty in the declination axis is small while the uncertainty in the right ascension axis is relatively larger.

While the results in Table 7.5 and in Fig. 7.6 are not obtained on the same night, they describe the same binary pair, β Crucis A-B. The results in Table 7.5 can be used to estimate the fringe packet separations observed in Fig. 7.6 to a first order of approximation since the binary has a relatively long period orbit. Given the on-sky separation and position angle obtained with PAVO, the projected fringe packet separation of the primary and secondary component of β Crucis A-B is estimated to be ∼0.3μm if they are observed with a 40m baseline (N3-S3) and ∼0.4μm

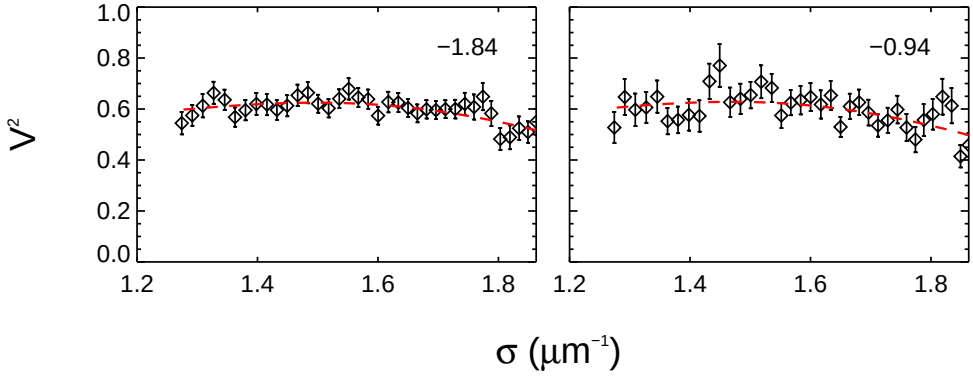

(a) 29 May 2013 (130529)

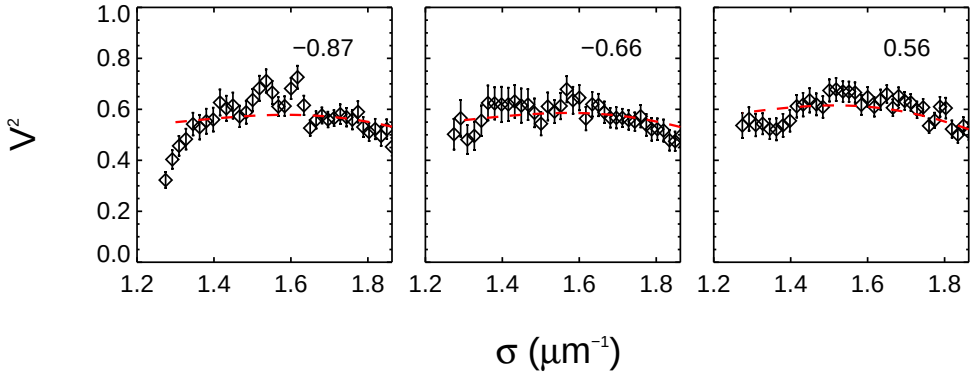

(b) 24 June 2013 (130624)

Figure 7.9: Calibrated V^2 data of β Cru obtained with PAVO and an 80m baseline (N4-S3). Binary star models that best fit the data are plotted as dashed lines. The model is fitted to a set of data from the same night simultaneously. The legend in each plot indicates the hour angle (in hours) the data was taken.

if they are observed with a 60m baseline (N4-S2). According to Fig. 7.8, this range of fringe packet separation lies across a boundary where a phase delay jump can occur. Despite the consistency between the phase delay jump observed with MUSCA and the projected fringe packet separation estimated from the analysis of data recorded with PAVO, it is not definitive to claim that the true projected fringe packet separation lies within the estimated range because none of the PAVO V^2 data recorded with baselines shorter than 80m can be fitted with a binary star model, probably due to the small separation of the binary, and no usable MUSCA data has been recorded with the 80m baseline.

The results in this section suggest that the effects of an unseen secondary fringe packet, that of β Crucis B, caused the systematic error in the relative position of the fringe packet of β Crucis A. In general, if a secondary fringe packet is partially resolved or buried within the primary fringe packet of a binary star, the double fringe packet may not be easily distinguished from the data especially when the integration time is for long enough for the secondary to move by more than one fringe. However, the presence of the secondary fringe packet still affects systematic errors in the astrometry by causing the relative position of the primary fringe packet to fluctuate by one fringe cycle while maintaining good phase alignment. The reduced χ^2 values from a least square fit analysis carried out to determine the relative position of fringe packets can be used to estimate the *correct* position in such circumstances.

7.1.4 δ Orionis Aa-Ab

δ Orionis Aa-Ab (HR1852; Del Ori in Table 8.1) is a close binary star system which has an expected on-sky separation of $0.3''$, a position angle of 131° (WDS, 2013) and an orbital period of 201 years (Mason et al., 2009). The primary component is itself a known eclipsing binary (δ Orionis Aa1-Aa2) which has an orbital period of 5.7 days (Harvey et al., 1987). The primary component is a spectral type O star but it is suspected to have yet another tertiary component of the same spectral type (Mayer et al., 2010; Zasche et al., 2009). Despite the extended astrophysical structure of the primary component, observations of δ Orionis Aa-Ab were attempted because it is one of the stars in the MUSCA science target list which will be discussed in Chapter 8.

δ Orionis Aa-Ab was observed with MUSCA in 2013 as a target for testing the dual-star phase-referencing mode of the instrument as well as the data reduction pipeline. Table 7.6 lists the total number of observations attempted on this ternary system. An observation session is considered successful when there are at least 3 sets of bracketed observations of the secondary fringe packet and a bracketed

Table 7.6: Observations of δ Orionis Aa-Ab

Date	Baseline	Outcome	Range of HAs (hr)	Calibrators
130105	N4-S2	Fail	–	–
130106	N1-S2	Fail	–	–
130107	N4-S2	Success	0.5 – 2.0	Bellatrix
130108	N4-S2	Fail	–	–
130110	N4-S2	Fail	–	–
130111	N4-S2	Success	0.0 – 2.5	Bellatrix
130115	N4-S2	Fail	–	–

N1-S2=10m, N4-S2=60m

observation consists of a well phase-referenced primary fringe packet and then a well phase-referenced secondary packet and finally another well phase-referenced primary fringe packet. Since the time span for phase-referencing one fringe packet typically last about 10 minutes, the success rate of an astrometric observation of a binary system with MUSCA is not high because not only is it highly dependent on good atmospheric seeing, but also the duration of the good seeing. Out of 7 consecutive attempts, 2 successful observations were made.

The PAVO V^2 data from the successful observations were analyzed to evaluate the structure of the primary component. The V^2 data showed no amplitude modulation from the secondary (δ Orionis Ab) fringe packet because the separation of the primary-secondary fringe packet pair ($\sim$35–55μm) is larger than the width of a single fringe packet and hence there is little overlap. However, the presence of incoherent flux from the secondary component limits the maximum V^2 of the primary to $\sim$0.66. Taking this into account, the data when fitted with a simple uniform disk (UD) model suggests that the primary star has an average angular diameter (over two observations) of 1.05$\pm$0.02mas. The data and the fitted models are shown in Fig. 7.10. The estimated UD diameter corresponds to $\sim$48 solar radii ($R_\odot$) at $\sim$212pc (computed from parallax measurement (van Leeuwen, 2007)). This is consistent with the estimated diameters of the eclipsing components (δ Orionis Aa1 and δ Orionis Aa2), which consist of an O-type and a B-type star and have estimated angular diameters of $\sim$30$R_\odot$ and $\sim$10$R_\odot$ respectively (Mayer et al., 2010). Due to such astrophysical structures, the phase of the primary (δ Orionis Aa) fringe packet changes over time as the asymmetry of the structure rotates with respect to the baseline of the interferometer. For the sake of estimating the magnitude of the fringe packet separation of the eclipsing components, the binary separation is assumed to be of the order of the estimated UD diameter, i.e. $\approx$1mas, and the position angle is assumed to be parallel to the

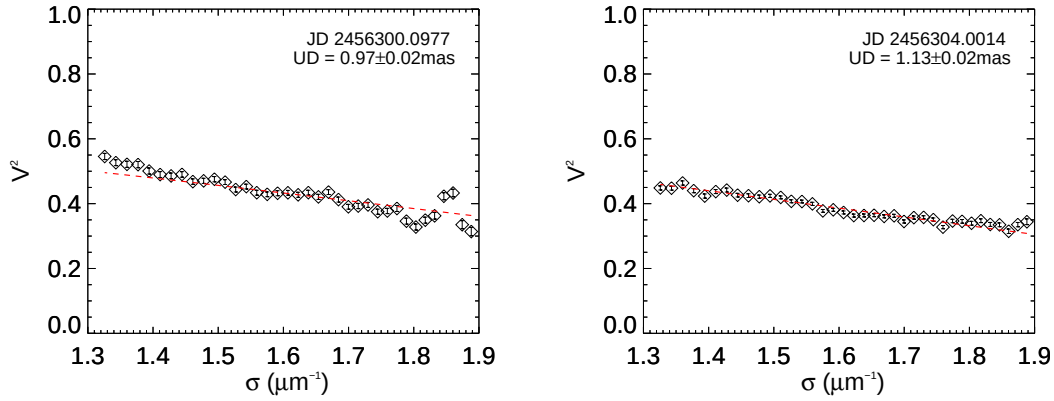

Figure 7.10: Calibrated V^2 data of δ Orionis Aa obtained with PAVO and a 60m baseline (N4-S2). Uniform disk (UD) models that best fit the data are plotted as dashed lines and the UD diameters from the fits are indicated in the plots.

baseline. In this case, the fringe packet separation observed with a 60m baseline (N4-S2) is $\lesssim 0.3\mu$m. Given the sensitivity of the phase delay computation algorithm to a secondary fringe packet at this separation, as discussed in the previous section, the MUSCA measurement of the fringe packet separation of the close binary is anticipated to have one MUSCA wavelength jump.

Fig. 7.11 shows the expected jumps in the relative position between fringe packets of the primary (δ Orionis Aa1) recorded at different times. As shown in the figure, the jumps occur for the primary as well as the secondary (δ Orionis Ab) fringe packets because they were both phase-referenced to the fringes of the primary component. As the fringe packets in the figure are recorded without perturbing the position of the DDL, the phase alignment (see Fig. 6.9) between the fringe packets is measured to be better than 1/12th of a MUSCA wavelength. However, if the DDL is displaced then the phase alignment degrades to as much as 1/4 of a MUSCA wavelength ($\sim$1.5 radian), which is as expected. The latter is shown in Table 7.7 in the form of phase differences between the first and the second primary fringe packet of each bracketed observation.

Fig. 7.12 and 7.13 show the separation between the primary and the secondary fringe packets of δ Orionis Aa-Ab. For each measurement of the fringe packet separation, 3 possible values are plotted. The first is the fringe separation computed from the phase measurement and the remaining two are the computed fringe separation plus and minus one MUSCA wavelength. The reduced χ^2 (also shown in the figures) computed during the least square fitting of the fringe separation to the

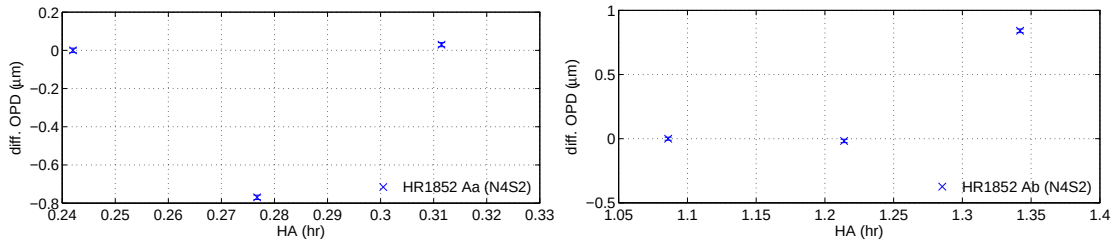

(a) (b)

Figure 7.11: Relative fringe packet position of δ Orionis Aa1 measured at different times showing jumps of one MUSCA wavelength occasionally due to the presence of an unresolved fringe packet of δ Orionis Aa2.

Table 7.7: Phase stability of fringes of δ Orionis Aa in MUSCA

Date	Hour Angle (Hr)	Differential Phase (rad)
130107	0.5	-0.21±0.06
	1.0	-0.33±0.11
	1.8	0.10±0.11
130111	0.1	-0.51±0.07
	1.0	-1.48±0.07
	2.2	-1.28±0.08

measured differential phases of the fringe packets is used to choose one from the 3 possible values that produces the smallest residual when the fringe separation data are fitted with a binary star model. This is done because the fringe separation obtained from the best least square fit may not be the *correct* value as it is ambiguous by one MUSCA wavelength due to the astrophysical effect discussed earlier. The selected data points are indicated in the plots with square symbols. In addition to correcting the one MUSCA wavelength ambiguity, the fringe separation measurements are also empirically compensated for errors arising from the phase delay drift effect and the accuracy of the DL metrology using the phase misalignment measured with the primary fringe packets earlier. Fringe packet separation measurements from the two observations have residuals of less than ∼100nm and the binary star model used for the fit is given in Eq. (2.13)–(2.16). The magnitude of the residuals is consistent with the intrinsic misalignment observed in the internal phase stability test discussed earlier.

The relative astrometry of δ Orionis Aa-Ab obtained from the two observations

Table 7.8: Relative astrometry of δ Orionis Aa-Ab

Parameter	As fitted		Eq=J2000	
Epoch	2013.0178	2013.0287	2013.0178	2013.0287
$\Delta\alpha_{\rm Aa,Ab}$ (mas)	267.6±5.4	252.6±0.8	267.3±5.4	252.3±0.8
$\Delta\delta_{\rm Aa,Ab}$ (mas)	-231.8±0.6	-231.0±0.1	-232.1±0.6	-231.3±0.1
$\rho_{\rm Aa,Ab}$ (mas)	354.0±4.1	342.3±0.6	354.0±4.1	342.3±0.6
$\theta_{\rm Aa,Ab}$ ($^\circ$)	130.90±0.57	132.44±0.09	130.97±0.88	132.51±0.14
$\chi^2_{\rm R}$	35.2	2.3	–	–

is summarized in Table 7.8. Since the position of the vernal equinox, which is the origin of the equatorial coordinate system, changes over time due to perturbation in the Earth's rotation axis, the astrometric parameters in the table are also expressed in an equatorial coordinate system that is based on equinox 2000[3] for comparison with astrometry performed with other techniques and published values in the literature. The coordinate transformation involved took the effect of precession and nutation of the Earth's rotation axis into account.

The binary separations in the declination axis ($\Delta\delta_{\rm Aa,Ab}$) measured on the two different nights of observation differ by less than 1mas, which is consistent with the dimension of the angular diameter of the primary component or the binary separation of δ Orionis Aa1-Aa2. Since the two observations were 3.9 days apart, this consistency is also supported by the orbital period of the eclipsing binary (5.7 days) which suggests the photo center of the primary component could be on opposite sides of the uniform disk on the two nights of observation. On the other hand, the binary separations in the right ascension axis ($\Delta\alpha_{\rm Aa,Ab}$) measured on the two different nights differ by more than 10mas. This discrepancy cannot be an effect of the orbital motion of the secondary component (Ab) around the primary (Aa) because the estimated orbital period for the pair is 201 years (Mason et al., 2009) and the estimated motion within $\sim$4 days is $\ll$0.1mas. It is also unlikely to be an effect of narrow-angle baseline misalignment because in order to produce the astrometric uncertainty ($\sim$10mas over $\sim$260mas of projected separation) obtained from the data analysis the East-West component of the narrow-angle baseline on the two nights must differ by $\sim$30cm, a dimension which is larger than the diameter of the main siderostat mirror. Therefore, the discrepancy in the right ascension axis suggests that there are systematic errors on top of the known phase misalignment which are not accounted for in the data analysis.

[3]The origin of the coordinate system is centered on the position of the vernal equinox in the year 2000

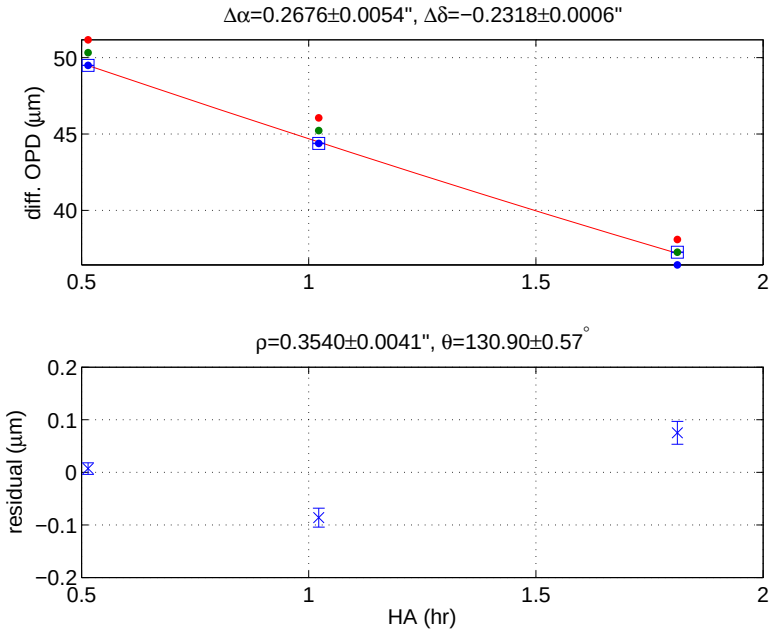

(a)

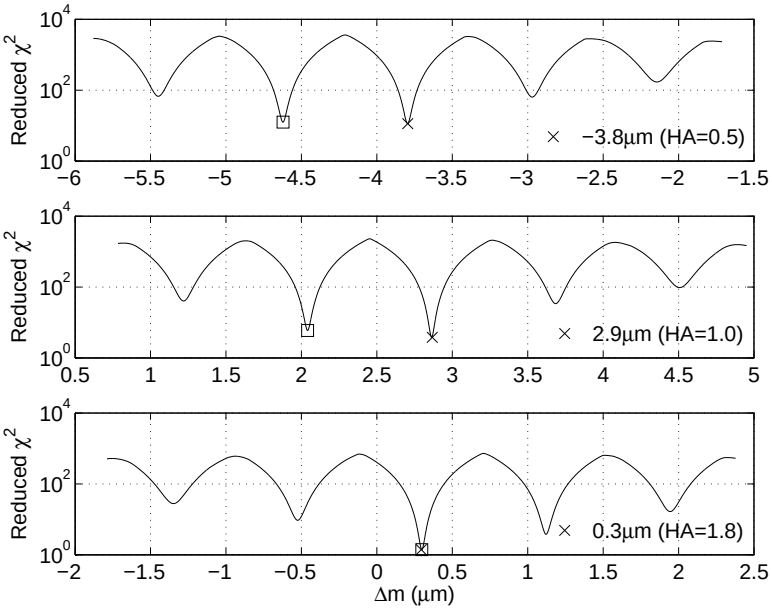

(b)

Figure 7.12: Fringe packet separation of δ Orionis Aa-Ab at different hour angles measured by MUSCA with a 60m baseline (N4-S2) on 7 Jan 2013. Plots in (b) show the reduced χ^2 values of probable apparent separation of the fringe packets. The symbol $\times$ represents the global minimum and the symbol $\square$ represents the most probable value based on the model-fitting in (a).

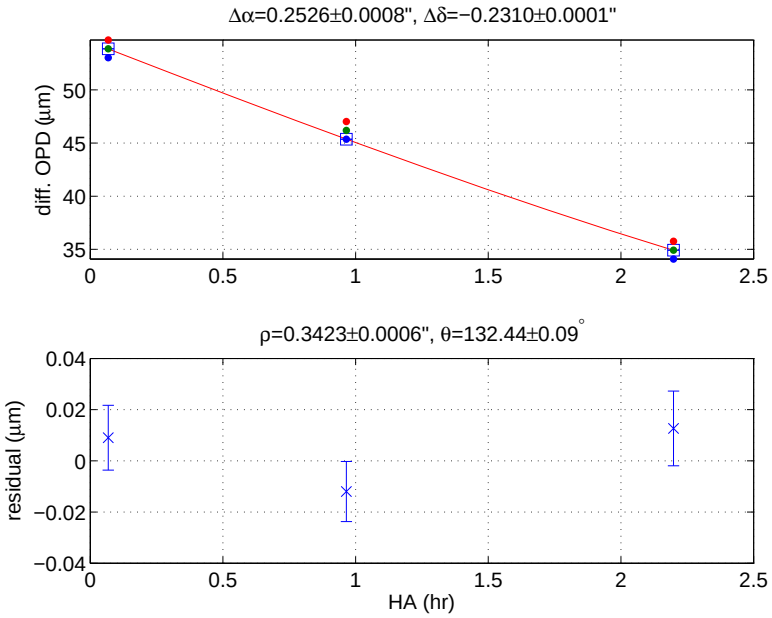

(a)

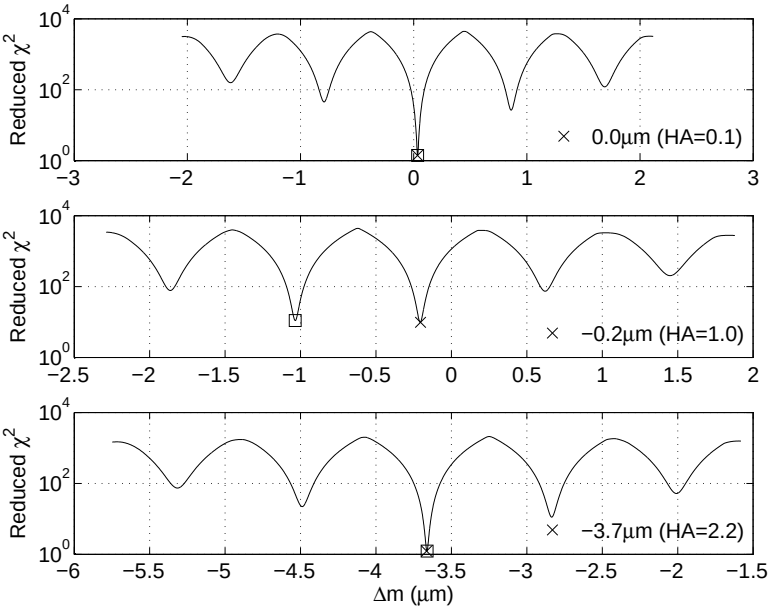

(b)

Figure 7.13: Similar to Fig. 7.12 but with data taken on 11 Jan 2013.

Table 7.9: Comparison of δ Orionis Aa-Ab astrometry.

Source	Epoch (+2000)	θ ($^\circ$)	$\delta\theta$ ($^\circ$)	ρ ($''$)	$\delta\rho$ (mas)
WDS	13.1311	131.0	–	0.3273	0.2
Ephemeris*	13.1000	130	–	0.31	–
This work	13.0287	132.51	0.14	0.3423	0.6
	13.0178	130.97	0.88	0.3540	4.1
MA2010†	08.0449	132.66	0.47	0.325	1.6

*based on a grade 4 orbit from ORB6 catalog

†Maíz Apellániz (2010)

For comparison, measurements of the separation and position angle of δ Orionis Aa-Ab obtained from the Fourth Catalog of Interferometric Measurements of Binary Stars (INT4, 2013) and the Washington Visual Double Star catalog (WDS, 2013) are listed in Table 7.9 and plotted in Fig. 7.14. The measurements obtained in this thesis agree only moderately well (to within $\sim 1^\circ$ in position angle and $\sim 0.02''$ in binary separation) with measurements from the WDS catalog. An ephemeris of the secondary component computed based on parameters from the Sixth Catalog of Orbits of Visual Binary Stars (ORB6, 2013) is also included for comparison.

The results in this section show an attempt to measure the separation and position angle of a close binary star with MUSCA. However, the astrometric accuracy of MUSCA is unclear at this stage because the presence of an eclipsing companion is likely to have changed the photo center of the reference star, δ Orionis Aa, between two observations. Based on a model of this eclipsing binary given by Mayer et al. (2010, Solution III of Table 6), the maximum change in position of the primary star is $\sim$0.06AU or $\sim$0.3mas (assuming their orbits are circular). This change is similar in magnitude to the difference between the two MUSCA observations. Fig. 7.15 shows a visualization of this model using an online eclipsing binary simulator[4]. Therefore, more observations are required in order to ascertain the performance and to further characterize the instrument.

[4]`http://astro.unl.edu/naap/ebs/animations/ebs.html`

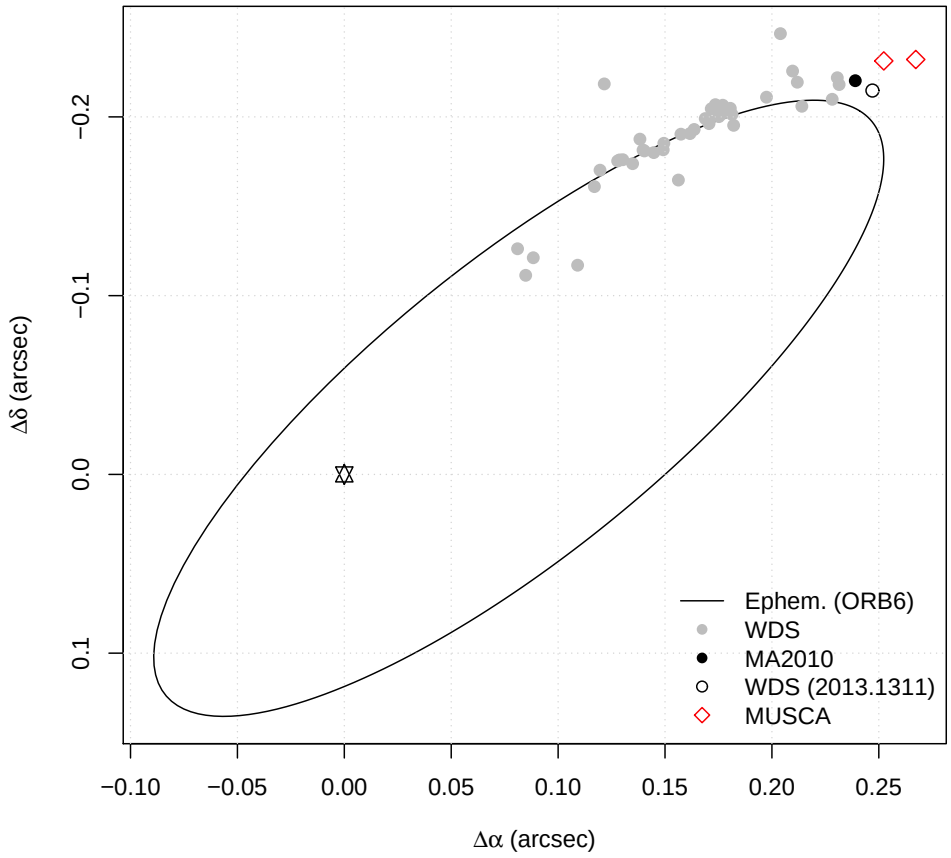

Figure 7.14: Relative position of δ Orionis Aa-Ab. The primary star is positioned at (0,0). The positions of the secondary star measured by various sources are indicated as points in the plot. The ellipse in the plot represents the best estimated orbit of secondary star around the primary. The declination (y-) axis is reversed (pointed downwards) according to the binary star convention.

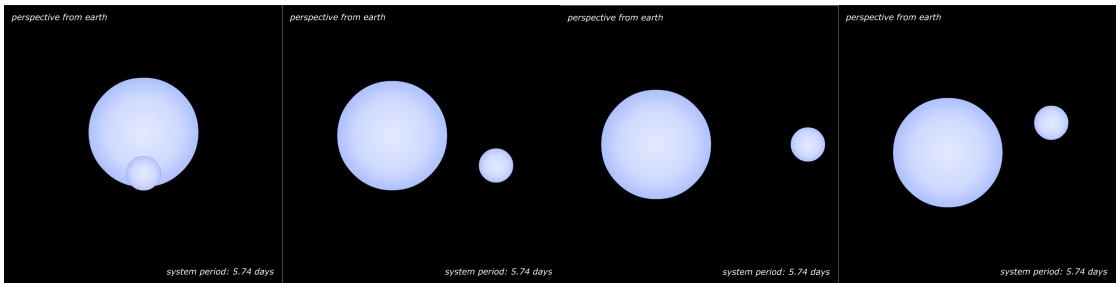

(a) Phase 0/8 (b) Phase 1/8 (c) Phase 2/8 (d) Phase 3/8

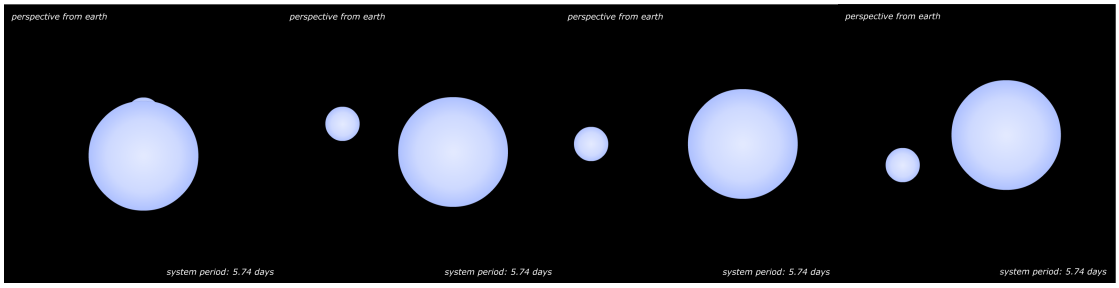

(e) Phase 4/8 (f) Phase 5/8 (g) Phase 6/8 (h) Phase 7/8

Figure 7.15: Computer rendered images showing the eclipse phases of δ Orionis Aa1-Aa2. The parameters used for the rendering is obtained from Mayer et al. (2010, Solution III of Table 6). Each image has a field of view of $\sim$0.6mas.

7.2 PAVO only observations

The current method that MUSCA uses to measure the fringe separation of two closely separated stars has degraded precision when the stellar fringe packets become partially overlapped and start to interact with each other. By interact, it is meant that the visibilities and the phases of the fringe packets are altered due to the in- or out-of-phase addition of fringes from the adjacent stars. In such situations, a more advanced data analysis, e.g. model-fitting the fringes directly (Dyck et al., 1995), or the indirect method which rely on the fringe visibility modulation (see Section 2.4.1) could be used to estimate the separations of overlapping fringe packets accurately.

Each fringe packet in MUSCA has a width of about 10μm, fringe separation measurements of fringe packet pairs that are separated by less than this amount are affected. If a 100m baseline is used, these separations correspond to projected on-sky separations of $>0.02''$. Although stars selected for MUSCA observations have true separations of much greater than $0.02''$, their projected separations may have values less than this limit depending on their positions and position angles on the sky. Binary stars like γ Lupi (Gam Lup) and ζ Sagittarii (Zet Sgr) are good examples. The fringe packet separation of each binary reduces to zero and the pair of fringe packets, which belong to the primary and secondary components, crossover each other when the binary is at a certain elevation on sky. This occurs because the angular separation vector, $\Delta\vec{s}$, defined in Section 2.4, is perpendicular to the baseline vector of the interferometer in used. There are two consequences from such an event. Firstly, MUSCA should avoid observing these binaries during or some period of time before and after the event. Secondly, the fringe packet crossover event gives PAVO an opportunity to observe and perform narrow-angle astrometry on these binaries using the indirect method which otherwise would not be possible due to their wide separation.

This subsection discusses the observations of γ Lupi and ζ Sagittarii with PAVO during and close to their fringe packet crossover events. Table 7.10 shows a list of binary stars which also display such an event at different elevations and times. The hour angles (HA) and elevations of the binary stars are estimated with the N4-S2 baseline but should be within $\pm$5mins and $\pm1^\circ$ for all other SUSI baselines. The local sidereal times (LST) are estimated based on the geographical longitude of SUSI.

Table 7.10: List of binary/multiple stars with fringe packet crossover events observable with PAVO

HR	Name	m_1 (V)	m_2 (V)	$\rho^\dagger$ ($''$)	$\theta^\dagger$ ($^\circ$)	Epoch†	FP crossover event‡ HA (Hr)	LST (Hr)	Elev. ($^\circ$)
1931	Sig Ori	4.07	5.27	0.30	89	2010	-0.1	5.5	62
3786	Psi Vel	3.91	5.12	0.80	103	2010	1.7	11.2	66
3852	Omi Leo	3.52	-	0.60	268	1997	-0.2	9.5	49
4167	p Vel	4.13	5.76	0.40	280	2010	1.3	11.9	66
5089	d Cen	4.64	5.03	0.20	64	2009	-3.7	9.8	44
5477	Zet Boo	4.46	4.55	0.60	290	2010	2.2	16.8	36
5626	Lam Lup	4.43	5.23	0.10	70	2011	-2.6	12.5	55
5776	Gam Lup*	2.95	4.45	0.81	276	2013	0.8	16.4	76
7194	Zet Sgr*	3.27	3.48	0.50	265	2013	-0.7	18.4	81
8368	Del Ind	4.80	5.96	0.10	75	2009	-1.8	20.1	58

†data from WDS (2013), except for Gam Lup and Zet Sgr

‡estimated for SUSI with the N4-S2 baseline

*MUSCA targets

7.2.1 γ Lupi

γ Lupi (HR5776; Gam Lup in Table 7.10) is a triple star system where its primary component (γ Lupi A) is itself a suspected spectroscopic binary (γ Lupi Aa-Ab) (Levato et al., 1987). Its primary and secondary components (γ Lupi A-B) form a visual binary. Apart from the goal of observing the fringe packet crossover event described earlier, observations of this binary system were attempted because it is one of the stars in the MUSCA science target list which will be discussed in Chapter 8. Table 7.11 shows the successful observations of γ Lupi A-B carried out with PAVO and the calibrator stars used for the data analysis.

A brief description of the processing of the PAVO interferograms, which produces a set of calibrated V^2 data, is given in Section 7.1.3. A binary star model (see Eq. (2.18)) is then fitted to each set of calibrated V^2 data (one set per observation) to determine the relative astrometry of the binary star. Comparisons between the two-dimensional V^2 data and the fitted model are shown in Fig. 7.16–7.17 in the form of grayscale images. The grayscale level represents the relative amplitude of V^2 in a given image. Also shown in the figures are cross-sectional plots of V^2 versus wavenumber at different hour angles. In the model-fitting, the parameters β and V_1^2 were allowed to vary but V_2^2 was kept at 1, as the secondary component

Table 7.11: Successful observations of γ Lupi A-B

Date	Baseline	Range of HAs (Hr)	Calibrators
100805	N3-S1	0.99 – 1.50	HR4205, Tet Lup
100806	N3-S1	1.02 – 1.35	13 Sco
100813	N3-S3	0.74 – 1.02	Alf Tel
130705	N4-S2	0.60 – 1.20	Bet Lup, Del Lup

N3-S1=15m, N3-S3=40, N4-S2=60m

is assumed to have an unresolved angular diameter. The accuracy of the values of β, V_1^2 and V_2^2 are less important as far as astrometry is concerned because the sinusoidal component of V^2 depends only on the term ϕ in Eq. (2.19) which is related to the fringe packet separation of the primary and secondary components of the binary. Furthermore, the values of the 3 parameters are sensitive to how well the V^2 data are calibrated.

One drawback of this approach to determine the fringe packet separation indirectly from the modulation of the square of the fringe visibility is that the estimated position angle has a 180° ambiguity. This ambiguity arises because the position of individual fringe packets could not be determined from the visibility modulation. Therefore the position angle extracted from the model fit could either be 96° or 276°, if without any prior knowledge. In the case of γ Lupi, the ambiguity is resolved by cross checking the values obtained with other techniques (e.g. speckle interferometry (Tokovinin et al., 2010)).

Table 7.12 shows the parameters extracted from the model-fitting as well as the number of V^2 data used and the reduced χ^2 of the each fit. The values of reduced χ^2 are larger than one because a binary model is used in the model-fitting despite the primary component has a suspected spectroscopic companion. The discrepancy between the model and data is most obvious (see Fig. 7.17 when HA$\approx$0.79) at a time close to the the instance when the fringe packets cross over because the modulation of the fringe visibility is dominated by the astrophysical feature of the primary component. Nevertheless, the astrometry of the wider pair (γ Lupi A-B) based on the fitting of the sinusoidal component of the V^2 model is still good. The same extracted parameters but expressed in an equinox 2000 equatorial coordinate system are given in Table 7.13. Also given in the table are astrometry from other techniques (mainly speckle interferometry) for comparison. The values reported by Tokovinin et al. (2010) in a series of papers given in the table have systematic errors of $\lesssim$0.5% in binary separation and $\sim$2° in position angle (Hartkopf et al., 2012). Similarly, due to uncertainties in the baseline solutions and the wavelength

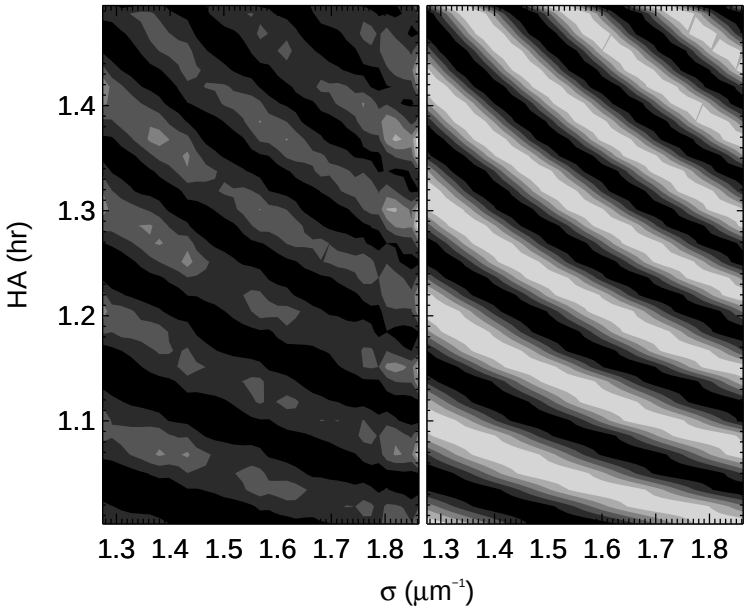

(a)

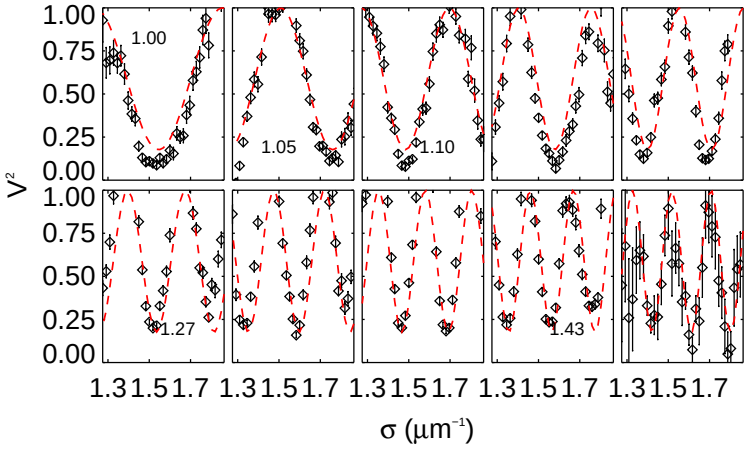

(b)

Figure 7.16: Calibrated V^2 (left panel of (a)) of γ Lupi A-B obtained with PAVO on 5th August 2010 and the best fit binary star model (right panel of (a)). The grayscale in the images in (a) represents the relative amplitude of V^2 within each image. The difference in contrast between the data and model does not represent a discrepancy. Cross-sections of (a) at different hour angles (indicated in the legend) are plotted in (b) as V^2 versus wavenumber with the best fit model represented by the dashed lines.

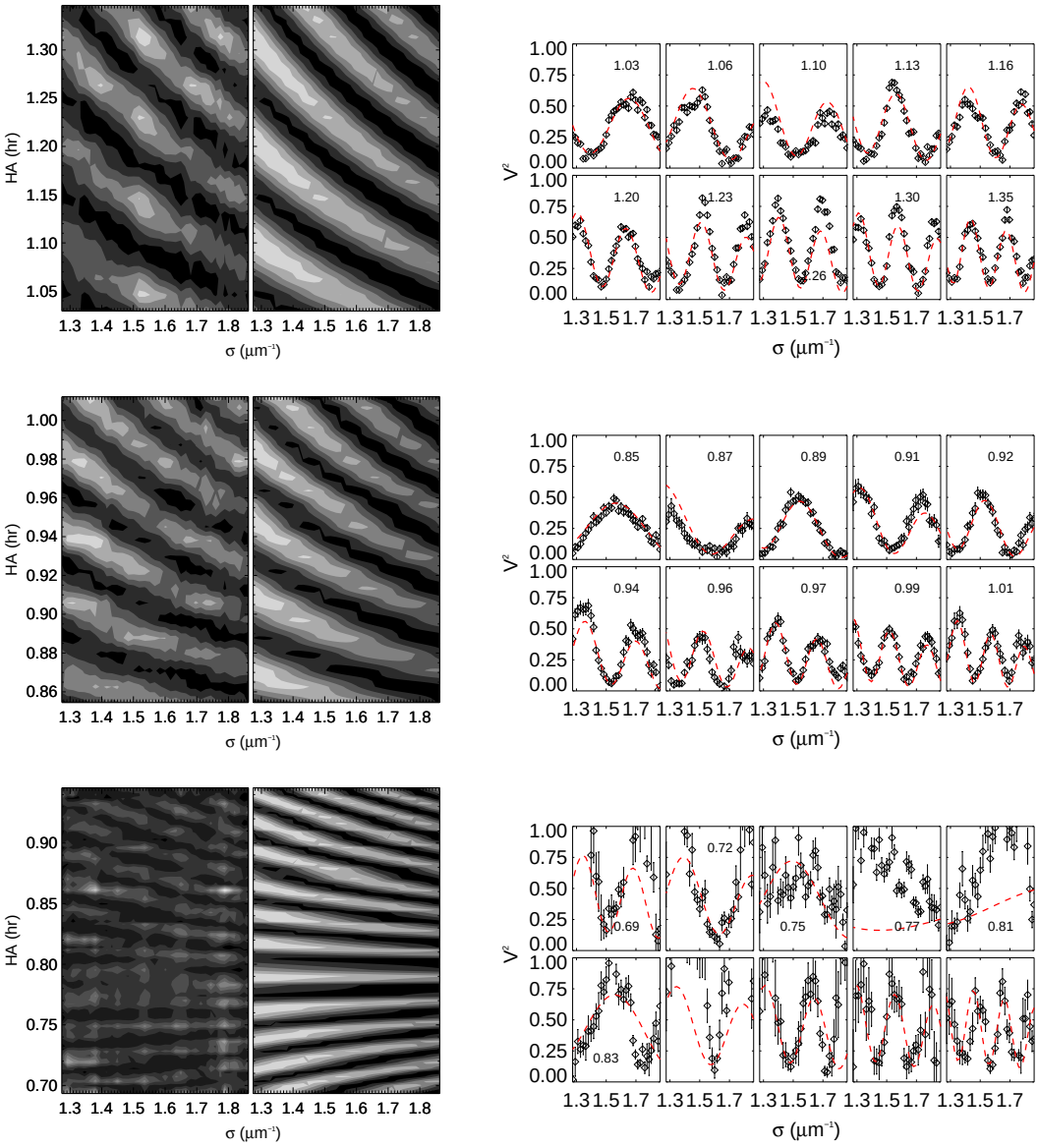

Figure 7.17: Similar to Fig. 7.16 but with data taken on 6th & 13th August 2010 and 5th July 2013 for plots on each row from top to bottom.

Table 7.12: Relative astrometry of γ Lupi A-B

Parameter	2010.5925	2010.5952	2010.6143	2013.5078
N_{V^2}	37×31	37×20	37×31	37×142
LST_X (Hr)	16.371	16.376	16.378	16.374
$\beta_{\mathrm{A,B}}$	0.408±0.001	0.312±0.001	0.304±0.003	0.303±0.004
$\Delta\alpha_{\mathrm{A,B}}$ (mas)	-798.40±0.26	-803.64±0.29	-805.06±0.59	-811.81±0.31
$\Delta\delta_{\mathrm{A,B}}$ (mas)	84.76±0.04	85.82±0.05	85.86±0.07	86.05±0.03
$\rho_{\mathrm{A,B}}$ (mas)	802.9±0.3	808.2±0.3	809.6±0.6	816.4±0.3
$\theta_{\mathrm{A,B}}$ ($^\circ$)	276.06±0.04	276.10±0.04	276.09±0.06	276.05±0.03
χ^2_{R}	32.0	43.5	4.4	9.1

scale used in the data reduction, the binary separation and position angle measurements obtained with PAVO may have systematic errors not reflected in the uncertainty numbers reported in the table. For these observations, instead of using the MUSCA approach optical alignment were carried out with the standard SUSI alignment. The latter typically aligns the apertures of the PAVO 2-hole mask with the pivot points of the siderostats to within 2cm. Assuming this offset is parallel to the *uv*-plane centered on the primary component of the binary star, this translates to a systematic error of $\lesssim 0.08^\circ$ in the position angle measurements. An uncertainty in the baseline solution also translates to an uncertainty in the binary separation but the magnitude is smaller than the effect of an uncertainty in the wavelength scale. The estimated relative uncertainty in the wavelength scale[5] is $\sim$1% ($\sim$6nm over $\sim 0.6\mu$m). Since the relative uncertainty in wavelength scale directly translates to an uncertainty in the projected fringe packet separation measurement the systematic error in the binary separation measurements for γ Lupi A-B is $\sim$8mas ($\sim$1% of $\sim 0.8''$). Therefore the measurements obtained with PAVO are consistent with the values obtained with speckle interferometry (Hartkopf et al., 2012; Tokovinin, 2012; Tokovinin et al., 2010).

The results in this section demonstrate the potential of the fringe packet crossover observation technique in performing high precision astrometry on binary stars which have on-sky separations that are larger than the interferometric field of view (usually defined by the ratio of the width of a fringe packet to the baseline of an interferometer) of a beam combiner.

[5]Based on the typical pixel offset obtained during the PAVO wavelength scale calibration (Ireland et al., 2013, in prep.)

Table 7.13: Comparison of γ Lupi A-B astrometry.

Source	Epoch (+2000)	θ ($^\circ$)	$\delta\theta$ ($^\circ$)	ρ ($''$)	$\delta\rho$ (mas)
TOK2010†	09.2603^y	275.7	0.0	0.8107	0.1
	09.2603^H	275.8	0.1	0.8125	0.3
This work	10.5925	276.01	0.03	0.8033	0.3
	10.5952	276.05	0.04	0.8086	0.3
	10.6143	276.04	0.06	0.8101	0.6
	13.5078	275.99	0.03	0.8170	0.3
HAR2012$^\#$	11.3028^y	275.5	0.2	0.8199	0.2
	11.3028^I	275.5	0.0	0.8197	0.0
TOK2012‡	12.1845^y	275.7	0.0	0.8242	0.1
Ephemeris*	13.5000	276.7	–	0.8271	–

†Tokovinin et al. (2010)

$^\#$Hartkopf et al. (2012)

‡Tokovinin (2012)

*based on a grade 3 orbit from ORB6 catalog

^{y}measured at ∼550nm wavelength

^{H}measured at Hα (∼650nm) wavelength

^{I}measured at ∼770nm wavelength

Table 7.14: Successful and failed observations of ζ Sagittarii

Date	Baseline	Outcome	Range of HAs (Hr)	Calibrators
121003	N3-S1	Fail	2.5 – 3.5	Phi Sgr
130726	N4-S2	Success	-1.0 – -0.3	Phi Sgr

N3-S1=15m, N4-S2=60m

7.2.2 ζ Sagittarii

ζ Sagittarii (HR7194; Zet Sgr in Table 7.10) is a close binary star system which has an expected on-sky separation of 0.5″, a position angle of 265° (ORB6, 2013) and an orbital period of 21 years (De Rosa et al., 2012). The primary component (ζ Sagittarii A) is suspected to have an unresolved companion based on a discrepancy between the observed dynamical mass of the binary and its theoretical mass estimated from mass-magnitude relation (De Rosa et al., 2012). Similar to γ Lupi, this binary system were attempted because it is one of the stars in the MUSCA science target list which will be discussed in Chapter 8.

Table 7.14 shows the number of observations attempted on this binary system. Despite being unsuccessful, the observation in 2012 hinted at the presence of a tertiary component because the PAVO V^2 data did not show any modulation and the fringe visibility was low, even with a short baseline. A successful follow up observation in 2013 resolved the tertiary component (ζ Sagittarii Ab).

Fig. 7.18 shows the calibrated V^2 data obtained from the observation and the model that best fits the data. The high frequency modulation is contributed by the primary-secondary (ζ Sagittarii Aa-B) pair while the low frequency modulation is contributed by the primary-tertiary (ζ Sagittarii Aa-Ab) pair. The V^2 model of a triplet (Tango, 2006) used to fit the data is,

$$V^2_{1,2,3} = \frac{1}{(1+\beta_2+\beta_3)^2} \left\{ \begin{array}{l} V_1^2 + V_2^2\beta_2^2 + V_3^2\beta_3^2 \\ +2\sqrt{V_1^2V_2^2}\,\beta_2\cos\phi_{1,2} + 2\sqrt{V_1^2V_3^2}\,\beta_3\cos\phi_{1,3} \\ +2\sqrt{V_2^2V_3^2}\,\beta_2\beta_3\cos(\phi_{1,2}-\phi_{1,3}) \end{array} \right\}, \quad (7.1)$$

where V_i^2 are the visibility squared of the fringes of the individual component stars, β_i is the brightness ratio of the secondary or the tertiary component with respect to the primary, and,

$$\begin{aligned} \phi_{1,2} &= 2\pi\sigma\Delta\vec{s}_{1,2}\cdot\vec{B}, \\ \phi_{1,3} &= 2\pi\sigma\Delta\vec{s}_{1,3}\cdot\vec{B}. \end{aligned} \quad (7.2)$$

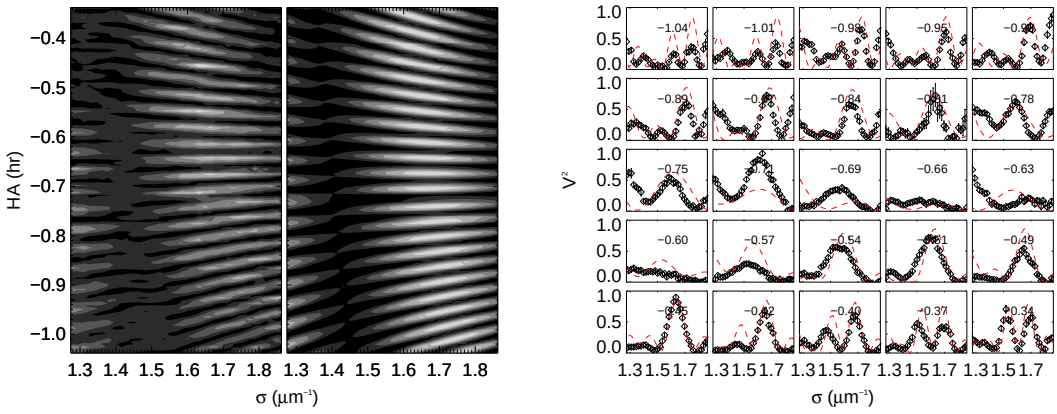

(a) (b)

Figure 7.18: Calibrated V^2 (left panel of (a)) of ζ Sagittarii obtained with PAVO on 26th July 2013 and the best fitted ternary star model (right panel of (a)). The grayscale in the images in (a) represents the amplitude of V^2. The high and low frequency modulations are associated with the Aa-B and Aa-Ab component pairs respectively. Cross-sections of (a) at different hour angles are plotted in (b) as V^2 versus wavenumber with the best fitted model represented by the dashed lines. Discrepancy between the best fitted model and the data as seen in some of the panels in (b) suggests additional astrophysical structures which are not included in the triplet model.

The subscript of $\Delta\vec{s}$ represents the pair of component stars the vector is related to. The remaining symbols in the equation are defined earlier in Chapter 2. The astrometric parameters extracted from the model-fitting are listed in Table 7.15. Also included in the table are astrometry from published work and ephemeris of the wider component pair for comparison. Although the statistical uncertainties of the parameters shown in the table are small, the true astrometric precision is limited by the systematic errors discussed in previous section. The estimated systematic errors in binary separation measurements are ∼5mas (∼1% of ∼0.5″) for the Aa-B pair and ∼0.08mas (∼1% of ∼0.008″) for the Aa-Ab pair. The estimated systematic error in position angle measurements is ∼0.02° (the angle subtended by ∼2cm at a distance of 60m).

Besides the newly resolved component star, the results in this section further demonstrate the potential of the fringe packet crossover observation technique in performing high precision astrometry on close binary stars.

Table 7.15: Relative astrometry of ζ Sagittarii

Parameter	As fitted	Eq=J2000		
Source	This work	This work	Ephemeris*	DRS2012†
Epoch	2013.5654	2013.5654	2013.5	2011.31
N_{V^2}	37×126	–	–	–
LST_X (Hr)	18.396	–	–	–
$\beta_{\mathrm{Aa,B}}$	0.847±0.002	–	–	–
$\beta_{\mathrm{Aa,Ab}}$	0.778±0.002	–	–	–
$\Delta\alpha_{\mathrm{Aa,B}}$ (mas)	-501.36±0.02	-501.20±0.02	–	–
$\Delta\delta_{\mathrm{Aa,B}}$ (mas)	-42.610±0.002	-43.213±0.002	–	–
$\Delta\alpha_{\mathrm{Aa,Ab}}$ (mas)	4.11±0.02	4.10±0.02	–	–
$\Delta\delta_{\mathrm{Aa,Ab}}$ (mas)	6.537±0.002	6.542±0.002	–	–
$\rho_{\mathrm{Aa,B}}$ (mas)	503.17±0.02	503.06±0.02	500	304±4
$\theta_{\mathrm{Aa,B}}$ (°)	265.142±0.004	265.072±0.004	265	285.59±0.17
$\rho_{\mathrm{Aa,Ab}}$ (mas)	7.72±0.01	7.72±0.01	–	–
$\theta_{\mathrm{Aa,Ab}}$ (°)	32.1±0.2	32.1±0.2	–	–
χ^2_{R}	57.8	–	–	–

*based on a grade 1 orbit from ORB6 catalog

†De Rosa et al. (2012)

7.3 Discussion and summary

The observational results shown and discussed in this chapter demonstrate the current astrometric performance of MUSCA as well as an alternative astrometric observation method with PAVO. The latter, which is suitable when MUSCA is not, has the potential for achieving similar level of astrometric precision as MUSCA. At the time of writing, none of the close binary systems observed for performance testing, either with MUSCA or PAVO, consists of just 2 component stars. More MUSCA observations, especially with targets that do not have spectroscopic companions, and data analyses are needed to understand the source of the systematic errors in MUSCA which may or may not be related to the differential delay line and the dual-laser metrology. In that aspect, the low success rate of a MUSCA observation is a challenge that must be overcome especially for future observation campaigns. The initial performance of MUSCA has been demonstrated, one new companion star has been resolved and a preliminary astrometry for another suspected companion star was estimated during the course of testing the instrument.

Chapter 8

Exoplanet detection limits of MUSCA

This chapter describes a forecast of the number of exoplanet detections MUSCA can achieve given its current as well as targeted performance. Simplistic models based on astrophysical parameters of an individual star are used to estimate the probability of detecting an exoplanet around that target star in a binary system. Finally, an overall probability of exoplanet detection is given.

8.1 MUSCA target stars

MUSCA is a companion instrument and cannot operate standalone even in a non-astrometric mode, as PAVO is needed for tip-tilt correction. It relies on PAVO to track and keep the stellar fringes visible within the range of its scanning mirror. Therefore, the binary stars that are observable with MUSCA must be first and foremost observable with PAVO. Using this and several other criteria listed below, a list of target stars is built for PAVO+MUSCA astrometric observations by querying the well maintained and daily updated Washington Visual Double Star Catalog (WDS, 2013).

- Magnitude of the primary star in V-band, $m_{V,1} \leqslant 3.5$[1]
- Magnitude of the secondary star in V-band, $m_{V,2} \leqslant 6.0$
- Angular separation of the primary and secondary stars, $0.02'' \leqslant \rho < 2''$

[1]The current limit for PAVO to lock-on to the fringes continuously for at least 60ms at long baselines.

- Declination of the primary star, $\delta \leqslant 15^{\circ}$

The magnitude of the primary component is limited by the ability of PAVO to track the stellar fringes at long baselines. At the peak of its performance PAVO is expected to be able to fringe-lock on a 5th magnitude star during good atmospheric seeing. However in practice this has not been achieved especially in typical seeing conditions. Therefore, a limiting magnitude of 3.5 is used to select brighter stars as first priority targets for the discussion in this chapter. The complete list which consists of binary stars with primary components as faint as 5th magnitude is given in Appendix F. The brightness limit of the secondary star is set by MUSCA's photon counting noise and is currently estimated to be ∼6.0 which is an optimistic limit. The upper limit of the angular separation of the binary star is determined by the field of view of SUSI while the lower limit ensures the dual fringe packets of the binary remain separated with baselines up to 100m long. The last constraint is set by the geographical location of SUSI.

The number of first priority stars, based on the above constraints, is 14 and the list is given in Table 8.1. This number would grow to 43 if the constraint for $m_{V,1}$ is increased to 5. The full list is given in Table F.1. Fig. 8.1 shows the distribution of relevant physical parameters of binary stars in the MUSCA target list given in Table. 8.1 and Table F.1. The orbital parameters in the figure, namely $a_{\rm crit}$ (defined in next section) and periastron distance, are computed from the orbital elements of the binary stars. Out of the 14 targets in Table 8.1, 11 have known orbital elements better than grade 5. In the full list, 30 binary stars have known orbital elements. The orbital elements were obtained from the Sixth Catalog of Orbits of Visual Binary Stars (ORB6, 2013) and the grade indicates the reliability of the orbital elements with grade of 1 being definitive and 5 having intermediate reliability.

8.2 Types of exoplanet orbits

Exoplanets around binary stars can have 3 types of orbits, i.e. S-type (satellite-type, circumprimary or circumsecondary orbits), P-type (planet-type, circumbinary orbits) and lastly L-type (Librator-type, in which the planet librates around a stable Lagrangian L4 or L5 point for a binary with mass ratio, $M_{\star,1}/(M_{\star,1} + M_{\star,2}) < 0.04$) orbits (Dvorak, 1986). For the type of binary stars observable with MUSCA, exoplanets with P-type orbit will have orbital periods much longer than a typical observation campaign. No exoplanet search campaign to date has carried out more than 20 years of observation (Cumming et al., 2008, 1999; Marcy et al., 2005). Exoplanets with L-type orbits are not only rare, since there is no

Table 8.1: List of *selected* binary/multiple stars observable with MUSCA

HR	Name	$m_{V,1}$	$m_{V,2}$	$\rho^{\dagger}$ ($''$)	$\theta^{\dagger}$ ($^{\circ}$)	Epoch†	Spectral Type	$\pi^{\ddagger}$ (mas)	Grade*
1852	Del Ori*,[1]	2.41	3.76	0.30	133	2008	B0III+O9V	4.71	4
3307	Eps Car	2.25	3.86	0.50	141	2010	K3III+B2V	5.39	–
3485	Del Vel	1.99	5.57	0.40	280	2012	A1V+F8V	40.49	4
3482	Eps Hya	3.49	5.00	0.30	163	2011	F8V	25.23	1
4819	Gam Cen	2.82	2.88	0.50	335	2007	A1IV	25.06	3
4825	Gam Vir	3.48	3.53	1.60	16	2011	F0V+F0V	85.58	2
5267	Bet Cen*,[2]	0.58	3.95	0.40	204	2011	B1III	8.32	2
5576	Kap Cen	3.34	4.71	0.10	157	2009	B2IV	8.51	–
5776	Gam Lup*,[3]	2.95	4.45	0.80	276	2012	B2IV	7.75	3
5953	Del Sco	2.39	4.62	0.10	14	2010	Be	6.64	2
6084	Sig Sco*,[4]	3.06	5.24	0.50	244	2000	B1	4.68	8
6378	Eta Oph	3.05	3.27	0.60	237	2009	A1IV+A1IV	36.91	2
6556	Alp Oph	2.10	5.00	0.70	238	2009	A5III	67.13	4
7194	Zet Sgr*,[5]	3.27	3.48	0.30	286	2011	A2III	36.98	1

†data from WDS (2013)
‡data from Hipparcos reduction (van Leeuwen, 2007)
*data from ORB6 (2013), 1=definitive, 5=indetermine, 8=interferometry
*primary is a known binary
[1]Mayer et al. (2010)
[2]Davis et al. (2005)
[3]Levato et al. (1987)
[4]North et al. (2007)
[5]this thesis (see Section 7.2.2)

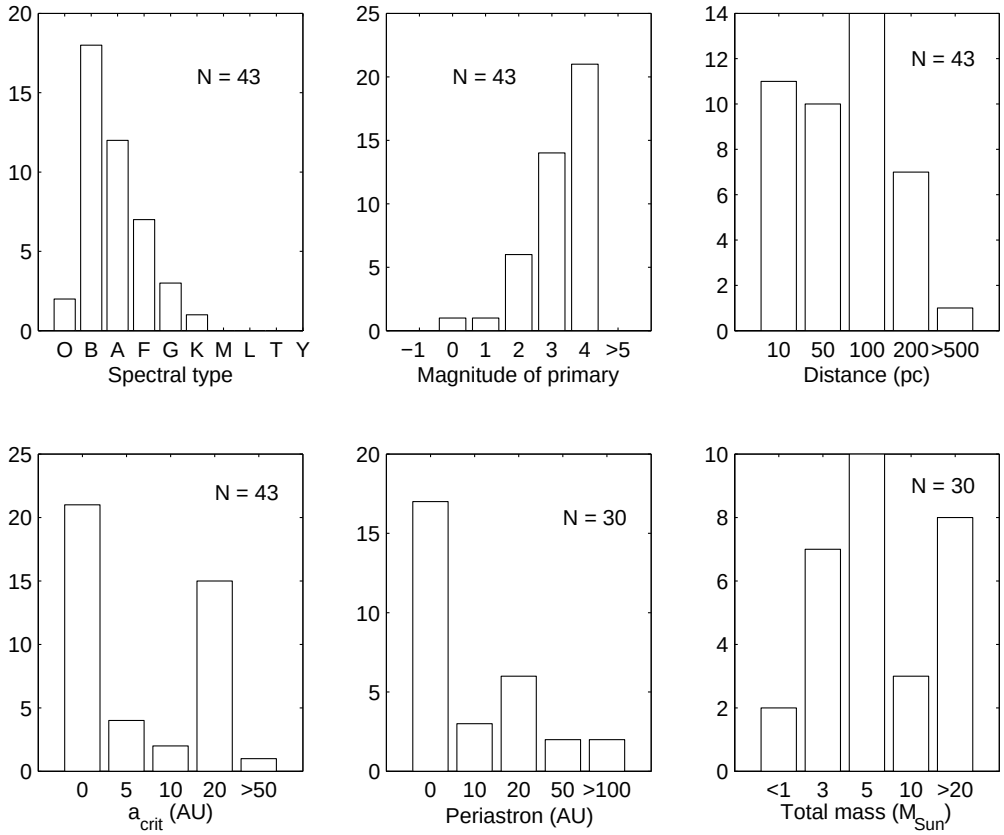

Figure 8.1: Distribution of relevant physical parameters of the binary stars in Table F.1.

observational evidence to date to support the existence of any such orbit, but they are also not detectable by MUSCA or any other astrometric technique. Therefore the detectability analysis carried out for MUSCA and described in the following sections focuses on exoplanets in S-type orbits only.

In the case of S-type orbits, Holman & Wiegert (1999) showed that exoplanets have stable orbits and can survive up to 10^4 orbits around their host stars if their semi-major axes, a_P, are less than a critical value, $a_{\rm crit}$, which is a function of the mass ratio (μ), eccentricity (e_b) and semi-major axis (a_b) of the binary host stars. The mass ratio, μ, is defined as

$$\mu = \frac{M_{\bigstar,2}}{M_{\bigstar,1} + M_{\bigstar,2}}, \tag{8.1}$$

where $M_{\bigstar,1}$ is the host star the planet is orbiting while $M_{\bigstar,2}$ is the other star in the binary system. For a binary system with $0.1 \leqslant \mu \leqslant 0.9$ and $0.0 \leqslant e_b \leqslant 0.8$, the ratio of $a_{\rm crit}$ to a_b was found by Holman & Wiegert (1999) to be,

$$\begin{aligned}\frac{a_{\rm crit}}{a_b} = (0.464 \pm 0.006) + (-0.380 \pm 0.010)\mu + (-0.631 \pm 0.034)e_b + \\ (0.586 \pm 0.061)\mu e_b + (0.150 \pm 0.41)e_b^2 + (-0.198 \pm 0.074)\mu e_b^2.\end{aligned} \tag{8.2}$$

In the following analysis, binary systems with $e_b > 0.8$ are assumed to have $a_{\rm crit} = 0$, that is none are stable.

8.3 Occurrence of exoplanets

The rate of occurrence of exoplanets in wide binary stars is similar to the occurrence in single stars (Bonavita & Desidera, 2007; Kraus et al., 2012; Raghavan et al., 2010) while the rate of occurrence in close binary stars is lower in comparison. Kraus et al. (2012) found that the rate of occurrence of protoplanetary disks, where planets are formed, is statistically lower in close binary systems with projected separation of $\lesssim$40AU as compared to the rate for single stars. This is consistent with the rate found by Bonavita & Desidera (2007), which is a factor of 2 lower for binary systems with a periastron distance of less than 50AU. However, Bonavita & Desidera (2007) have also conservatively estimated the rate to be no more than a factor of 3 lower. Since most of the binary stars in the MUSCA target list have periastron of less than 50AU, a uniform rate of occurrence of exoplanets is used in the detection analysis.

Exoplanets detectable by MUSCA in a 4-year observation period lie in an area of parameter space where the RV method is also sensitive. The plot in Fig. 8.2 which

is discussed in the next section illustrates this. The frequency of exoplanets in this area has been well studied (Bonavita & Desidera, 2007; Janson et al., 2011; Vigan et al., 2012) but has a big spread of values. In a sample of 850 FGK-type stars surveyed by the radial velocity (RV) method, the rate of occurrence of exoplanets per binary system is about 6% for exoplanets with mass of 0.3–1M_J (Jupiter mass) and lies less than 2.5AU away from their host stars (Bonavita & Desidera, 2007). While in another sample of 31 intermediate-mass ($1.5M_\odot \lesssim M_\star \lesssim 2.0M_\odot$) evolved A-type stars surveyed with the same technique, the observed occurrence is 26^{+9}_{-8}% for exoplanets with mass of 0.2–1.3M_J and lies up to 3AU away from their host star (Bowler et al., 2010). An adaptive optics (AO) direct imaging survey of a sample of 42 mainly A-type stars reported an observed rate of occurrence of $8.7^{+10.1}_{-2.8}$% for exoplanets with mass of 3–14M_J and lies within 5–320AU from their host star (Vigan et al., 2012).

Most of the component stars in the MUSCA target list are AB-type stars and belong to the intermediate-mass star category. Most of the binary systems in the list have estimated total mass of more than $3M_\odot$. The rate of occurrence of exoplanets for these type of stars is expected to be higher (about a factor of 2 or more) than the rate of solar type stars. With reference to the reported rates in the 3 examples above, the uniform rate of occurrence of exoplanets in a binary system used in the detection analysis discussed in this chapter, $\mathcal{P}_{\rm occ}$, is 10% (a little less than the mean of the 2 rates mentioned above for main-sequence and evolved A-type stars). For simplicity, the rate is assumed to be uniform across exoplanet mass up to $10M_J$ and across exoplanet distance from host star up to $a_{\rm crit}$ because most of the binary systems in the MUSCA target list have estimated periastron distance of $\lesssim$80AU and factors affecting the occurrence rate of exoplanets around systems with binary separations (or periastron distance) below 50AU are not yet certain due to lack of observation data (Bonavita & Desidera, 2007). The model of $\mathcal{P}_{\rm occ}$ is summarized below:

$$\mathcal{P}_{\rm occ}(M_P, a_P) = 0.1 \quad ; \quad \begin{matrix} M_P < 10M_J \\ a_P < a_{\rm crit} \end{matrix} \tag{8.3}$$

8.4 Probability of exoplanet detections

The probability of exoplanet detection with MUSCA is estimated using the physical parameters of the target stars listed in Table 8.1. The estimation is based on the occurrence rate of exoplanets in binary stars from existing discovery and research, the principle of astrometric detection based on the sensitivity of MUSCA and the duration of an observation program, the location of the planet and the stability its orbit.

8.4.1 Principle of detection

An exoplanet host star exhibits a tiny reflex motion due to the gravitational pull of an orbiting exoplanet. The amplitude of this reflex motion, which is in the order of tens of microarcseconds, is proportional to the semi-major axis of the host star around a common barycenter for the star-planet system, $a_\star$. However, in the case of MUSCA, this should not be confused with the semi-major axis of the binary system, a_b, the host star is also a part of. The orbital parameter $a_\star$ is proportional to the ratio of the mass of the planet, M_P, to the mass of the host star, $M_\star$, and inversely proportional to the semi-major axis of the orbiting exoplanet, a_P.

$$a_\star = \frac{M_P}{M_\star} a_P. \tag{8.4}$$

MUSCA measures the relative position of two stars in a binary system to detect any such reflex motion caused by presence of exoplanets orbiting either star in the system. In order to perform such narrow-angle astrometry, MUSCA is designed to have a maximum angular resolution of 10μas which essentially sets the instrumental limit to the reflex motion detectable by MUSCA. Since angular resolution translates to different physical resolution depending on the distance of the binary star systems, the limit of $a_\star$ detectable depends the distance of the exoplanetary system from Earth. Suppose this instrumental limit is defined as a_{ins}, then,

$$a_{\text{ins}} = 10d \times 10^{-6}, \tag{8.5}$$

where d is the distance of the binary system measured in parsec.

8.4.2 Criteria of detection

In order for an exoplanet of a given mass around a host star to be detectable with astrometry, the semi-major axis of its orbit, a_P, must meet certain criteria. Fig. 8.2 illustrates the limit of a_P from the exoplanet distribution parameter space point of view while Fig. 8.3 illustrates its limit from the physical point of view while. Both figures will be described in the following subsections.

Stable orbit

In order to successfully detect the presence of an exoplanet the planet itself must exist for detection. It must have a stable orbit that lasts as long as the lifetime

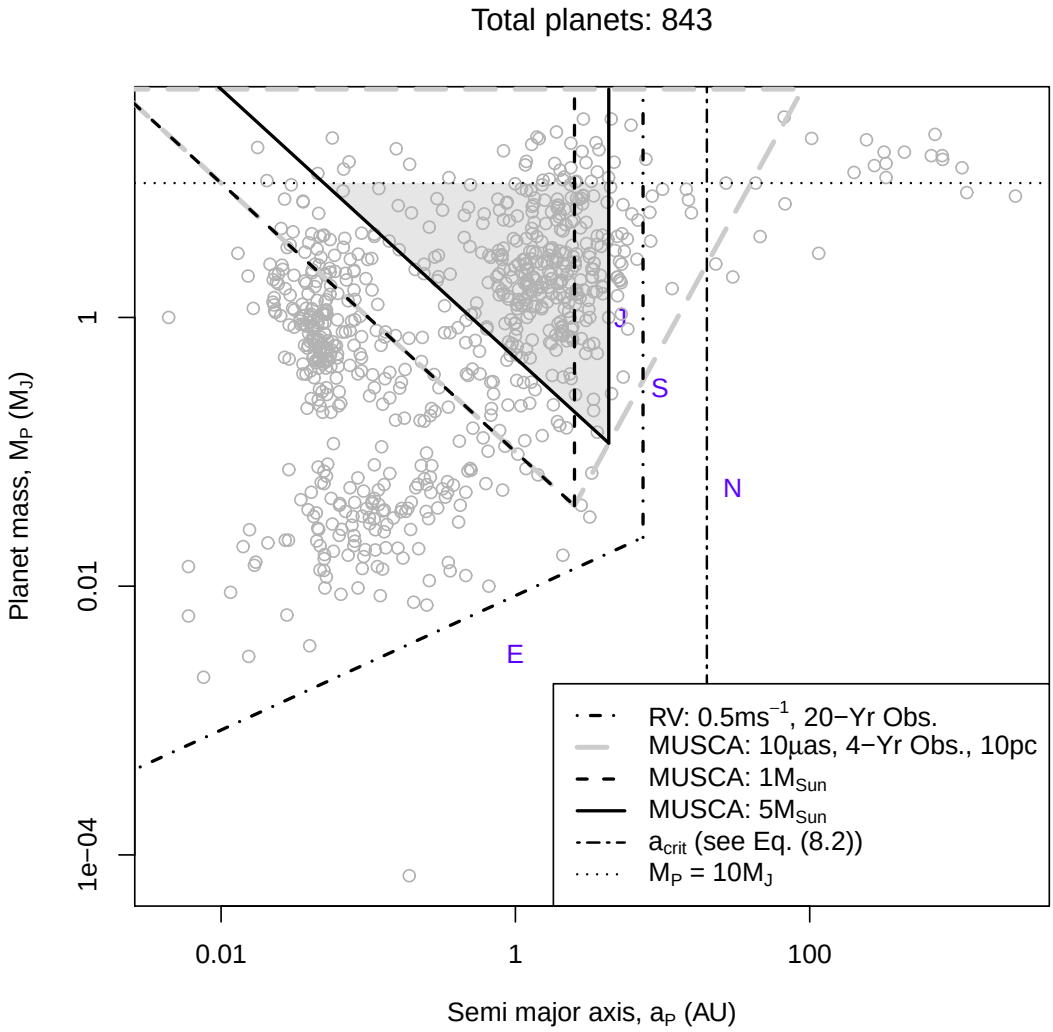

Figure 8.2: The limits of exoplanet detection using MUSCA (or other astrometric technique with similar sensitivity) as compared to the radial velocity (RV) technique. The distribution of exoplanets discovered until October 2012 (gray open circle symbols) is also plotted in the background.

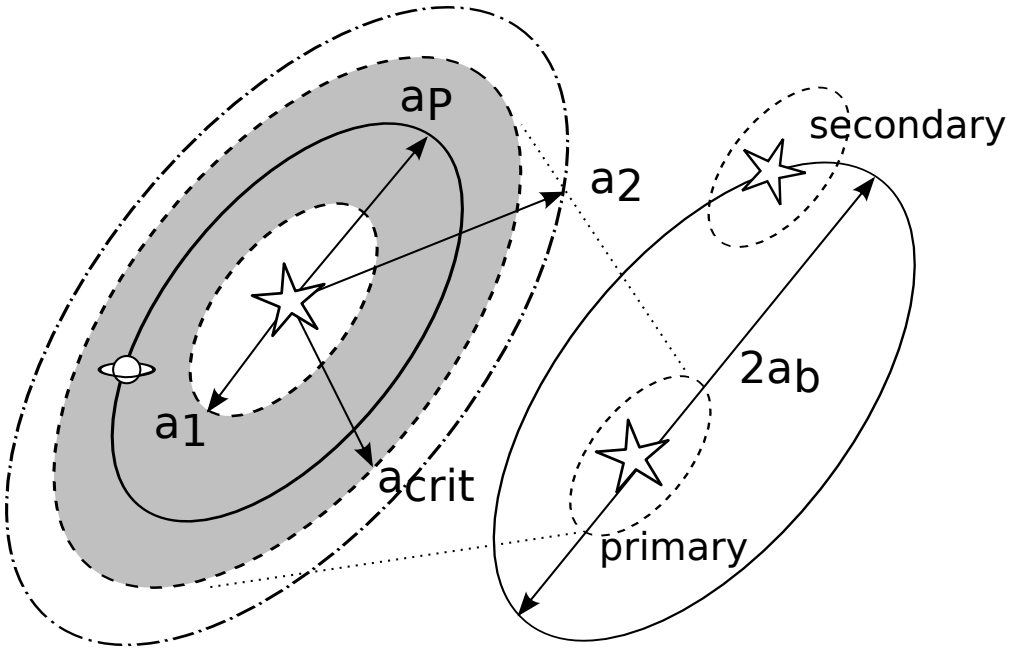

Figure 8.3: Favorable exoplanet orbit around a component star of a binary system for astrometric detection.

of its host star. Therefore it is more likely to detect an exoplanet which has a semi-major axis, a_P, that satisfies the condition,

$$a_P < a_{\rm crit}. \tag{8.6}$$

Within the sensitivity of the instrument

In order to detect the presence of an exoplanet of a given mass M_P by means of narrow-angle astrometry, the semi-major axis of the orbit of the planet must be

$$a_P > a_1 = \frac{M_\star}{M_P} a_{\rm ins}. \tag{8.7}$$

In Fig. 8.2, this limit corresponds to the dashed and solid lines with slope of -1 (on the left side of the shaded region) in the plot. The slope of the solid lines are computed for a given stellar mass ($5M_\odot$) at a distance of 10pc. However, they are also applicable to scenarios with smaller stellar masses. For example, the limit of detection for a system with a star of $1M_\odot$ at 50pc is the same as for a system with a star of $5M_\odot$ at 10pc away. In Fig. 8.3, this limit is illustrated by the radius a_1.

Duration of observation campaign

In order to detect the presence of an exoplanet within the duration of an observation campaign, the planet must complete one or more orbits around its host star. Suppose the campaign duration is $P_{\rm obs}$ years, then according to Kepler's third law of planetary motion there is a limit on the exoplanet semi-major axis for a given exoplanet and stellar mass. This limit is given as,

$$a_P < a_2 = P_{\rm obs}^{2/3} \left(M_P + M_\star\right)^{1/3}. \tag{8.8}$$

Since the mass of the host star is usually many orders of magnitude larger than the planet, this limit of a_P is represented by the dashed and solid vertical lines (on the right side of the shaded region) in the plot of Fig. 8.2. For a range of binary stars of different masses, the minimum detectable mass of an exoplanet (tip of the shaded region) traces the faint long dashed line in the plot. This line has a slope of +2 because for a range of stellar mass,

$$a_P < \left(\frac{M_P}{a_{\rm ins}}\right)^{\frac{1}{2}} P_{\rm obs}. \tag{8.9}$$

In Fig. 8.3, this limit is illustrated by the radius a_2.

8.4.3 Probability of detection with MUSCA

Combining the inequalities in the previous section, the probability of detecting an exoplanet of a given mass, M_P, orbiting one of the two stars in a binary system of given orbital parameters (a_b, e_b and μ) within the duration of a $P_{\rm obs}$-year observation campaign is modeled as:

$$\mathcal{P}_{\rm det,i} = \frac{\int_{a_1}^{a_2 \wedge a_{\rm crit}} M_{P,\rm lim} - \frac{a_{\rm ins}}{a_P} M_{\star,i}\, da_P}{M_{P,\rm lim}\, a_{\rm crit}} \tag{8.10}$$

The limits of the integration, a_1, a_2 and $a_{\rm crit}$ are defined in equations (8.7), (8.8) and (8.2) respectively. The notations $\wedge$ denotes the minimum of two variables respectively. The subscript i refers to either one of the stars in the binary system. The mass limit of the exoplanet, $M_{P,\rm lim}$, can be varied but in this analysis it is set to $10M_J$. The numerator of the above model describes the area of the shaded region in Fig. 8.3 and 8.2. This model assumes that if a planet is present, it has a uniform probability of residing anywhere in semi-major axis space between $a_P = 0$ and $a_P = a_{\rm crit}$, and a uniform probability of residing anywhere in mass

space between $M_P = 0$ and $M_P = M_{P,\mathrm{lim}}$. The combined probability of detection for a binary star system is,

$$\mathcal{P}_{\mathrm{bin}} = \mathcal{P}_{\mathrm{occ}} \times \mathcal{P}_{\mathrm{det}}, \tag{8.11}$$

where $\mathcal{P}_{\mathrm{occ}}$ is the rate of occurrence of exoplanets in binary stars discussed earlier and $\mathcal{P}_{\mathrm{det}}$ is the probability that at least one star in the binary system hosts a planet, which is given as,

$$\mathcal{P}_{\mathrm{det}} = 1 - \prod_{i=1}^{2} (1 - \mathcal{P}_{\mathrm{det,i}}). \tag{8.12}$$

In order to compute the probability of detecting an exoplanet around the target stars, remaining parameters, besides a_b and e_b which can be obtained directly from ORB6, are estimated in various ways. The following describes each parameter and the method used to estimate its values.

- Total mass of the binary system, $M_{\mathrm{T}} = M_{\star,1} + M_{\star,2}$
  Estimated from the semi-major axis, a_b, and the period, P_b, of the binary system based on the Kepler's third law of planetary motion where $M_{\mathrm{T}} = a_b^3/P_b^2$.
- Mass ratio, μ
  Estimated from the difference in brightness of the two stars, $\Delta m = m_1(V) - m_2(V)$ and the mass-luminosity relation where,

$$\left(\frac{M_{\star,1}}{M_{\star,2}}\right)^4 \approx \frac{L_{\star,1}}{L_{\star,2}} = 10^{-\Delta m/2.5}. \tag{8.13}$$

- Distance of the binary system, d
  Estimated from the parallax of the system, π, which is obtained from the Hipparcos reduction (van Leeuwen, 2007).

Stars without any orbital elements listed in ORB6 (2 in the first priority list and 13 in the full list) are assumed to have a total mass, $M_{\mathrm{T}} = 4M_{\odot}$, mass ratio, $\mu = 0.5$ and $a_{\mathrm{crit}} = 20$AU. Binary systems with known or suspected spectroscopic companions (5 in the first priority list and 12 in the full list) are assumed to have reduced possibility of detection and only host exoplanets around their single star (secondary) components. Those listed in Table 8.1 are indicated with references to published works regarding their spectroscopic binarity.

Table 8.2 shows the probability of an exoplanet orbiting a binary star and the probability of detecting the planet within a 4-year observation period if it has a

Table 8.2: The probability of detecting an exoplanet orbiting either or both stars in a binary, $\mathcal{P}_{\rm det}$, within a 4-year observation period if it has a mass of $10M_J$ (Jupiter mass) or less. Also listed is the minimum detectable mass of a planet, $\lfloor M_P \rfloor$, at a_2 or $a_{\rm crit}$, whichever is smaller. The last column gives the ratio of the estimated nuclear time scale, $\tau_{\rm nuc}$, of the less massive star in the binary system to 10^4 times the orbital period of the system. Dashes can either mean the values of a parameter cannot be computed due to lack of information or not applicable.

HR	Name	$\mathcal{P}_{\rm det}$	a_1 (AU)	a_2 (AU)	$a_{\rm crit}$ (AU)	a_b (AU)	e_b	$\lfloor M_P \rfloor$ (M_J)	$\frac{\tau_{\rm nuc}}{(P_b \times 10^4)}$
1852	Del Ori	0.53	0.45	3.04	6.04	55.20	0.56	1.47	36
3307	Eps Car	0.18	0.45	3.17	20.00	–	–	1.40	–
3485	Del Vel	0.83	0.05	3.01	7.46	49.44	0.48	0.17	12
3482	Eps Hya	0.82	0.09	3.11	0.82	10.10	0.66	1.09	350
4819	Gam Cen	0.86	0.17	3.87	1.45	37.35	0.79	1.20	24
4825	Gam Vir	0.00	0.02	2.78	0.00	42.52	0.88	–	240
5267	Bet Cen	0.00	1.34	5.30	0.00	3.04	0.82	–	12
5576	Kap Cen	0.21	0.28	3.17	20.00	–	–	0.89	–
5776	Gam Lup	0.22	1.07	4.80	10.67	84.52	0.51	2.81	0
5953	Del Sco	0.00	1.92	5.54	0.00	14.92	0.94	–	1
6084	Sig Sco	0.09	0.51	3.17	20.00	–	–	1.62	–
6378	Eta Oph	0.00	0.11	3.80	0.00	37.82	0.95	–	24
6556	Alp Oph	0.00	0.02	2.66	0.00	6.36	0.92	–	970
7194	Zet Sgr	0.86	0.08	3.44	2.78	13.23	0.20	0.32	250

mass of $10M_J$ or less. The table also lists the ratio of the estimated nuclear time scale, $\tau_{\rm nuc}$, of the less massive star in the binary system to the orbital period of the system. This puts the stable orbit time scale suggested by (Holman & Wiegert, 1999) in the perspective of the lifetime of the binary system. The nuclear time scale, in 10^9 year unit (GYr), is estimated from the stellar mass (Karttunen et al., 2007, Chap. 11) as,

$$\tau_{\rm nuc} \approx 10 M_\star^{-3}. \tag{8.14}$$

From Table 8.2, the average probability of detection (over binary systems with non-zero $\mathcal{P}_{\rm det}$), $\langle \mathcal{P}_{\rm bin} \rangle$ is $\lesssim$5%. The values of $\mathcal{P}_{\rm bin}$ for individual stars are not listed in the table because it can be easily obtained by scaling $\mathcal{P}_{\rm det}$ with $\mathcal{P}_{\rm occ}$, which is 10%. From the average probability, the total expected number of binary stars in the list to host an exoplanet less is than 1. The probability of detecting an exoplanet from at least one binary star system in the list, which can be estimated from the following,

$$\mathcal{P}_{\rm mus} = 1 - \prod_{i=1}^{N_\star} \left(1 - \mathcal{P}_{\rm bin,i}\right), \tag{8.15}$$

Table 8.3: The average probability of detection per binary system and the probability of detecting one exoplanet ($M_P \leqslant 10 M_J$) from at least one binary system in the MUSCA target list.

MUSCA astrometric precision (μas)	$P_{\rm obs}$ (Yr)	$N_\star$	$\langle \mathcal{P}_{\rm bin} \rangle$	$\mathcal{P}_{\rm mus}$
10	4	9	0.05	0.38
50	4	8	0.02	0.15
100	4	3	0.03	0.07
10	8	9	0.06	0.45
50	8	9	0.02	0.20
100	8	5	0.02	0.10

which gives a probability of $\lesssim$38%. $N_\star$ in the equation is the number of stars in the list (9, in this case because 5 binary systems have $\mathcal{P}_{\rm det} = 0$) and $\mathcal{P}_{\rm bin,i}$ is defined earlier in (8.11). Table 8.3 lists probabilities for a few scenarios where the MUSCA astrometric sensitivity is varied between 10–100μas and if the observation campaign is extended to 8 years. The results of the same analysis with the full list are given in Appendix F.

8.5 Discussion and summary

The computation of the probability of detection did not take into account the inclination, $i_\star$, and the argument of periastron, $\omega_\star$, of the star-planet orbits. They influence the above analysis because the reflex motion amplitude of the host star, which is the measurable quantity in astrometry, is maximum ($a_\star$) if the star-planet orbit is face-on ($i_\star = 0^\circ$) or the argument of periastron $\omega_\star$ is zero. The amplitude of the reflex motion is otherwise smaller by a factor determined by two orbital parameters. Despite that, the parameter $a_\star$ is still used for the detection analysis because it is a parameter that is influenced by gravitational force and therefore a proxy for measuring the mass of a substellar companion. Since $a_\star$ is the maximum reflex motion amplitude a star can exhibit, the estimated probabilities are optimistic.

Furthermore, the uncertainty of measurements (e.g. parallax measurement from the Hipparcos catalog, orbital parameters, etc) are not taken into account. How-

ever, given that they contribute only in a minor way the outcome of the analysis would not have changed significantly.

Given the odds in an optimistic analysis, it is less likely for MUSCA to detect an exoplanet in the next 4 years of observation with the current list of targets. Although an S-type orbit type planet around γ Cephei A (Hatzes et al., 2003) was detected from a list of 16 stars (Campbell et al., 1988), a larger sample of targets will certainly increase the chances of detection. In order to increase the number of stars observable with MUSCA, the performance of the PAVO beam combiner must be enhanced. The latter must be able to not only track but remain locked-on to fringes of stars as faint as 5th magnitude under typical seeing conditions. As shown in Chapter 7, intermittent fringe locks are inadequate for MUSCA operation. A larger target list corresponding to this improved PAVO performance is given in Appendix F. With a target list of 43 binary stars, the same analysis would estimate a $\lesssim$74% chance of MUSCA detecting an exoplanet of $10M_J$ mass or less and the expected number of detections is at most 2.

Chapter 9

Conclusions

This thesis documented the development of a high-precision astrometric facility at SUSI as well as the characterization tests and astronomical observations carried out to assess the performance of the facility. This thesis also provided an estimate of exoplanet detectability of SUSI based on a projected observation campaign of several years using the facility. The highlights of the work completed for this thesis are as follows:

- A beam-combiner, at visible (0.77–0.91μm) wavelengths which forms the core of the astrometric facility, was successfully designed, constructed and commissioned at SUSI (Chapter 3).
- A computer framework which simulates the operation of the dual beam-combiner setup at SUSI was developed and its utility to assess the accuracy of the data reduction pipelines for both beam combiners was demonstrated (Chapter 4).
- A low-cost scheme to carry out high-precision displacement metrology was demonstrated with an existing hardware and a newly written analysis software package (Chapter 5).
- A network of metrology systems (Chapter 5) that not only measure the non-common optical paths between two beam combiners but also eliminate non-common path error between paths of the science and metrology beams was demonstrated (Chapter 7).
- A data reduction pipeline to post-process data from observations using the new facility and produce projected as well as true on-sky separations of pairs of stars for narrow-angle astrometry purposes was written (Chapter 6) and its usage demonstrated (Chapter 7).

Table 9.1: Breakdown of astrometric error

Error-term/subsystem	in nm*/mm+		in μas	
	Best	Worst	Best	Worst
*OPD-related errors in nm				
Anisoplanatism	<3	5	<6	10
Phase-referencing	3	10	6	21
Differential delay line (*cf.* Sec. 7.1.2)	10	110	21	227
+Baseline-related errors in mm				
Wide-angle baseline solution	0.1	0.2	1	2
Placement of alignment LEDs	1	2.5	10	25
Narrow-angle baseline alignment	1	6	10	60
Combined error			26	237

Conversion from nm/mm to μas assumed:
(a) binary separation is 1″
(b) baseline is 100m

- A performance evaluation of the hardware and the software for the facility through a series of astronomical observations (Chapter 7) was carried out and Table 9.1 shows the breakdown of the astrometric error (normalized to a baseline of 100m and a binary separation of 1″). In the worst case scenario, the error is larger than the upper bound level of accuracy needed to start searching for exoplanet by means of astrometry but further work has been planned to improve on it.
- A forecast of the number of exoplanets detectable with SUSI was given (Chapter 8) and it showed that the probability of detection increases significantly if PAVO is operating at its peak performance and under good seeing conditions.

Although the facility at its current stage is capable of performing its basic function of measuring projected separations of close binary stars, there are many important future works that must be implemented to improve the performance of the facility before long term astrometric survey work can begin. They are listed below according to their importance:

- Monitor the long term stability of the wide-angle baselines of SUSI and characterize the stability of the *very* narrow-angle baseline alignment method. This step is important so that the accuracy of astrometric measurements

are repeatable and long term astrometry of binary star systems can be performed.

- Replace the dichroic filters (M16) which are suspected of producing unwanted spatially modulated fringes across the laser pupil in MUSCA with a pair that are fabricated with anti-reflection coated wedge glass and have a designed leak in the dichroic coatings around the metrology lasers wavelengths. This will reduce the observed spurious laser beams reflections.

- Replace the 2-element differential delay line (DDL) in MUSCA with one which is based on a single element retro-reflector. This revision ensures the tilt of the beam exiting the DDL depends only on the input tilt. This change will improve on the phase alignment of fringe packets when the position of the DDL is altered.

- Upgrade the data reduction pipeline to correct for systematic errors currently not taken into account. This will improve the accuracy of the narrow-angle astrometry.

- Increase the sensitivity of PAVO, thereby allowing a faster fringe-tracking servo loop. This will increase the number of stars PAVO can fringe-track and reduce the amount of integration time on a star needed to produce a phase-referenced fringe packet of adequate phase precision.

- Upgrade the real time software that controls PAVO to estimate the number of good scans recorded and to advise the observer when MUSCA can be switched to observe the other star in a binary system. This will optimize the amount of integration time spent on the reference and the target stars.

- Replace the existing metrology lasers with frequency-stabilized versions so that the range of the different delay line offsets that the metrology can measure will be extended beyond 0.5mm.

- Install a field lens in between the primary and the secondary mirrors of each BRT to increase the effective field of view of MUSCA to $\sim 10''$. Currently, it is limited by the aperture of the focusing lenses in SUSI which vignette starlight beams from an off-axis star that is further than $\sim 2''$ from the reference star.

Despite the improvements that can be made to the astrometric facility at SUSI, there are a couple of drawbacks which are inherent to the unique method developed in this work. Firstly, in order to obtain a single fringe packet separation measurement, which is the main observable, MUSCA requires at least 3 phase-referencing observations (collectively known as a bracketed observation) to be carried out and each observation typically lasts about 10 minutes. This lengthy observation time

is on top of the minimum observation time set by the turbulent atmosphere when observing the target star. Secondly, the success of a phase-referencing observation is not only dependent on the atmospheric conditions but also the duration of the good seeing. Essentially, good atmospheric seeing must persist throughout the duration of one fringe packet separation measurement. Should the seeing condition deteriorate considerably before a bracketed observation can be completed, measurement precision will be degraded or in the worst case, lost and the measurement has to be restarted. The architecture of the facility would have to be redesigned if these drawbacks are to be overcome.

In conclusion, this thesis has documented a successful attempt at high-precision narrow-angle astrometry by means of optical long baseline interferometry. The astrometric facility setup at SUSI is now operational and its first generation results have been demonstrated. Further improvements after the completion of this thesis are needed to optimize the performance of the facility. The detection principles outlined in this thesis could also be applied to interferometers at other sites, especially a potential astrometric interferometer located on the high Antarctic plateau.

Appendix A

Differential fringe motion

Using the Kolmogorov spectrum of phase fluctuations given in Eq. (2.7) and the Taylor hypothesis of frozen turbulence, the power spectrum of temporal differential fringe motion for fringes formed with a pair of pinhole sized apertures is given by Glindemann (2011) as,

$$\begin{aligned}
\Phi_{\mathrm{dOPD},t}(f) &= 0.628\lambda^2 \left(\frac{\bar{v}}{r_0}\right)^{5/3} \left(\frac{\Delta s\,\bar{h}}{\bar{v}}\right)^2 \left(\frac{B}{\bar{v}}\right)^{2/3} \\
&\quad \times \left(1 + 4.84\, f^{4/3} \left(\frac{B}{\bar{v}}\right)^{4/3}\right) \qquad ; \qquad f \ll 0.12\frac{\bar{v}}{B} \\
\Phi_{\mathrm{dOPD},t}(f) &= 0.193\lambda^2 \left(\frac{\bar{v}}{r_0}\right)^{5/3} \left(\frac{\Delta s\,\bar{h}}{\bar{v}}\right)^2 f^{-2/3}; \quad 0.12\frac{\bar{v}}{B} \ll f \ll 0.2\frac{\bar{v}}{\Delta s\,\bar{h}} \\
\Phi_{\mathrm{dOPD},t}(f) &= 0.0078\lambda^2 \left(\frac{\bar{v}}{r_0}\right)^{5/3} f^{-8/3} \qquad ; 0.2\frac{\bar{v}}{\Delta s\,\bar{h}} \ll f
\end{aligned} \quad , \tag{A.1}$$

where $\bar{v}$ is the effective wind speed, r_0 is the Fried parameter, Δs is the separation of two stars whose differential fringe motion are to be measured, $\bar{h}$ is the effective height of the atmospheric turbulent layer and B is the baseline of an interferometer used to observe the stellar fringes. The power spectrum has a unit of m^2/Hz if the variables in the equation are in S.I. units. The variance of the fringe separation due to their differential motion can be computed by applying a low-pass filter function $\mathrm{sinc}^2(\pi T f)$ to the power spectrum and then integrating the filtered power spectrum from 0 to ∞. The parameter T is the amount of time spent measuring the fringe separation, which is usually more than 2 minutes ($\lesssim 8\times10^{-3}$Hz). With this long measurement time, $1/T \ll 0.12\bar{v}/B$, the first null of the *sinc* function, lies within the first part of the power spectrum for most atmospheric conditions

at long baselines ($B \gtrsim 100$m). Therefore only the low frequency component of the power spectrum contributes to the variance of the fringe separation measurements. Suppose for the sake of first order approximation, only the main lobe of the *sinc* function is considered in the integration so that,

$$\mathrm{sinc}^2(\pi T f) \approx \begin{cases} 1 - \pi T^2 f^2 & ; f \ll 1/T \\ 0 & ; f \gg 1/T \end{cases} . \tag{A.2}$$

Then, the variance of the fringe separation measurement is obtained by solving the integral below,

$$\begin{aligned} \sigma^2_{\mathrm{dOPD},T} &= \int_0^\infty \Phi_{\mathrm{dOPD},t}\ \mathrm{sinc}^2(\pi T f)\, df \\ &\approx \int_0^{1/T} C_A \left(1 + C_B\, f^{4/3}\right) \left(1 - T^2 f^2\right)\, df \end{aligned} , \tag{A.3}$$

where,

$$\begin{aligned} C_A &= 0.628\lambda^2 \left(\frac{\bar{v}}{r_0}\right)^{5/3} \left(\frac{\Delta s \bar{h}}{\bar{v}}\right)^2 \left(\frac{B}{\bar{v}}\right)^{2/3} \\ C_B &= 4.84 \left(\frac{B}{\bar{v}}\right)^{4/3} \end{aligned} . \tag{A.4}$$

The solution of the integral yields the standard deviation of the fringe separation, which is given as,

$$\sigma_{\mathrm{dOPD},T} \approx 0.79\lambda\, r_0^{-5/6}\, \bar{v}^{-1/2}\, \bar{h}\, \Delta s\, B^{1/3}\, T^{-1/2}. \tag{A.5}$$

The fringe separation fluctuation is independent of wavelength because the product of $\lambda\, r_0^{-5/6}$ is the turbulence profile of the atmosphere and is constant over wavelength.

Appendix B

SUSI optics

B.1 Naming convention

Each mirror along the light path is named according to the arm of the interferometer it is on and its position from the siderostats. The first character in the name denotes the interferometer arm, either N for North or S for South, a mirror is associated with. The numbers that follow indicate the number of reflective surface from the siderostats towards the beam combiner with the siderostat being the first. For example, mirrors N15 and S15 are the 15th reflecting surfaces or the 14th mirror after the siderostats. Mirrors of the same stage are collectively referred to with a prefix M instead of N or S. In the previous example, those mirrors are collectively called M15.

On top of this convention, mirrors within MUSCA have an additional postfix of M to distinguish their associations with the beam combiner. For example, N18M and S18M or collectively as M18M are MUSCA mirrors.

Other than mirrors, there is no specific rule in naming optical elements at SUSI.

B.2 BRT characterization

Table B.1 shows the coefficients for the Zernike polynomials that describe the wavefront propagating out from the new North and South beam reducing telescopes. The values in the table are for reference and comparison with similar measurements of an older BRT system in SUSI. The measurements for the latter

Table B.1: The first 7 Zernike coeffiencts (excluding the tip-tilt and piston terms) in units of wave (or cycle) measured from a Twyman-Green interferometer setup to assess the optical quality of the BRTs. The reference beam aberrations have been substracted off the North and South measurements.

Zernike coef.	North	South	Ref.
A_2^{-2}	-0.068	-0.000	-0.005
A_2^0	0.359	0.208	-0.004
A_2^2	-0.253	0.340	0.004
A_3^{-3}	0.000	0.001	0.000
A_3^{-1}	-0.001	-0.003	-0.000
A_3^1	-0.054	-0.002	-0.001
A_3^3	0.117	-0.001	-0.000

and technique employed to acquire these measurements is described in (Ireland, 2006).

B.3 Profile of dichroic filters

The profile of the tip-tilt (NTT and STT) and science dichroic (M16) filters are given in Fig. B.1. The former reflects starlight of shorter wavelengths to the tip-tilt system and transmits longer wavelengths to the beam combiners while the latter reflects shorter wavelengths to PAVO and transmits longer wavelengths to MUSCA. The filters are custom made and their predicted reflectance profiles were obtained from the manufacturer, Optical Coating Associates[1].

[1] `http://www.opticalcoating.com.au/`

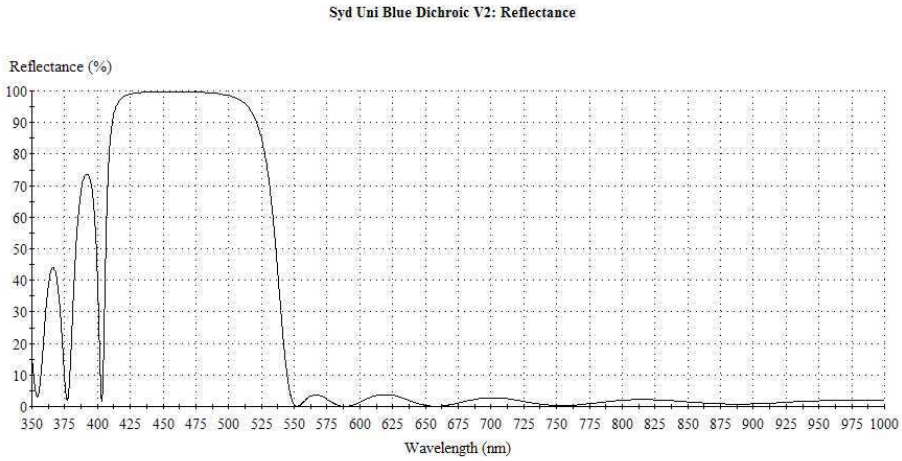

(a)

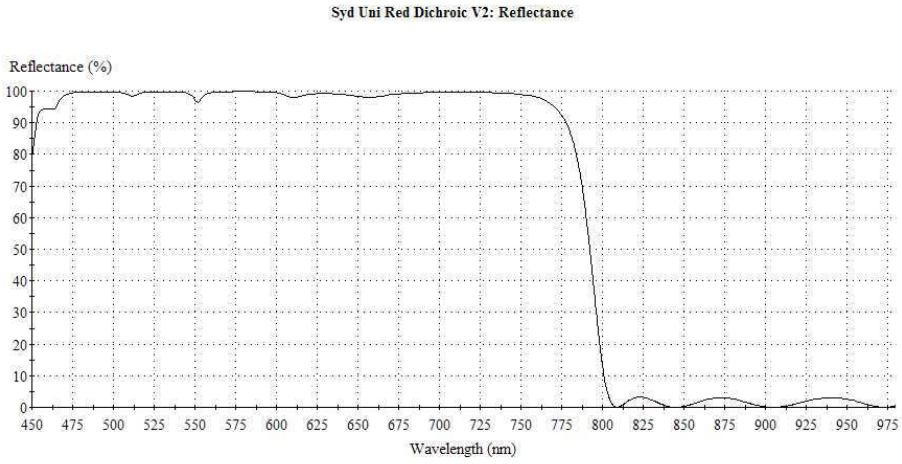

(b)

Figure B.1: Wavelength profile of (a) the tip-tilt (ND1 and SD1) and (b) the science (M16) dichroic filters.

Appendix C

Determining for the wide-angle baseline solution

A baseline solution is a description of a baseline vector of an interferometer in a coordinate system. It is common to report the vector in a local zenith Cartesian-based coordinate system in which the x-axis points to East, y-axis points to North and the z-axis points to zenith. This also called the local zenith coordinate system. Using SUSI as an example, the baseline vector of an interferometer is determined iteratively as follows.

First, the expected values of each component of the baseline vector, $\vec{B}$, are used to compute the expected OPD between two arms of the interferometer that will produce fringes of a star, given its position in the sky. The expected OPD is given as,

$$E[\text{OPD}] = \hat{s} \cdot E[\vec{B}], \tag{C.1}$$

where $\hat{s}$ is a unit vector pointing from the pivot point of a siderostat to the star under observation and $E[\vec{B}]$ is the expected baseline vector of the interferometer. $\hat{s}$ can be computed from the siderostat pointing direction and $\vec{B}$ can be estimated using a less precise measuring system (e.g. theodolite). However, due to error in the estimation of $E[\vec{B}]$, the actual OPD is given as,

$$\text{OPD} = \hat{s} \cdot \vec{B} + C, \tag{C.2}$$

where C is an internal optical path constant of the baseline.

Then, the next step is to accurately measure the offset between the actual and the expected OPD for a given star. This can be done using a laser metrology to measure the optical path of each delay line in each arm of the interferometer.

Suppose the unit vector, $\hat{s}$, in the local zenith coordinate system is given as,

$$\hat{s} = \begin{bmatrix} s_x & s_y & s_z \end{bmatrix}, \tag{C.3}$$

and the baseline vector is given as,

$$\vec{B} = \begin{bmatrix} B_x & B_y & B_z \end{bmatrix}, \tag{C.4}$$

then the offset between the actual and expected OPD is,

$$\begin{aligned} \Delta\text{OPD} &= \text{OPD} - E[\text{OPD}] \\ &= s_x \Delta B_x + s_y \Delta B_y + s_z \Delta B_z + C' \end{aligned} \tag{C.5}$$

where $\Delta B_i = B_i - E[B_i]$ and i represents one of the three vector components.

Next, the pointing of the siderstat and OPD offset measurements are repeated with different stars from different parts of the sky. The collection of measurements can then be used to solve for ΔB_i using the following linear algebra,

$$\Delta\mathbf{O} = \mathbf{S}\,\Delta\mathbf{B} + C, \tag{C.6}$$

where $\Delta\mathbf{O}$ is a vector of the OPD offsets and $\mathbf{S}$ is a matrix of $\hat{s}$ of different stars and $\Delta\mathbf{B}$ is the vector form of ΔB_i. Eq. (C.6) can be solved using the linear least square method.

Finally, the true value of the baseline vector can then be determined as follows,

$$\vec{B} = E[\vec{B}] + \Delta\mathbf{B}. \tag{C.7}$$

The entire procedure can be repeated by substituting the expected baseline vector in Eq. (C.1) with the vector obtained in Eq. (C.7). Fig. C.1 shows a set of OPD offsets obtained using the SUSI N3-S1 baseline as an example. The offsets are plotted against different component vectors of $\hat{s}$. The strong linear trend of the OPD offsets with s_y (middle column in the figure) shows a relatively large error between the expected and the actual dimension of the baseline in that axis.

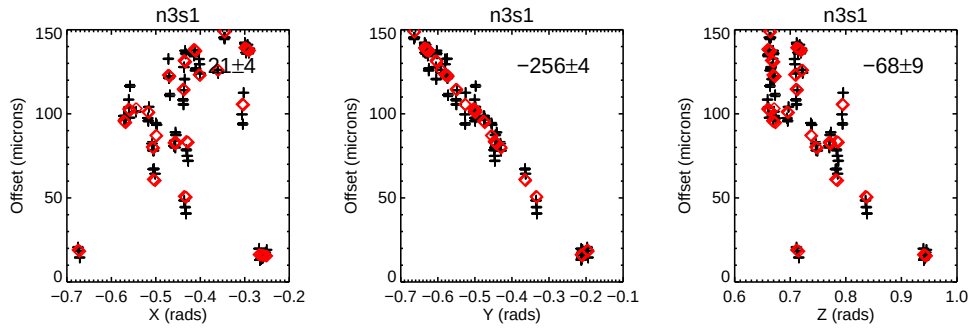

(a)

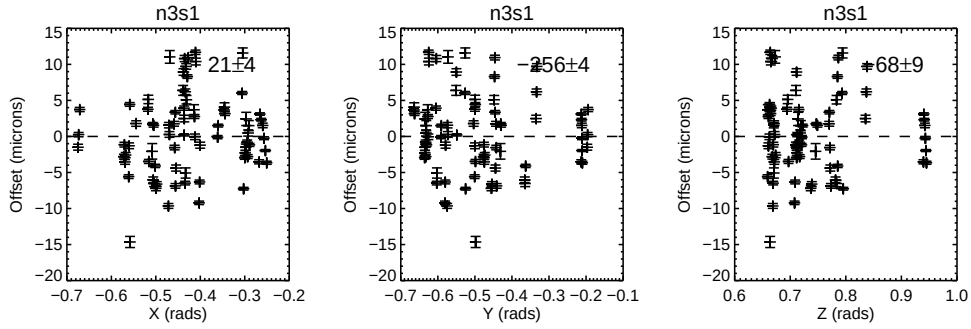

(b)

Figure C.1: The plots in (a) show the measured OPD offsets (crosses) of different stars observed with the N3S1 baseline of SUSI. The horizontal axes are the components of the pointing vector, $\hat{s}$. The errors between the components of the actual and expected baseline vectors are reported in their corresponding plot windows (. The diamond data points are computed OPD offsets using the extracted baseline error, $\mathbf{\Delta B}$. The plots in (b) show the linear least square residuals of the OPD offsets.

Appendix D

PAVO spectrograph wavelength scale calibration

This section describes the model used to calibrate the wavelength scale of the PAVO spectrograph. The importance of this calibration step as one of the subprocesses in the PAVO+MUSCA data reduction pipeline is discussed in Section 6.1.1.

The wavelength scale is determined by solving a general prism equation, which is given as,

$$\theta = \sin^{-1}\left(n \sin\left(\alpha - \sin^{-1}\left(\frac{\sin\phi}{n}\right)\right)\right), \tag{D.1}$$

where α is the apex angle of the glass prism, ϕ and θ are the incidence and output (after refraction through the glass) angles of a beam with respect to the normal of surface of the prism and n is the refractive index of the glass (BK7) [1], which is given as,

$$n = \left(1 + \frac{1.03961212\lambda^2}{\lambda^2 - 0.00600069867} + \frac{0.231792344\lambda^2}{\lambda^2 - 0.0200179144} + \frac{1.01046945\lambda^2}{\lambda^2 - 103.560653}\right)^{\frac{1}{2}}, \tag{D.2}$$

where λ is the wavelength of light in units of μm.

In the context of the PAVO beam combiner setup, the angle of incidence, ϕ, and the output angle, θ, can be expressed as,

$$\begin{aligned} \phi_{\ell,\lambda} &= \phi_0 + \Delta\phi_{\ell,\lambda} \\ \theta_{\ell,\lambda} &= \theta_0 + \Delta\theta_{\ell,\lambda} \end{aligned}, \tag{D.3}$$

[1] `http://www.us.schott.com`

where $\phi_{\ell,\lambda}$ and $\theta_{\ell,\lambda}$ are the angle of incidence from a lenslet and the angle of output to a column of pixels on the camera for a given wavelength of light, λ. The terms ϕ_0 and θ_0 are the mean of the angles across all lenslets used for calibration while $\Delta\phi_{\ell,\lambda}$ and $\Delta\theta_{\ell,\lambda}$ are the deviations from the mean angles for each lenslet. With a lenslet array pitch of 500μm and a collimating lens of 50mm, $\Delta\phi_{\ell,\lambda}$ is an integer multiple of 0.01 radian. On the other hand, with another collimating lens of the same focal length $\Delta\theta_{\ell,\lambda}$ is an integer multiple of 0.32 milliradian because the pitch of a pixel is 16μm. The apex angle of the prism used in PAVO is $\sim$36°. So with one or more calibration sources of known wavelengths, the parameters ϕ_0 and θ_0 in (D.3) can be determined by fitting the model in (D.1) to PAVO interferograms that contain the sources. Finally, with all the parameters known, the wavelength scale can then be estimated by substituting (D.3) into (D.1) and then taking the inverse of the latter.

Practical consideration

In practice the focal length of the collimating lens may not be exactly 50mm. In order to address this, a scaling factor, S, is introduced to account for an offset from the true focal length value (Ireland, 2010b). Therefore instead of (D.1), the equation used for model fitting is,

$$\Delta\theta_\ell = -\theta_0 + S\sin^{-1}\left(n\sin\left(\alpha - \sin^{-1}\left(\frac{\sin(\phi_0 + \Delta\phi_\ell)}{n}\right)\right)\right), \tag{D.4}$$

since,

$$\frac{\Delta\theta_\ell}{S} = \frac{\Delta x}{Sf}, \tag{D.5}$$

where Δx is the width of a pixel of the PAVO camera and f is the focal length of the focusing lens.

Three types of sources are used for calibration. They are namely an IR LED (λ = 0.940μm), a green (λ=0.5431μm) and a red (λ=0.6328μm) He-Ne laser. Previous work by Ireland (2010b) only used the green He-Ne laser.

Appendix E

Coordinate transformation matrix

The matrix to transform a local zenith coordinate system (X,Y,Z) to the astrometric coordinate system defined by Fomalont & Wright (1974) is given below. The local zenith coordinate is a natural frame of reference for an alt-azimuth mounted telescope or a person on the ground. It has its X-axis pointing to the East, Y-axis pointing to the North and Z-axis pointing to zenith. On the other hand, the astrometric coordinate system is a natural frame of reference for describing the sky as seen from a telescope. It has its u-axis pointing to the East, v-axis pointing to the North and w-axis pointing towards the sky from the observer.

$$\mathbf{T} = \begin{bmatrix} \cos \mathrm{HA} & \sin\phi \sin \mathrm{HA} & \cos\phi \sin \mathrm{HA} \\ \sin\delta \sin \mathrm{HA} & \cos\phi\cos\delta + \sin\phi\sin\delta\cos \mathrm{HA} & \sin\phi\sin\delta - \cos\phi\sin\delta\cos \mathrm{HA} \\ -\cos\delta \sin \mathrm{HA} & \cos\phi\sin\delta - \sin\phi\cos\delta\cos \mathrm{HA} & \sin\phi\sin\delta + \cos\phi\cos\delta\cos \mathrm{HA} \end{bmatrix} \quad \text{(E.1)}$$

The terms HA and δ represents the hour angle and declination of a source in the sky in an equatorial coordinate system while ϕ represents the geographical latitude of the observer. The above matrix is a product of 2 matrices in Appendix II of (Fomalont & Wright, 1974).

In order to transform the astrometric coordinate system to a local zenith coordinate system, the inverse of $\mathbf{T}$ is used. The following matrix, which was originally derived from Murray (1983, Eq. (4.5.17)), was obtained from Tango (2006).

$$\mathbf{T}^{-1} = \begin{bmatrix} \cos \mathrm{HA} & \sin\delta \sin \mathrm{HA} & -\cos\delta \sin \mathrm{HA} \\ -\sin\phi \sin \mathrm{HA} & \cos\phi\cos\delta + \sin\phi\sin\delta\cos \mathrm{HA} & \cos\phi\sin\delta - \sin\phi\cos\delta\cos \mathrm{HA} \\ \cos\phi \sin \mathrm{HA} & \sin\phi\cos\delta - \cos\phi\sin\delta\cos \mathrm{HA} & \sin\phi\sin\delta + \cos\phi\cos\delta\cos \mathrm{HA} \end{bmatrix} \quad \text{(E.2)}$$

For example, a North-South oriented 10m baseline of SUSI ($\phi \approx 30^\circ$S) when projected onto a plane centered at HA = 0hr and $\delta = 0^\circ$ on the sky can be

described using the following vector in the astrometric coordinate system to the nearest meter,

$$\vec{B} = \mathbf{T} \begin{bmatrix} 0 \\ 10 \\ 0 \end{bmatrix} = \begin{bmatrix} 0 \\ 9 \\ 5 \end{bmatrix} \quad [\mathrm{m}]. \tag{E.3}$$

At the same instance in time, the separation between two components of a binary star with a separation of $0.3''$ and a position angle of 130° when projected onto the local coordinate system centered at SUSI can be described using the following vector to the nearest 0.1μrad,

$$\Delta\vec{s} = \mathbf{T}^{-1} \begin{bmatrix} 1.1 \\ -0.9 \\ 0.0 \end{bmatrix} = \begin{bmatrix} 1.1 \\ -0.8 \\ 0.5 \end{bmatrix} \quad [\mu\mathrm{rad}]. \tag{E.4}$$

Appendix F

MUSCA target stars

This section gives the complete list of MUSCA target stars and the result of the detectability analysis as described in Chapter 8. The list was queried from the well maintained and daily updated Washington Visual Double Star Catalog (WDS, 2013) with the following criteria.

- Magnitude of the primary star in V-band, $m_{V,1} \leqslant 5.0$[1]
- Magnitude of the secondary star in V-band, $m_{V,2} \leqslant 6.0$
- Angular separation of the primary and secondary stars, $0.02'' \leqslant \rho < 2''$
- Declination of the primary star, $\delta \leqslant 15^{\circ}$

Table F.1 shows the list of target stars while Table F.2 shows the probability of detecting an exoplanet of one Jupiter mass or less, $\mathcal{P}_{\rm det}$, around each star in the list. The probabilities in Table F.2 are computed with an exoplanet occurrence rate of $\mathcal{P}_{\rm occ} = 0.10$. With a projected precision of 10μas and for an observation period of 4 years, the average probability of detection, $\langle \mathcal{P}_{\rm bin} \rangle$ (see Eq. (8.11)), is $\sim$4%. This gives an expected number of detections of at most 2. The probability of detecting at least one exoplanet from all the stars (only 33 stars with non-zero $\mathcal{P}_{\rm det}$) in the list is $\lesssim$74%. Table F.3 lists probabilities for different scenarios where the MUSCA astrometric precision is varied between 10–100μas and if the observation campaign is extended to 8 years.

[1]The expected peak fringe-tracking performance of PAVO.

Table F.1: List of binary/multiple stars observable with MUSCA

HR	Name	$m_{V,1}$	$m_{V,2}$	$\rho^{\dagger}$ ($''$)	$\theta^{\dagger}$ ($^{\circ}$)	Epoch†	Spectral Type	$\pi^{\ddagger}$ (mas)	Grade*
322	Bet Phe	4.10	4.19	0.40	106	2010	G8IIIv	0.12	4
595	Alp Psc	4.10	5.17	1.90	266	2011	A0p A3m	21.66	4
1465	Alp Dor	3.62	4.57	0.20	187	2008	A0IIIs	19.34	2
1788	Eta Ori*	3.56	4.87	1.80	78	2012	B1V B2e	3.34	3
1839	32 Ori	4.44	5.75	1.30	44	2011	B5V	10.77	4
1852	Del Ori*	2.41	3.76	0.30	133	2008	B0III+O9V	4.71	4
1931	Sig Ori	4.07	5.27	0.30	89	2010	O9.5V	3.04	2
2456	15 Mon*	4.66	5.90	0.10	258	2010	O7Ve	3.55	4
3307	Eps Car	2.25	3.86	0.50	141	2010	K3III B2V	5.39	–
3485	Del Vel	1.99	5.57	0.40	280	2012	A1V+F8V	40.49	4
3482	Eps Hya	3.49	5.00	0.30	163	2011	F8V	25.23	1
3786	Psi Vel	3.91	5.12	0.90	108	2012	F0IV+F3IV	53.15	2
4167	*	4.13	5.76	0.40	272	2012	F4IV+F3	37.26	2
4390	Pi Cen	4.08	5.65	0.10	254	2012	B5Vn	9.12	2
4552	Bet Hya	4.67	5.47	0.70	37	1998	B9IIIpSi	10.53	–
4689	Eta Vir*	3.89	5.90	0.10	334	2008	A2IV	12.29	2
4819	Gam Cen	2.82	2.88	0.50	335	2007	A1IV	25.06	3
4825	Gam Vir	3.48	3.53	1.60	16	2011	F0V+F0V	85.58	2
4844	Bet Mus	3.52	3.98	1.00	48	2007	B2.5V	9.55	5
5034		4.49	5.20	0.10	142	2009	B2.5Vn	9.20	–
5089		4.64	5.03	0.20	64	2009	G9Ib	3.60	3
5267	Bet Cen	0.58	3.95	0.40	204	2011	B1III	8.32	2
5396	Tau2Lup	4.93	5.55	0.20	180	2008	A7+F4IV	10.22	3
5477	Zet Boo	4.46	4.55	0.60	290	2010	A0V+A0V	18.56	2
5576	Kap Cen	3.34	4.71	0.10	157	2009	B2IV	8.51	–
5605	Pi Lup	4.56	4.60	1.70	67	2007	B5V	7.36	–
5626	Lam Lup	4.43	5.23	0.10	91	2012	B3V	4.20	2
5683	Mu Lup	4.99	4.93	0.90	308	2007	B8V	9.72	–
5708	Eps Lup*	3.56	5.04	0.30	118	2009	B2IV-V	6.37	5
5704	Gam Cir	4.94	5.73	0.80	1	2012	B5IV F8	7.27	4
5776	Gam Lup*	2.95	4.45	0.80	276	2012	B2IV	7.75	3
5787	Gam Lib	4.00	4.20	0.10	191	1940	G8III	19.99	–
5881	Mu Ser	3.75	5.39	0.20	174	2009	A0V	19.23	5
5953	Del Sco*	2.39	4.62	0.10	14	2010	Be	6.64	2
6026	Nu Sco*	4.35	5.31	1.40	1	2012	B8V+B9VpSi	6.88	–
6084	Sig Sco*	3.06	5.24	0.50	244	2000	B1	4.68	8
6149	Lam Oph	4.15	5.15	1.40	37	2010	A0V+A0V	18.84	2
6378	Eta Oph	3.05	3.27	0.60	237	2009	A1IV+A1IV	36.91	2
6556	Alp Oph	2.10	5.00	0.70	238	2009	A5III	67.13	4
7194	Zet Sgr*	3.27	3.48	0.30	286	2011	A2III	36.98	1

†data from WDS (2013)

‡data from Hipparcos reduction (van Leeuwen, 2007)

*data from ORB6 (2013), 1=definitive, 5=indetermine, 8=interferometry

*primary is a known binary

Table F.1: (continued)

HR	Name	$m_{V,1}$	$m_{V,2}$	$\rho^\dagger$ ($''$)	$\theta^\dagger$ ($^\circ$)	Epoch†	Spectral Type	$\pi^\ddagger$ (mas)	Grade*
7264	Pi Sgr	3.60	3.60	0.10	179	1989	F2II	6.40	–
7882	Bet Del*	4.11	5.02	0.40	24	2009	F5IV+F2V	32.33	1
8368	Del Ind	4.80	5.96	0.10	75	2009	F0IV	17.34	2

†data from WDS (2013)
‡data from Hipparcos reduction (van Leeuwen, 2007)
*data from ORB6 (2013), 1=definitive, 5=indetermine, 8=interferometry
*primary is a known binary

Table F.2: The probability of detecting an exoplanet orbiting either or both stars in a binary, $\mathcal{P}_{\rm det}$, within a 4-year observation period if it has a mass of $10M_J$ (Jupiter mass) or less. Also listed is the minimum detectable mass of a planet, $\lfloor M_P \rfloor$, at a_2 or $a_{\rm crit}$, whichever is smaller. The last column gives the ratio of the estimated nuclear time scale, $\tau_{\rm nuc}$, of the less massive star in the binary system to 10^4 times the orbital period of the system. Dashes can either mean the values of a parameter cannot be computed due to lack of information or not applicable.

HR	Name	$\mathcal{P}_{\rm det}$	a_1^* (AU)	a_2 (AU)	$a_{\rm crit}^\dagger$ (AU)	$a_b^\ddagger$ (AU)	$e_b^\ddagger$	$\lfloor M_P \rfloor$ (M_J)	$\frac{\tau_{\rm nuc}}{(P_b \times 10^4)}$
322	Bet Phe	0.00	>99	>99	>99	>99	0.72	–	0
595	Alp Psc	0.46	0.18	3.70	12.49	184.67	0.70	0.47	1
1465	Alp Dor	0.25	0.21	3.79	0.46	10.39	0.78	4.57	110
1788	Eta Ori	0.00	3.94	5.60	1.90	13.20	0.45	–	3
1839	32 Ori	0.17	0.42	3.91	32.95	148.93	0.22	1.06	1
1852	Del Ori	0.53	0.45	3.04	6.04	55.20	0.56	1.47	36
1931	Sig Ori	0.00	4.66	5.74	24.59	87.57	0.05	8.12	0
2456	15 Mon	0.17	0.52	2.91	1.69	27.04	0.72	4.76	160
3307	Eps Car	0.18	0.45	3.17	20.00	–	–	1.40	–
3485	Del Vel	0.83	0.05	3.01	7.46	49.44	0.48	0.17	12
3482	Eps Hya	0.82	0.09	3.11	0.82	10.10	0.66	1.09	350
3786	Psi Vel	0.99	0.04	2.94	2.41	16.22	0.43	0.15	320
4167		0.57	0.05	2.84	0.54	9.88	0.75	1.50	660
4390	Pi Cen	0.06	0.83	4.65	1.22	28.40	0.79	6.76	3
4552	Bet Hya	0.22	0.23	3.17	20.00	–	–	0.72	–
4689	Eta Vir	0.48	0.29	3.63	3.13	10.98	0.08	2.01	72
4819	Gam Cen	0.86	0.17	3.87	1.45	37.35	0.79	1.20	24
4825	Gam Vir	0.00	0.02	2.78	0.00	42.52	0.88	–	240
4844	Bet Mus	0.22	0.25	3.17	20.00	–	–	0.79	–
5034		0.21	0.26	3.17	20.00	–	–	0.82	–

*planet minimum distance from host star to be detected (see Eq. (8.7))
†planet maximum distance from host star to have stable orbit (see Eq. (8.2))
‡semi-major axis, a_b, and eccentricity, e_b, of host binary star orbit

Table F.2: (continued)

HR	Name	$\mathcal{P}_{\rm det}$	a_1^* (AU)	a_2 (AU)	$a_{\rm crit}^\dagger$ (AU)	$a_b^\ddagger$ (AU)	$e_b^\ddagger$	$\lfloor M_P \rfloor$ (M_J)	$\frac{\tau_{\rm nuc}}{(P_b \times 10^4)}$
5089		0.22	2.46	4.91	6.07	45.75	0.46	5.02	2
5267	Bet Cen	0.00	1.34	5.30	0.00	3.04	0.82	–	12
5396	Tau2Lup	0.00	0.15	2.71	0.00	12.23	0.94	–	1300
5477	Zet Boo	0.00	>99	40.7	0.00	123.92	1.00	–	0
5576	Kap Cen	0.21	0.28	3.17	20.00	–	–	0.89	–
5605	Pi Lup	0.20	0.33	3.17	20.00	–	–	1.03	–
5626	Lam Lup	0.00	6.73	7.22	7.09	65.48	0.55	9.49	0
5683	Mu Lup	0.22	0.25	3.17	20.00	–	–	0.78	–
5708	Eps Lup	0.10	0.38	3.17	20.00	–	–	1.19	–
5704	Gam Cir	0.00	50.2	16.9	0.00	354.33	0.93	–	0
5776	Gam Lup	0.22	1.07	4.80	10.67	84.52	0.51	2.81	0
5787	Gam Lib	0.25	0.12	3.17	20.00	–	–	0.38	–
5881	Mu Ser	0.25	0.12	3.17	20.00	–	–	0.39	–
5953	Del Sco	0.00	1.92	5.54	0.00	14.92	0.94	–	1
6026	Nu Sco	0.10	0.35	3.17	20.00	–	–	1.10	–
6084	Sig Sco	0.09	0.51	3.17	20.00	–	–	1.62	–
6149	Lam Oph	0.92	0.19	3.63	4.44	48.30	0.61	0.53	14
6378	Eta Oph	0.00	0.11	3.80	0.00	37.82	0.95	–	24
6556	Alp Oph	0.00	0.02	2.66	0.00	6.36	0.92	–	970
7194	Zet Sgr	0.86	0.08	3.44	2.78	13.23	0.20	0.32	250
7264	Pi Sgr	0.19	0.38	3.17	20.00	–	–	1.18	–
7882	Bet Del	0.85	0.06	2.92	2.30	13.52	0.36	0.35	530
8368	Del Ind	0.92	0.16	3.31	2.42	9.23	0.10	0.65	310

*planet minimum distance from host star to be detected (see Eq. (8.7))

†planet maximum distance from host star to have stable orbit (see Eq. (8.2))

‡semi-major axis, a_b, and eccentricity, e_b, of host binary star orbit

Table F.3: The average probability of detection per binary system and the probability of detecting one exoplanet ($M_P \leqslant 10 M_J$) from at least one binary system in the MUSCA target list.

MUSCA astrometric precision (μas)	$P_{\rm obs}$ (Yr)	$N_\star$	$\langle \mathcal{P}_{\rm bin} \rangle$	$\mathcal{P}_{\rm mus}$
10	4	33	0.04	0.74
50	4	25	0.02	0.40
100	4	14	0.02	0.21
10	8	33	0.05	0.80
50	8	26	0.03	0.52
100	8	21	0.02	0.30

References

Aerts, C., De Cat, P., Cuypers, J., Becker, S. R., Mathias, P., De Mey, K., Gillet, D., & Waelkens, C. (1998). Evidence for binarity and multiperiodicity in the β Cephei star β Crucis. A&A, 329:137–146.

Airy, G. B. (1846). Account of some circumstances historically connected with the discovery of the planet exterior to Uranus. MNRAS, 7:121–144.

Anglada-Escudé, G., Shkolnik, E. L., Weinberger, A. J., Thompson, I. B., Osip, D. J., & Debes, J. H. (2010). Strong Constraints to the Putative Planet Candidate around VB 10 Using Doppler Spectroscopy. ApJ, 711:L24–L29.

Armstrong, J. T., Clark, III, J. H., Gilbreath, G. C., Hindsley, R. B., Hutter, D. J., Mozurkewich, D., & Pauls, T. A. (2004). Precision narrow-angle astrometry of binary stars with the Navy Prototype Optical Interferometer. In Proc. SPIE, volume 5491, pages 1700–1706.

Armstrong, J. T., Mozurkewich, D., Rickard, L. J., Hutter, D. J., Benson, J. A., Bowers, P. F., Elias, II, N. M., Hummel, C. A., Johnston, K. J., Buscher, D. F., Clark, III, J. H., Ha, L., Ling, L., White, N. M., & Simon, R. S. (1998). The Navy Prototype Optical Interferometer. ApJ, 496:550–571.

Bean, J. L., Seifahrt, A., Hartman, H., Nilsson, H., Reiners, A., Dreizler, S., Henry, T. J., & Wiedemann, G. (2010). The Proposed Giant Planet Orbiting VB 10 Does Not Exist. ApJ, 711:L19–L23.

Bessell, M. S. (1979). UBVRI photometry. II - The Cousins VRI system, its temperature and absolute flux calibration, and relevance for two-dimensional photometry. PASP, 91:589–607.

Boden, A. F. (1999). *Principles of Long Baseline Stellar Interferometry*, course notes Elementary theory of interferometry. Michelson Summer School. JPL Publication.

Bonavita, M. & Desidera, S. (2007). The frequency of planets in multiple systems. A&A, 468:721–729.

Bowler, B. P., Johnson, J. A., Marcy, G. W., Henry, G. W., Peek, K. M. G., Fischer, D. A., Clubb, K. I., Liu, M. C., Reffert, S., Schwab, C., & Lowe, T. B. (2010). Retired A Stars and Their Companions. III. Comparing the Mass-Period Distributions of Planets Around A-Type Stars and Sun-Like Stars. ApJ, 709:396–410.

Buscher, D. F. (1994). A thousand and one nights of seeing on Mt. Wilson. In Proc. SPIE, volume 2200, pages 260–271. SPIE.

Campbell, B., Walker, G. A. H., & Yang, S. (1988). A search for substellar companions to solar-type stars. ApJ, 331:902–921.

Casertano, S., Lattanzi, M. G., Sozzetti, A., Spagna, A., Jancart, S., Morbidelli, R., Pannunzio, R., Pourbaix, D., & Queloz, D. (2008). Double-blind test program for astrometric planet detection with Gaia. A&A, 482:699–729.

Caussin de Perceval, A. P. (1804). Le livre de la grande table Hakémite. *Notices et extraits des manuscrits de la Bibliothèque nationale*, 7:16–240.

Chelli, A. (2000). Optimizing Doppler estimates for extrasolar planet detection. I. A specific algorithm for shifted spectra. A&A, 358:L59–L62.

Colavita, M., Wallace, J., Hines, B., Gursel, Y., Malbet, F., Palmer, D., Pan, X., Shao, M., Yu, J., Boden, A., & Others (1999). The Palomar testbed interferometer. ApJ, 510:505–521.

Colavita, M. M. (1992). Phase Referencing for Stellar Interferometry. In Beckers, J. M. & Merkle, F., editors, *European Southern Observatory Conference and Workshop Proceedings*, volume 39 of *European Southern Observatory Conference and Workshop Proceedings*, pages 845–851.

Cumming, A., Butler, R. P., Marcy, G. W., Vogt, S. S., Wright, J. T., & Fischer, D. A. (2008). The Keck Planet Search: Detectability and the Minimum Mass and Orbital Period Distribution of Extrasolar Planets. PASP, 120:531–554.

Cumming, A., Marcy, G. W., & Butler, R. P. (1999). The Lick Planet Search: Detectability and Mass Thresholds. ApJ, 526:890–915.

Daendliker, R., Thalmann, R., & Prongue, D. (1988). Two-wavelength laser interferometry using superheterodyne detection. *Optics Letters*, 13:339–341.

Davis, J., Lawson, P. R., Booth, A. J., Tango, W. J., & Thorvaldson, E. D. (1995). Atmospheric path variations for baselines up to 80m measured with the Sydney University Stellar Interferometer. MNRAS, 273:L53–L58.

Davis, J., Mendez, A., Seneta, E. B., Tango, W. J., Booth, A. J., O'Byrne, J. W., Thorvaldson, E. D., Ausseloos, M., Aerts, C., & Uytterhoeven, K. (2005). Orbital parameters, masses and distance to β Centauri determined with the Sydney University Stellar Interferometer and high-resolution spectroscopy. MNRAS, 356:1362–1370.

Davis, J. & Tango, W. (1996). Measurement of the Atmospheric Coherence Time. PASP, 108:456–+.

Davis, J., Tango, W. J., Booth, A. J., ten Brummelaar, T. A., Minard, R. A., & Owens, S. M. (1999). The Sydney University Stellar Interferometer - I. The instrument. MNRAS, 303:773–782.

De Rosa, R. J., Patience, J., Vigan, A., Wilson, P. A., Schneider, A., McConnell, N. J., Wiktorowicz, S. J., Marois, C., Song, I., Macintosh, B., Graham, J. R., Bessell, M. S., Doyon, R., & Lai, O. (2012). The Volume-limited A-Star (VAST) survey - II. Orbital motion monitoring of A-type star multiples. MNRAS, 422:2765–2785.

de Santillana, G. & von Dechend, H. (1977). *Hamlet's Mill*. David R. Godine.

Delplancke, F. (2008). The PRIMA facility phase-referenced imaging and microarcsecond astrometry. *New Astronomy Review*, 52:199–207.

Dumusque, X., Pepe, F., Lovis, C., Ségransan, D., Sahlmann, J., Benz, W., Bouchy, F., Mayor, M., Queloz, D., Santos, N., & Udry, S. (2012). An Earth-mass planet orbiting α Centauri B. Nature, 491:207–211.

Dvorak, R. (1986). Critical orbits in the elliptic restricted three-body problem. A&A, 167:379–386.

Dyck, H. M., Benson, J. A., & Schloerb, F. P. (1995). Imaging a Binary Star With a Two-Telescope Michelson Stellar Interferometer. AJ, 110:1433–+.

Edlén, B. (1966). The refractive index of air. *Metrologia*, 2(2):71.

Erickson, K. E. (1962). Investigation of the invariance of atmospheric dispersion with a long-path refractometer. *J. Opt. Soc. Am.*, 52(7):777–780.

Fomalont, E. B. & Wright, M. C. H. (1974). *Galactic and Extra-Galactic Radio Astronomy*, chapter Interferometry and Aperture Synthesis, pages 256–290. Springer.

Fried, D. L. (1965). Statistics of a Geometric Representation of Wavefront Distortion. *Journal of the Optical Society of America (1917-1983)*, 55:1427–1431.

Fritz, T., Gillessen, S., Trippe, S., Ott, T., Bartko, H., Pfuhl, O., Dodds-Eden, K., Davies, R., Eisenhauer, F., & Genzel, R. (2010). What is limiting near-infrared astrometry in the Galactic Centre? MNRAS, 401:1177–1188.

Galland, F., Lagrange, A.-M., Udry, S., Beuzit, J.-L., Pepe, F., & Mayor, M. (2006). Extrasolar planets and brown dwarfs around A-F type stars. IV. A candidate brown dwarf around the A9V pulsating star HD 180777. A&A, 452:709–714.

Galland, F., Lagrange, A.-M., Udry, S., Chelli, A., Pepe, F., Queloz, D., Beuzit, J.-L., & Mayor, M. (2005). Extrasolar planets and brown dwarfs around A-F type stars. I. Performances of radial velocity measurements, first analyses of variations. A&A, 443:337–345.

Gillessen, S., Eisenhauer, F., Perrin, G., Brandner, W., Straubmeier, C., Perraut, K., Amorim, A., Schöller, M., Araujo-Hauck, C., Bartko, H., Baumeister, H., Berger, J., Carvas, P., Cassaing, F., Chapron, F., Choquet, E., Clenet, Y., Collin, C., Eckart, A., Fedou, P., Fischer, S., Gendron, E., Genzel, R., Gitton, P., Gonte, F., Gräter, A., Haguenauer, P., Haug, M., Haubois, X., Henning, T., Hippler, S., Hofmann, R., Jocou, L., Kellner, S., Kervella, P., Klein, R., Kudryavtseva, N., Lacour, S., Lapeyrere, V., Laun, W., Lena, P., Lenzen, R., Lima, J., Moratschke, D., Moch, D., Moulin, T., Naranjo, V., Neumann, U., Nolot, A., Paumard, T., Pfuhl, O., Rabien, S., Ramos, J., Rees, J. M., Rohloff, R., Rouan, D., Rousset, G., Sevin, A., Thiel, M., Wagner, K., Wiest, M., Yazici, S., & Ziegler, D. (2010). GRAVITY: a four-telescope beam combiner instrument for the VLTI. In Proc. SPIE, volume 7734.

Gilliand, Y. (1992). Optical Path Length Compensator for SUSI. Master's thesis, The University of Sydney.

Glindemann, A. (2011). *Principles of Stellar Interferometry*. Astronomy and Astrophysics Library. Springer.

Glindemann, A., Abuter, R., Carbognani, F., Delplancke, F., Derie, F., Gennai, A., Gitton, P. B., Kervella, P., Koehler, B., Leveque, S. A., Menardi, S., Michel, A., Paresce, F., Duc, T. P., Richichi, A., Schoeller, M., Tarenghi, M., Wallander,

A., & Wilhelm, R. (2000). The VLT Interferometer: a unique instrument for high-resolution astronomy. In Proc. SPIE, volume 4006, pages 2–12.

Hanbury Brown, R., Davis, J., & Allen, L. R. (1974). The angular diameters of 32 stars. MNRAS, 167:121–136.

Hartkopf, W. I., Tokovinin, A., & Mason, B. D. (2012). Speckle Interferometry at SOAR in 2010 and 2011: Measures, Orbits, and Rectilinear Fits. AJ, 143:42.

Hartner, W. (1980). Ptolemy and Ibn Yunus on solar parallax. *Arch. Int. Hist. Sci., Vol. 30, p. 5 - 26*, 30:5–26.

Harvey, A. S., Stickland, D. J., Howarth, I. D., & Zuiderwijk, E. J. (1987). Spectroscopic binary orbits from photoelectric radial velocities. Paper 3: delta Orionis. *The Observatory*, 107:205–210.

Hatzes, A. P., Cochran, W. D., Endl, M., McArthur, B., Paulson, D. B., Walker, G. A. H., Campbell, B., & Yang, S. (2003). A Planetary Companion to γ Cephei A. ApJ, 599:1383–1394.

Holman, M. J. & Wiegert, P. A. (1999). Long-Term Stability of Planets in Binary Systems. AJ, 117:621–628.

INT4 (2013). Fourth Catalog of Interferometric Measurements of Binary Stars. `http://ad.usno.navy.mil/wds/int4.html`.

Ireland, M. J. (2006). *Optical Interferometry and Mira Variable Stars*. PhD thesis, The University of Sydney.

Ireland, M. J. (2010a). How many bright stars of the night sky harbour planets? ARC Discovery Project Proposal (ARC grant #: DP1094977).

Ireland, M. J. (2010b). The PAVO wavelength scale (Internal SUSI report). The University of Sydney.

Ireland, M. J., Mérand, A., ten Brummelaar, T. A., Tuthill, P. G., Schaefer, G. H., Turner, N. H., Sturmann, J., Sturmann, L., & McAlister, H. A. (2008). Sensitive visible interferometry with PAVO. In Proc. SPIE, volume 7013.

Ishimaru, A. (1997). *Wave propagation and scattering in random media*. IEEE Press.

Janson, M., Bonavita, M., Klahr, H., Lafrenière, D., Jayawardhana, R., & Zinnecker, H. (2011). High-contrast Imaging Search for Planets and Brown Dwarfs around the Most Massive Stars in the Solar Neighborhood. ApJ, 736:89.

Johnson, J. A., Howard, A. W., Bowler, B. P., Henry, G. W., Marcy, G. W., Wright, J. T., Fischer, D. A., & Isaacson, H. (2010). Retired A Stars and Their Companions. IV. Seven Jovian Exoplanets from Keck Observatory. PASP, 122:701–711.

Kanas, N. (2007). *Star Maps: History, Artistry, and Cartography*. Springer.

Karttunen, H., Krüger, P., Oja, H., Poutanen, M., & Donner, K. J. (2007). *Fundamental Astronomy*. Springer, 5th edition.

Kennedy, G. M. & Kenyon, S. J. (2008). Planet Formation around Stars of Various Masses: The Snow Line and the Frequency of Giant Planets. ApJ, 673(1):502–512.

Kervella, P., Mérand, A., Petr-Gotzens, M. G., Pribulla, T., & Thévenin, F. (2013). The nearby eclipsing stellar system δ Velorum. IV. Differential astrometry with VLT/NACO at the 100 microarcsecond level. A&A, 552:A18.

King, D. A. (1973). Ibn Yunus' Very Useful Tables for Reckoning Time by the Sun. *Archive for History of Exact Sciences*, 10(3-5):342–394.

Kobulnicky, H. A. & Fryer, C. L. (2007). A New Look at the Binary Characteristics of Massive Stars. ApJ, 670:747–765.

Kok, Y., Ireland, M. J., Robertson, J. G., Tuthill, P. G., Warrington, B. A., & Tango, W. J. (2013a). Low-cost scheme for high-precision dual-wavelength laser metrology. Appl. Opt., 52(12):2808–2814.

Kok, Y., Maestro, V., Ireland, M. J., Tuthill, P. G., & Robertson, J. G. (2013b). Simulating a dual beam combiner at SUSI for narrow-angle astrometry. *Experimental Astronomy*, 36:195–221.

Kouwenhoven, M. B. N., Brown, A. G. A., Portegies Zwart, S. F., & Kaper, L. (2007). The primordial binary population. II.. Recovering the binary population for intermediate mass stars in Scorpius OB2. A&A, 474:77–104.

Kraus, A. L. & Ireland, M. J. (2012). LkCa 15: A Young Exoplanet Caught at Formation? ApJ, 745:5.

Kraus, A. L., Ireland, M. J., Hillenbrand, L. A., & Martinache, F. (2012). The Role of Multiplicity in Disk Evolution and Planet Formation. ApJ, 745:19.

Kurucz, R. L. (2012). Linelists. http://kurucz.harvard.edu/linelists.html.

Lane, B. F. & Muterspaugh, M. W. (2004). Differential Astrometry of Subarcsecond Scale Binaries at the Palomar Testbed Interferometer. ApJ, 601:1129–1135.

Lane, R. G., Glindemann, A., & Dainty, J. C. (1992). Simulation of a Kolmogorov phase screen. *Waves in Random Media*, 2:209–224.

Lawson, P. R., Colavita, M. M., Dumont, P. J., & Lane, B. F. (2000). Least-squares estimation and group delay in astrometric interferometers. In Proc. SPIE, volume 4006, pages 397–406.

Levato, H., Malaroda, S., Morrell, N., & Solivella, G. (1987). Stellar multiplicity in the Scorpius-Centaurus association. ApJS, 64:487–503.

Lindegren, L. (1980). Atmospheric limitations of narrow-field optical astrometry. A&A, 89:41–47.

Lovis, C. & Mayor, M. (2007). Planets around evolved intermediate-mass stars. I. Two substellar companions in the open clusters NGC 2423 and NGC 4349. A&A, 472:657–664.

Lucas, R. E. (2004). Electronic subsystems for the Sydney University Stellar Interferometer. Master's thesis, The University of Sydney.

Maestro, V., Kok, Y., Huber, D., Ireland, M. J., Tuthill, P. G., White, T., Schaefer, G., ten Brummelaar, T. A., McAlister, H. A., Turner, N., Farrington, C. D., & Goldfinger, P. J. (2012). Imaging rapid rotators with the PAVO beam combiner at CHARA. In Proc. SPIE, volume 8445.

Maíz Apellániz, J. (2010). High-resolution imaging of Galactic massive stars with AstraLux. I. 138 fields with $\delta > -25^{\circ}$. A&A, 518:A1.

Malbet, F., Léger, A., Shao, M., Goullioud, R., Lagage, P.-O., Brown, A. G. A., Cara, C., Durand, G., Eiroa, C., Feautrier, P., Jakobsson, B., Hinglais, E., Kaltenegger, L., Labadie, L., Lagrange, A.-M., Laskar, J., Liseau, R., Lunine, J., Maldonado, J., Mercier, M., Mordasini, C., Queloz, D., Quirrenbach, A., Sozzetti, A., Traub, W., Absil, O., Alibert, Y., Andrei, A. H., Arenou, F., Beichman, C., Chelli, A., Cockell, C. S., Duvert, G., Forveille, T., Garcia, P. J. V., Hobbs, D., Krone-Martins, A., Lammer, H., Meunier, N., Minardi, S., Moitinho de Almeida, A., Rambaux, N., Raymond, S., Röttgering, H. J. A., Sahlmann, J., Schuller, P. A., Ségransan, D., Selsis, F., Surdej, J., Villaver, E., White, G. J., & Zinnecker, H. (2012). High precision astrometry mission for the detection and characterization of nearby habitable planetary systems with the Nearby Earth Astrometric Telescope (NEAT). *Experimental Astronomy*, 34:385–413.

Marcy, G., Butler, R. P., Fischer, D., Vogt, S., Wright, J. T., Tinney, C. G., & Jones, H. R. A. (2005). Observed Properties of Exoplanets: Masses, Orbits, and Metallicities. *Progress of Theoretical Physics Supplement*, 158:24–42.

Marois, C., Macintosh, B., Barman, T., Zuckerman, B., Song, I., Patience, J., Lafrenière, D., & Doyon, R. (2008). Direct Imaging of Multiple Planets Orbiting the Star HR 8799. *Science*, 322:1348–.

Mason, B. D., Hartkopf, W. I., Gies, D. R., Henry, T. J., & Helsel, J. W. (2009). The High Angular Resolution Multiplicity of Massive Stars. AJ, 137:3358–3377.

Mayer, P., Harmanec, P., Wolf, M., Božić, H., & Šlechta, M. (2010). Physical elements of the eclipsing binary δ Orionis. A&A, 520:A89.

Mayor, M. & Queloz, D. (1995). A Jupiter-mass companion to a solar-type star. Nature, 378:355–359.

McAlister, H. A., ten Brummelaar, T. A., Gies, D. R., Huang, W., Bagnuolo, Jr., W. G., Shure, M. A., Sturmann, J., Sturmann, L., Turner, N. H., Taylor, S. F., Berger, D. H., Baines, E. K., Grundstrom, E., Ogden, C., Ridgway, S. T., & van Belle, G. (2005). First Results from the CHARA Array. I. An Interferometric and Spectroscopic Study of the Fast Rotator α Leonis (Regulus). ApJ, 628:439–452.

McGlamery, B. L. (1976). Computer simulation studies of compensation of turbulence degraded images. In Proc. SPIE, volume 74, pages 225–233.

Michelson, A. A. & Pease, F. G. (1921). Measurement of the diameter of alpha Orionis with the interferometer. ApJ, 53:249–259.

Monnier, J. D. (2003). Optical interferometry in astronomy. *Reports on Progress in Physics*, 66:789–857.

Monnier, J. D. (2007). Phases in interferometry. *New Astronomy Reviews*, 51(8-9):604 – 616. Observation and Data Reduction with the VLT Interferometer - Proceedings of the VLTI Euro Summer School held in Goutelas, France, 4-16 June 2006.

Murray, C. A. (1983). *Vectorial astrometry*. Adam Hilger.

Muterspaugh, M. W., Lane, B. F., Kulkarni, S. R., Konacki, M., Burke, B. F., Colavita, M. M., Shao, M., Hartkopf, W. I., Boss, A. P., & Williamson, M. (2010a). The Phases Differential Astrometry Data Archive. V. Candidate Substellar Companions to Binary Systems. AJ, 140:1657–1671.

Muterspaugh, M. W., Lane, B. F., Kulkarni, S. R., Konacki, M., Burke, B. F., Colavita, M. M., Shao, M., Wiktorowicz, S. J., & O'Connell, J. (2010b). The Phases Differential Astrometry Data Archive. I. Measurements and Description. AJ, 140:1579–1622.

Noll, R. J. (1976). Zernike polynomials and atmospheric turbulence. *J. Opt. Soc. Am.*, 66(3):207–211.

North, J. R. (2007). *Fundamental stellar astrophysics with an improved SUSI array*. PhD thesis, The University of Sydney.

North, J. R., Davis, J., Tuthill, P. G., Tango, W. J., & Robertson, J. G. (2007). Orbital solution and fundamental parameters of σ Scorpii. MNRAS, 380:1276–1284.

Obukhov, A. M. (1949). Temperature field structure in a turbulent flow. *Izv. Acad. Nauk SSSR Ser. Geog. Geofiz*, 13:58–69.

ORB6 (2013). Sixth Catalog of Orbits of Visual Binary Stars. `http://ad.usno.navy.mil/wds/orb6.html`.

Perryman, M. A. C., Lindegren, L., Kovalevsky, J., Hoeg, E., Bastian, U., Bernacca, P. L., Crézé, M., Donati, F., Grenon, M., Grewing, M., van Leeuwen, F., van der Marel, H., Mignard, F., Murray, C. A., Le Poole, R. S., Schrijver, H., Turon, C., Arenou, F., Froeschlé, M., & Petersen, C. S. (1997). The HIPPARCOS Catalogue. A&A, 323:L49–L52.

Popper, D. M. (1968). On the Narrabri Scale of Absolute Stellar Fluxes. ApJ, 151:L51.

Pravdo, S. H. & Shaklan, S. B. (2009). An ultracool Star's Candidate Planet. ApJ, 700:623–632.

Raghavan, D., McAlister, H. A., Henry, T. J., Latham, D. W., Marcy, G. W., Mason, B. D., Gies, D. R., White, R. J., & ten Brummelaar, T. A. (2010). A Survey of Stellar Families: Multiplicity of Solar-type Stars. ApJS, 190:1–42.

Robertson, J. G., Ireland, M. J., Tango, W. J., Davis, J., Tuthill, P. G., Jacob, A. P., Kok, Y., & Ten Brummelaar, T. A. (2010). Instrumental developments for the Sydney University Stellar Interferometer. In Proc. SPIE, volume 7734.

Robertson, J. G., Ireland, M. J., Tango, W. J., Tuthill, P. G., Warrington, B. A., Kok, Y., Rizzuto, A. C., Cheetham, A., & Jacob, A. P. (2012). Science and technology progress at the Sydney University Stellar Interferometer. In Proc. SPIE, volume 8445.

Roddier, F. (1981). The Effects of Atmospheric Turbulence in Optical Astronomy. Prog. Optics, 19:281–376.

Sasiela, R. J. & Shelton, J. D. (1993). Transverse spectral filtering and Mellin transform techniques applied to the effect of outer scale on tilt and tilt anisoplanatism. *J. Opt. Soc. Am. A*, 10:646–660.

Scargle, J. D. (1989). Studies in astronomical time series analysis III. Fourier transforms, autocorrelation functions, and cross correlation functions of unevenly spaced data. ApJ, 343:874–887.

Schuhler, N., Salvadé, Y., Lévêque, S., Dändliker, R., & Holzwarth, R. (2006). Frequency-comb-referenced two-wavelength source for absolute distance measurement. *Optics Letters*, 31:3101–3103.

Seneta, E. B. (1992). A video acquisition system for the Sydney University Stellar Interferometer. Master's thesis, The University of Sydney.

Shaklan, S. B. (1989). *Multiple Beam Correlation Using Single-Mode Fiber Optics with Application to Interferometric Imaging.* PhD thesis, The University of Arizona.

Shao, M. & Colavita, M. (1992). Potential of long-baseline infrared interferometry for narrow-angle astrometry. A&A, 262:353–358.

Sozzetti, A. (2011). Astrometry and Exoplanets: The Gaia Era and Beyond. In *EAS Publications Series*, volume 45 of *EAS Publications Series*, pages 273–278.

Svelto, O. (1998). *Principles of Lasers.* Plenum Press, 4th edition.

Tango, W. J. (1990). Dispersion in stellar interferometry. Appl. Opt., 29:516–521.

Tango, W. J. (2006). The determination of the orbital elements of binary stars (Internal SUSI report). The University of Sydney.

Tango, W. J., Davis, J., Jacob, A. P., Mendez, A., North, J. R., O'Byrne, J. W., Seneta, E. B., & Tuthill, P. G. (2009). A new determination of the orbit and masses of the Be binary system δ Scorpii. MNRAS, 396:842–848.

Tango, W. J. & Ireland, M. J. (2010). A new embedded control system for SUSI. In Proc. SPIE, volume 7734.

Taylor, G. I. (1938). The Spectrum of Turbulence. *Royal Society of London Proceedings Series A*, 164:476–490.

ten Brummelaar, T. (1994). Taking the Twinkle Out of the Stars: an Adaptive Wavefront Tilt Correction Servo and Preliminary Seeing Study for SUSI. PASP, 106:915.

Tokovinin, A. (2012). Speckle Interferometry and Orbits of "Fast" Visual Binaries. AJ, 144:56.

Tokovinin, A., Mason, B. D., & Hartkopf, W. I. (2010). Speckle Interferometry at the Blanco and SOAR Telescopes in 2008 and 2009. AJ, 139:743–756.

Tuthill, P., Davis, J., Ireland, M., Jacob, A., North, J., Owens, S., Robertson, J. G., Tango, W., & ten Brummelaar, T. (2008). The SUSI instrument: new science and technology. In Proc. SPIE, volume 7013.

Valley, G. C. (1979). Long- and short-term Strehl ratios for turbulence with finite inner and outer scales. Appl. Opt., 18:984–987.

van Leeuwen, F. (2007). Validation of the new Hipparcos reduction. A&A, 474:653–664.

Vigan, A., Patience, J., Marois, C., Bonavita, M., De Rosa, R. J., Macintosh, B., Song, I., Doyon, R., Zuckerman, B., Lafrenière, D., & Barman, T. (2012). The International Deep Planet Survey. I. The frequency of wide-orbit massive planets around A-stars. A&A, 544:A9.

Walkup, J. F. & Goodman, J. W. (1973). Limitations of fringe-parameter estimation at low light levels. *J. Opt. Soc. Am.*, 63:399.

WDS (2013). Washington Visual Double Star Catalog. `http://ad.usno.navy.mil/wds/orb6.html`.

Woillez, J. & Lacour, S. (2013). Wide-angle, Narrow-angle, and Imaging Baselines of Optical Long-baseline Interferometers. ApJ, 764:109.

Zaber (2006). *T-Series Positioning Products Technical Notes*. Zaber Technologies Inc, 2006-02-03 edition.

Zasche, P., Wolf, M., Hartkopf, W. I., Svoboda, P., Uhlař, R., Liakos, A., & Gazeas, K. (2009). A Catalog of Visual Double and Multiple Stars With Eclipsing Components. AJ, 138:664–679.

Zernike, F. (1938). The concept of degree of coherence and its application to optical problems. *Physica*, 5:785–795.